Dipl.-Ing. Gernot Bukovnik

Computational and Experimental Study on the Impact of Numerical Wheel Rotation Methods on Road Vehicle Aerodynamics Simulations

PhD Thesis
to achieve the university degree of
„Doktor der Technischen Wissenschaften“

submitted to
Graz University of Technology

Supervisor
Univ.-Prof. Dipl.-Phys. Dr.rer.nat. Wolfgang von der Linden
Institute of Theoretical and Computational Physics

Co-Supervisor
Univ.-Prof. Dr.-Ing. habil. Günter Brenn
Institute of Fluid Mechanics and Heat Transfer

Graz, April 2020

Statutory Declaration

I declare that I have authored this thesis independently, that I have not used other than the declared sources/resources, and that I have explicitly indicated all material which has been quoted either literally or by content from the sources used.

Date

Signature

Kurzfassung

Frühere Studien haben gezeigt, dass Räder einen der einflussreichsten Faktoren auf die Aerodynamik des Fahrzeugs darstellen, da der Interaktion des Strömungsfeldes mit ihnen und den daraus entstehenden Interferenzeffekten bis zu 25% des aerodynamischen Luftwiderstands zugeordnet werden können. In Anbetracht der Anforderungen, welche die Einführung des *WLTP* (Worldwide harmonized Light vehicles Test Procedure) an die aerodynamische Entwicklungsstrategie repräsentiert, ist der Einfluss von rotierenden Rädern auf das Verhalten des fluiddynamischen Systems im Nahbereich des Fahrzeuges eine entscheidende Komponente für die Zielwerterreichung in der industriellen Fahrzeugentwicklung. Die Simulation der Radrotation stellt jedoch eine vergleichsweise neue und anspruchsvolle Disziplin in der numerischen Strömungsmechanik dar. Aktuell existieren keine validierten Simulationsmethoden zur Modellierung der aerodynamischen Effekte der Radrotation auf das Fahrzeug.

Den Kern dieser Arbeit bildet daher die Untersuchung des Einflusses numerischer Radrotationsverfahren auf die aerodynamischen Eigenschaften von Personenkraftwagen mit besonderem Fokus auf relevante Aspekte für die aerodynamische Entwicklung von Serienfahrzeugen. Zentrales Thema dieser Studie ist die Untersuchung und Validierung des Einflusses von *MW* (Moving Wall) und *MRF* (Multiple Reference Frame) basierten Rotationsmethoden auf die lokale Umströmung des Rades im Radhaus und in weiterer Folge auf die Strömungstopologie um das Fahrzeug, welche schlussendlich die aerodynamischen Fahrzeugkräfte beeinflusst.

Im Rahmen dieser Untersuchung wurden sowohl Messungen im Windkanal, als auch numerische Studien auf Basis von stationären *RANS* (Reynolds-Averaged Navier-Stokes) Simulationen eines voll detaillierten Serienfahrzeuges durchgeführt und verschiedene Aspekte des Einflusses der Radrotation auf das aerodynamische Verhalten eines Straßenfahrzeugs untersucht. In der ersten Projektphase wurde sowohl der Einfluss von verschiedenen Felgengeometrien, als auch von der Felgenorientierung auf die Strömungstopologie und den integralen Gesamtwiderstandsbeiwert des Fahrzeugs ermittelt, wobei gezeigt wurde, dass beide Parameter einen nicht vernachlässigbaren Faktor des aerodynamischen Verhaltens des Fahrzeuges darstellen. In der nachfolgenden Projektphase wurde der Einfluss der einzelnen numerischen Radrotationsmethoden auf die simulierte Aerodynamik des Versuchsfahrzeugs untersucht. Hierfür wurde zunächst die Veränderung der Strömungstopologie innerhalb des Radhauses und in weiterer Folge die des gesamten Fahrzeuges analysiert, wobei Analysen des Strömungsfeldes, der Oberflächendrucksituation und der Entwicklung des integralen, aerodynamischen Gesamtfahrzeugwiderstands durchgeführt wurden. Die numerischen Ergebnisse wurden mit den Daten der Experimente und der Literatur validiert, wobei eine gute Korrelation erzielt werden konnte. Bekannte Strömungsphänomene konnten durch Anwendung der einzelnen Rotationsmethoden reproduziert werden, allerdings mit unterschiedlicher Vorhersagequalität. Dies schließt aerodynamische Effekte im Radhaus und im Bereich des Vorderrades, sowie Änderungen der Strömungssituation auf Grund von Interferenzeffekten stromabwärts entlang des Fahrzeuges bis in dessen Nachlaufgebiet mit ein, welche zu Druckerhöhungen in diesem Bereich führen und sich in weiterer Folge durch eine Erhöhung des Heckbasisdrucks direkt auf den Fahrzeugwiderstand auswirken und diesen reduzieren. Auch der dominante Einfluss der Hinterradrotation auf die Struktur des Fahrzeugnachlaufgebiets und die Tatsache, dass der Großteil der Widerstandsänderung am Fahrzeugkörper und nicht an den Rädern auftritt konnten nachgewiesen und bestätigt werden.

Basierend auf der Vorhersagequalität der Strömungstopologie- und Fahrzeugwiderstandsänderung konnte eine Empfehlung für die Auswahl geeigneter numerischer Radrotationmethoden in der aerodynamischen Serienfahrzeugentwicklung gegeben werden.

Abstract

Previous studies have shown that wheels are one of the most influential factors on the vehicle's aerodynamics, as the interaction of the flow field with them and the resulting interference effects can be attributed to up to 25% of the aerodynamic drag. Considering the requirements of the introduction of the *WLTP* (Worldwide harmonized Light vehicles Test Procedure) to the aerodynamic development strategy, the impact of rotating wheels on the behavior of the fluid dynamical system in the vicinity of the vehicle represents a crucial component for the target achievement in the industrial vehicle development. However, the simulation of wheel rotation represents a comparatively new and challenging discipline in numerical fluid dynamics. Currently there are no validated simulation methods for modeling the aerodynamic effects of wheel rotation on the vehicle.

The core of this work is therefore the investigation of the influence of numerical wheel rotation methods on the aerodynamic properties of passenger cars with special focus on relevant aspects for the aerodynamic development of production vehicles. The central topic of this study is the investigation and validation of the impact of *MW* (Moving Wall) and *MRF* (Multiple Reference Frame) based rotation methods on the local flow around the wheel in the wheel arch and subsequently on the flow topology in the vicinity of the vehicle, which ultimately affects the aerodynamic vehicle forces.

In this study, wind tunnel measurements as well as numerical studies based on steady-state *RANS* (Reynolds-Averaged Navier-Stokes) simulations of a fully detailed production vehicle were carried out and various aspects of the influence of wheel rotation on the aerodynamic behavior of a road vehicle were investigated. In the first phase of the project, the impact of three series rim geometries, as well as the rim orientation on the flow topology and the integral drag of the vehicle was determined. It was shown that both parameters represent a significant factor of the aerodynamic behavior of the vehicle. In the following project phase, the influence of the individual numerical wheel rotation methods on the aerodynamic behaviour of the test vehicle were investigated. For this purpose, first the change of the flow topology within the wheel house and subsequently the whole vehicle was analysed, where investigations of the flow field, the surface pressure distribution and the development of the integral, aerodynamic total vehicle resistance were carried out. The numerical results were validated with the data of the experiments and literature, whereby a good agreement could be achieved. Known flow phenomena could be reproduced by applying the individual rotation methods, but with different predictive quality. This includes aerodynamic effects in the wheel arch and in the region of the front wheel, as well as changes of the flow situation downstream along the vehicle to its wake region due to interference effects. These flow topology alterations lead to pressure increases in the rear area and subsequently directly affect and reduce the vehicle drag due to an increase in the rear base pressure. The dominant impact of the rear wheel rotation on the structure of the vehicle's wake topology, and the fact that the majority of the drag alterations occur at the vehicle body and not on the wheels, could be detected and confirmed.

Based on the predictive quality of the flow topology and vehicle drag change, a recommendation for the selection of suitable numerical wheel rotation methods in the aerodynamic production vehicle development could be made.

Acknowledgements

During my employment in the field of complete vehicle engineering at Magna Steyr, I had the opportunity to work on various research projects with the aim of improving the physical and virtual aerodynamic development process. These activities sparked the desire to contribute with my own research work in this fascinating branch of science, which finally led to the initiation of this project. Since the accomplishment of this study would not have been possible during my occupation and my regular duties, the majority of this dissertation was carried out in my free time as a student of the Doctoral School of Physics at the Graz University of Technology. Throughout this project, I received the generous help and encouragement of many people. At this point I wish to thank all those persons who contributed to the success of this thesis with their valuable professional and personal support.

First of all, I would like to express my deepest appreciation and respect to Prof. Wolfgang von der Linden and Prof. Günter Brenn, who supervised and examined my dissertation. The guidance, helpful suggestions, as well as the critical and fruitful discussions have made me think beyond my borders and have contributed a great deal to the completion of this work. The numerous conversations will always be remembered as an enriching and constructive exchange, which I have always found encouraging and motivating. For the time and effort that was invested in this thesis, as well as for the patience, I would like to thank you.

Furthermore, I would like to extend my sincere thanks to Prof. Andreas Dillmann from the German Aerospace Center (DLR) for the time he invested in the assessment of this work and for his generous scientific support as a second reviewer.

I greatly appreciate the cooperative support received from Dr. Felix Wittmeier from the Research Institute of Automotive Engineering and Vehicle Engines Stuttgart (FKFS), who has always provided valuable advice on important scientific and technical details.

My colleagues at Magna Steyr have made a major contribution to ensure that this dissertation is now available in the actual form. First and foremost I wish to express my deepest gratitude to Robert Premstaller and Michael Kalunder, who gave me the opportunity to start and complete this project successfully through their support and trust.

Furthermore, I would like to recognize the invaluable assistance that my colleagues of the aerodynamics team provided during my study. I am extraordinarily grateful to my friend and colleague Lorenz Schantl, who relentlessly supported me during the last years through many difficult stages of this project with all his experience, resources, interest and helpfulness. Without his generous support, and endless effort, this work would not have been accomplished. Many thanks for all the honest, encouraging and motivating dialogues that have developed those ideas, which contributed significantly to the completion of this dissertation.

I am profoundly indebted to Michael Mandl, who promoted and accompanied my research constantly with his valuable professional and personal support. Without his effort, patient understanding and tolerance it would never have been possible to complete this thesis.

Moreover, I am grateful for the help of Mark Hennings whose constructive criticism on the basis of many years of extensive experience in the aerodynamic field has made a vital contribution to this dissertation. I very much appreciate the time invested in correcting this work, especially for

pointing out weaknesses and showing where there was still need for explanation.

I would like to pay my special regards to my colleagues of the CFD team, in particular to Nicola Di Nardo and Paul Bischof, for their patience and all the fascinating dialogues about the complex computational realm.

I also had great pleasure of working with Christian Neuper and Claudiu Vasiu, whom I could co-supervise in their Bachelor's and/or Master's theses, from which countless fruitful debates and interesting ideas have developed. In this context, I would like to express my gratitude to Christian for the comprehensive assistance and enlightening discussions concerning defying mathematical and physical challenges.

Furthermore, I am grateful to all my friends who were there for me during the time I was working on this demanding project and have supported me morally with much patience. In particular, I wish to thank my cousin Alexander Blümel for consistently encouraging me with professional words of advice and motivation, for his support in dealing with complex analytical problems, as well as for all the long nights of debate (without the latter, this thesis might perhaps have been completed somewhat earlier).

Many thanks to Brigitte Schwarz for the encouraging conversations and for the swift support in handling all the required administrative processes, which has made my activities in this area considerably easier.

Finally, I would like to thank my family, who have always supported me in all my decisions and have made this path of life possible for me. To them I dedicate this work.

Contents

Nomenclature

Latin Symbols

A_p	Projected frontal area of the vehicle	$[m^2]$
A_{part}	Part of the vehicle surface	$[m^2]$
A_{RIM}	Open rim area	$[m^2]$
C_D	Aerodynamic drag coefficient	[-]
C_L	Aerodynamic lift coefficient	[-]
C_P	Aerodynamic pressure coefficient	[-]
C_S	Aerodynamic side force coefficient	[-]
$C_{D,\mathrm{acc}}$	Accumulated aerodynamic drag coefficient	[-]
$C_{D,\mathrm{BODY}}$	Aerodynamic vehicle body drag coefficient	[-]
$C_{D,\mathrm{cool}}$	Aerodynamic cooling drag coefficient	[-]
$C_{D,\mathrm{CV}}$	Aerodynamic vehicle drag coefficient	[-]
$C_{D,\mathrm{WHEELS}}$	Aerodynamic wheel drag coefficient	[-]
F_D	Aerodynamic drag	$[N]$
$F_{D,\mathrm{acc}}$	Accumulated aerodynamic drag	$[N]$
F_L	Aerodynamic lift	$[N]$
F_S	Aerodynamic side force	$[N]$
F_T	Aerodynamic total force	$[N]$
$F_{L,\mathrm{fr}}$	Aerodynamic lift at the front axle	$[N]$
$F_{L,\mathrm{rr}}$	Aerodynamic lift at the rear axle	$[N]$
g	Gravitational acceleration	$[m\,s^{-2}]$
m	Mass	$[kg]$
$\dot{m}$	Air mass flow rate	$[kg\,s^{-1}]$
Ma	Mach number	$[-]$
$\vec{M}_\mathrm{Pitch}$	Aerodynamic pitching moment	$[Nm]$
$\vec{M}_\mathrm{Roll}$	Aerodynamic rolling moment	$[Nm]$

$\vec{M}_{\text{Yaw}}$	Aerodynamic yawing moment	$[Nm]$
$\vec{n}$	Normal unit vector	$[-]$
p	Static pressure	$[Pa]$
p_0	Total pressure	$[Pa]$
p_∞	Free-stream static pressure	$[Pa]$
q	Dynamic pressure	$[Pa]$
Re	Reynolds number	$[-]$
T	Temperature	$[K]$
t	Time	$[s]$
$\vec{u}(u,v,w)$	Velocity vector	$[m\,s^{-1}]$
v_∞	Free-stream air velocity	$[m\,s^{-1}]$
x, y, z	Cartesian coordinates	$[m]$
$x/y/z_{\text{min/max,CV}}$	Minimum and maximum complete-vehicle positions	$[m]$
y^+	Dimensionless wall distance	[-]

Greek Symbols

Δ	Laplace operator	$[m^{-2}]$
μ	Dynamic viscosity	$[N\,s\,m^{-2}]$
∇	Nabla operator	$[m^{-1}]$
ν	Kinematic viscosity	$[m^2\,s^{-1}]$
Ω	Control volume	$[-]$
ω	Rotational velocity	$[rad\,s^{-1}]$
$\partial\Omega$	Surface area of a control volume	$[-]$
σ	Normal stress	$[Pa]$
τ	Shear stress	$[Pa]$
ρ	Air density	$[kg\,m^{-3}]$
$\boldsymbol{\sigma}$	Stress tensor	$[Pa]$

Abbreviations

(U)RANS	(Unsteady) Reynolds-Averaged Navier-Stokes
CAD	Computer-Aided Design
CAE	Computer-Aided Engineering
CFD	Computational Fluid Dynamics
CV	Complete-Vehicle

DNS	Direct Numerical Simulation
HXC	Heat Exchanger
LDV	Laser Doppler Velocimetry
LES	Large Eddy Simulation
MRF	Multiple Reference Frame
MW	Moving Wall
NR	No Rotation (stationary wheels)
OEM	Original Equipment Manufacturer
PIV	Particle Image Velocimetry
RT	Rotation (rotating wheels)
SM	Sliding Mesh
TW	Track Width
VZ	Vehicle Zone
WB	Wheel Base
WH	Wheel House
WLTP	Worldwide harmonized Light vehicles Test Procedure
WT	Wind Tunnel

Definitions

Base	Rearmost part of a vehicle

Chapter 1

Motivation

In recent years, the difference in fuel consumption of road vehicles between real road performance and the published indications of vehicle manufacturers has significantly increased [1, 2]. In 2017, the average difference between published and real fuel consumption of a passenger car was around 39% (Fig. 1.1). According to forecasts, this difference might grow to 46% by 2020, with the same trend.

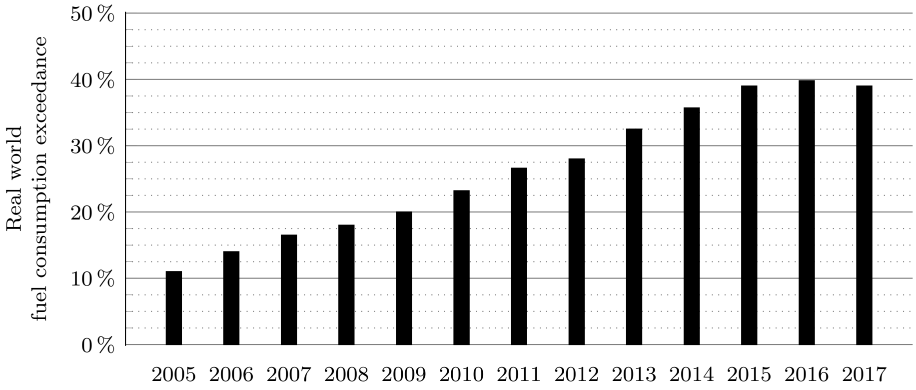

Figure 1.1: Growing gap between real world and experiment [2].

In order to eliminate the deviations in fuel consumption data and CO_2 emissions of a vehicle between the indications of car manufacturers and the actual real-world vehicle performance, a new regulatory standard, also known as *WLTP* (Worldwide harmonized Light Vehicles Test Procedure) [3], has been developed. This standard is currently introduced and implemented across Europe and Japan, and other markets could follow in the coming years.

The discrepancies in consumption data can be attributed to several causes, such as differing test processes and test methods during the vehicle development, divergences between the test environment and the real conditions on the road, as well as unrealistic driving cycles. Some of these deviations can partly be attributed to vehicle aerodynamics. Significant in this context are test tolerances and correction approaches of measuring methods, as well as idealized boundary conditions for wind tunnel experiments and coasting tests, as well as tolerances in vehicle production and simplifications in the creation of numerical simulation models. However, one of the biggest and most important impacts is that current regulations facilitate the possibility to classify various configurations of the same vehicle by specifying a single physical quantity, namely the aerodynamic drag coefficient. Usually, only one drag value is published for all vehicle configurations, which in many cases corresponds to the aerodynamically most efficient setup, irrespective of the sales figures of this configuration. For this reason, the published drag value is usually too optimistic compared to the real value of a vehicle.

The *WLTP* tries to solve this problem by requiring all vehicle configurations to be certified, which means that the consumption must be specified for each vehicle configuration. Furthermore, an additional test standard will be introduced together with the *EU6d Emission Regulation* [3] by 2020, which is intended to complement laboratory-based test procedures in the future. This *Real Driving Emission* or *RDE* [3] test procedure stipulates that fuel consumption values for each vehicle configuration must be verified in real on-road tests. Thus, the real road is introduced as an additional test environment for emission verification, which represents a new challenge for the automotive industry since the measurements take place directly on the road. Compared to currently used test environments, which have been developed for idealized boundary conditions, real boundary conditions and external influences, such as the road profile, environmental conditions, traffic, driving behavior of the driver, are taken into account when measuring a vehicle on the road. This is the last and decisive step to minimize or even eliminate the difference between the OEM's consumption claims and the real values on the road.

The introduction of the *WLTP* requires the aerodynamic developers in the vehicle industry to publish and verify the consumption and thus the aerodynamic coefficient of all vehicle configurations. If a vehicle manufacturer does not want to test and identify all possible configurations, there are only two alternative ways to meet *WLTP* requirements: Either one consumption value has to be published which corresponds to the vehicle configuration with the highest fuel consumption, or the number of available configurations of a vehicle must be reduced in order to perform fewer tests. However, if an OEM would only publish one worst-case value for all vehicle configurations, it would also automatically apply to configurations that have much better and more efficient energy consumption. Since the fleet consumption is based on the consumption values of each individual vehicle produced by the vehicle manufacturer, the specification of a single worst-case value for a vehicle series would automatically raise the total fleet consumption value, which in the worst case could lead to penalty payments for the OEM [4]. Moreover, since in some countries the vehicle tax is calculated on the basis of the CO_2 emissions of the vehicle, this scenario would result directly in higher operating costs of its vehicle for many end users, which could adversely affect the customer's purchasing decision. The customer typically desires to individualize his/her vehicle and extend the basic configuration by additional equipment such as higher engine variances or larger tires and rims and/or choose a higher trim level. Such additional equipment generates additional profit for the vehicle manufacturer, wherefore a reduction in the number of vehicle configurations is not a possible option for many OEMs as this would have a direct negative impact on the expected profit. Since none of these two options is attractive for the vehicle manufacturer, it will ultimately have to test and verify all configurations to be able to identify the energy consumption of all vehicle configurations in order to neither publish a worst-case fuel consumption value nor reduce the number of configurations. Considering the fact that a variety of optional equipment exists for a vehicle, such as various trim levels, different engine variants, or rim/tire combinations, it can be concluded that the number of vehicles to be tested by the OEMs will increase significantly in the future.

Although the *WLTP* is initially only introduced to the European and Japanese markets, vehicle manufacturers in other parts of the world have to face similar challenges. Due to increasing exhaust gas regulations worldwide, vehicle manufacturers are forced to develop new technologies to meet these requirements and continue to exist on the world market. One of these technologies is, for example, electric vehicles. The electrification of vehicles presents the OEMs with similar challenges as the *WLTP*. Since the recharge of these vehicles is still time-intensive and also complicated due to the general lack of infrastructure, it is very interesting for the customer to know the remaining available range of his vehicle. In order to be able to produce an exact range prognosis, it is imperative to know the exact aerodynamic drag of its specific vehicle configuration. In order to be able to precisely determine the range of each vehicle and make it available to the customer, all OEMs must therefore know the aerodynamics of each individual offered vehicle configuration.

The introduction of the *WLTP* also demands an adaptation of the aerodynamic development process in the vehicle industry. Typically, a basic variant is developed and optimized during the entire development process. Only in a very late phase of the development process, vehicle details, such as different rim and tire combinations, are considered in order to determine their impact on the vehicle aerodynamics and thus define the aerodynamically optimal configuration. Since the aerodynamic coefficients of all vehicle configurations are published under the *WLTP*, project target values are also defined for each configuration. Therefore all configurations must be taken into account already from the beginning of the development process in order to finally reach the project targets and furthermore fulfill also the aerodynamic fleet targets. In accordance with these requirements, a new development strategy has to be found which considers the impact of rim and tire combinations on vehicle aerodynamics from early project phases on and also minimize the risk of not fulfilling aerodynamics project targets. Due to the high number of possible combinations of various trim levels, rim geometries, tire variants and variations of other aerodynamically relevant components, on the one hand, and the limited development time in the wind tunnel on the other hand, development and verification in the wind tunnel alone is just not feasible. An alternative development strategy is provided by numerical methods, such as Computational Fluid Dynamics (*CFD*), which allow these additional studies to be performed in relatively short times and at low costs. As numerical methods have evolved into an important additional development tool in recent years, they represent a natural and reasonable way to test and evaluate these numerous vehicle combinations.

The validation of vehicle aerodynamics under *WLTP* also includes a large number of rim and tire combinations, as these have a significant influence on the vehicle aerodynamics and therefore must not be neglected. Previous studies have shown that wheels represent one of the most influential aerodynamic areas of the vehicle, as up to 25% of the overall aerodynamic vehicle resistance can be attributed to these components, although they have comparatively small geometric dimensions and thus represent only small subcomponents of the vehicle [5]. The simulation of rotating rims and tires, however, represents a comparatively new and demanding discipline in computational fluid dynamics. A validated solution to this problem does currently not exist, which is why appropriate procedures have yet to be developed and validated. Therefore, the validation of various numerical rotation methods used to simulate rotating wheels form the core of this work.

Chapter 2

Introduction

In the first section of this chapter, relevant work and studies on the aerodynamic effects of wheels is presented and the current status of the technology is summarized. Based on this knowledge the research objectives of this study are derived and the limitations are defined. Finally the structure of this work will be presented.

2.1 Literature review

Historical introduction to ground simulation in aerodynamic wind tunnel testing

At the beginning of aerodynamic automotive wind tunnel testing, experiments were carried out without a proper ground simulation and without turning wheels. A major impact on the vehicle aerodynamics has consequently been neglected. Furthermore the application of stationary ground planes resulted in an increasing boundary layer thickness, which affected the air flow situation along vehicle parts close to the floor and thus caused experimental inaccuracies. Eiffel was the first to address this issue and finally proposed the concept of a system to simulate the moving road in the wind tunnel at the beginning of the 20th century. This concept was adopted and successfully implemented in 1934 by Klemin [6].

Investigations of the rotating isolated wheel

Some time after these first attempts to consider the moving ground for automotive wind tunnel experiments, the study of wheel movement became the focus of the aerodynamic development. Towards the end of the 1960s, rudimental experiments were carried out to develop a fundamental understanding of the basic fluid dynamic mechanisms of rotating wheels, wherefore the first fundamental studies were conducted on the isolated single wheel. Aggravating was the fact that no sophisticated road simulation techniques existed that could have been utilized in the automotive wind tunnels, which is why the first studies were carried out with stationary ground.

Initial investigations of the aerodynamic impact of wheel rotation on the flow field of isolated wheels were performed by Morelli [7, 8] in 1969 and by Stapleford and Carr [9] in

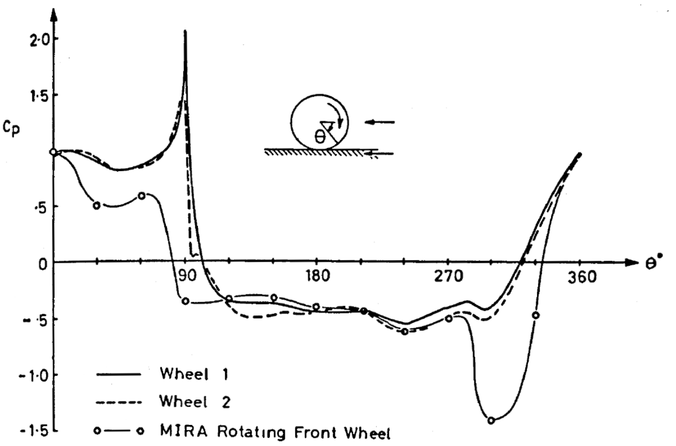

Figure 2.1: Static pressure distribution around two rotating wheels with different tire tread profiles by Fackrell and Harvey [10].

1970. For both studies a stationary ground plane was used, while a small gap between wheel and floor allowed the wheel to rotation through an external engine. It has been shown that an air stream flows through this gap, which affects the aerodynamic coefficients of the wheel and thus affects the measurement results.

The foundation for a detailed description of the flow field in the proximity of the isolated wheel has been created by Fackrell and Harvey [10, 11] in the early 1970s, who performed a series of aerodynamic force and pressure measurements of the rotating wheel on moving ground. The wheel had a smooth surface and was manufactured from aluminum, wherefore it was undeformable. A significant impact of the wheel rotation on the flow field around the rotating wheel, as well as on the surface pressure at the tire tread (Fig. 2.1) was observed. Furthermore, the rotation caused the air flow separation point on the upper side of the tire to shift upstream in the front half and not in the rear half of the wheel, as it is the case for the stationary setup. The cause of this altered detachment behavior is the rotation of the upper tire tread against the direction of the free air stream, which causes additional shear in the boundary layer and therefore separation. This effect leads to a reduction of the lift force. Moreover, a sharp pressure peak above the stagnation point was observed in the area upstream from the contact line between rotating wheel and moving ground. This peak arises due to additional energy transported to this area by the rotating tire tread and the floor, which are both moving towards this line, resulting in an increase of total pressure in this area. Accordingly, this effect does not occur with stationary wheel and ground, resulting in a maximum pressure coefficient of $C_P = 1$. Furthermore, a pressure gradient is formed between the region upstream and the sides of the wheel, which causes the air to accelerate towards the sides, forming a lateral jet stream and finally creating a *horseshoe* ground vortex. This phenomenon, which has a significant impact on the surrounding flow field, was therefore called "*jetting*". Accordingly, a negative pressure peak point in the area downstream from the line of contact between rotating wheel and moving ground was predicted, but not observed.

Cogotti [12], as well as Stapleford and Carr [9], also used a moving ground setup for their experiments, but left a small gap between wheel and floor in order to avoid disturbing

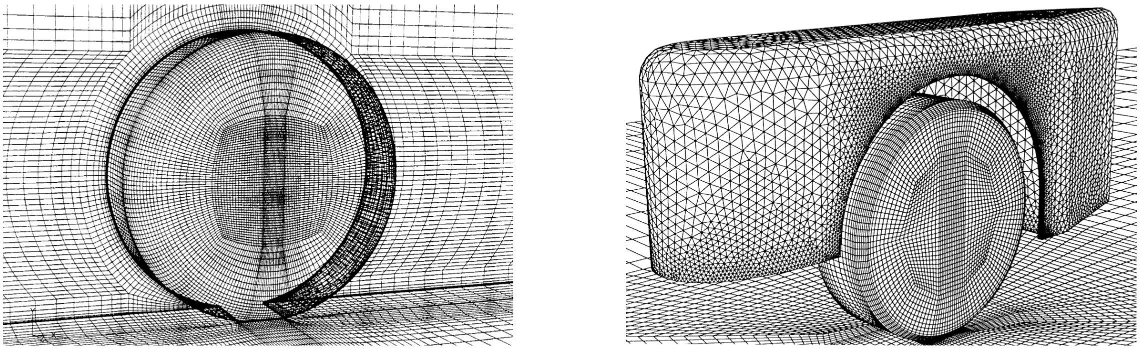

(a) Computational mesh of a separate wheel.

(b) Computational mesh of a wheel in a simplified wheel house.

Figure 2.2: Computational meshes used by Axon et al. [15, 16].

interference due to wheel-ground contact forces that would have had an impact on the force measurements. Cogotti observed that this gap had an non-negligible impact on the surrounding flow field, since both, stationary as well as rotating wheels with sealed gap, produced positive lift. The positive lift was also measured for a stationary wheel with open gap, while downforce was measured for a rotating wheel with this setup. This effect was attributed to the air accelerated by the wheel rotation in the gap between tire and ground. The higher velocity leads to a pressure decrease in this region, which pulls the wheel towards the ground. These experiments revealed that the wheel must necessarily be in contact with the ground for stationary as well as moving setups in order to simulate the aerodynamic behaviour of the wheel correctly. Furthermore it was demonstrated that an isolated rotating wheel produces less drag and lift than a stationary one.

Maers et al.[13] reproduced the wind tunnel experiments performed by Fackrell and Harvey [10], using a newly developed radio telemetry system to measure surface pressure at the center line of a pneumatic, smooth slick tire on a stationary and a rotating, isolated wheel. The jetting phenomenon, as well as a strong negative pressure peak in the area downstream of the line of contact between rotating wheel and moving ground were observed, as predicted by Fackrell and Harvey. Flow-field investigations downstream of the wheel revealed that two regions of lower pressure existed and that the stationary wheel had a much wider wake structure than the rotating wheel. In an additional work, Maers et al. [14] investigated the front and rear jetting phenomenon at a simplified, isolated wheel experimentally and also numerically and found good agreement between both approaches.

Axon et al. published two of the first numerical investigations of the air flow around an isolated wheel [15], as well as a wheel in a simplified wheel house cavity [16], using a steady RANS modeling with the two-layer RNG $k - \epsilon$ turbulence model for their investigations. Simplified tire geometries and closed rims were used in both studies (Figs. 2.2a and 2.2b). A stationary case with a fixed wheel on motionless ground and a rotating wheel on moving ground have been investigated. Wheel rotation and floor movement were modeled through a tangential moving wall boundary condition. Examinations of the aerodynamic wheel forces, the surface pressure at the tire tread, as well as the total pressure within the wake area, were conducted. Based on the validation with Fackrell's and Harvey's experi-

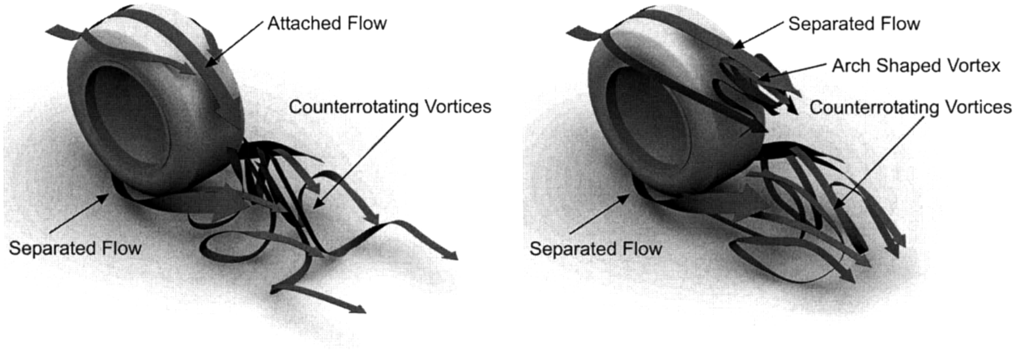

(a) Stationary wheel. (b) Rotating wheel.

Figure 2.3: Schematic diagrams of the general isolated wheel flow from McManus and Zhang [17].

mental data [10, 11] of the isolated wheel, as well as with their own experimental data of a wheel within a simplified wheel house, it was concluded that numerical simulations can give good qualitative results for the flow situation around the isolated and the enclosed wheel for rotating and stationary boundary conditions, although discrepancies in total aerodynamic forces existed. The drag and lift reducing effects of wheel rotation could be confirmed for the isolated wheel on moving ground. Conversely, a wheel located in a wheel house cavity produces more drag when rotating on a moving plane than when it is fixed on stationary ground. Evidence of the jetting phenomenon postulated by Fackrell and Harvey [10, 11] was observed due to pressure coefficients greater than 1 in the front of the contact patch between wheel and ground plate.

McManus and Zhang [17] tried to reproduce the wind tunnel experiments of Fackrell and Harvey [10] in a numerical study by remodelling the exact same wheel geometry as used for the measurements. The transient URANS method was used to investigate the aerodynamic behaviour of a simplified, isolated wheel with closed rim geometry in contact with the ground for stationary and a rotating setup, where wheel rotation was modeled with a *MW* boundary condition. Surface pressure as well as aerodynamic drag and lift forces were computed and compared against the experimental data of Fackrell and Harvey. Good qualitative agreement could be found between numerical and experimental results. However, surface pressure values near the rear wheel-ground contact line for the rotating wheel showed some discrepancy compared to the hardware test, for which errors in the experimental methods were suspected as the cause. Based on the simulation results it was possible to create a schematic model of the flow structures around the wheel (Fig. 2.3).

The focus of the study by Wäschle et al. [18] was the validation of transient CFD methods, which were used for the simulation of a scaled, isolated, slick wheel (Fig. 2.4a) with stationary and rotating boundary conditions. Two industrial CFD codes were chosen for this examination, namely *STAR-CD*, which uses the steady-state *RANS* approach and *EXA PowerFLOW*, which is based on the transient *Lattice-Boltzmann* method. In the first case, wheel rotation was modeled with the *MRF* approach, while in the latter case a velocity boundary was applied at the surface of the wheel. As part of this validation, detailed

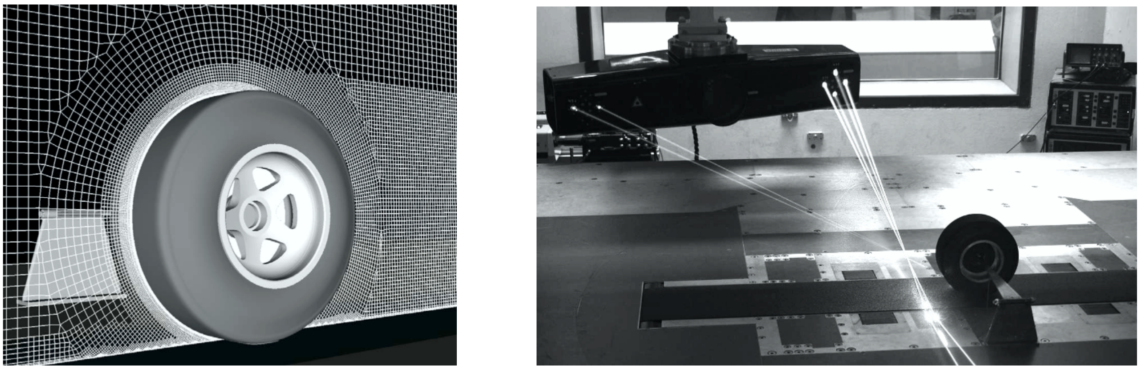

(a) Computational mesh.

(b) Experimental setup for LDA measurement: The wheel moves on the center-belt.

Figure 2.4: Numerical and experimental setup used by Wäschle et al. [18].

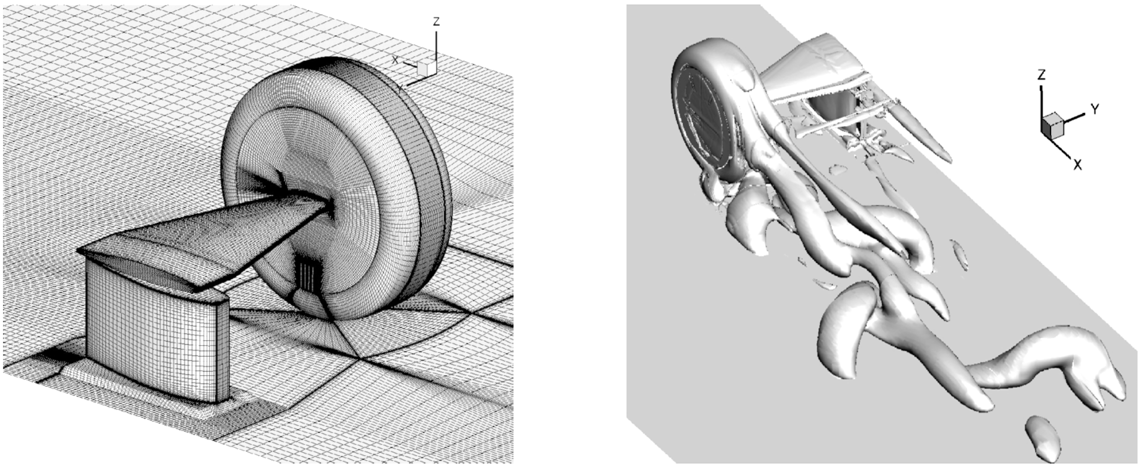

(a) Computational mesh.

(b) 3D iso-surface of Q criterion.

Figure 2.5: Computational mesh and air flow topology analysis by Croner et al. [19].

LDA-based flow field investigations (Fig. 2.4b), as well as force measurements were performed and correlated with the results of the numerical simulations. It was demonstrated that both solver technologies are able to reproduce the main air flow structures and to achieve good qualitative agreement with the integral aerodynamic coefficients measured in the experiments. Therefore, it was concluded that both solver technologies are capable to reproduce the aerodynamic behavior of rotating wheels.

Croner et al. [19] used an unsteady numerical simulation approach to investigate the main vortical structures in the near-wake of an isolated rotating wheel, as well as the unsteady evolution of the wake and the flow surrounding the wheel. Numerical data from URANS simulations with the ONERA $k - kL$ two-equation turbulence model and simplified tire geometries with closed rims (Fig. 2.5a) were compared against experimental wind tunnel data gained by PIV and hot-wire anemometry measurements. Eventually, the computational model was able to reproduce the flow topology (Fig. 2.5b) and characteristic flow structures, such as the jetting phenomenon, as well as its unsteady behaviour in accor-

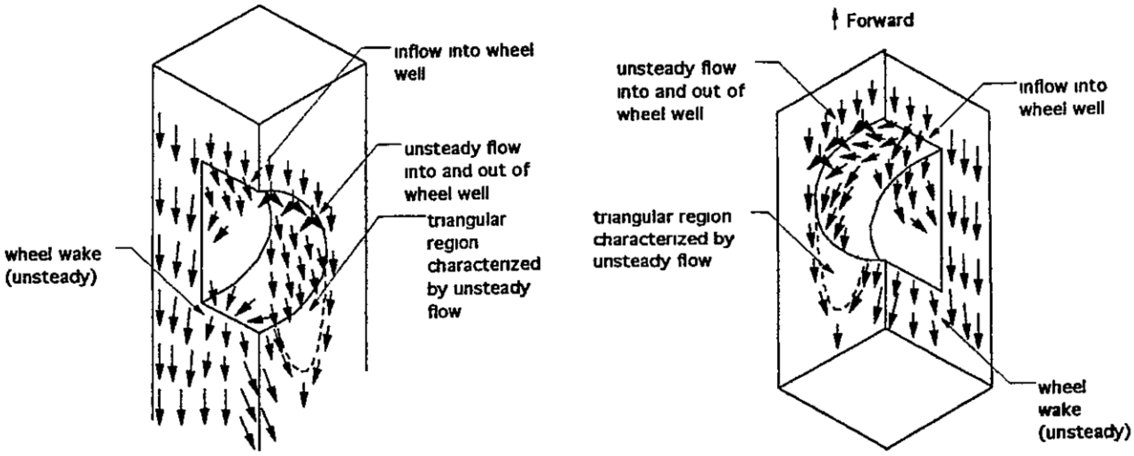

(a) Front view.

(b) Rear view.

Figure 2.6: General surface flow in and around wheel-well from Fabijanic [21].

dance with the experimental results.

In a more recent study, Gérardin et al. [20] utilized the transient URANS approach and applied a moving-wall boundary condition to compute the flow field around a rotating, isolated wheel in order to determine the particle dispersion in its wake area. Eventually the numerical results were validated with results of the experiment. However, while two types of wheels with slick and patterned surfaces and realistic rim geometries were investigated in the wind tunnel, only the slick tire model with a simplified rim geometry could be investigated numerically due to the high computational requirements. Good agreement between simulation and experiment was found, and known air flow patterns and effects, such as the jetting phenomenon, could be reproduced.

Investigations on rotating wheels in a wheel house cavity and on simplified vehicle models

These first studies on the isolated wheel already pointed out the importance of proper ground simulation and wheel rotation for the aerodynamic behaviour of this system. A variety of succeeding studies focused on the fluid dynamical effects of ground simulation and rotation of the wheel within a wheel house cavity and on simplified vehicle models.

The aim of the parametric study carried out by Fabijanic [21] was to describe the alterations of the air flow situation around a wheel within a simplified wheel house cavity due to changes of its geometry. Various geometrical parameters of the wheel arch, such as radius, height and depth, were modified and the impact on the aerodynamic behaviour was investigated experimentally. The examinations included analyses of the surface pressure as well as of the aerodynamic forces on the wheel, which were measured independently from its cavity. Furthermore, surface oil flow visualizations have been carried out to describe and understand the air flow situation around the examined geometry (Fig. 2.6). The flow visualization analyses revealed that the low pressure zones, which form due to the rapid

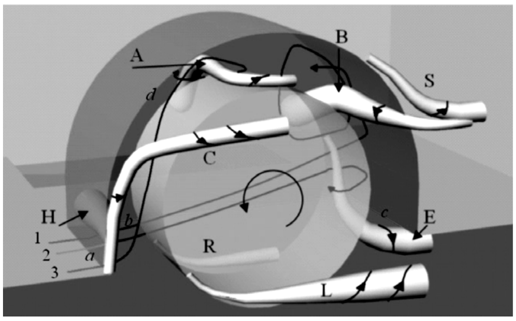

Figure 2.7: Vortex skeleton model of the wheel house flow field [24].

air streams around the front corners of the vehicle, are the major cause of yawed air flow on the front wheels. The results further showed that the drag increases primarily with the wheel house radius, while lift increases with the wheel house depth. It was also concluded that a reduction of the distance between the tire and wheel housing causes a reduced flow over the upper part of the rotating tire, which leads to a reduction of drag.

Régert and Lajos [22–24] used RANS and URANS simulations to investigate the flow field situation of an isolated wheel and a wheel within a simplified wheel cavity in detail. The studies focused on identifying and characterizing dynamically significant structures of the air flow that were crucial for the distinctive development of the flow field downstream of the isolated wheel and within the wheel arch. Various simulation parameters and boundary conditions were modified, such as the shape of the vehicle body, computational grid, numerical scheme, turbulence model and wheel rotation, which was modeled utilizing the moving wall boundary condition. The results revealed six complex re-circulation zones (vortices) that formed independently of these parameters (Fig. 2.7). Furthermore, the validation of the numerical results with experimental data from other studies demonstrated the superior predictive accuracy properties of the $k - \omega$ SST turbulence model in comparison to the $k - \epsilon$ approach for these aerodynamic systems.

The impact of moving ground on the air flow around a simple generic vehicle body (Ahmed body) was investigated numerically by Krajnović and Davidson [25]. LES simulations were used to show that a moving floor setup causes a global air flow change around the body, which yields a drag reduction of 8% and a lift reduction of 16%. Due to the impact on the air flow and the surface pressure of the simplified body geometry it was concluded that a moving floor setup is essential for numerical and experimental investigations.

Hackett et al. [26] showed the significance of ground treatment through wind tunnel experiments with a simplified .154-scaled vehicle models with various degrees of streamlining. This work focused mainly on the influence of ground simulations at wind tunnel test facilities, but also included studies of the impact of rotating wheels. Examinations of the vehicle wake, as well as vehicle drag and lift, which were measured through a balance and by wake integration, were carried out for configurations with rolling and stationary wheels. The results revealed a reduction of the wake width in comparison to analogous test cases with flat-bottom wheels and moving ground. It was concluded that the impact of rotating wheels on the aerodynamic forces is rather limited for passenger cars, although a tendency to decrease vehicle drag by means of active ground simulation was observed. It was also shown that rotating wheels and moving floor caused a vortex pair which made the lift increase.

Damiani et al. [27] utilized steady and unsteady RANS simulations to examine the air flow around a wheel for three geometrical setups. For this study, an isolated wheel, a wheel within a cavity and at a basic vehicle model were investigated. CFD simulations have been carried out with stationary and rotating wheels for each case. The numerical results showed good qualitative agreement with the experiment, although the correlation for the unsteady approach was better than for the steady one. For the simplified isolated wheel configuration, a drag increase caused by wheel rotation was shown for steady and unsteady simulations, while the results of the wheel in a simplified cavity revealed a decrease in drag, both in agreement with experimental data. For the simplified vehicle setup, a drag increase caused by the rotating wheel was shown for steady and unsteady simulations. However, unfortunately no experimental data was available for the validation of the numerical results for this setup.

Dimitriou and Klussmann [28] performed detailed experimental investigations with half-scaled models, including an isolated wheel with open and closed rim geometry, wheels attached to a simplified race car and to a simplified passenger vehicle body with and without front wheel spoilers (Fig. 2.8). These studies focused on the aerodynamic forces acting on the wheel itself and on the surface pressure distribution at the tire tread, as well as on the flow topology under various circumstances. The investigations involved analyses of the surface pressure distribution at the tire tread through pressure probes integrated at the wheel surface. On the basis of the experimental data, and complemented with numerical simulations, a model of the complex air flow situation in proximity of rotating wheels was postulated. Furthermore it was concluded that the jetting effect, i.e. the region with $C_P > 1$ in front of the wheel, might diminish for setups with a connection between the high pressure area upstream and the low pressure region downstream of the tire near the ground through longitudinal grooves. The reason for this phenomenon was assumed to be the reduction of the high pressure area in front of the wheel due to a fast air stream through the tire grooves, which compensates for this pressure difference and at the same time causes the pressure inside the grooves to decrease as the flow accelerates through. Additionally it was recommended to represent the suspension components in detail for further studies, since these parts might influence the diverged, oblique incident air flow entering the wheel housing and, furthermore, the aerodynamic forces on the wheels. Finally evidence of a spoiler vortex was presented.

Mlinaric [29] studied numerically various aspects and influencing factors of tire geometry on the aerodynamic behavior of a road vehicle. The investigations were carried out on a geometrically simplified semi-vehicle model with closed gaps and without engine compartment flow. Furthermore, two different rim geometries were considered. As a part of a preliminary study, the simulation of the wheel rotation itself was examined. For this purpose, three rotational methods, namely *MW*, *MRF* and *SM* were compared, and it was concluded that the most realistic way to model the rotation of spoked rims is the sliding mesh method, in which the rim geometry is rotated. However, this approach requires implicitly transient simulations, which are currently too computationally costly for daily

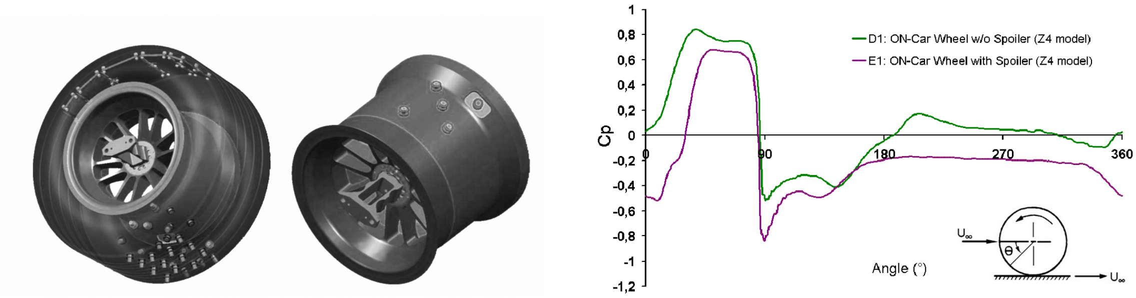

(a) Electronics and tranducer installation at the wheel surface.

(b) Centerline C_P distribution – Wheel within the wheel arch of a scaled model without and with spoiler.

Figure 2.8: Test setup and resulting centerline surface pressure distribution by Dimitriou and Klussmann [28].

industrial aerodynamic simulations. However, it was demonstrated that both steady-state methods *MRF* and *MW* capture the shape of the unsteady mean solution with sufficient accuracy and are therefore suitable for computing the flow around a rotating wheel. In this context, the importance of well defined *MRF* boxes was demonstrated, where a proprietary generation strategy was developed and the simulation results of three differently defined *MRF* zones were compared. Finally it was demonstrated that rim geometries have a significant impact on the structure of the wheel wake, and thus also on the vehicle aerodynamics.

Investigations on rotating wheels on production vehicles

Studies that examine the air flow situation in proximity of the isolated wheel, as well as the wheel within a wheel arch cavity or at simplified vehicle geometries, were presented in the previous section. However, for the industrial aerodynamics development, especially investigations on detailed series production vehicles are of great interest. These studies are summarized and discussed in the following.

Oswald and Browne [30] were among the first to perform detailed measurements of the flow field of a wheel within the wheel house of an operating series vehicle on the road in 1981. The flow field measurements were carried out with yarn pieces attached to a grid surrounding the left front wheel, which were photographed by a side car and by two windows installed in the wheel arch. In addition, hot-wire anemometry measurements were performed to examine the local flow velocity and turbulence levels. Based on these measurements, a model of the air flow situation in close proximity of the wheel was created (Fig. 2.9), revealing complex flow patterns within the wheel house. The results showed that the air flow situation in proximity of the wheel was independent of the vehicle speed, which was varied from 32 to 96 km/h. The air velocities around the wheel varied in a range from near zero to slightly above the vehicle speed, and turbulence levels were rather high everywhere in this region. It was furthermore concluded that the flow patterns are similar to those for an almost not-rotating tire within a wheel arch.

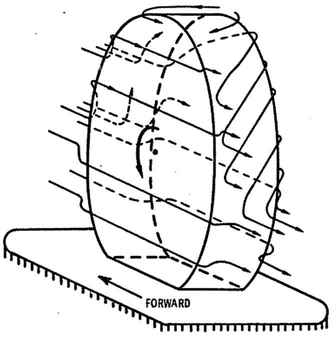

Figure 2.9: Sketch of the overall flow direction around the left front tire [30].

Mercker et al. [5] conducted wind tunnel experiments with a full-scale passenger vehicle in various configurations in order to study the aerodynamic effects of rotating wheels. In this study, the aerodynamic forces were determined, and pressure-based flow field measurements at the front and rear wheel wake zones were carried out to investigate the flow mechanisms in proximity of the wheels. Vehicle configurations with stationary and moving wheels were compared against setups without wheels and closed wheel arch geometries. The analysis results revealed that stationary wheels and the wheel houses contribute more than 35% of the total vehicle drag for a configuration with a flat underbody. Furthermore, a significant impact of rotating wheels on the aerodynamic behavior of road vehicles was determined, and it has been demonstrated that wheel rotation reduces the vehicle resistance, while the lift is increased. Alterations in the structure of the upper and lower bonded vortices of the wheel were indicated as the cause for the drag reduction.

Based on the results of Mercker et al. [5], Wickern et al. [31] emphasized the importance of considering tire rotation in the aerodynamic development of road vehicles as well in their study. As the results of Mercker et al.'s work are based on flat-bottom vehicle configurations, this study repeated the experiments with a production vehicle with a realistic underbody. The analyses at stationary wheel configurations and wheel-less setups with covered wheel arch liners revealed that the interaction of the flow field with the wheel structures accounts for approximately 25% of the total vehicle drag. Furthermore it was shown that the wheel geometry and not the wheel arches is the biggest contributor of this share. It was further concluded that it is necessary to consider wheel rotation with the same priority as the moving ground for an accurate aerodynamic measurement. However, this represented some methodical difficulties and subsequently led to the introduction of the so-called *fan moment*.

Wiedemann [32] investigated the influence and interaction of wind tunnel floor simulation and wheel rotation technologies on the air flow situation of a production vehicle and a touring car. The analyses were carried out by means of flow field measurements with a pyramid sample. Especially the yaw angle of the approaching air flow at the front wheels and their wake regions were examined in the context of this study. It was found that stationary front wheels are approached by an inclined air flow pointing outward from the vehicle center, resulting in an asymmetric flow structure at the lower part of the front wheels. An active floor simulation system, consisting of moving belts and rotating wheels, reduces this flow angularity, and thus also the size of their wake area compared to the

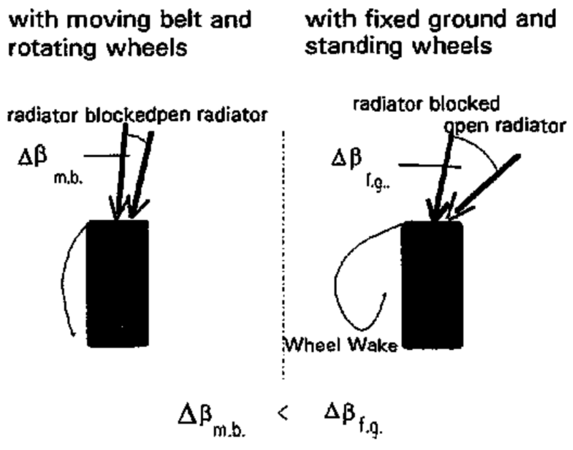

Figure 2.10: Schematic diagram of the yaw angle situation at the front left wheel (horizontal projection) for the stationary case with fixed ground (f.g.) and moving belt (m.b.) [32].

stationary case without ground simulation and with stationary wheels (Fig. 2.10). As a result, less energy dissipates in the recirculation regions downstream of the wheel, and the local drag is reduced. Based on these observations it was concluded that the reduction of vehicle drag is related to the moving ground and rotating wheels, which reduce the yaw angle onto the front wheels, which consequently results in a pressure deficit in their wake area. Furthermore, a strong interaction between the cooling air flow and the local front wheel drag has been established. It was demonstrated that engine compartment flow causes an increased yaw angle onto the front wheels, and thus an enlargement of the wake region that raises the local drag. As a result, a significant interaction between the cooling-drag, as the drag component that determines the aerodynamic quality of the cooling air flow, and the ground simulation has been postulated, since a part of this resistance component is generated at the front wheels. It was found that the moving belt reduced the cooling drag, whereas the rotating tires yield the opposite effect. It was concluded that it depends on the investigated vehicle, which of these two effects is ultimately more dominant. Eventually, the importance of ground simulation and rotating wheels for the aerodynamic vehicle development process was emphasized due to their significant impact on the aerodynamic characteristics of the vehicle.

Wickern and Lindener [33] conducted experiments in the wind tunnel and investigated the influence of various ground simulation and wheel rotation boundary conditions on the aerodynamic forces of a sports vehicle. It has been shown that rotating wheels reduce the vehicle drag and increase the lift compared to the stationary case with deactivated wheel and ground simulation. Especially the rear wheel rotation could be identified as the cause of the drag reducing effect. The lift increase occurred especially at the front axle and could be attributed to the front wheel rotation. It was also concluded that the effects of front and rear wheel rotation are not strongly dependent on each other.

Elofsson and Bannister [34] performed wind tunnel experiments to investigate the impact of ground simulation and rotating wheels on vehicle aerodynamics with focus on the analysis of the drag-reduction mechanisms of these boundary conditions. The investigations were carried out separately for moving and stationary ground, as well as stationary and rotating front and rear wheels. The measurements included the aerodynamic forces, the surface pressure at the vehicle base, as well as the flow field and the microdrag in the relevant regions of a Sedan and a Squareback configuration. From the results it was concluded that the rear wheel rotation in particular is responsible for the reduction of the aerodynamic drag of the vehicle. This effect was attributed to the interferences of the wake regions of rear wheels, wheel arches and vehicle, which increases the pressure in the tail area and thus has a reducing effect on the vehicle resistance. Furthermore, it was shown that the interaction of these two wake areas strongly depends on the vehicle's basic shape. The activated road simulation system resulted in a higher drag reduction for the Sedan than for the Squareback configurations. This phenomenon was attributed to an improved air flow situation at the rear of the Sedan, which, however, could not be detected at the Squareback. In contrast, pure front wheel rotation showed little or no impact on the integral vehicle resistance, although a distinctive local drag reduction was detected in the front wheel arch region. It was concluded that this drag reducing phenomenon neutralizes until the rear of the vehicle due to interference effects.

Elofsson and Bannister's studies were later numerically continued by Koitrand and Rehnberg [35] and Koitrand et al. [36]. The aim of their work was the investigation of the influence of moving ground, as well as the front and rear wheel rotation on the local and global flow field and the integral aerodynamic forces of two production vehicles. For the numerical studies, the *Lattice Boltzmann Method*-based CFD solver Exa PowerFLOW was utilized. The rotation of the wheels was simulated using the *MRF* approach. Rotating wheels and moving ground yield a remarkable reduction in the integral vehicle drag and lift, especially of the rear lift component, in agreement with the experiments of Elofsson and Bannister [34]. The largest influences on the aerodynamics of the vehicles could be attributed to the rear wheel rotation, which decreases drag and rear lift considerably. However, pure front wheel rotation affects the flow field, but still has little impact on the integral aerodynamic coefficient of the vehicle, except the front-lift, which is increased. Furthermore, it was concluded that the aerodynamic effects of front and rear wheel rotation are additive. It has also been demonstrated that simulating only the moving floor increases the vehicle's drag and front lift, while the rear lift decreases.

Wäschle [37] performed detailed numerical and experimental investigations on a simplified, scaled model, as well as on a production vehicle, using three different rim geometries with the aim to create a model to determine the flow topology of the wheel within the wheel arch. For this purpose, force measurements as well as examinations of the flow field were conducted on the scaled model, utilizing the LDV measurement technique. These experiments were extended by numerical methods, using the steady-state RANS approach, while the wheel rotation was modeled using the *MRF* method. Based on the numerical and experimental data, an elementary model of the flow topology and vortex structure close to stationary and rotating wheels within the wheel arch was created and the aerodynamic mechanisms identified (Fig. 2.11). The differences in the flow topology to the isolated single wheel have been presented, and it has been revealed that the mechanisms that reduce drag and lift on a rotating isolated wheel are not the same for a wheel in a wheel house. Furthermore, it has been shown that the changes reducing the vehicle drag

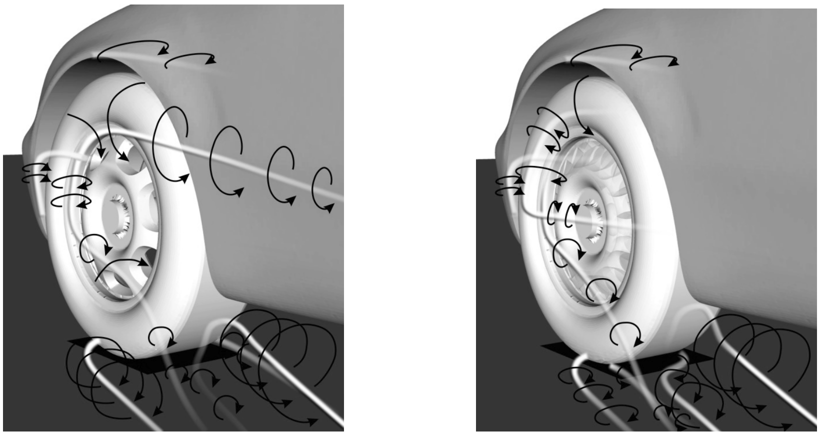

(a) Stationary wheels. (b) Rotating wheels.

Figure 2.11: Vortex structure behind the front wheel in the wheel arch [37].

do not act on the wheels, but on the vehicle body. This phenomenon could be attributed to interference effects between the rear wheel wake and the wake of the vehicle. In general, a good correlation between the numerical and experimental results was achieved in this study, demonstrating that steady state RANS simulations can predict the flow field around a series vehicle with sufficient accuracy.

Landström et al. [38] studied the effect of active ground simulation with a moving belt system and rotating wheels on the aerodynamic coefficients of a passenger car for different yaw angles. For this purpose, a production vehicle was investigated in various configurations in the wind tunnel, where the integral aerodynamic forces were measured and the flow topology alterations were analysed by means of local surface pressure examinations. Configurations with zero yaw and rotating wheels led to an increase of the rear base pressure and subsequently to a reduction of the drag of the vehicle. Furthermore, wheel rotation caused surface pressure reductions within the wheel arch. However, the studies conducted under yawed wind conditions revealed that the drag of the vehicle increases more with increasing yaw angle and active ground simulation than for stationary floor and wheels. The formation of the wake region of the front wheels, and the deflection of the windward wheel wake in the underbody, were suspected as cause for this behavior.

Schnepf investigated in his dissertation [39] various influencing factors on the flow around the wheels of a production vehicle and around the isolated single wheel. Driving tests were carried out to determine the dynamic ride height changes due to lift, as well as tire expansion and driving torque for different rims. The results confirmed the relevance of the ride height for the absolute aerodynamic forces of the vehicle, but revealed being negligible for assessing the drag alterations between individual rim geometries. Furthermore, the impact of three rim geometries and different ground simulation methods on the local flow situation, the surface pressure distribution and the aerodynamic coefficients of the vehicle were determined by means of wind tunnel experiments, as well as numerical simulations. The Lattice-Boltzmann solver Exa PowerFLOW was used to carry out the numerical investigations, where the rims were transiently rotated by the *SM* method. The ground vortex, which arises at the contact patch of the tires, could be identified as the biggest influencing factor on the vehicle drag. Furthermore, the largest changes in resistance were found on the wheels themselves, and only to a small extent on the vehicle. In addition, the influence of the tire tread on the wheel flow was investigated in detail, for which numerical simulations with different complex tire geometries were carried out. This study was validated on the basis of wind tunnel measurements on the isolated single wheel. It was demonstrated that, for this simulation approach, only a quadrupling of the surface mesh resolution with corresponding computational costs led to results comparable with the experiment.

Investigation of the impact of rim geometry on complete vehicle aerodynamics

The influence of rim geometry on the aerodynamic properties of road vehicles has also been investigated in previous studies. In particular, studies of Landström et al. have dealt in detail with the influence of rims and tire geometries of rotating wheels. The results of the individual studies were summarized by Landström in his dissertation [40] and will be discussed separately from each other.

Landström et al. [41] conducted wind tunnel measurements with a road vehicle to investigate the impact of ground simulation and rim geometry on the aerodynamic properties of the vehicle. For this purpose, detailed flow field investigations near the front and rear wheels, as well as force measurements, were carried out on the vehicle for two wheels with different tires and rim geometries. The results revealed a clear dependence of the rim geometry on the air flow situation and the drag of the vehicle. Furthermore, a drag reduction could be determined for all configurations due to active ground simulation.

To investigate the influence of rim geometries and rim opening areas on vehicle aerodynamics, Zhiling et al. [42] carried out wind tunnel experiments with two production vehicles, which were equipped with a module-based prototype system, that made it possible to investigate different rim inserts. In this study, the influence of the rim opening surfaces and therefore also of different rim geometries on the aerodynamic behavior of the vehicle could be demonstrated. Thus, alterations of the front wheel wake structure were detected and could be attributed to changes in the lateral flow that streams from the underbody through the rims into the main lateral flow adjacent to the vehicle. Furthermore, effects on the rear base pressure and also on the drag value of the vehicle could be determined, whereas larger rim covering caused a greater reduction in aerodynamic drag. The covering of the front wheels separately resulted in a reduction of the wheel wake and thus also of the local resistance in this area. However, an increase of the base drag was detected and it was suspected that this effect can be attributed to alterations of the underbody flow. In contrast, the covering of the rear wheels resulted in the largest increase in the rear base pressure. The cover of both, front and rear wheels, showed the largest reduction of the vehicle air resistance. It was concluded that this effect occurs due to the combination of both drag reducing effects of front and rear wheels. Furthermore, the examination revealed that the increase in the rear base pressure does not necessarily correlate with the drag reduction of the vehicle, since that configuration with the greatest pressure increase at the rear did not show the greatest vehicle drag decrease.

Landström et al. [43] investigated the influence of different wheel design parameters on the aerodynamic drag of a production vehicle. Validation measurements in the wind tunnel, as well as numerical investigations of various rim configurations were carried out, with the geometry changes of the front and rear wheel rims considered separately. The rims were prepared with different inserts to represent partial closures, thus varying the rim blockage ratio. The results revealed that the rim geometry has an impact on the aerodynamic coefficients of the vehicle. The increased blockage of the rear rims led to local drag reductions in the area of the rear wheel arches, the rear underbody and the at the vehicle base, where the greatest effect was achieved with completely closed rim geometries. The closure of the front rims altered the flow situation up- and downstream of the front wheels. Based on these findings, the potential of different rim geometries for front and rear wheels for aerodynamic drag reduction was discussed.

Landström et al. [44] tried to determine important rim design parameters and investigated a large number of various rim geometries at a series vehicle in the wind tunnel, where the evaluation of the measurement data was carried out with the aid of statistical methods. The most important wheel design parameters for the vehicle's drag reduction, such as wheel covering, rim and spoke radii and rim smoothness were identified. Based on these findings, a mathematical model was developed that allowed for the prediction of the resistance reduction potential of the individual specifications. However, this simple model was limited to predict the impact of incremental changes for each rim geometry.

In another experimental study, Landström et al. [45] examined the influence of different wheels on the aerodynamics of a production vehicle in various configurations. The research included two tires and three different rim designs. The results showed a significant influence of the tires, as well as the rim geometry, on the aerodynamic coefficients of the vehicle. Both drag and lift were affected up to $\Delta C_{D/L} = 0.010$ depending on the wheel design and vehicle configuration. The flow field investigations revealed minor structural alterations in the wake of the front wheels. However, the wake area of the vehicle has been greatly affected due to the different wheel modifications, especially at the lateral interference area with the rear-wheel wake.

Buscariolo and Carbon [46] conducted numerical studies to determine the influence of different sized rim openings on the aerodynamic drag of a Sedan vehicle. For this purpose, two setups were compared for each rim opening: On the one hand, stationary wheels and ground, and on the other hand rotating wheels and moving ground. The influence of individual rim geometries on the vehicle drag was demonstrated. Furthermore the results confirmed a reduction of the aerodynamic drag due to the wheel rotation and the moving floor compared to the stationary case for all rim opening configurations.

Landström et al. [47] conducted a numerical sensitivity study on the influence of wheel geometry orientation on the flow field and aerodynamic forces of a vehicle. For this purpose, flow fields and the integral aerodynamic coefficients of two simulation cases with different rim orientation were compared. Both, steady-state and transient RANS simulations were carried out in this study, where the modeling of the wheel rotation was implemented by means of the *MRF* method, and additionally by the *sliding mesh* approach for steady-state and for transient simulations, respectively. The results showed large deviations between the individual flow fields, and also effects on the aerodynamic forces of the vehicle. These changes were attributed to the cross flow through the rims, which had an effect on the wheel wake, and also on the outflow behavior of the cooling air.

In a similar study, Cederlund and Vikström [48] investigated numerically the effects of rim geometry changes on the aerodynamic characteristics of a sports car. Within the scope of this master thesis, the interaction of wheel design and diffuser, as well as diffuser and rear spoiler, were also examined. The simulations were based on the time-averaged RANS and unsteady RANS approach, where the realizable $k - \epsilon$ model for turbulence modeling and non-equilibrium wall functions for the resolution of the boundary layer were chosen. The wheel rotation was realized by the *MRF* and the sliding mesh methods. The effects on the integral aerodynamic forces as well as the flow situation in the area of the wheels and in the underbody area of the vehicle were analysed. The influence of the rim geometry on the aerodynamic forces was demonstrated, and it was shown that, with an optimized rim construction, a considerable reduction of the air resistance can be achieved. The blockage of the crossflow through the front rims resulted in increased static pressure in the front wheel housing and thereby also in an increase in lift. Furthermore, a reduction of the vehicle resistance could be determined by this modification. Blocking the crossflow of the rear rims resulted in increased downforce due to an increased flow rate through the diffuser. However, contrary to previous studies, no significant reduction in vehicle resistance was detected. In addition, it was found that the resulting flow around the rear wheels is highly dependent on the front wheel geometry.

Floor simulation technique at current wind tunnel test facilities

The experimental part of the aerodynamic development process of series vehicles takes place at wind tunnel facilities. In contrast to the real road drive, the vehicle and not the environment remains stationary during these measurements, requiring certain technologies to simulate the aerodynamic effects of a moving road as realistic as possible.

Nevertheless, in the past the development of series vehicles was initially carried out with stationary ground and fixed wheels. The reason for this was, on the one hand, the limited knowledge of the impact of floor motion and wheel rotation on the aerodynamic behavior of the vehicle and, on the other hand, the challenging technical development and implementation of ground simulation technology. However, in the last few decades, the importance of correct floor simulation has been recognized, and much effort has been made to develop appropriate road simulation methods and establish them by default in the aerodynamic wind tunnel test process [33, 49–62].

Nowadays, the movement of the vehicle relative to its surroundings is still being simulated by systems that accelerate the air around the vehicle at a velocity that would correspond to the driving speed on the road. In modern test facilities, the ground is also set in motion with the same velocity, which contributes to prevent the formation of a floor boundary layer that would cause unrealistic fluid dynamical effects at the vehicle and therefore would not correspond to the conditions on the road. Furthermore, the wheels are set in rotation in order to account for their impact on the aerodynamic behaviour of the vehicle.

Synopsis

The literature review shows that proper ground simulation, including road motion and wheel rotation as well as the tire-ground contact, is essential for accurate determination of the aerodynamic properties of a vehicle. Studies that investigated the distribution of aerodynamic drag components of the individual parts of a road vehicle have revealed that the contribution of the wheels and wheelhouses is about 25% of the total drag force. Thus, the wheels with rims and tires represent one of the aerodynamically most significant components of a vehicle. Further, the wheel rotation, rim and tire geometries are important factors.

In preceding studies, the aerodynamics of the isolated wheel has been studied experimentally and numerically in detail, thus creating a broad knowledge as foundation for further investigations on more complex setups. Physical models of the air flow situation in proximity of the stationary as well as the rotating wheel could be created, and the occurring physical phenomena were described. The studies have shown that the wheel rotation reduces the aerodynamic drag and lift forces of the wheel at straight flow condition. The increasing rotational speed shifts the separation position of the flow from the tire surface upstream of the highest point of the tire and offset from its surface, in contrast to the stationary setup, where the detachment position is located downstream from the apex of the wheel. At the contact area between the rotating wheel and the moving floor, a pressure peak with $C_P > 1$ arises and results in two laterally directed jets, which subsequently roll up into two strong, counter-rotating floor vortices. Accordingly, this phenomenon is called *jetting*. Furthermore, so-called *rear jetting* occurs downstream of the wheel, which is noticeable on basis of a negative pressure peak at the contact region between the tire and the road. The jetting phenomenon occurs only with smooth tire treads and can be reduced or even eliminated due to pressure equalization between the front and rear pressure areas through longitudinal grooves within the tire surface.

The placement of a rotating wheel in a wheel house geometry or into the wheel arch of a vehicle immensely increases the complexity of the flow topology of this system. The air flow situation at the part of the wheel, located in the gap between the road and the underbody, which is therefore not covered by the wheel arch shell, resembles partly the flow structure of the isolated wheel. However, due to displacement effects of the vehicle front end, the flow approaches the wheel inclined to the direction of motion and thus asymmetrically at a certain outward inclined angle. The wheel rotation has a reducing effect on this yaw angle, which furthermore makes the wheel wake smaller and, therefore, has a positive effect on the local drag of the wheel. The flow situation within the wheel house itself is highly complex. This includes fluid dynamical phenomena like air flow separation, recirculation areas and three-dimensional vortices. High discontinuities due to vortex shedding, cavity pressure oscillation and interactions of the wheel vortices with the ground boundary layer are possible. However, previous studies have shown that so far it has not been possible to agree on an exact description of the flow topology within the wheel arch.

Furthermore, rotating wheels show a major impact on the air flow situation and on the integral aerodynamic forces of a production vehicle. A reduction in drag and an increase in lift have been demonstrated in various studies for setups with rotating wheels in comparison to the stationary case. However, it was shown that these findings cannot be generalized and applied to every vehicle configuration. Interference effects were determined between the underbody flow, as well as the wake areas of the rear wheel-houses, with the wake of the vehicle as the main reason for the drag reduction. This interaction leads to a increase of the surface pressure at the rear base, which consequently reduces the vehicle drag. Due to this correlation, the rear wheels were attributed the more dominant influence on the vehicle drag. The increase in lift, however, was attributed mainly to the front wheel rotation. Furthermore, numerical studies have demonstrated that RANS simulation techniques can correctly predict the flow situation of production vehicles.

The impact of rim geometry parameters, such as opening area or spoke orientation, on the vehicle aerodynamics has been investigated in various experimental and numerical studies. The effects on the aerodynamic behavior of the vehicle were shown, and the potential of rim geometries for drag optimization was demonstrated. The effect on drag could be attributed to changes in the lateral crossflow from the underbody through the front rims into the main transverse stream adjacent to the vehicle, and also to alterations of the cooling air outflow behavior from the engine compartment. Both factors are influenced by the rim geometry, and thus also by the blockage ratio. The greater the blockage ratio of the rims were, the greater was the reduction in drag, whereby the greatest effect could be achieved with completely closed rims. The reduction in resistance was accompanied by a raise in lift, especially at the front axle, due to the increased static pressure in the wheel arch due to the blockage.

2.2 Research targets and project objectives

The literature review has shown that the aerodynamic behavior of the isolated, rotating wheel has already been extensively studied, and computational methods have been used to create different models to describe the fluid dynamical effects in this system. It could be demonstrated that numerical approaches can reproduce the occurring aerodynamic phenomena in accordance with the experiment. The same applies to the aerodynamic behavior of a wheel in an isolated wheel house shell or on simplified vehicle models. However, the subject of the air flow around the rotating wheel within a wheel arch of a geometrically highly-complex production vehicle, and thus the aerodynamic effects on the vehicle itself, are still not fully understood, and the available studies on this topic are limited. Although individual fluid dynamical effects of wheel rotation on the production vehicle have been experimentally investigated, these phenomena have so far been little considered numerically. This can partly be attributed to the immense computational effort, and furthermore to the low prioritization of wheel aerodynamics in the automotive industry in the past, which has only recently changed due to legal requirements. Accordingly, the effects of individual numerical rotation methods on the aerodynamic behavior of production vehicles are hardly investigated, and correspondingly few numerical studies exist that validate the results of the wind tunnel experiment. This includes not only the integral aerodynamic forces acting on the vehicle, but also the impact on the flow topology in proximity of the vehicle and within the wheel arch, as well as the influence on the engine compartment flow. Nevertheless, the application of detailed simulation models has been common for years in the industrial aerodynamics development process. Furthermore it was determined that various numerical approaches to model rotating components in CFD simulations are currently available. This raises the question, which rotation method is best suited to simulate the aerodynamic effects and phenomena of wheel rotation of a production vehicle.

Therefore this research focuses on the investigation of the impact of individual numerical wheel rotation methods on the simulated aerodynamic properties of passenger cars, with focus on relevant influences for the industrial vehicle development. The emphasis is on the study of the impact of numerical rotation methods on the local flow situation around the wheel within the wheel arch and thus on the vehicle flow topology, which ultimately affects the aerodynamic forces of the vehicle.

Currently, none of the rotation methods available for steady-state CFD simulations are directly suitable for the numerical modeling of rotating wheels. The *MRF* method was originally developed for turbo-machinery and is therefore valid for use on rims only to a limited extent [63], while the *MW* approach physically mismatches the rotation of the wheel spokes [29]. Neglecting tire and rim rotation entirely is obviously also an unsatisfactory approach and not acceptable. For this reason, it needs to be investigated which of the available numerical methods models wheel rotation of a road vehicle most accurately, in spite of their limitations.

The aim of this study is therefore the evaluation and validation of the various numerical rotation methods in terms of their suitability for the qualitative prediction of fluid dynamical effects of rotating wheels and their impact on the aerodynamic behaviour of serial vehicles. The validation process is performed based on the correlation of relevant aerodynamic effects, such as alterations of the flow topology of the entire vehicle or of the integral aerodynamic forces, between simulation and experiment. The correlation considers alterations of the flow field and the surface pressure situation in proximity of the wheel, as well as inside and next to the wheel arch, and additionally in the underbody, in the tail area and in the vehicle wake region. Moreover, the origin and magnitude of drag differences are determined, and it is distinguished in detail between the effects of front and rear wheel rotation. The required experimental data is provided by the wind tunnel experiments, which were carried out within the scope of this study, or by the research of others. Based on these evaluations, a rotation method should be recommended that reflects the influence of the wheel rotation on the aerodynamic properties of the vehicle at the best possible agreement with the experiment. Furthermore, these findings should ultimately be applied to advance the industrial vehicle development process, which is why a realistic and therefore fully detailed road vehicle, including detailed underbody and engine compartment geometry, and also the cooling package is used for these studies. In the following, relevant simulation boundary conditions, such as rim geometry, as well as rim orientation, are initially examined, and suitable simulation load cases are derived from these results.

Limitations

An objective of this work is the implementation of the gained research results in the current numerical development process of *Magna Steyr* in order to ultimately extend and enhance these procedures. Therefore, most numerical and experimental investigations base on the state-of-the-art industrial aerodynamics development processes and best-practice methods of *Magna Steyr*. This also includes software resources and computational capacities. Due to strict confidentiality, not all details of the individual simulations and experiments may be reported. In order to be able to implement these findings in an industrial process with manageable pre-processing and computational times and expenses, it has also been ensured that the effort for the preparation of the simulation meshes and the computational costs are kept at a minimum, while still achieving a high quality statement.

Aside from that, the focus of the investigation of this thesis is on the energy management aspect of vehicle aerodynamics, which is why drag and not lift is considered in the following studies. Since this work examines the aerodynamic performance of wheel rotation methods rather than that of the test vehicle, and because the integral aerodynamic parameters of the vehicle are subject to secrecy, drag data is presented as differential values and not as absolute ones.

Magna Steyr's numerical aerodynamics process bases on the *Fluent* CFD solver of *ANSYS*, which is therefore utilized for the numerical investigations conducted in this research. Furthermore, a steady-state simulation model was selected and applied using the Reynolds-Averaged Navier-Stokes (*RANS*) method. No studies are carried out by means of transient methods, since they are, on the one hand, not a part of *Magna Steyr*'s current standard simulation process and, on the other hand, due to the much higher computational effort and costs. All rotation methods currently offered by *ANSYS* Fluent were investigated, with the exception of the *SM* method, since the application of this approach implicitly requires transient simulations.

Additional factors, which would also affect the flow behavior of the wheels, such as deformed tire geometry and detailed-structured tire treads, were not considered in this research, since these extensive topics would go beyond the scope of this work. In order to eliminate the impact of these two factors as far as possible, differential analyses between load cases with the same tire configuration are mainly carried out in the following investigations.

2.3 Outline

The following chapter describes the methodology and therefore the theoretical foundations and physical concepts on which this study is based. The fundamental equations of motion of fluid mechanics are derived, and the aerodynamic fundamentals of passenger car development in the vehicle industry are discussed. Furthermore, the methods and processes used in this work to gain the experimental and numerical data are presented. This includes both the experimental methods and the numerical principles and concepts of computational fluid mechanics. Finally, the analysis methods, processes and tools utilized and applied during this research are presented and discussed for both the experimental and the numerical part.

In order to define the numerical load cases examined in the scope of this work, two preliminary studies were carried out initially. On the one hand, the impact of different rim geometries on the aerodynamic parameters of the test vehicle was investigated experimentally. On the other hand, numerical methods were utilized to investigate the effects of different rim orientations on the flow topology, as well as on the aerodynamic drag of the vehicle [64]. The results of these analyses have been considered for the definition of the numerical simulation cases.

The majority of this work deals with the effects of individual numerical wheel rotation methods on the overall vehicle aerodynamics. In order to understand the alterations and the impact of rotating wheels on the highly complex flow topology of the vehicle, the air flow situation within the wheel arch was analysed initially. For this purpose, aerodynamic wind tunnel experiments, as well as numerical investigations, were carried out. The effects of numerical wheel rotation methods on this fluid dynamical system were discussed and validated with the experiment and the results of other studies.

The flow topology of the entire vehicle was subsequently examined, and the impact of wheel rotation on this aerodynamic system was analysed. Again, wind tunnel measurements, as well as corresponding numerical investigations using various rotation methods, were carried out, and the effects on vehicle aerodynamics were investigated, including flow topology studies as well as analyses of the integral aerodynamic forces on the vehicle. The results were expanded and detailed by studies on the influence of front and rear wheel rotation. Finally, the distributions of aerodynamic drag alterations were analysed separately for vehicle body, wheels, tires and rims.

Finally, the findings are summarized and discussed. Afterwards, suggestions for further research as well as recommendations will be presented.

Chapter 3

Methodology

In this chapter, the physical concepts, as well as methods and processes developed and utilized to gain the experimental and numerical data for this study, are described. Accordingly, this chapter is divided into four main parts.
In the first section, the basic physical principles of the aerodynamic development are discussed. Basic fluid dynamical concepts are described, and the fundamental equations of motion of fluid mechanics are derived. This is followed by formal definitions of fluid dynamics commonly used in vehicle aerodynamics, including the coordinate system, fundamental fluid mechanical quantities, as well as relevant forces and field parameters.

The experimental section presents the methods and processes developed and used to gain the experimental data of this thesis. A description of the aerodynamic wind tunnel test facility, the test vehicle and wheel hardware models, load cases and setups, boundary conditions, measuring equipment, as well as the processes and methods utilized to investigate the vehicle forces, the surface pressure distribution or the flow field topology are presented.

In the numerical part, principles of computational fluid dynamics and relevant methods of turbulence modelling are discussed. Furthermore, the virtual development process is outlined, and details of the vehicle, wheel and wind tunnel simulation models are presented. Finally, simulation boundary conditions and solver-settings are detailed.

At the end of the chapter, analysis methods, techniques and tools used for data post-processing are described. Furthermore, the self-developed analysis software *ASDAT* is introduced.

The processes and methods described in this section are valid in the majority of the subsequent chapters (such as, for example, the description of the test vehicle or the numerical process) and will therefore not to be repeated again hereafter. However, methods relevant only for individual research subjects are described in the corresponding chapters.

3.1 Fluid dynamic principles of vehicle development

Road vehicle geometries are highly complex. Additional to the detailed, bluff body of a vehicle, a fractured, rough underbody and the chassis, as well as add-on components such as exterior mirrors, windscreen wipers, strips and door handles, as well as the engine compartment flow and the flow through the wheel arches, characterize the flow topology of a vehicle. Rotating vehicle parts, such as rims, tires or fans, as well as ground effects due to the relative movement between the vehicle and the road, are also distinguishing features of this fluid dynamical system.

The asymmetric flow field around a vehicle is characterized by high pressure gradients, as well as flow separation with and without reattachment, resulting in open and closed separation areas of various sizes. Due to the transient nature of these flow fields, the detachment regions are time-dependent and subject to random fluctuations. The boundary layer, which forms in the flow around the vehicle, is generally fully turbulent with Reynolds numbers greater than 10^6 based on the vehicle length. However, the turbulence is limited to a small area around the vehicle, since the resulting boundary layer is relatively thin, in contrast to the wake area downstream of the vessel, which is heavily turbulent.

The motion of these air flows can be described using the Navier-Stokes equations, from which further, fundamentally important relationships of fluid mechanics can be derived. For this reason, the following section describes basics of fluid mechanics and vehicle aerodynamics and derives the general basic equations of motion for three-dimensional flow. This system of equations forms the basis for the numerical solution methods in the following chapters.

3.1.1 Basic equations of fluid dynamics

The basic equations of fluid dynamics consist of the equations of mass balance, the equations of momentum balance (as they describe the balance of forces between pressure forces, inertia forces and frictional forces in the flow) and, for compressible flows, the equation of energy balance with the thermodynamic process. Those balances can, as described below, be derived from the fundamental axioms of conservation laws of mass, momentum, and energy. In particular, these equations also include the representation of turbulence and boundary layers, and therefore a basic mathematical model of fluid mechanics. Furthermore, the following considerations are based on the assumption that fluids correspond to the continuum assumption, i.e. that they do not consist of a number of discrete particles, but rather are a continuous substance. In this section, initially the material derivative is defined, and the general form of the continuity equation is developed. Based on the physical principle of mass conservation, the continuity equation for mass is obtained. Finally, the momentum equations for fluids (Navier-Stokes equations) are derived from Newton's second law of motion.

In the following, it is appropriate for the subsequent considerations to define the investigated velocity regime, since compressibility effects differ in distinct velocity ranges and various physical phenomena occur that require varying physical and mathematical approaches. The Mach number Ma can be used to define these velocity regimes. This physical quantity indicates the ratio of the velocity of a body or of a fluid v_∞ to the speed of sound of the fluid c and is thus a dimensionless index of the velocities in a fluid dynamic system. Air flows with

$$Ma = \frac{v_\infty}{c} < 0.3, \tag{3.1}$$

as is the case in series-production aerodynamics, are treated as incompressible, which simplifies the flow-physical equations with negligible error.

Lagrangian and Eulerian approaches to specify the balance equations

The balance equations for mass, momentum and energy can either be defined according to the *Lagrangian* or according to the *Eulerian* approach [65, 66]. With the Lagrangian approach, the fluid is divided into individual partial volumes, hereinafter referred to as material volumes (MV), which always contain the same fluid particles. These volumes therefore move with the flow through space and time and are surrounded by a boundary that can change over time. In contrast, the Eulerian approach takes into account a finite volume, called the control volume (CV), which is fixed in space. This control volume has a fixed, but arbitrarily selectable and penetrable boundary. The balances for mass, momentum and energy thus depend on the fluxes caused by flows through the boundary of the control volume. Consequently, the alterations of the properties of a fluid can either be described by tracking certain fluid packets of the flow (Lagrange) along their path, or at a specific location in space through which fluid parcels flow (Euler).

Material and local derivative

In accordance with the two approaches described above, the derivative of a field variable of any physical quantity of the flow $\phi\,(t, \vec{x}(t))$ with $\vec{x} = (x, y, z)$ in regard to a fixed position in space ($\partial\phi/\partial t$) is referred to as the *Eulerian*, or *local derivative*, while the derivation for a moving fluid parcel ($D\phi/Dt$) is called the *Lagrangian* or *material derivative.*

The *material derivative* of variable ϕ is defined as [67]:

$$\begin{aligned} \frac{D\phi}{Dt} &= \frac{dt}{dt}\frac{\partial\phi}{\partial t} + \underbrace{\frac{dx}{dt}}_{u}\frac{\partial\phi}{\partial x} + \underbrace{\frac{dy}{dt}}_{v}\frac{\partial\phi}{\partial y} + \underbrace{\frac{dz}{dt}}_{w}\frac{\partial\phi}{\partial z} \\ &= \frac{\partial\phi}{\partial t} + \vec{u}\cdot\nabla\phi \end{aligned} \tag{3.2}$$

where $\vec{u}$ is the velocity vector with

$$\vec{u} = (u, v, w)$$

in Cartesian components, and ∇ is the gradient operator according to

$$\nabla = \left(\frac{\partial}{\partial x}, \frac{\partial}{\partial y}, \frac{\partial}{\partial z}\right)$$

The first summand in the last line on the right side in Eq. (3.2) corresponds to the local rate of change and describes the explicit time dependency of the field. This term therefore specifies how ϕ changes at a fixed location $\vec{x}$. The second summand is the convective rate of change and describes the change additionally caused by the movement of the fluid parcel. The material derivative therefore describes that the total rates of change of the physical quantity ϕ is equal to the sum of its local and convective rate of change.

Reynolds transport theorem

The balance equations for mass, momentum and energy apply to moving material volumes and not to fixed points of the flow or control volume [66, 68]. To describe these laws using the Eulerian approach, Euler's equivalent of an integral over a moving volume must be known. This relation can be expressed by the Reynolds transport theorem. It states that, the instantaneous change of any extensive property B in a material volume MV must be equal to the total instantaneous change of B within the control volume Ω, plus the netto flow lost or gained through its bounding surface area $\partial\Omega$, and the amount that is generated or consumed by sources and sinks within the volume:

$$\left(\frac{dB}{dt}\right)_{\mathrm{MV}} = \frac{d}{dt}\int\limits_{\Omega} b\rho \; \mathrm{d}V + \int\limits_{\partial\Omega} b\rho \; \vec{u}\cdot\vec{n} \; \mathrm{d}A + \int\limits_{\Omega} Q \; \mathrm{d}V \tag{3.3}$$

Here, b is the intensive value of B (per unit mass m) in any small element of the fluid, according to

$$b = \frac{dB}{dm} \tag{3.4}$$

Furthermore, ρ is the fluid density and $\vec{u}$ the flow velocity, $\vec{n}$ is the normal vector pointing outward of the control volume, Q represents the sources and sinks of the flow inside the control volume, while $\mathrm{d}V$ and $\mathrm{d}A$ are volume and surface elements, respectively. The first term on the right side of Eq. (3.3) represents the temporal rate of change of the property b within the control volume. The second term corresponds to the flux, which represents how much of property b flows into or out of the control volume over its bounding $\partial\Omega$. The third term describes how much of property b enters or exits the volume due to sources or sinks, with sources taken to be positive. However, in the following neither sources or sinks are assumed to exist in the control volume ($Q = 0$). Therefore, this term is not considered in the following.

Applying Leibnitz's rule on the first term on the right side of Eq. (3.3) yields:

$$\frac{d}{dt}\int\limits_{\Omega} b\rho \; \mathrm{d}V = \int\limits_{\Omega} \frac{\partial}{\partial t} b\rho \; \mathrm{d}V \tag{3.5}$$

By means of the Gauss Divergence Theorem, the surface integral in Eq. (3.3) can be transformed into a volume integral:

$$\int\limits_{\partial\Omega} b\rho\vec{u}\cdot\vec{n} \; \mathrm{d}A = \int\limits_{\Omega} \nabla\cdot(b\rho\;\vec{u}) \; \mathrm{d}V \tag{3.6}$$

Inserting Eqs. (3.5) and (3.6) in Eq. (3.3) and combining all integrals results in:

$$\left(\frac{dB}{dt}\right)_{\mathrm{MV}} = \int\limits_{\Omega} \left[\frac{\partial}{\partial t}(b\rho) + \nabla\cdot(\rho\vec{u}b)\right] \mathrm{d}V \tag{3.7}$$

An alternative form of Eq. (3.7) can be obtained through expansion of the second term inside the square brackets and by using the material derivative (Eq. (3.2)), which gives

$$\left(\frac{dB}{dt}\right)_{\mathrm{MV}} = \int\limits_{\Omega} \left[\frac{D}{Dt}(b\rho) + \rho b \nabla \cdot \vec{u}\right] \mathrm{d}V \tag{3.8}$$

Through this general form of the continuity equation, three important balance equations can be derived: the mass, momentum and energy balances.

Mass balance

The continuity equation results from the mass balance, which states that the temporal change of mass within the control volume corresponds to the difference between incoming and outgoing mass flows. This relation can be expressed in the material (Lagrangian) coordinate system as

$$\left(\frac{dm}{dt}\right)_{\mathrm{MV}} = 0 \tag{3.9}$$

Equating the property B with mass ($B = m$) in the general form of continuity equation (Eq. (3.8)) and by using the corresponding intensive quantity $b = 1$ (from Eq. (3.4)) gives the equivalent for the mass balance in the Eulerian coordinate system:

$$\left(\frac{dm}{dt}\right)_{\mathrm{MV}} = \int\limits_{\Omega} \left[\frac{D\rho}{Dt} + \rho \nabla \cdot \vec{u}\right] \mathrm{d}V = 0 \tag{3.10}$$

Equation (3.10) must apply to any control volume Ω, which can only be true if the integrand itself is zero. It follows directly:

$$\frac{D\rho}{Dt} + \rho \nabla \cdot \vec{u} = 0 \tag{3.11}$$

For the case of an incompressible fluid, with constant density independent of space and time, so that

$$\frac{D\rho}{Dt} = 0 \tag{3.12}$$

Eq. (3.11) can be simplified to

$$\nabla \cdot \vec{u} = 0 \tag{3.13}$$

which describes that the velocity field is divergence-free.

Momentum balance

The momentum equation is based on Newton's second law of motion, the principle of linear momentum, which states that the temporal change of the total momentum of a closed system (control volume) corresponds to the sum of the external forces acting on the system:

$$\left(\frac{d(m\vec{u})}{dt}\right)_{\mathrm{MV}} = \left(\int\limits_{\Omega} \vec{f}\,\mathrm{d}V\right)_{\mathrm{MV}} \tag{3.14}$$

From Eq. (3.14) and with $B = m\vec{u}$ and $b = \vec{u}$ (from Eq. (3.4)) results with Eq. (3.8):

$$\int\limits_{\Omega} \left[\frac{D}{Dt}(\rho\vec{u}) + \rho\vec{u}\nabla \cdot \vec{u} - \vec{f} \right] \mathrm{d}V = 0 \tag{3.15}$$

Again, Eq. (3.15) must apply to any control volume Ω, wherefore the integrand itself must be zero. It follows:

$$\frac{D}{Dt}(\rho\vec{u}) + \rho\vec{u}\nabla \cdot \vec{u} = \vec{f} \tag{3.16}$$

Expansion of the material derivation, as well as regrouping results in the non-conservative form of the momentum equation:

$$\rho\frac{D\vec{u}}{Dt} + \vec{u} \underbrace{\left(\frac{D\rho}{Dt} + \rho\nabla \cdot \vec{u} \right)}_{\text{Continuity}} = \vec{f} \tag{3.17}$$

The use of mass balance (Eq. (3.11)) and the expansion of the material derivative reduce the non-conservative form of the momentum equation to

$$\rho \left[\frac{\partial \vec{u}}{\partial t} + (\vec{u} \cdot \nabla)\, \vec{u} \right] = \vec{f} \tag{3.18}$$

The full form of the momentum equation is obtained by specifying the acting forces $\vec{f}$. The total force $\vec{f}$ in the control volume Ω can be separated into two parts:

$$\int\limits_{\Omega} \vec{f}\, \mathrm{d}V = \int\limits_{\Omega} \rho\vec{f_b}\, \mathrm{d}V + \int\limits_{\partial\Omega} \boldsymbol{\sigma}\vec{n}\, \mathrm{d}A \tag{3.19}$$

The first term in Eq. (3.19) corresponds to the body forces (with $\vec{f_b}$ as distributed body forces) acting on each element in the control volume (such as gravity, electromagnetic forces, etc.) and the second term describes surface forces such as pressure and frictional forces. The latter are, in turn, composed of normal forces and shear forces, which can be expressed by the Cauchy stress tensor $\boldsymbol{\sigma}$ (Fig. 3.1):

$$\boldsymbol{\sigma} = \begin{bmatrix} \sigma_{11} & \tau_{12} & \tau_{13} \\ \tau_{21} & \sigma_{22} & \tau_{23} \\ \tau_{31} & \tau_{32} & \sigma_{33} \end{bmatrix} \tag{3.20}$$

where the diagonal components σ_{11}, σ_{22}, and σ_{33} represent normal stresses, and τ_{12}, τ_{13}, τ_{21}, τ_{23}, τ_{31} and τ_{32} correspond to the shear stresses.

The stress tensor is often divided into two terms, the isotropic part (pressure), and the anisotropic part, which represents the forces determined by body deformation and movement and is composed of the viscous stresses on the fluid. Thus, $\boldsymbol{\sigma}$ is broken down into

$$\boldsymbol{\sigma} = -p\boldsymbol{I} + \boldsymbol{T} = -\begin{bmatrix} p & 0 & 0 \\ 0 & p & 0 \\ 0 & 0 & p \end{bmatrix} + \begin{bmatrix} \tau_{11} & \tau_{12} & \tau_{13} \\ \tau_{21} & \tau_{22} & \tau_{23} \\ \tau_{31} & \tau_{32} & \tau_{33} \end{bmatrix} \tag{3.21}$$

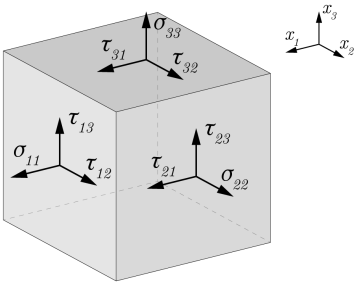

Figure 3.1: Stress tensor components.

where p represents the pressure, considered as negative normal stress, $\boldsymbol{I}$ is the identity tensor and $\boldsymbol{T}$ corresponds to the stress deviator tensor.

Inserting the stress tensor (Eq. (3.21)) into Eq. (3.19) and after applying the Gauss Theorem to each surface integral yields:

$$\begin{aligned} \int\limits_{\Omega} \vec{f} \ \mathrm{d}V &= -\int\limits_{\partial\Omega} p\vec{n} \ \mathrm{d}A + \int\limits_{\partial\Omega} \boldsymbol{T} \cdot \vec{n} \ \mathrm{d}A + \int\limits_{\Omega} \rho \vec{f_b} \ \mathrm{d}V \\ &= -\int\limits_{\Omega} \nabla p \ \mathrm{d}V + \int\limits_{\Omega} \nabla \cdot \boldsymbol{T} \ \mathrm{d}V + \int\limits_{\Omega} \rho \vec{f_b} \ \mathrm{d}V \end{aligned} \tag{3.22}$$

with the divergence of the stress deviator tensor

$$\nabla \cdot \boldsymbol{T} = \sum_{i,j=1}^{3} \frac{\partial \boldsymbol{T}_{ij}}{\partial x_i} \hat{e}_j \tag{3.23}$$

where $\boldsymbol{T}_{ij}$ are the components of the stress deviator tensor $\boldsymbol{T}$ with respect to the standard basis $\hat{e}_{1,2,3}$. The first term of Eq. (3.22) represents the pressure as a negative normal stress, the second term represents the shear forces and normal stresses acting on the volume element, and the third term is the sum of the body forces acting on the mass of the volume element.

The substitution of the sum of the integrands from Eq. (3.22) into Eq. (3.18) yields the final form of the momentum equation in conservative form:

$$\rho \left[\frac{\partial \vec{u}}{\partial t} + (\vec{u} \cdot \nabla) \vec{u} \right] = -\nabla p + \nabla \cdot \boldsymbol{T} + \rho \vec{f_b} \tag{3.24}$$

or by considering material derivation in a non-conservative form:

$$\rho \frac{D\vec{u}}{Dt} = -\nabla p + \nabla \cdot \boldsymbol{T} + \rho \vec{f_b} \tag{3.25}$$

The Eqs. (3.24) are called the Navier-Stokes equations. The left side of Eq. (3.24) can physically be interpreted as the acceleration of the fluid particle, while the right side represents the sum of forces acting on each particle. The acceleration consists of two parts, where $\frac{\partial \vec{u}}{\partial t}$ represents the local acceleration, which describes the velocity alteration of the particle observed from a fixed point within the flow. $\vec{u} \cdot \nabla \vec{u}$ is the convective acceleration and describes the velocity change in space, while the particle is moving from one position of the flow field to another.

The right side of Eq. (3.24) consists of three terms. The pressure term $-\nabla p$ indicates that the fluid streams in the direction of the largest pressure alteration. The stress term $\nabla \cdot \boldsymbol{T}$ represents the frictional force due to viscosity and causes change of momentum due to friction, which furthermore may cause turbulence and velocity profiles. The body force term $\vec{f_b}$ represents the forces that act on and affect every single particle of the fluid, due to force fields in space.

Newtonian Fluids

As this work deals with incompressible Newtonian fluids (especially air), the Navier-Stokes equations are subsequently discussed for this case. For a Newtonian fluid, the relationship between viscous stress and strain rate (the derivative of its deformation) is linear. The proportionality constant is the viscosity μ of the fluid. The basis for Newtonian fluid equations is therefore the assumption about the nature and definition of the stress tensor:

$$\tau_{ij} = \mu \left(\frac{\partial u_i}{\partial x_j} + \frac{\partial u_j}{\partial x_i} \right) \tag{3.26}$$

Using this approach in Eq. (3.21) and assuming that the viscosity μ is constant, the stress divergence $\nabla \cdot \boldsymbol{T}$ follows as

$$\nabla \cdot \boldsymbol{T} = \mu \nabla \cdot \begin{bmatrix} 2\frac{\partial u}{\partial x} & \frac{\partial u}{\partial y} + \frac{\partial v}{\partial x} & \frac{\partial u}{\partial z} + \frac{\partial w}{\partial x} \\ \frac{\partial u}{\partial y} + \frac{\partial v}{\partial x} & 2\frac{\partial v}{\partial y} & \frac{\partial v}{\partial z} + \frac{\partial w}{\partial y} \\ \frac{\partial u}{\partial z} + \frac{\partial w}{\partial x} & \frac{\partial v}{\partial z} + \frac{\partial w}{\partial y} & 2\frac{\partial w}{\partial z} \end{bmatrix} \tag{3.27}$$

For the x-component follows:

$$\begin{aligned} (\nabla \cdot \boldsymbol{T})_x &= \mu \left[\frac{\partial}{\partial x} \left(2\frac{\partial u}{\partial x} \right) + \frac{\partial}{\partial y} \left(\frac{\partial u}{\partial y} + \frac{\partial v}{\partial x} \right) + \frac{\partial}{\partial z} \left(\frac{\partial u}{\partial z} + \frac{\partial w}{\partial x} \right) \right] = \\ &= \mu \left[\frac{\partial^2 u}{\partial x^2} + \frac{\partial^2 u}{\partial y^2} + \frac{\partial^2 u}{\partial z^2} \right] + \mu \left[\frac{\partial^2 u}{\partial x^2} + \frac{\partial^2 v}{\partial x \partial y} + \frac{\partial^2 w}{\partial x \partial z} \right] = \\ &= \mu \nabla^2 u + \mu \frac{\partial}{\partial x} \underbrace{\left(\frac{\partial u}{\partial x} + \frac{\partial v}{\partial y} + \frac{\partial w}{\partial z} \right)}_{= \nabla \cdot \vec{u} = 0} = \\ &= \mu \nabla^2 u \end{aligned} \tag{3.28}$$

where the mass balance for incompressible fluids (Eq. (3.13)) was applied.

The stress divergence for all components yields

$$\nabla \cdot \boldsymbol{T} = \mu \nabla^2 \vec{u} \tag{3.29}$$

The Navier-Stokes equations for an incompressible Newtonian fluid can be derived through substitution of Eq. (3.29) into Eq. (3.24) reads:

$$\rho \left(\frac{\partial \vec{u}}{\partial t} + \vec{u} \cdot \nabla \vec{u} \right) = -\nabla p + \mu \Delta \vec{u} + \rho \vec{f_b} \tag{3.30}$$

with the Laplace operator Δ:

$$\Delta = \nabla \cdot \nabla = \nabla^2 \tag{3.31}$$

Energy balance

Since the influence of the compressibility of flows in vehicle aerodynamics can be neglected at air speeds < 250 km/h (such that $Ma < 0.3$) [69], and also no heat exchange between the vehicle and its surroundings will be considered, it is refrained from deriving the energy equation here.

3.1.2 Characterization of fluid dynamical systems

Aerodynamic tasks are usually distinguished in that a body with the characteristic size L moves with a relative velocity u_∞ within an (incompressible) fluid, which is defined through the density ρ_∞ and the kinematic viscosity ν. In vehicle aerodynamics, the length of the vehicle in the flow direction is usually selected as the characteristic length. The Navier-Stokes equations (Eq. (3.30) can be non-dimensionalized by length, velocity and density and rewritten by using dimensionless variants (indicated by *) of the physical quantities defined as:

$$\vec{x}^* := \frac{\vec{x}}{L} \qquad \vec{u}^* := \frac{\vec{u}}{u_\infty} \qquad t^* := \frac{u_\infty t}{L} \qquad p^* := \frac{p}{\rho u_\infty^2} \tag{3.32}$$

$$\vec{f}^* := \frac{L\vec{f_b}}{u_\infty^2} \qquad \nabla^* := L\nabla \qquad \Delta^* := L^2\Delta \tag{3.33}$$

where μ represents the dynamic viscosity of the fluid and $\vec{f}^*$ the dimensionless body force density. This yields the dimensionless momentum equation:

$$\frac{\partial \vec{u}^*}{\partial t^*} + (\vec{u}^* \cdot \nabla^*)\vec{u}^* = -\nabla^* p^* + \frac{1}{\mathrm{Re}}\Delta^* \vec{u}^* + \vec{f}^* \tag{3.34}$$

with the Reynolds number Re, which represents the ratio of inertial forces to viscous forces in a fluid:

$$Re = \frac{u_\infty\, L}{\nu} = \frac{\rho\, u_\infty\, L}{\mu} \tag{3.35}$$

Thus, the Navier-Stokes equations for all dynamic problems of incompressible Newtonian fluids depend only on the Reynolds number, which shows that the relative behavior of a flow is significantly dependent on this parameter. Due to the low kinematic viscosity of air, in aerodynamics one usually deals with fluid dynamical systems of very large Reynolds numbers ($Re > 10^7$), where the inertia terms play a dominant role and the flow is essentially inviscid. The Reynolds number Re, together with the Mach number Ma, serve as important fluid mechanical key quantities to characterize such fluid dynamical systems.

3.1.3 Euler equations

The Navier-Stokes equations include the Euler equations as the special case in which the friction of the fluid is zero. This yields the Euler equation from Eq. (3.24):

$$\frac{\partial \vec{u}}{\partial t} + \vec{u} \cdot \nabla \vec{u} = -\frac{1}{\rho} \nabla p + \vec{f_b} \tag{3.36}$$

3.1.4 Bernoulli equation

The Bernoulli equation can be derived from the Euler equations [69]. For incompressible and stationary flows ($\frac{\partial \vec{u}}{\partial t} = 0$) and with the Lame vector identity,

$$(\vec{u} \cdot \nabla)\vec{u} = \frac{1}{2} \nabla \left(\vec{u}^2\right) - \vec{u} \times (\nabla \times \vec{u}) \tag{3.37}$$

the Euler Eq. (3.36) can be rewritten as follows:

$$\frac{1}{2} \nabla \left(\vec{u}^2\right) - \vec{u} \times (\nabla \times \vec{u}) = -\nabla \frac{p}{\rho} + \vec{f_b} \tag{3.38}$$

The projection of this equation onto a curve S is then

$$\frac{1}{2} \nabla \left(\vec{u}^2\right) \cdot \vec{ds} - [\vec{u} \times (\nabla \times \vec{u})] \cdot \vec{ds} = -\nabla \frac{p}{\rho} \cdot \vec{ds} + \vec{f_b} \cdot \vec{ds} \tag{3.39}$$

with $\vec{ds}$ as a vectorial curve element with infinitesimal length ds and tangent to the curve. The second term on the left side of Eq. (3.39) equals zero when the flow is free of rotation, i.e. $\nabla \times \vec{u} = \vec{0}$, or curve S is a streamline. For these two cases, and with the assumption that the body forces have a potential, i.e. $\vec{f_b} = -\nabla G$, Eq. (3.39) yields after rearranging

$$\frac{1}{2} \nabla \left(\vec{u}^2\right) \cdot \vec{ds} + \nabla \frac{p}{\rho} \cdot \vec{ds} + \nabla G \cdot \vec{ds} = 0 \tag{3.40}$$

Integration of Eq. (3.40) along the curve S, due to the identity

$$\nabla f \cdot \vec{ds} = \frac{\partial f}{\partial x} dx + \frac{\partial f}{\partial y} dy + \frac{\partial f}{\partial z} dz = df \tag{3.41}$$

and multiplication by the density ρ, results in the Bernoulli equation for stationary, incompressible, inviscid flows along a streamline:

$$p + \rho\, G + \frac{\rho}{2}\, u^2 = \text{const.} \tag{3.42}$$

3.1.5 Vehicle aerodynamics

The movement of a body, such as a passenger car, displaces the approaching air and thus irreversibly converts pressure into kinetic energy of the surrounding medium. As a result of the relative movement between air and body, a surface pressure distribution forms due to the local velocities of the air flow. This pressure distribution and acting shear stresses cause aerodynamic forces and moments that affect the vehicle. In vehicle aerodynamics, these forces can be categorized into two fields, namely those that arise due to the flow around the vehicle and all its components, and those caused by flow effects, for example through the engine compartment and the cooling package. In the following, these forces and moments, as well as their aerodynamic coefficients, will be described in detail.

From the flow field around a vehicle and the corresponding velocities, local pressures can be determined by means of the Bernoulli equation for stationary, incompressible, inviscid flows (Eq. (3.42)) for the simplified case of vehicle aerodynamics. In vehicle aerodynamics, the change in the body force term along the streamline is so small compared with the other terms that it can be neglected. Equation (3.42) can then be simplified to

$$p + \frac{\rho}{2} u^2 = \text{const.} \tag{3.43}$$

or

$$p + q = p_0 \tag{3.44}$$

with

$$q = \frac{\rho}{2} u^2 \tag{3.45}$$

In Eq. (3.44), p_0 corresponds to the total pressure which is the sum of the static pressure p and the dynamic pressure q. The total pressure is constant along a streamline in a flow without friction and can generally be different from streamline to streamline. An acceleration of the flow thus always corresponds to a decrease in static pressure, while conversely, a deceleration of the flow always leads to an increase in static pressure.

The dynamic pressure q results from the kinetic energy of the fluid elements in a flow. Furthermore, the dynamic pressure of the undisturbed flow corresponds to the static pressure increase at the stagnation point (of a body within a flow) over the free-stream static pressure p.

Aerodynamic forces

Aerodynamic forces and moments result from the above described pressure distribution, which act in the normal direction on the body surface, as well as wall shear stresses that form on the surface of a vehicle moving through the atmosphere. A velocity gradient is formed, since air particles adhere to the body surface (no-slip condition). This results in a shear stress distributions due to the viscous forces in the fluid, that transmits a force in the direction of the air flow. These effects ultimately result in the formation of a boundary layer, in which the velocity of the flow decreases from the value of the undisturbed free flow to zero relative to the body at the surface.

Since no other force fields are considered, the pressure and shear stress distribution are the only forces acting on the body. Therefore, by integration, a resulting fluid dynamic flow force $\vec{F}_T$, acting on a body in a flowing fluid, results:

$$\vec{F}_T = \oint_{\partial\Omega} \boldsymbol{\sigma} \cdot \vec{n} \, \mathrm{d}A = - \oint_{\partial\Omega} p \, \vec{n} \, \mathrm{d}A + \oint_{\partial\Omega} \boldsymbol{T} \cdot \vec{n} \, \mathrm{d}A \tag{3.46}$$

with $\partial\Omega$ as the total surface of the body, $\boldsymbol{\sigma}$ as the Cauchy stress tensor, $\boldsymbol{T}$ as the stress deviator tensor, and $\vec{n}$ as the local normal unit vector pointing outwards of the body at the surface element $\mathrm{d}A$. This force is composed of two parts: The pressure resistance corresponds to the first term on the right side of Eq. (3.46) and results from integration of the fluid pressure p over the entire body surface. The second term expresses the frictional resistance, which results from integration of the shear stress distribution over the total surface of the body.

The total aerodynamic force acting on a body moving in a fluid is typically split into three components, corresponding to the directions of the body-fixed coordinate system (as shown schematically in Fig. 3.2):

$$\vec{F}_T = \begin{bmatrix} F_D \\ F_S \\ F_L \end{bmatrix} \tag{3.47}$$

with the aerodynamic drag F_D, lift F_L and lateral force F_S:

$$\begin{aligned} F_D &= \oint_{\partial\Omega} \sum_{i=1}^{3} \sigma_{ix}\, n_i \,\mathrm{d}A \\ F_L &= \oint_{\partial\Omega} \sum_{i=1}^{3} \sigma_{iz}\, n_i \,\mathrm{d}A \\ F_S &= \oint_{\partial\Omega} \sum_{i=1}^{3} \sigma_{iy}\, n_i \,\mathrm{d}A \end{aligned} \tag{3.48}$$

where n_i are the components of the local normal unit vector of the body surface element $\mathrm{d}A$, and the indices i from 1 to 3 represent the three Cartesian directions x, y and z.

The aerodynamic drag F_D is usually the force component in the direction of the air flow. In case of a symmetric flow, this coincides with the vehicle's longitudinal axis and counteracts the relative movement of the vehicle through the air. A major part of this force originates due to the pressure distribution on the vehicle surface, since the pressure over large areas of the surface is much greater than viscous stresses. Only a small portion is created by frictional forces at the vehicle surface [69]. Aerodynamic lift F_L is an upward force that counteracts the gravitational force and thus has a great impact on the stability and traction of the vehicle. It is caused by the pressure difference between the vehicle upper side and the underbody and is largely determined by the vehicle shape and ground effects. The lateral force F_S acts on the side of the vehicle and is an important factor, especially at high speeds and for example at inclined flow, such as side wind or at overtaking manoeuvers.

Furthermore, moments occur around the vehicle's main axes. These are a rolling moment $\vec{M}_{\mathrm{Roll}}$ about the longitudinal axis, a pitching moment $\vec{M}_{\mathrm{Pitch}}$ about the transverse axis and a yawing moment $\vec{M}_{\mathrm{Yaw}}$ about the vertical axis.

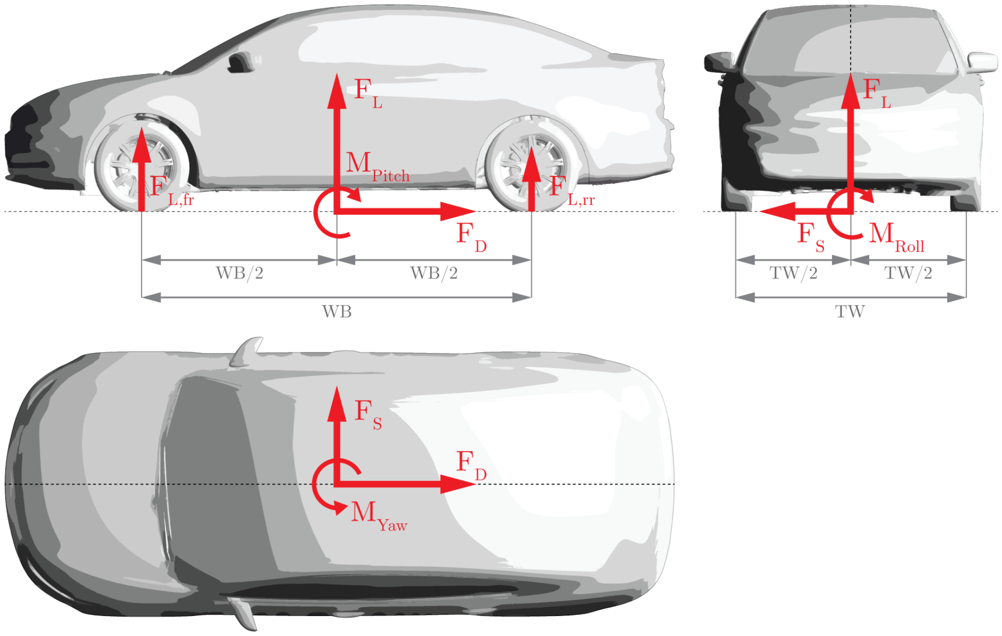

Figure 3.2: Aerodynamic vehicle forces.

Aerodynamic coefficients

In aerodynamics it is common to specify and use dimensionless coefficients instead of dimensional forces, moments and pressures. Thus, pressures are represented by their difference against the static pressure of the free flow divided by the dynamic pressure of the air flow, i.e. by the pressure coefficient C_P:

$$C_P = \frac{p - p_\infty}{\frac{\rho}{2} u_\infty^2} \tag{3.49}$$

with the static pressure p at the point where the pressure coefficient is evaluated, and the static pressure p_∞ in the free stream, i.e. remote from any disturbance. ρ is the fluid density in the free stream, u_∞ is the fluid velocity in the free stream, or the velocity of the object relative to the fluid.

While $C_P = 0$ prevails in the undisturbed flow, $C_P = 1$ results at the stagnation state on the bluff body or the vehicle. This represents the highest value the pressure coefficient in an incompressible flow can reach on bodies moving through a fluid and without energy input. Conversely, there is no minimum for the pressure coefficient. It can be stated that a negative pressure coefficient is possible, as soon as the local velocity is higher than that of the free flow.

The aerodynamic forces F_D, F_L and F_S acting on the vehicle, can be derived from the dimensionless Navier-Stokes equations (Eq. (3.34)) as a function of the Reynolds number (Eq. (3.35)) [69]. For this, however, the forces must also be represented dimensionless. By choosing the dynamic pressure and the vehicle frontal area A_p (projected in flow direction on a plane x = constant) as scaling factors for the aerodynamic drag F_D, the

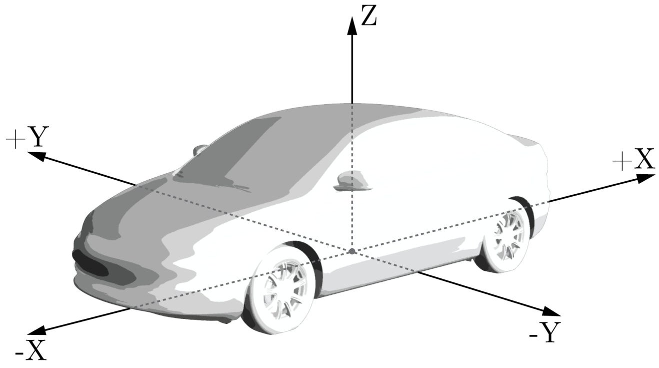

Figure 3.3: Vehicle-fixed coordinate system.

drag coefficient C_D is defined as

$$C_D := \frac{F_D}{\frac{\rho}{2}\, u_\infty^2\, A_p} = f(Re) \tag{3.50}$$

C_D can be understood as a physical quantity of the *wind slipperiness* or the aerodynamic form quality of the vehicle.

With the same consideration, the aerodynamic coefficients for lift C_L and side force C_S are defined:

$$C_L := \frac{F_L}{\frac{\rho}{2}\, u_\infty^2\, A_p} = g(Re) \tag{3.51}$$

$$C_S := \frac{F_S}{\frac{\rho}{2}\, u_\infty^2\, A_p} = h(Re) \tag{3.52}$$

where F_L represents the lift force and F_S the side force, respectively.

As a consequence, the values of these coefficients each collapse on single characteristic curves (typical for the investigated body), for all parameters of the flow (air velocity u_∞, density ρ and kinematic viscosity ν) and of the body (characteristic vehicle dimensions).

3.2 Coordinate system

In vehicle aerodynamics it is common to define a vehicle-fixed coordinate system and to position its origin at the wind tunnel floor, in the middle between the two vehicle axles and the track width. The x axis points in the air flow direction. Starting from the center of the vehicle, x therefore increases in the direction of the vehicle rear and decreases towards the vehicle front. The y axis points to the right with respect to the driving direction, and the z axis vertically upwards. The resulting coordinate system shown in Fig. 3.3 has been used for both the numerical calculations and the experiments in the aerodynamic wind tunnel.

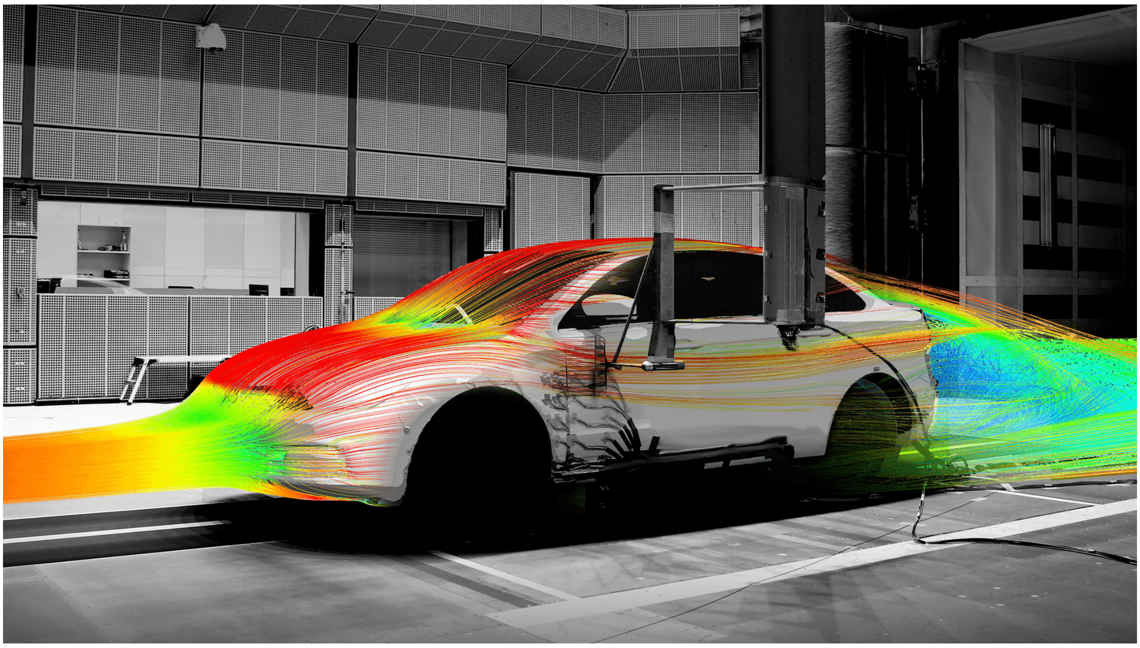

Figure 3.4: Test vehicle with simulated streamlines.

3.3 Experimental and virtual test vehicle

A primary goal of this work is to integrate the results and findings of this study into the currently used aerodynamic development process of road vehicles. The air flow situation, as well as the impact of rotating wheels and the aerodynamic flow phenomena, must therefore be investigated on a real production vehicle, considering the effects of cooling air flow through the engine compartment, as well as the impact of a detailed underbody on the vehicle flow topology, among other aerodynamic effects.

A Sedan (subsequently referred to as the *test vehicle*) was selected as a representative production vehicle for the investigations of this study, since the required CAD data, as well as a hardware test carrier, including the required tires and rims were available. Relevant vehicle information and dimensions are listed in Table 3.1, while Fig. 3.4 shows the test vehicle installed in the full-scale aerodynamic wind tunnel with an overlay by the virtual simulation model. Due to strict confidentiality, neutralized images of the test vehicle are used subsequently.

Total vehicle length	4.6 m
Wheelbase	2.7 m
Total vehicle width	1.8 m
Total vehicle height	1.5 m

Table 3.1: Test vehicle dimensions.

With a vehicle length of 4.6 m, x = -2.3 m results for the foremost point and x = 2.3 m for the rearmost point of the test vehicle in the utilized coordinate system. The wheelbase of 2.7 m resulted in a front axle position of x = -1.35 m, while the rear axle was located at x = 1.35 m.

3.4 Experimental methodology

The main objective of the experimental phase was to obtain measurement data as a basis for the comparison with results of the numerical simulations. The validation of the numerical simulations with the experiment can be performed using different approaches. In this study, aerodynamic vehicle forces and moments are analysed, surface pressure distributions are investigated and the air flow topologies at various vehicle areas are examined. Details of the measurement setup and the test vehicle configuration, the defined boundary conditions for the wind tunnel and the vehicle, as well as the measurement methods and processes are presented and described below in this chapter. Furthermore it should be noted that this work does not attempt to validate the wind tunnel, since no effort has been made in the simulation to illustrate the specific boundary conditions of the wind tunnel facility used.

3.4.1 Aerodynamic wind tunnel test facility

All aerodynamic experiments discussed in this thesis were carried out in the aeroacoustics, vehicle wind tunnel at the Research Institute of Automotive Engineering and Vehicle Engines Stuttgart (FKFS). This test facility is a full-size, Göttingen-type wind tunnel with a horizontal, closed-loop routing of the air flow and an open-nozzle test section with a length of 9.95 m and a maximum free stream velocity of 265 km/h. The dimensions of the nozzle at the exit are 5.8 m in width and 3.87 m in height, which leads to a total nozzle exit area of 22.45 m^2.

A combination of various subsystems was used for ground simulation. The main component of the moving ground system is a 5-belt road simulation system consisting of four wheel drive units and one moving center belt which runs between the wheel drive units below the vehicle. Various conditioning mechanisms prevent the formation of the boundary layer at the floor level. Further details to the components and systems of the wind tunnel facility can be found in [52], [62] and [70].

3.4.2 Test procedure and boundary conditions

All experiments were carried out at an air velocity of 140 km/h and with a yaw angle direction of 0°. Considering the vehicle geometry with a length of 4.6 meters as the characteristic length in vehicle aerodynamics, this setting resulted in a Reynolds number of $Re \approx 10^7$. Therefore, the air flow around the present vehicle can be assumed turbulent. Ideal flow conditions were used in order to ensure comparability with the computational investigations. The 5-belt ground simulation system was utilized for measurements with rotating wheels, while only the center belt was active for test cases with stationary wheels.

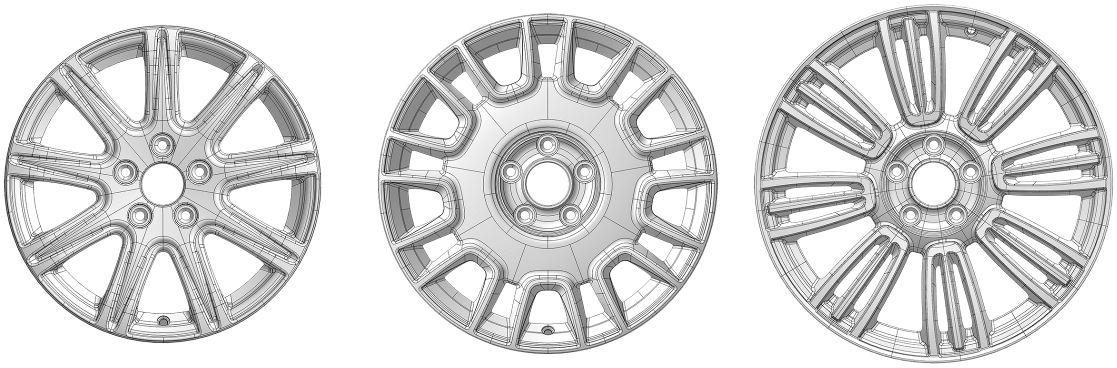

(a) *Rim16* (b) *Rim17* (c) *Rim18*

Figure 3.5: Rim geometries.

3.4.3 Vehicle setup

The test vehicle was prepared for the experiments in a way to minimize any geometrical differences, such as joints and gaps, between hardware and simulation model and therefore to match the ideal CAD dataset as accurately as possible. The riding height was set according to the CAD data and was kept constant for all measurements. The cooling grill area was prepared to represent the base configuration with enabled engine compartment air flow, as well as with completely sealed cooling grills, which is subsequently referred to as *mockup* configuration. The fan of the cooling package was fixed to eliminate cooling air flow interference due to windmilling (rotation of the non-powered fan due to under-hood air flow) and thus to correspond to the setup of the simulation.

The test vehicle was installed in the test section and connected with the plenum and the wheel drive units through four rocker panel struts positioned behind the front wheels and in front of the rear wheels. The plenum, including the rolling road simulation system, was connected to an external balance system, which was used to measure the external forces and moments acting on the test vehicle, as described in Chapter 3.4.4.

Three different rim geometries and sizes were tested during this study to cover a representative range of production vehicle rim variants. It was assumed that these three models cover common rim geometry parameters and thus allow the study of aerodynamic effects of relevant rim designs. The selected rims had a diameter of 16 inch, 17 inch and 18 inch, which will be referred to as *Rim16*, *Rim17* and *Rim18* in the following. The used CAD geometries are shown in Fig. 3.5.

3.4.4 Force and moment measurements

Vehicle drag

The aerodynamic forces and moments acting on the test vehicle are determined by means of a multi-component balance. This external balance system is arranged below the plenum in the wind tunnel floor and connected to the vehicle at the wheel contact points and rocker panel struts. From the measured forces, the aerodynamic drag can be calculated. In order to determine the drag coefficient (Eq. (3.50)), it is necessary to determine the projected frontal area in the longitudinal direction of the vehicle, which was measured through analysis of the CAD data. The accuracy of the experimentally determined drag coefficients is $C_D = \pm 0.001$.

Cooling air drag

Air flowing through the engine compartment experiences energy losses which are composed of losses at the cooling grill inlet and its surroundings, pressure losses during engine compartment flow, and the flow through the cooling package and heat exchanger, impulse losses at the engine bay outlet, as well as losses due to interactions with the vehicle flow (in particular with the front wheels) and interference effects with the air flow under the vehicle [71]. The contribution of the cooling-air flow to the total vehicle resistance in the experiment and simulation is expressed by the cooling-air drag. The cooling-air drag coefficient $C_{D,\text{cool}}$ is defined by the difference in drag between the total vehicle resistance with open and closed cooling grill. It therefore combines drag losses caused by air flow through the engine compartment as well as losses caused through air guidance to parts such as brakes or the gearbox and can be derived with:

$$C_{D,\text{cool}} = C_{D,\text{base}} - C_{D,\text{mockup}} \tag{3.53}$$

where $C_{D,\text{base}}$ represents the vehicle drag with open cooling grill and $C_{D,\text{mockup}}$ is the vehicle drag with closed and sealed cooling air inlet surfaces, which corresponds to the *mockup* configuration.

3.4.5 Surface pressure measurements

Surface pressure measurements and analysis were carried out in order to be able to conclude on the pressure situation of the flow around the vehicle. Details of this measurement method are presented hereinafter in this section.

Measuring points

Initially, five aerodynamics-sensitive zones of interest have been determined at the vehicle, in which surface pressure measurements were carried out. These were the area up- and downstream of the front wheel arch on the driver's side (subsequently referred to as vehicle zone VZ_{sideA} and VZ_{sideB}), as well as within this wheel arch (referred to as VZ_{WH}), as well as the center line of the upper vehicle surface (referred to as VZ_{top}) and the vehicle tail (referred to as VZ_{tail}). Afterwards measuring planes consisting of several measuring points were defined in these regions. In VZ_{sideA}, 9 probes were positioned, measuring a zone from x_1 = -1738 mm to x_2 = -1678 mm, and z_1 = -200 mm to z_2 = -700 mm, while VZ_{sideB} covers an area from x_1 = -1010 mm to x_2 = -650 mm, as well as z_1 = -200 mm to z_2 = -700 mm with 21 probes. In order to reduce the number of measuring points, only the left half-side of the tail was instrumented, which resulted in 24 surface pressure probes in a zone from y_1 = -780 mm to y_2 = 0 mm, and z_1 = 304 mm to z_2 = 1000 mm. Furthermore, a surface pressure probe was positioned at the center position of the number

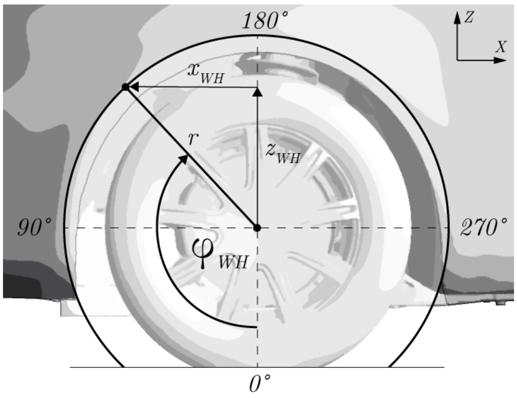

Figure 3.6: Angular notation inside the wheel arch.

plate at the front bumper in order to measure the dynamic pressure of the free air flow, which is needed for the non-dimensionalization of the pressures and forces.

The surface pressure distribution in the wheel arch is examined within a defined strip along the surface of the wheel house. This strip was defined in the middle of the wheel arch and covers a zone from y_1 = -780 mm (which corresponds to the middle of the tire tread) to y_2 = -550 mm. To be able to describe, display and plot the examined area in a flat plane, despite the curved surface of the inside of the wheel arch, the surface coordinates of the measuring points were converted from the vehicle-fixed coordinate system to a wheel house-fixed coordinate system, with the origin placed at the position of the front axle:

$$x_{\mathrm{WH}} = x_{\mathrm{vehicle}} + \Delta x_{\mathrm{FA}}$$
$$z_{\mathrm{WH}} = z_{\mathrm{vehicle}} + \Delta z_{\mathrm{FA}}$$

Here x_{WH} and z_{WH} represents the x and z coordinates of the measuring point in the wheel house-fixed coordinate system, and x_{vehicle} and z_{vehicle} the same in the vehicle-fixed system. Δx_{FA} and Δz_{FA} are the respective correction values between the two coordinate systems.

Subsequently, Cartesian coordinates were transferred to angular coordinates in order to be able to display the analysis results in a plane. The conversion was carried out using the following formula, where the front axle position has been defined as the cylinder axis:

$$\varphi_{\mathrm{WH}} = \begin{cases} \dfrac{3\pi}{2} - \arccos\left(\dfrac{x_{\mathrm{WH}}}{r}\right) & \text{for } z_{\mathrm{WH}} > 0 \\ \arccos\left(\dfrac{x_{\mathrm{WH}}}{r}\right) - \dfrac{\pi}{2} & \text{for } z_{\mathrm{WH}} \leq 0 \text{ and } x_{\mathrm{WH}} \leq 0 \\ \arccos\left(\dfrac{x_{\mathrm{WH}}}{r}\right) + \dfrac{3\pi}{2} & \text{for } z_{\mathrm{WH}} \leq 0 \text{ and } x_{\mathrm{WH}} > 0 \end{cases} \tag{3.54}$$

$$with \quad r = \sqrt{x_{\mathrm{WH}}^2 + z_{\mathrm{WH}}^2}$$

Figure 3.6 describes schematically the angular notation inside the wheel arch. This notation was used to evaluate the pressure distribution along the measurement plane at the

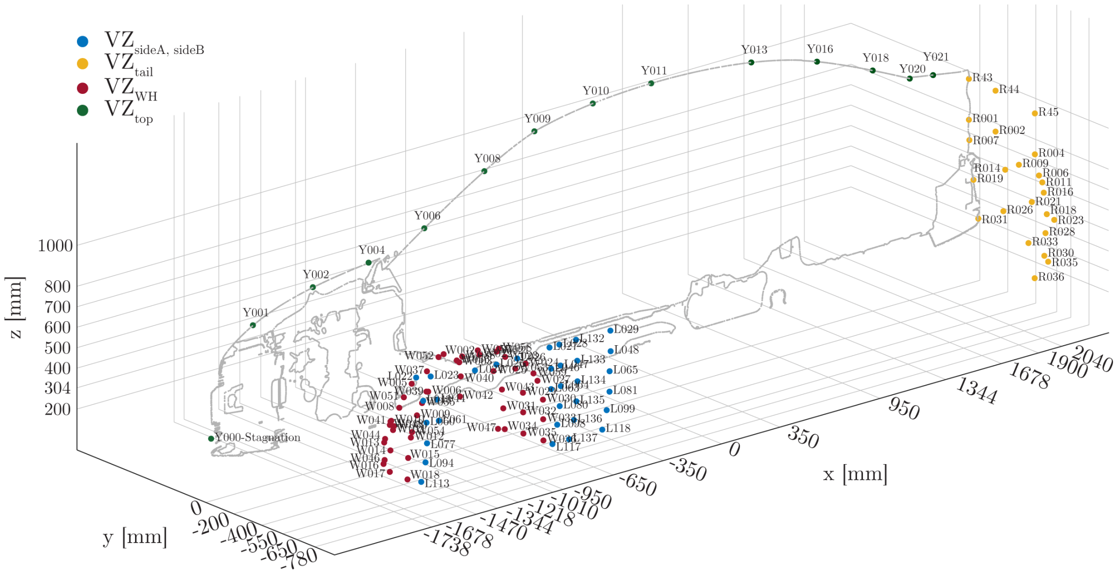

Figure 3.7: CAD overview of surface pressure measuring points.

wheel house surface. In the diagram, the polar coordinates are plotted clockwise, with $\varphi_{\mathrm{WH}} = 0^\circ = 360^\circ$ located at the wind tunnel floor, directly under the front axle of the vehicle. Due to the missing bottom side of the wheel arch, the analysis is carried out in an angular segment of the wheel house surface from $\varphi_{\mathrm{WH}} = 70^\circ$ to $\varphi_{\mathrm{WH}} = 290^\circ$.

In total, 127 pressure measuring points were defined - 77 on the vehicle surface and 50 within the wheel arch. An overview of all surface pressure probes on the vehicle is shown in Fig. 3.7. The positions of the individual measuring points were measured in the CAD system and marked by means of surveying technology on the vehicle where the measuring probes were subsequently applied.

Measurement technology

Pressure measurements on the vehicle surface were carried out through surface pressure probes provided by FKFS. This approach is not as optimal with regard to flow interference as measurements by means of holes in the surface, but it was not possible to damage the vehicle. However, surface probes provide a good representation of the actual pressure, if a considerable disturbance of the air flow can be avoided through deliberate arrangement of probes and tubes. For this reason, the application of this measurement method was considered acceptable for this study. Pressure probes were attached to the vehicle surface, and the tubing led downstream. The individual tubes were taped in flow direction in order to minimize any impact on the flow field. In the wheel arch, however, pressure measurements could be carried out without surface probes, since holes could be drilled in this region. Therefore the tubing could be guided on the inside of the wheel-housing, so that they had no disturbing influence on the air flow at all. In total, more than 2000 meters of tubing were installed in and on the vehicle in order to connect the probes to the measuring instruments. Details of the final measurement setup are shown in Fig. 3.8 for

VZ_{top}, VZ_{sideA} and VZ_{sideB}, as well as VZ_{WH} and VZ_{tail}.

The pressure sensors were connected to a PSI pressure measuring system, which consisted of several ESP miniature scanners (ESP-32HD) that were used in parallel. This system was connected to the measuring computer which performed the signal sampling with a frequency of $50Hz$ and calculated an average value over a period of 30 seconds. However, transient data was not provided by the software and is not available. The entire system was calibrated prior to measurement to achieve a precision of ±3 Pa, which corresponds to an accuracy of the surface pressure coefficient of $C_P = \pm 0.003$ at an air flow velocity of 140 km/h.

Post-processing and analysis

In order to evaluate the measured raw data, the corresponding dimensionless surface pressure coefficients C_P were initially calculated according to Eq. (3.49). The resulting values are plotted for the defined analysis planes within the stationary vehicle coordinate system or the wheel house coordinate system and are displayed as contour plots using the analysis tool *ASDAT* (see Chapter 3.6).

Since neither the probes on the vehicle surface, nor the surface mesh elements of the virtual vehicle are regularly distributed, the analyses are carried out by means of interpolation of the pressure values in the analysis area. This was performed by positioning the experimentally and virtually obtained data according to the coordinates of the measuring probes or of the surface elements within the previously defined two-dimensional analysis surface. For the numerical investigations, all pressure values in the evaluation area are used. Thus, a higher resolution was achieved than for the experiment, where the number of measuring probes was strongly limited. Subsequently, a grid was defined for each plane, wherein an interpolation of the measured values was carried out.

In the following studies, the experimentally and numerically determined relative pressure values were converted into values of the corresponding dimensionless pressure coefficients C_P according to Eq. (3.49) for further analysis. Differential analyses are carried out between various load cases in the individual analysis planes to investigate the alterations between these setups. For this purpose, differential surface pressure coefficient values for the particular measuring ranges are calculated according to

$$\Delta C_{P_i} = C_{P,A_i} - C_{P,B_i} \tag{3.55}$$

and the results are likewise visualized as contour plot. In this equation ΔC_{P_i} represents the differential pressure coefficient of probe i between the measured surface pressure coefficients of load cases A (C_{P,A_i}) and B (C_{P,B_i}).

In addition, a representative mean surface pressure value is computed for every measurement plane, which allows for a simple quantification of the pressure alterations in the examined area. Therefore, the surface pressure differentials of two load cases are formed for each measurement point and then summed over all points of the interpolation grid in the analysis area. In order to obtain the average deviation of the pressure coefficients

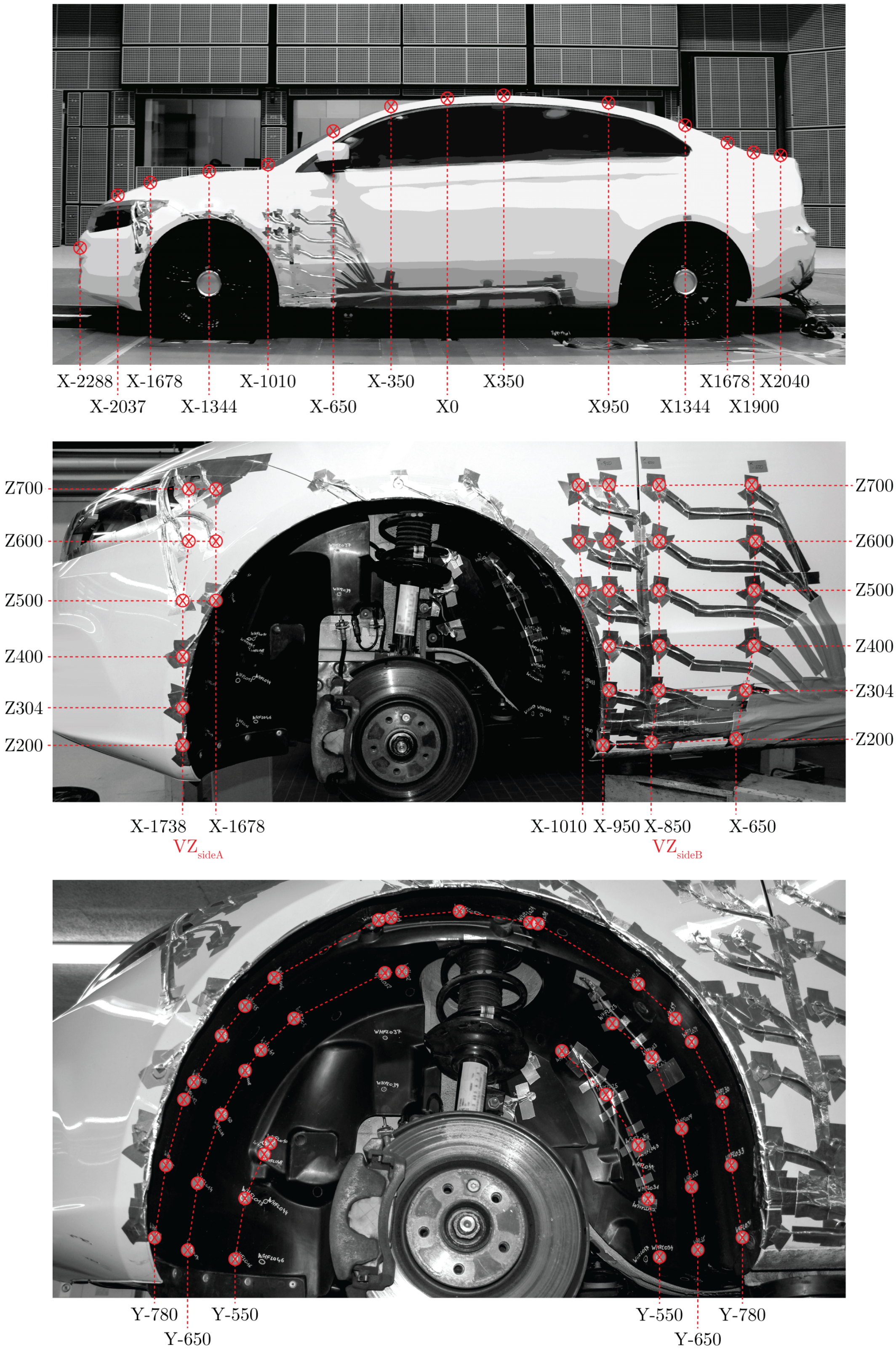

Figure 3.8: Surface pressure probes at VZ_{top} (top), VZ_{sideA} and VZ_{sideB} (center) and VZ_{WH} (bottom).

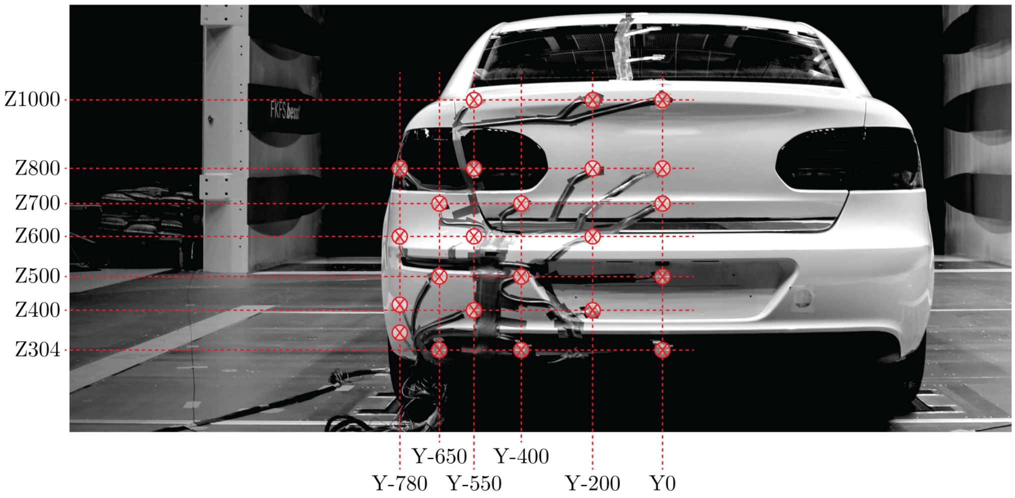

Figure 3.8: Surface pressure probes at vehicle tail $\mathrm{VZ}_{\mathrm{tail}}$.

per probe in all areas, the sums are normalized by the respective number of probes or measurement points contained in this plane. The calculation is carried out according to:

$$\overline{\Delta C_P} = \frac{1}{N} \sum_{i=1}^{N} \left(C_{P,A_i} - C_{P,B_i} \right) \tag{3.56}$$

where $\overline{\Delta C_P}$ is the mean deviation of the surface pressure coefficient and N is the number of probes in the examined vehicle area.

To detail the analysis in the wheel arch, the investigated surface was subdivided into six equal circular segments, for which the surface pressure probes were summed and the mean surface pressure coefficient calculated separately. The individual sections thus cover an angular range of $\varphi_{\mathrm{WH}} = 36.67°$ and are subsequently classified according to their position as WH_{A} to WH_{F}, where WH_{A} corresponds to the wheel arch surface from $\varphi_{\mathrm{WH},1} = 70°$ to $\varphi_{\mathrm{WH},2} = 106.67°$.

3.4.6 Flow topology measurement

The analysis of the flow topology in proximity of the test vehicle was carried out pressure-based, evaluating the pressure coefficient (Eq. (3.49)) in various analysis planes. Details of these measurements are discussed below.

Analysis planes

Four planes were defined to investigate the flow field in the vicinity of the test vehicle in order to identify all the flow phenomena relating to forces. Three of them are located in close proximity and downstream of the left-front wheel house, and one in the wake area of the vehicle. These planes are positioned as close as possible to the vehicle and to the wind tunnel floor in order to be able to catch all relevant flow phenomena. The positions

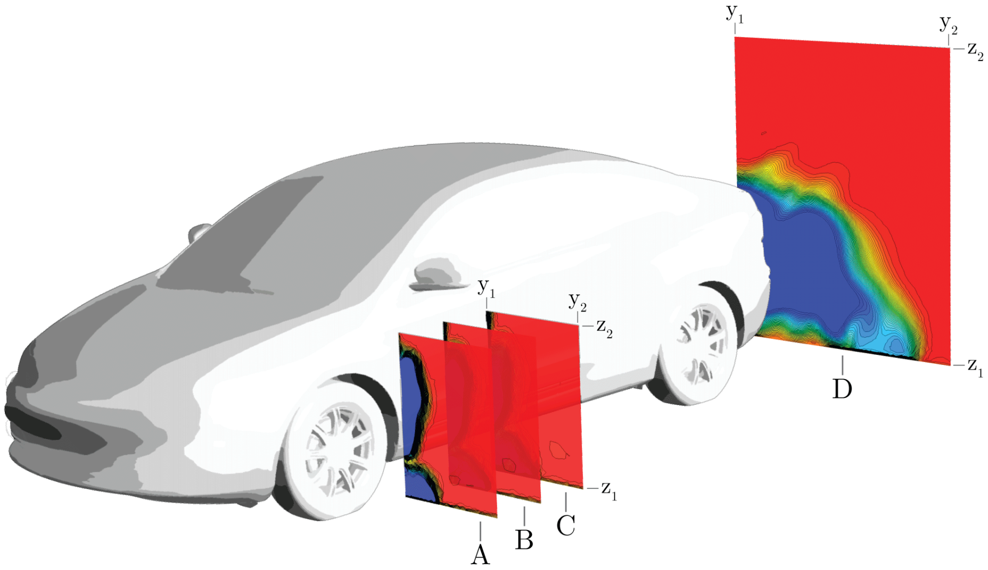

Figure 3.9: Analysis planes.

and dimensions relative to the test vehicle are shown in Fig. 3.9.

Analysis *plane A* is located at position x = -950 mm (corresponds to the rearmost point of the front wheel arch), *plane B* at position x = -650 mm (corresponds to 300 mm downstream of the rearmost point of the front wheelhouse), *plane C* at position x = -350 mm (corresponds to 600 mm downstream of the rearmost point of the front wheel arch) and *plane D* within the vehicle wake at position x = 2800 mm (corresponds to 460 mm downstream of the rearmost point of the vehicle). Planes A, B and C have dimensions in height from z_1 = 20 mm to z_2 = 900 mm from the ground and in width from y_1 = -916 mm to y_2 = -1316 mm, which corresponds to a distance of 12 mm from the outermost point of the vehicle's lateral surface. The measurement resolutions for planes A, B and C are 20 mm per measuring step in the vertical direction and 50 mm per measuring step in the horizontal direction. *Plane D* has dimensions in height from z_1 = 20 mm to z_2 = 1820 mm and in y-direction of y_1 = 0 mm to y_2 = -1500 mm, which covers the left half of the vehicle. The resolution is 60 mm per measuring step in the vertical and in the horizontal directions. The measuring process of the pressure distribution in various vehicle regions during the wind tunnel experiments is shown in Fig. 3.10.

Measurement technology

Pressure-based measurements of the flow field in a close environment around the vehicle were carried out by means of probes attached on a measuring arm mounted on a movable traverse. Two measuring arms with individual sample distances and therefore different resolutions were used. The scan of the flow field in the area downstream of the left front wheel was carried out with the small arm equipped with 15 pressure probes and a probe distance of 20 mm. The wake area behind the vehicle was measured with the large arm equipped with 31 probes and a distance of 60 mm, resulting in a total height of 1800 mm.

(a) Flow field measurement at the side region.

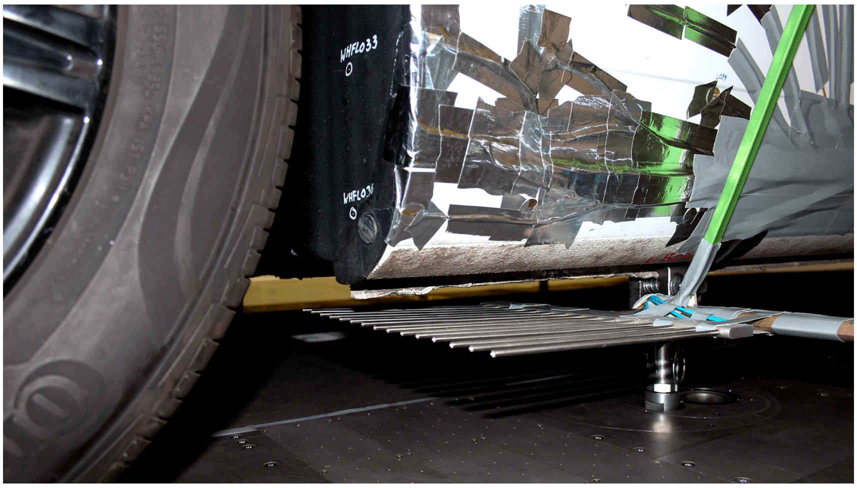

(b) Flow field measurement at the wheel wake.

(c) Flow field measurement at the vehicle wake.

Figure 3.10: Pressure distribution measurement in the aerodynamic wind tunnel.

The flow-field measurements were carried out analogously to the measurement process of the surface pressure. Two *PSI-9116* modules are used as a part of the PSI pressure measuring system. The analysis planes were scanned automatically, with the pressure at each measurement point averaged over a period of 15 seconds after a waiting period of 3 seconds. The measurement system was calibrated prior to the experiments to achieve a precision of ±4.2 Pa, which corresponds to an accuracy of the pressure coefficient of $C_P = \pm 0.005$ at an air flow velocity of 140 km/h.

Post-processing and analysis

According to the surface pressure analysis process described in Chapter 3.4.5, the measurement data was nondimensionalized, interpolated and used to generate contour plots for all analysis planes to illustrate and visualize the shape and expanses of the wake structures in these areas. Furthermore, differential evaluations are performed according to the same analysis process in order to indicate differences between two load cases.

3.5 Computational methodology

This work includes a large number of numerical investigations in various configurations and modifications, as well as with different boundary conditions. However, the basic computational methods and techniques, as well as the CFD processes, including the mesh generation strategy, are identical for all simulations and are described in detail in this chapter. Special methods, configurations or modifications required and applied for individual research topics are described in the corresponding chapters.

The computational work process in this thesis follows the standardized and industry-established numerical development process [69, 72–75], consisting of three phases - pre-processing, solving and post-processing - which will be described subsequently. During the pre-processing phase, the vehicle geometries as well as the virtual wind tunnel are defined. The simulation domain is determined by positioning the test vehicle in a virtual wind tunnel, followed by geometrically discretizing the resulting surfaces of the vehicle and the wind tunnel boundaries into individual surface elements by transferring them to a CAE surface mesh. Subsequently, the volume of the simulation domain is subdivided into suitable, discrete volume cells. This process ultimately leads to the final three-dimensional simulation mesh. Subsequently, boundary conditions are defined and applied to various elements of the simulation domain. This involves fluid parameters, boundary settings of all bounding surfaces, as well as parameters for porous media and rotating parts. During the simulation phase, the fluid dynamic equation system is applied to the geometrically discretized computational domain that consists of a finite number of control volumes, and solved iteratively until convergence is reached. Finally, in the post-processing phase, the resulting data of the simulation solution are extracted, analysed and visualized in various ways.

In this work, the basic simulation methods and processes are identical for every investigated load case and correspond to the state-of-the-art aerodynamic development process in

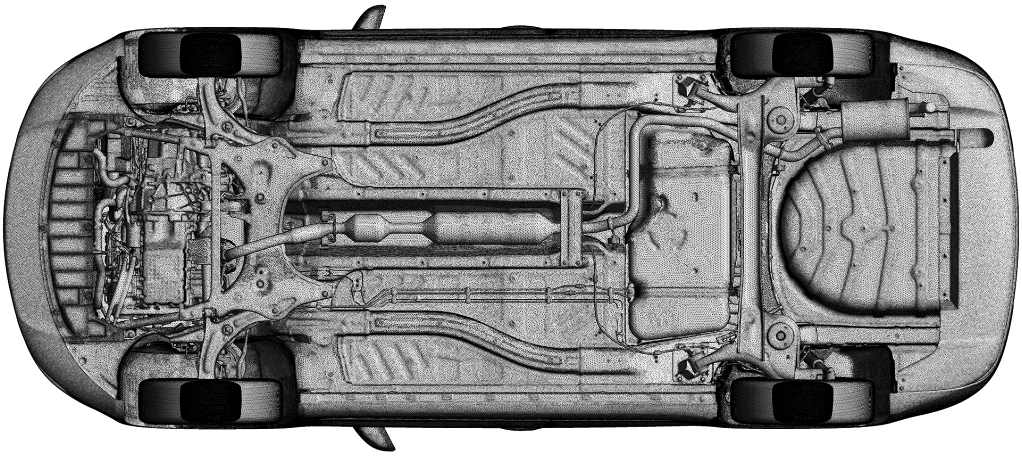

Figure 3.11: CAE surface mesh of the virtual test vehicle underbody.

the vehicle industry. Furthermore, the same solver software and computational resources were used for all simulations. However, details of the vehicle geometry, such as rim geometry or engine compartment flow, as well as individual boundary conditions like wheel rotation methods differ between the individual simulation cases.

According to the three numerical process phases, this chapter is also divided into three main sections. Initially, the simulation models and meshes of all vehicle configurations, wheels, tires and rims, as well as the virtual wind tunnel will be presented. Following this, solver technology basics will be outlined, fundamental equations derived and simulation boundary conditions presented. Finally, data post-processing methods will be discussed.

3.5.1 Simulation meshes

Numerical vehicle model

The numerical vehicle model represents all relevant geometrical details of the production vehicle, such as a detailed underbody and engine compartment with a cooling package, as well as a cooling fan and air guides. Due to the asymmetric geometry of a production vehicle, the complete vehicle, and not a half-model, was used for the simulations.

The CAD data used for this study correspond to the final-production CAD dataset, which was also used for the manufacturing of the test vehicle and the production of its components. Therefore, the CAD data used for the computational investigations offered a maximum level of detail and surface accuracy compared to the examined production vehicle in the experiments. CAD data cleaning and compiling, as well as model preparations, were performed using the *CATIA* software suite. During this process, aerodynamically irrelevant data, such as the interior, was removed. All other remaining CAD data was kept in the model to achieve a highly detailed model.

The CAE surface mesh generation was performed utilizing a combination of *TGrid* (by *ANSYS, Inc.*), *Hypermesh* (by *Altair Engineering*) and the *ANSA* software package (by

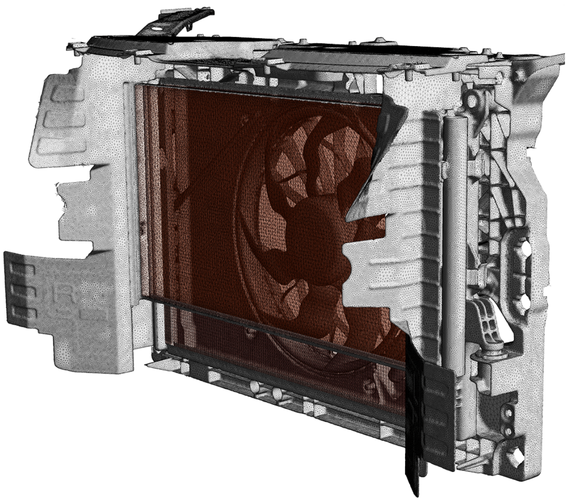

Figure 3.12: CAE model of the cooling package.

BETA CAE Systems SA). The areas of particular interest are modeled with an accordingly higher mesh resolution. The final CAE surface mesh consisted of approximately 1.8 $\cdot 10^7$ triangular surface cells with sizes of 0.8 to 8 mm. The computational model of the underbody is shown in Fig. 3.11. A detailed CAE model of the cooling package, consisting of radiator and condenser, as well as a cooling fan and air guides, was prepared and used for this study. Geometrical details of this model are shown in Fig. 3.12.

To perform investigations with a simplified vehicle (representing a vehicle in an early project phase), an additional CAE model with closed cooling air inlets was created. For this cooling mockup configuration, additional surfaces were constructed that closed and sealed the upper, center and lower grill inlet area of the original CAE model. However, the engine compartment was not sealed at the underbody in order to match the setup of the hardware model.

Numerical wheel model

Great attention was paid to the mesh generation of the wheels. The meshing process of the tires and rims generally corresponds to that of the vehicle described above. However, additional requirements had to be considered, and the meshing strategy had to be adopted accordingly. In order to be able to apply different boundary conditions to tires and rims, the wheels were split into two surface zones. Furthermore, an additional volume zone within the rim was created. Eventually, each wheel consisted of a tire and rim surface zone, and was equipped with an additional volume box within the rim (Fig. 3.13). All three wheel components will be described separately below.

In order to receive a bigger variation of cases, the CAD data sets of three production rims with different geometries and sizes of 16, 17 and 18 inch, were used for the investigations. The rim geometries were not simplified. Details of the surface mesh with *Rim16* are shown in Fig. 3.14.

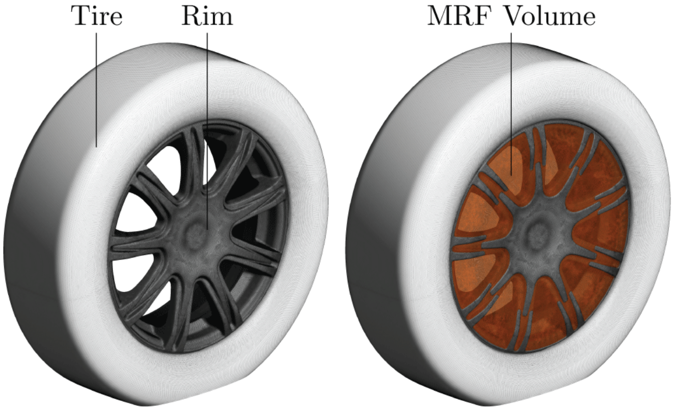

Figure 3.13: Numerical wheel model components.

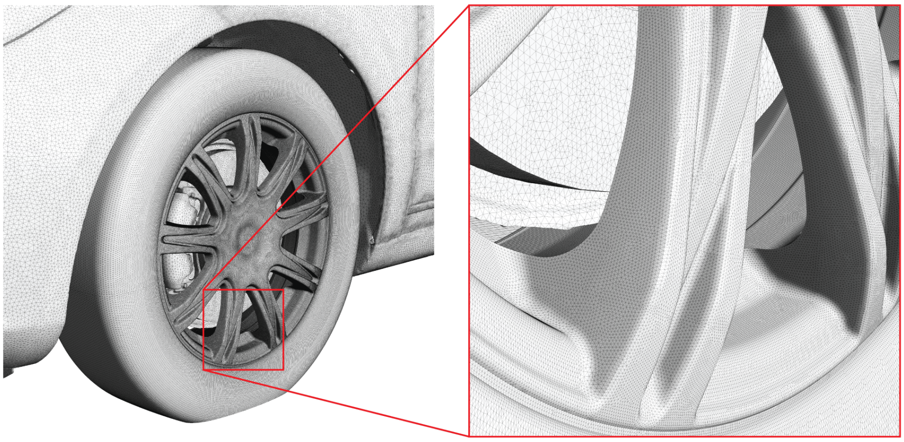

Figure 3.14: Details of the CAE wheel surface mesh for rims *Rim16*.

One of the applied methods to simulate rim rotation in this work is the use of Multiple Reference Frames (referred to as *MRF* in the following) [18, 29]. Details of this approach are discussed in Chapter 3.5.6. This method requires its own separate volume to which it can be applied.

A prerequisite for the application of the *MRF* method is that the flow at the interface between two reference systems is uniform. Otherwise the *MRF* approach does not provide reasonable solutions [37, 76]. In the case of a rotating frame, as in rim rotation, this means that the flow at the interface should be constantly rotational. The challenge is therefore to define an *MRF* volume which, on the one hand, encloses the spokes and, on the other, hand fulfills these requirements, so that both the air flow in the rotating and in the stationary reference system can be regarded as uniform. A satisfactory modeling of the rim rotation, and consequently the interaction of the air between the spokes, by means of the *MRF* method thus strongly depends on the shape of the defined volume. In earlier works [29, 37], the following approaches for the creation of *MRF* boxes were considered.

In the simple approach of the *"cylindrical MRF model"*, the *MRF* region is created within an imaginary cylinder that envelops the entire rim, representing the boundary of this rotating volume [37]. The advantage of this method is a very simple mesh creation, but at the expense of simulation accuracy, since the *MRF* volume also extends to regions outside the outer edge of the rim. Thus, an interface is positioned in a flow field dominated by a high translatory velocity along the vehicle side. The result of a translatory flow within a rotating reference frame with a rotation axis perpendicular to this stream is a not uniform flow at the interface between those two reference systems. Therefore, a negative impact on the quality of the simulation results is to be expected.

Wäschle et al.[18] solved this problem by modifying the approach of the cylindrical *MRF* model and constructing a virtual ring covering the rim openings as an outer interface for the *MRF* region. This interface surface was deliberately positioned very close to the rim surface, where the viscous friction is still strong enough to force fluid rotation and dominate the flow field. This minimizes the approximation error, because it allows the rotational flow at the interface of the moving and stationary reference systems to be considered as uniform. However, since this method requires a very fine mesh structure, a great deal of effort is required for the construction of this *MRF* box.

In order to reduce the construction effort of the *MRF* box, Mlinaric [29] proposes two further approaches in his work, where in both cases the smallest possible volume between the wheel spokes was enveloped by a set of "cake-piece" regions. For the creation of the inner *MRF* interface surface, two individual methods were used. Either the inner surfaces were represented by unconnected interface surfaces (*"cake-piece MRF model"*), or by a continuous surface (*"practical MRF model"*) due to the easier and therefore more feasible implementation. The results were several single subdomains, or a continuous *MRF* volume.

Since this work involves more complex rim geometries than the work of Mlinaric, an elaborate approach of the *"cake-piece MRF model"* was chosen as meshing strategy. Depending on the geometry of the rims, this resulted either in several individual or one coherent domain. The *MRF* volumes have been designed to encapsulate the fluid in between the spokes. It was taken care that these volumes close exactly with the spokes inside and outside surfaces in order to avoid the simulation of an unrealistic rotary motion of the fluid outside the desired region. Thus, all regions between the rim spokes were enveloped with an *MRF* volume, and the restrictions of the normal component of the frame velocity at the interface were fulfilled, as required by the *MRF* implementation [76].

Tire deformation and detailing is an important factor for the aerodynamic of vehicles, as shown by the work of others [5, 29, 40, 77–79]. However, since detailed tires are not yet implemented in the utilized numerical aerodynamic development process of *Magna Steyr* (partly due to the high degree of complexity), the investigations in this work used simplified (slick), standardized tire geometries - in line with best practice for external aerodynamic development. All three resulting CAE wheel surfaces meshes with the corresponding *MRF* volumes that were used are shown in Fig. 3.15.

Furthermore, it was decided to create the contact patch without deforming the geometry of the tires. On the one hand because this approach is also not yet part of the virtual aerodynamic process, on the other hand because no geometric information was available for the correct deformation of these tires. Furthermore, a deformation of the tire geometry would have resulted in an unrealistic impact on the flow topology in this area due to the *MW* boundary condition. Therefore, the tire geometries were intersected directly with the ground at a height of 10 mm with no additional deformation [37]. The challenge with this approach was to meet the high mesh quality requirements at the intersection areas, which is why the automatically generated volume mesh needed to be modified and optimized by hand in these regions.

Virtual wind tunnel

According to the current best practice for external aerodynamics it was decided to use a simplified, idealized wind tunnel geometry. On the one hand, this study should not be considered as a validation attempt of the FKFS test facility, on the other hand a fully detailed virtual wind tunnel model with all geometrical details would not have been feasible for this investigation, due to the limited number of surface and volume cells of the simulation mesh, as well as the lack of the required CAD data.

The virtual wind tunnel was created as a rectangular box with a length of 52 m, a width of 20 m and a height of 12 m. With respect to a vehicle length of 4.6 m, width of 1.8 m and height of 1.5 m and the position of the vehicle front 19 m downstream from the entry, this corresponds to dimensions of approximately four vehicle lengths in front of the vehicle, six vehicle lengths behind, seven vehicle heights above and five vehicle widths to both sides. This domain is large enough to avoid any significant blockage or boundary effects. The geometry of the virtual wind tunnel is shown in Fig. 3.16 with the test vehicle positioned inside the domain for scale. The simulation of the moving ground was also idealized by applying a slip wall boundary condition to the entire wind tunnel floor, which can therefore be considered as one large, moving belt. The hardware model of the test vehicle was fixed in the wind tunnel via rocker panel struts due to the 5-belt system for road simulation. These mounts were not represented in the simulation model.

Computational domain and simulation grid

The CAE volume mesh generation was performed using a combination of *TGrid* (by *ANSYS, Inc.*), *Hypermesh* (by *Altair Engineering*) and the *ANSA* software package. Due to the highly complex mesh geometry and the limited number of volume cells, a hybrid meshing strategy was used to create the three-dimensional volume mesh. With this approach, unstructured, non-uniform meshes of a combination of tetrahedral and prismatic elements were created. Flow field regions under viscous influence, such as the boundary layer, were resolved by means of a hexahedral prism layer with appropriate first cell heights on the vehicle surface to ensure suitable dimensionless wall distances $y^+ < 5$ for the near-wall air flow computation. The remaining volume was filled with tetrahedral cells. In addition, and according to best practice, several refinement zones near the vehicle have been defined in areas with expected air flow separation and in regions of higher interest. These refinement boxes have been defined for the area around the entire vehicle, the engine compartment, side mirrors and A-pillars, the wheels and wheel houses, the vehicle underbody and tail, as well as the wake area. Within these zones, the volume mesh was generated with a correspondingly finer resolution. The hexahedral prism layer and the tetrahedral

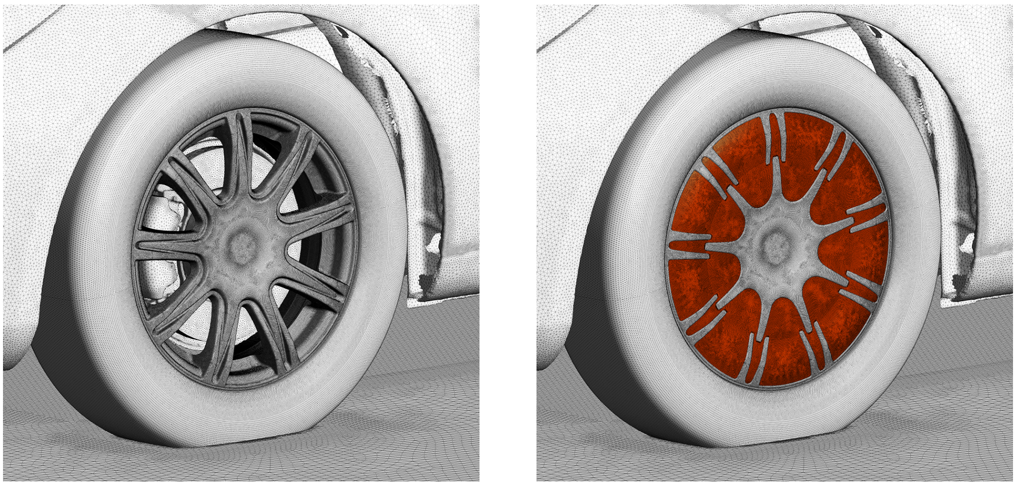

(a) *Rim16* (b) *Rim16* with *MRF* box (red)

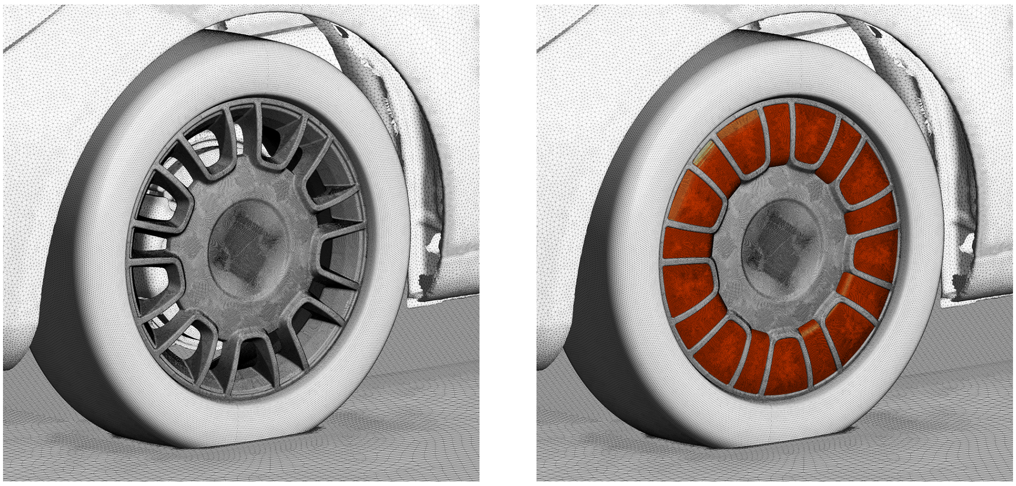

(c) *Rim17* (d) *Rim17* with *MRF* box (red)

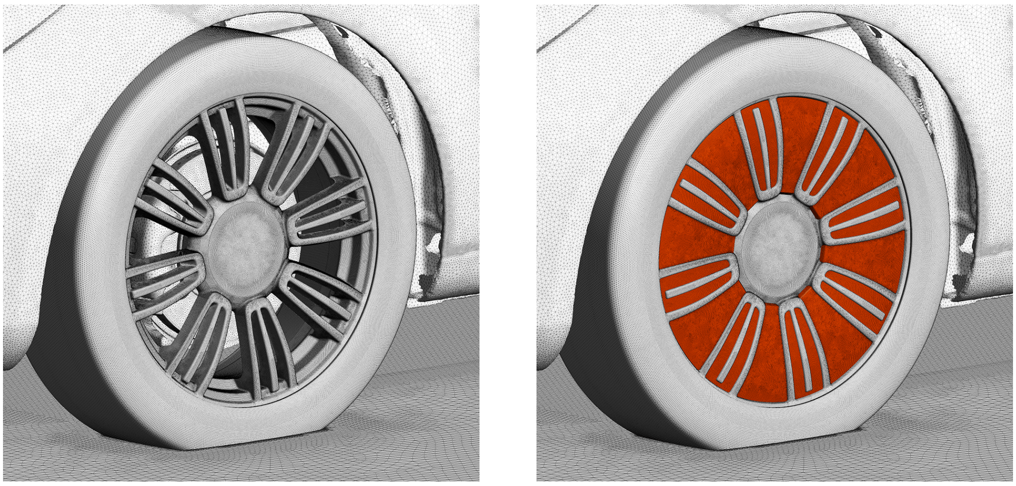

(e) *Rim18* (f) *Rim18* with *MRF* box (red)

Figure 3.15: CAE models of all wheel and rim geometries (*Rim16*, *Rim17* and *Rim18*) with corresponding *MRF* boxes.

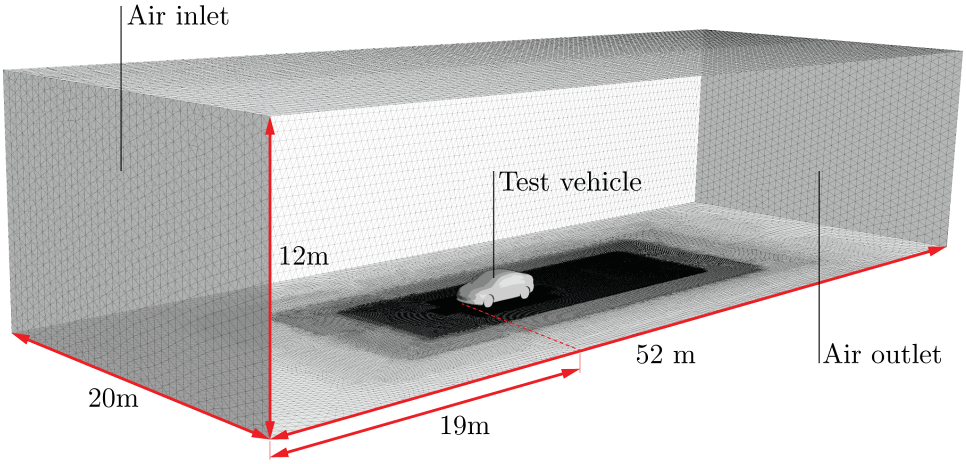

Figure 3.16: Virtual wind tunnel with test vehicle.

volume cells were coupled by means of a non-conformal interface, where flow quantities were interpolated at these boundaries during transition.

The mesh generation process resulted in final CAE meshes consisting of approximately $1.8 \cdot 10^7$ triangular surface cells and $1.6 \cdot 10^8$ volume cells, which also represents the limits of the computational resources available for this study. The computational domain including a simplified visualization of the virtual vehicle model is shown in Fig. 3.17.

In order to eliminate the impact of the vehicle mesh and the computational domain on the simulation results, all numerical investigations in this work were carried out with the identical vehicle mesh and simulation grid (in each case for *Rim16*, *Rim17* and *Rim18*). The differences between the individual simulation setups, such as the wheel rotation approach or cooling mockup, were realized by applying the corresponding boundary conditions.

3.5.2 Numerical methods and computational setup

The Navier-Stokes equations describe incompressible, frictional continuum flows without further restrictions, as presented and discussed in Chapter 3.1. An exact solution of this system of equations would therefore reproduce all spatial and temporal details of the flow.

However, exact solutions exist only for special flows. In most technical flows, various simplifications have to be made, and physical constraints must be defined to enable a numerical solution. In vehicle aerodynamics, these restrictions usually comprise the neglect of frictional forces, demand for irrotational flow, distribution of turbulent motion into coarse and fine structure fractions, as well as the modeling of stresses in turbulent flow through turbulence models [69]. Such models represent thus an idealization of real physical conditions in nature, resulting in corresponding phenomenological errors. To solve this system of equations, the Navier-Stokes equations are finally discretized. This implies that they are no longer applied to a continuum, but to small, finite volumes of computational space. Using various discretization methods, a numerical model is generated, which

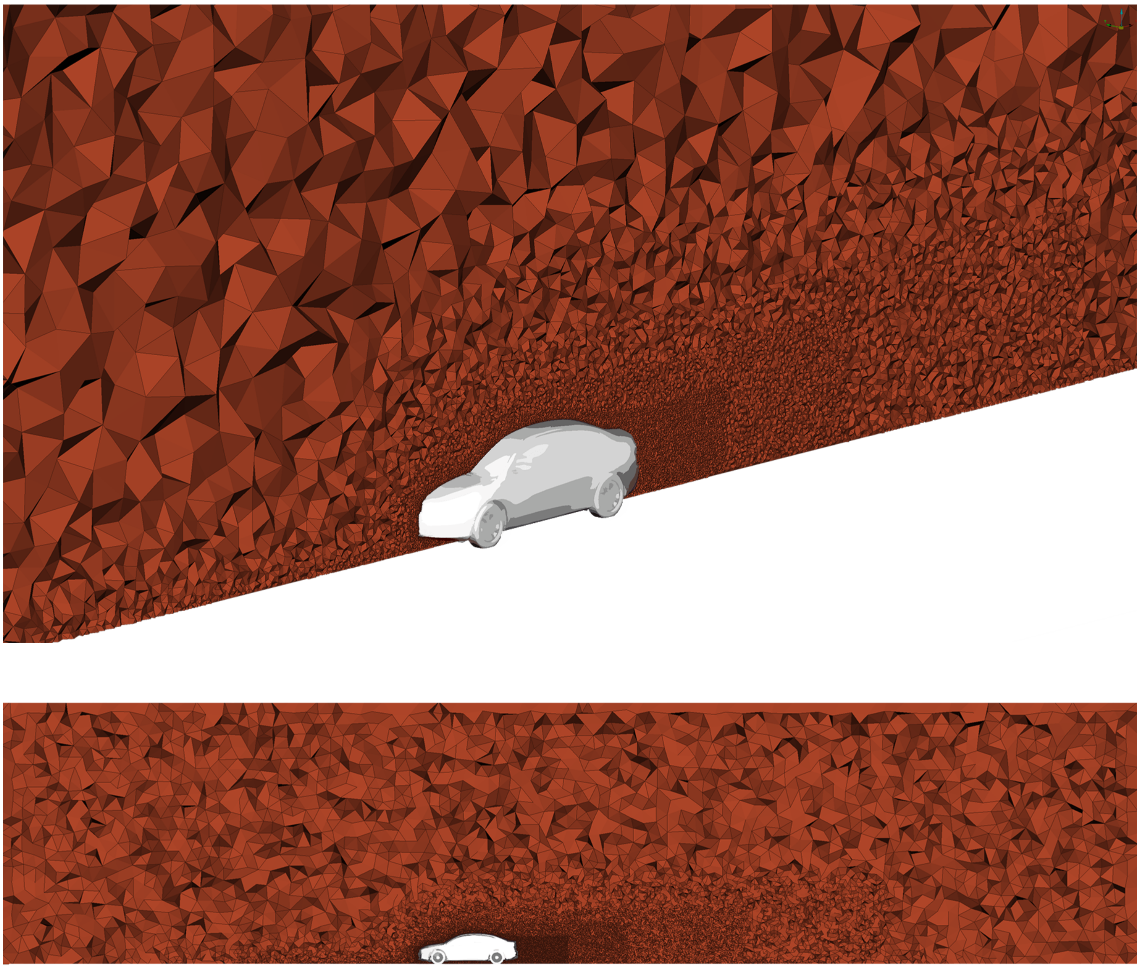

Figure 3.17: Cross section of the computational domain with virtual test vehicle.

approximates the differential equations by a system of solvable algebraic equations. This results in mathematical errors that emerge from approximations during the discretization process, errors when solving the discretized equations by iterative methods, or programming and rounding operations during the computational solution process. Although the numerical methods are based on the exact equations of motion for fluids, the numerical solutions of these systems are approximate.

3.5.3 Discretization

The goal of the discretization is to reformulate the Navier-Stokes equations so that they can be applied in computational fluid dynamics. For this purpose, the system of partial differential equations is transformed into a system of algebraic equations for the flow properties at discrete points in time and space, which can then be solved. This is done, on the one hand, by geometrical discretization of the simulation domain and, on the other hand, by the discretization of the Navier-Stokes equations using various methods. One of the most common approaches is the *Finite-Volume Method* (FVM), which was also applied during this work and will therefore be briefly discussed in the following.

The *FVM* transforms the system of partial differential Navier-Stokes equations into a system of algebraic equations, which are defined for finite control volumes or cells [66, 80]. For this purpose, the simulation domain is geometrically discretized, creating a three-dimensional simulation mesh consisting of an ensemble of individual discrete volume cells, as discussed in Chapter 3.5.1. The state variables are each defined in the centroid of the control volumes, at which the variable values are to be computed. The values of the variables on the surfaces of the control volumes are calculated through interpolation of the centroid values. The partial differential equations are integrated over each cell and thereby transformed or discretized into balance equations over each element. Here, the volume integral terms of the Navier-Stokes equations are converted into surface integrals for each cell, and thus into surface fluxes, by means of the Gauss integral theorem for each volume boundary surface, and furthermore evaluated on the finite volume surfaces. This system of algebraic equations is then solved through calculation of the variables for each element. This procedure is strictly conservative, since the flow entering a given volume is identical to that leaving the volume.

3.5.4 Turbulence modeling methodologies

The numerical simulations of this work were carried out with the commercial CFD software suite *ANSYS Fluent* (solver version 15.0). *Fluent* uses the steady-state Reynolds-Averaged Navier-Stokes (*RANS*) method, which is applied for incompressible air flow continuity and momentum balance. This approach will be discussed in more detail below. In the following, the *Reynolds Averaging Procedure* will be described, and thus the *RANS* equations derived. Finally, the resulting closure problem will be explained, which leads to the use of turbulence models.

Technical applications, such as vehicle aerodynamics, usually deal with turbulent flows [69], which are always three-dimensional, unsteady and characterized by strong mixing effects. Furthermore, pressure and flow velocity are characterized by irregular and chaotic changes, while the flow patterns are dominated by vorticity and contain eddies of all scale sizes. Energy is constantly streaming from the mean flow initially into large and further into small turbulence scales, where finally energy dissipation occurs. Due to the high complexity of this fluctuation, it can be described theoretically and computed in all details of its movement with extremely high effort only.

However, in many technical applications, the high-frequency fluctuations of the flow variables are barely significant, which is why often only temporal averages of the turbulent motion are considered in practice. However, the mixing process of the fluid caused by the fluctuation movement is of great importance for the resulting flow situation and can by no means be neglected. Therefore it is convenient for the computational treatment of a turbulent flow to decompose and describe it by a superposition of the mean flow with a statistical fluctuation. When establishing the equations of motion for the mean flow of the fluid, time averaging of the Navier-Stokes equations results in additional terms due to turbulent fluctuations. These terms represent additional unknown variables in the system of equations. Supplementary equations must be defined, which model the relation between

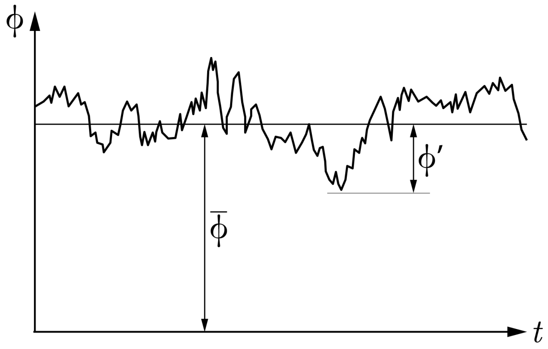

Figure 3.18: Turbulent velocity fluctuation.

these additional fluctuation terms and the mean velocity field, in order to close the system of equations of motion. Creating these model equations is called turbulence modeling.

Reynolds-Averaged Navier–Stokes (RANS) method

The focus of the *RANS* method is on the mean flow and the effects of the turbulence on it. This approach considers all turbulence scales, but limits itself to the calculation of time-averaged values of the flow quantities, while the effects of fluctuations are modeled. Accordingly, this approach cannot map all phenomena of turbulence. Nevertheless, depending on which properties of the flow are to be investigated, the approach can reproduce them with sufficient accuracy.

Reynolds Averaging Procedure

Initially, by means of the *Reynolds Averaging Procedure* [80, 81], the instantaneous values of the flow quantities ϕ in a statistically steady flow, which are the velocity components and the pressure in the case of isothermal and incompressible flows, are replaced by the respective sum of the time-average and a fluctuation (Fig. 3.18):

$$\phi\left(x_i, t\right) = \overline{\phi}\left(x_i\right) + \phi'\left(x_i, t\right) \quad \text{with } x_i = (x, y, z) \tag{3.57}$$

where ϕ represents the flow quantity, $\overline{\phi}$ its time-average, ϕ' the fluctuation, t the time and x_i the Cartesian coordinates.

The time average can be calculated using the integration over a sufficiently long time interval Δt, which should be greater than the period of the largest fluctuations, so that average values are time independent:

$$\overline{\phi}\left(x_i\right) = \lim_{\Delta t \to \infty} \frac{1}{\Delta t} \int_{t_0}^{t_0+\Delta t} \phi\left(x_i, t\right)\ dt \tag{3.58}$$

From Eq. (3.58) the Reynolds-averaging calculation laws can be derived. It follows, that the Reynolds-average of a Reynolds-averaged value equals again the same value, according to:

$$\overline{\overline{\phi}}\left(x_i\right) = \lim_{\Delta t \to \infty} \frac{1}{\Delta t} \int_{t_0}^{t_0+\Delta t} \overline{\phi}\left(x_i, t\right)\ dt = \overline{\phi}\left(x_i\right) \tag{3.59}$$

Furthermore, the time averages of the stochastic fluctuation quantities are equal to zero, according to Eq. (3.57), Eq. (3.58) and considering Eq. (3.59):

$$\begin{aligned}\overline{\phi'}\left(x_i\right) &= \lim_{\Delta t\to\infty}\frac{1}{\Delta t}\int_{t_0}^{t_0+\Delta t}\left[\phi\left(x_i,t\right)-\overline{\phi}\left(x_i,t\right)\right]\,dt = \\ &= \overline{\phi}\left(x_i\right)-\overline{\overline{\phi}}\left(x_i\right) = \\ &= 0\end{aligned} \tag{3.60}$$

Moreover, from Eqs. (3.58) and (3.59) the following additional calculation rules can be derived:

$$\overline{\overline{\phi}+\phi'} = \overline{\overline{\phi}} + \overline{\phi'} = \overline{\phi}, \qquad \overline{\overline{\phi}\,\phi'} = \overline{\phi}\,\overline{\phi'} = 0 \tag{3.61}$$

$$\overline{\frac{\partial\phi}{\partial t}} = \frac{\partial\overline{\phi}}{\partial t}, \qquad \overline{\frac{\partial\phi}{\partial x_i}} = \frac{\partial\overline{\phi}}{\partial x_i} \tag{3.62}$$

RANS equations

Introducing this model assumption into the incompressible Navier-Stokes equations, and averaging these over time, yields the *RANS* equations, which are the time-averaged equations of motion for fluid flow. For this reason, the *Reynolds Averaging Procedure* is applied to the individual flow quantities. The application of Eq. (3.57) on the velocity components and on the pressure yields:

$$u = \overline{u} + u', \quad v = \overline{v} + v', \quad w = \overline{w} + w', \quad p = \overline{p} + p' \tag{3.63}$$

where u, v and w represent the instantaneous velocity components and p is the instantaneous value of the pressure. $\overline{u}$, $\overline{v}$, $\overline{w}$ and $\overline{p}$ are the time-averaged values and u', v', w' and p' correspond to the respective fluctuation part.

From Eq. (3.60) follows:

$$\overline{u'} = 0, \quad \overline{v'} = 0, \quad \overline{w'} = 0, \quad \overline{p'} = 0 \tag{3.64}$$

Furthermore, the mass and momentum equations are expressed using the Einstein summation notation (sum each repeated index over i, j, and k) for Cartesian coordinates and the x-component where $(x_1,\, x_2,\, x_3) = (x,\, y,\, z)$ and $(u_1,\, u_2,\, u_3) = (u,\, v,\, w)$.

The **continuity equation** (Eq. (3.13)) in index notation yields:

$$\frac{\partial u_i}{\partial x_i} = 0 \tag{3.65}$$

Substituting the instantaneous quantity by the sum of mean value and stochastic fluctuations of Eq. (3.63) in Eq. (3.65) and then expanding yields:

$$\frac{\partial\left(\overline{u_i} + {u_i}'\right)}{\partial x_i} = 0 \tag{3.66}$$

$$\frac{\partial\overline{u_i}}{\partial x_i} + \frac{\partial {u_i}'}{\partial x_i} = 0 \tag{3.67}$$

Averaging Eq. (3.67) and applying (3.64) together with (3.61) and (3.62) results in:

$$\frac{\partial \overline{u_i}}{\partial x_i} = 0 \tag{3.68}$$

This means that a continuity equation of this kind applies for the velocity fluctuations also.

The **momentum equation** for Newtonian fluids (Eq. (3.30)) with the assumption of the absence of body forces ($\vec{f_b} = 0$) gives in tensor notation:

$$\rho \left[\frac{\partial u_i}{\partial t} + \frac{\partial (u_j u_i)}{\partial x_j}\right] = \frac{\partial}{\partial x_j}\left(\mu \frac{\partial u_i}{\partial x_j}\right) - \frac{\partial p}{\partial x_i} \tag{3.69}$$

Substituting the instantaneous quantity by the sum of mean value and stochastic fluctuations of Eq. (3.63) in Eq. (3.69) results after expanding:

$$\begin{aligned}\rho \left\{\frac{\partial (\overline{u_i} + u_i')}{\partial t} + \frac{\partial [(\overline{u_j} + u_j')(\overline{u_i} + u_i')]}{\partial x_j}\right\} &= \\ = \frac{\partial}{\partial x_j}\left[\mu \frac{\partial (\overline{u_i} + u_i')}{\partial x_j}\right] - \frac{\partial (\overline{p} + p')}{\partial x_i}\end{aligned} \tag{3.70}$$

$$\begin{aligned}\rho \left\{\frac{\partial u_i'}{\partial t} + \frac{\partial (\overline{u_j}\,\overline{u_i})}{\partial x_j} + \frac{\partial (\overline{u_j} u_i')}{\partial x_j} + \frac{\partial (\overline{u_i} u_j')}{\partial x_j} + \frac{\partial (u_j' u_i')}{\partial x_j}\right\} &= \\ = \frac{\partial}{\partial x_j}\left[\mu \left(\frac{\partial \overline{u_i}}{\partial x_j} + \frac{\partial u_i'}{\partial x_j}\right)\right] - \frac{\partial \overline{p}}{\partial x_i} - \frac{\partial p'}{\partial x_i}\end{aligned} \tag{3.71}$$

After averaging Eq. (3.71) and applying (3.64) together with (3.61) and (3.62) gives:

$$\rho \frac{\partial (\overline{u_j}\,\overline{u_i})}{\partial x_j} = \frac{\partial}{\partial x_j}\left[\mu \left(\frac{\partial \overline{u_i}}{\partial x_j}\right) - \rho\, \overline{u_i' u_j'}\right] - \frac{\partial \overline{p}}{\partial x_i} \tag{3.72}$$

For Eq. (3.69) and (3.72), the terms of the left-hand side and the pressure terms of the right-hand side, are the same, except for the difference that the time-dependent quantities u_i and p were replaced by their time averages $\overline{u}_i$ and $\overline{p}$.

However, by means of this Reynolds averaging, additional terms $\overline{u_i' u_j'}$, which consist of the mean product of two turbulent fluctuation quantities, are formed on the right-hand side of the momentum equation Eq. (3.72). These indicate that the turbulent motion is associated with an exchange of momentum, which creates additional stresses. The fluctuation u_i' influences the mean velocity $\overline{u_i}$ as if the resistance to deformation (the viscosity) is apparently increased for the fluid. In tensor form, these turbulent shear stresses yield the Reynolds stress tensor τ_{ij}^{Re}, whose diagonal elements represent normal stresses, while the remaining elements are shear stresses:

$$\tau_{i,j}^{Re} = -\rho\, \overline{u_i' u_j'} = -\rho \begin{pmatrix} \overline{u_1' u_1'} & \overline{u_1' u_2'} & \overline{u_1' u_3'} \\ \overline{u_2' u_1'} & \overline{u_2' u_2'} & \overline{u_2' u_3'} \\ \overline{u_3' u_1'} & \overline{u_3' u_2'} & \overline{u_3' u_3'} \end{pmatrix} \tag{3.73}$$

These additional terms $\rho\,\overline{u_i'u_j'}$ are the Reynolds stresses. Consequently, six more equations are needed to solve the equation system, which is why the equation system is no longer closed. This problem is referred to as the closure problem. The closure succeeds by additional information about the components of the Reynolds stress tensor in the form of equations. These additional equations are called turbulence models.

Turbulence model

Since turbulence is still not fully understood, mathematical models to simulate this phenomenon are mostly based on heuristics, with data from experiments used for validation. There are several models that are more or less suitable for various technical applications.

For this work, the $k-\omega$ based Shear Stress Transport (SST) turbulence model was selected [82] in accordance with actual best-practice for external aerodynamic simulations at *Magna Steyr* and with recommendations of previous studies [22]. This is a robust two-equation eddy-viscosity turbulence model, which is a hybrid model that combines the $k-\omega$ [83] and the $k-\epsilon$ turbulence models. With this approach, the $k-\omega$ model is used for the boundary layer treatment, where this formulation is valid from the buffer layer through the viscous sublayer to the vehicle surface, while the $k-\epsilon$ model is applied in the free flow. The $k-\omega$ SST model includes two transport equations to represent turbulent properties of the flow: the turbulent kinetic energy k, and the turbulent specific dissipation rate ω.

3.5.5 Domain boundaries

All numerical investigations of this study are performed at a wind speed of 38.89 m/s (or 140 km/h), in accordance to the experimental setup. A uniform velocity profile was applied at the virtual wind tunnel air inlet surface, using the velocity inlet boundary condition. The outflow condition was set to *pressure-outlet* with a value of 0 Pa at the downstream wind tunnel boundary. At the walls and top surfaces of the computational domain, the symmetry boundary condition was set, while the floor was defined as MW with the velocity of 140 km/h to match the free-stream air inlet speed. As air and ground move at the same velocity, this setup avoids the formation of a floor boundary layer, which would have had an impact on the simulation results as part of the tire geometry would be within this layer, and therefore reproduces the boundary conditions of the experiment. In the wind tunnel test facility, a complex floor simulation system, consisting of a combination of several belt systems and a suction mechanism, control the relative movement of the air flow and the ground. This prevents the formation and build-up of a boundary layer.

3.5.6 Wheel rotation

It is a challenge to model transient processes by means of steady-state simulations. This includes simulating the influence of moving parts of a submerged body surface, such as rotating wheels, on the flow around the body. For this kind of simulation, special approaches and methods are required, which are presented and discussed subsequently. Since in this work the *ANSYS* solver was used exclusively, the focus is on the methods provided by this solver for the steady-state case [76].

Stationary Wheels (*NR*)

The setup of stationary and therefore not rotating wheels (referred to as *NR* in the following) ignores the tire and rim rotation. All the wheel surfaces are then defined as wall boundaries with zero velocity. Modeling rotating wheels with this approach is of course unrealistic and physically incorrect, and will only be used as a reference setup to study the impact of the individual wheel rotation methods on the aerodynamic behaviour of the vehicle.

Moving Wall (*MW*)

One of the simplest and oldest approaches to model rotating geometries in a simulation is the *Moving Wall* method [63, 76]. A solid-body rotation around an axis of rotation is defined and applied as the boundary condition on the mesh surface for this approach. The air flow of a rotating wheel is thus mimicked, resulting in the formation of a boundary layer at the wheel surface. This boundary condition can be applied either to the entire wheel, or separately to the rims or tires. The rotation speed $\vec{u}$ is given by the angular velocity $\vec{w}$ and the radial distance from the rotation axis $\vec{r}$

$$\vec{u} = \vec{w} \times \vec{r}. \tag{3.74}$$

There is no actual rotation of the geometry during the simulation. The wheel geometries remain motionless and stationary and remain therefore in their initial positions. This method is suited for geometries that are uniform around the rotation axis, since this approach is only physically correct as long as no surfaces of the rotating geometry are normal to the rotation direction, due to reasons of mass conservation. Therefore, no velocities perpendicular to impenetrable, rotating walls should be defined. In case of rotating wheels, this poses a problem due to the geometry of the spokes. An unrealistic increase or reduction in pressure on the inner and outer surfaces of the spokes occurs as a result of applying this method for improper wheel geometries, as was shown by Mlinaric [29] in his work. Anyway, with *ANSYS Fluent* it is not possible to model a wall movement which, with respect to the adjacent cell zone, has a component perpendicular to the wall itself, since *Fluent* ignores any normal component of wall motion.

Multiple Reference Frame (*MRF*)

The MRF method [63, 76] is a steady-state technique to simulate rotating geometry by applying an angular momentum due to coordinate transformation to the air within a closed volume between the rim spokes. With this approach, stationary solutions of the equations of motion of a fluid in a rotating frame within a stationary system are possible.

At the interfaces between the stationary and rotating mesh zones, a local coordinate transformation of the flow variables is performed to allow for the calculation of fluxes at the boundary of these two adjacent regions. Steady-state flow conditions are assumed at the interface between the stationary and moving reference systems, which means that the flow rate at the interface must be the same for both systems. The *MRF* method also offers the possibility to introduce a translatory velocity. However, since that option is not

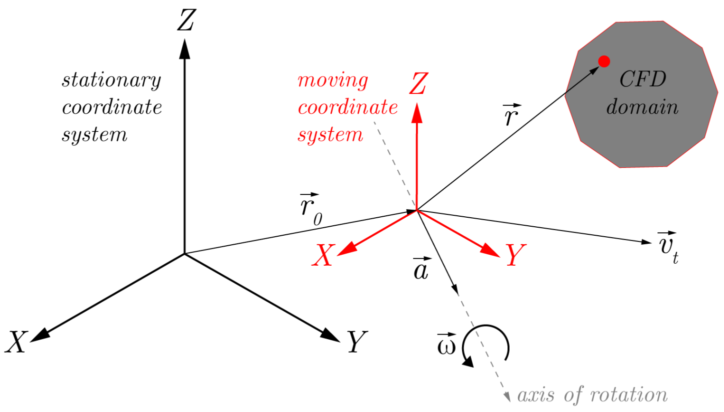

Figure 3.19: Stationary and rotating coordinate systems.

used in this thesis, the translation of the moving reference frame is subsequently neglected. The relative velocity $\vec{u}_r$ of a fluid within a reference system, which rotates at a constant angular velocity $\vec{\omega}$ relative to a stationary, inertial system, is given by

$$\vec{u}_r = \vec{u} - (\vec{\omega} \times \vec{r}) \tag{3.75}$$

where $\vec{u}$ represents the absolute velocity of the stationary system, $\vec{\omega}$ is the angular velocity vector or the angular velocity of the rotating frame, and $\vec{r}$ corresponds to the position vector from the origin of the rotating frame to any point in the rotating domain, as schematically shown in Fig. 3.19 [76].

When the equations of motion for the rotating system are solved, additional terms arise in the equations responsible for the rotation of the fluid. The governing balance equations of fluid flow for mass and momentum (Eqs. (3.13) and (3.24)) of the inertial system can be expressed in the rotating reference frame for absolute velocities:

$$\frac{\partial \rho}{\partial t} + \nabla \cdot (\rho \vec{u}_r) = 0 \tag{3.76}$$

$$\frac{\partial}{\partial t}(\rho \vec{u}) + \nabla \cdot (\rho \vec{u}_r \vec{u}) + \rho\,(\vec{\omega} \times \vec{v}) = -\nabla p + \nabla \cdot \boldsymbol{T} + \rho \vec{f}_b \tag{3.77}$$

or for relative velocities:

$$\frac{\partial \rho}{\partial t} + \nabla \cdot (\rho \vec{u}_r) = 0 \tag{3.78}$$

$$\begin{aligned} \frac{\partial}{\partial t}(\rho \vec{u}_r) + \nabla \cdot (\rho \vec{u}_r \vec{u}_r) + \rho\Big(\underbrace{2\vec{\omega} \times \vec{u}_r}_{\text{Coriolis acc.}} + \underbrace{\vec{\omega} \times \vec{\omega} \times \vec{r}}_{\text{Centrifugal acc.}} \Big) + \rho \frac{\partial \vec{\omega}}{\partial t} \times \vec{r} = \\ = -\nabla p + \nabla \cdot \boldsymbol{T} + \rho \vec{f}_b \end{aligned} \tag{3.79}$$

where the third term represents the Coriolis acceleration and the Centrifugal acceleration. Additional forces consequently arise through the interaction of the rotating fluid with the wheel spokes. The last term on the left side in Eq. (3.79) $\rho\frac{\partial \vec{\omega}}{\partial t} \times \vec{r}$ is neglected by *Fluent*, which is why a modeling of a time-varying angular velocity is not possible. However, this option is not required for the investigations carried out in this work.

In this research, the *MRF* method is applied to a separate volume mesh zones (*MRF* boxes) between the spokes of the rims. An actual rotation of the tire or rim geometry does not take place - the wheels are fixed at their starting position, hence the name *"Frozen Rotor Approach"*. This method was originally designed for turbomachines with axial flow and is therefore valid for use on rims to a limited extent only, since a non-axial flow experiences a non-physical rotation even without a rotating geometry. It is necessary for this approach to define a volume with interfaces to the rest of the simulation mesh and to build up the mesh in this area accordingly. Therefore, an additional effort for the correct preparation of the simulation grid is necessary, as described in Chapter 3.5.1.

Sliding Mesh (*SM*)

For the sake of completeness, the *Sliding Mesh* approach is mentioned as the third method offered by the *Fluent* Solver. However, this method requires transient simulations, which is why it is not used in this study. This approach is a physically correct description of a rotating geometry, because it provides the actual rotation of a sub-mesh and the geometry it contains during runtime. The sub-mesh rotates with respect to the global, static mesh with the wheel rotation velocity. A transfer of the interpolated values takes place between the two volumes on the axially symmetric interface. A major problem of this approach is the modeling of the intersection of tires and wind tunnel floor due to the requirements of the interface to be axially symmetric.

Applied rotation methods and combinations

Wheel rotation configurations applicable to the constraints and limitations of this work are defined and described in the following. It seems obvious to apply *MW* separately to tires and rims, since the boundary conditions differ between the respective situations: (1) tires without surface normal to the direction of rotation, and (2) rims, where the *MW* boundary condition is artificial and not physically real, as shown by Mlinaric [29]. Furthermore, it is obvious to utilize the two rotation methods *MW* and *MRF* separately, as well as in combination.

For this reason, rim and tire were separated into individual cell zones in the wheel meshing process. This procedure allows the application of stationary or moving wall boundary conditions separately to rims, tires, or complete wheels. Since the *MRF* method requires a closed volume in which it can be applied, *MRF* volumes were created inside the rims between the individual spokes for each wheel to enable the simulation of the rotating air flow between the spokes. Finally, the following combinations of rotation methods were defined for this investigation, as illustrated in Fig. 3.20:

No Rotation - stationary wheels (*NR*)
No rotation method is applied, and the wheels are stationary. A wall boundary with zero velocity is used on tires and rims, and the *MRF* volumes are not in rotation.

Moving Wall at the wheels (*MW*)
The velocity of a solid-body rotation is applied to the wheels, i.e. to tires and rims. The *MRF* volumes are not in rotation.

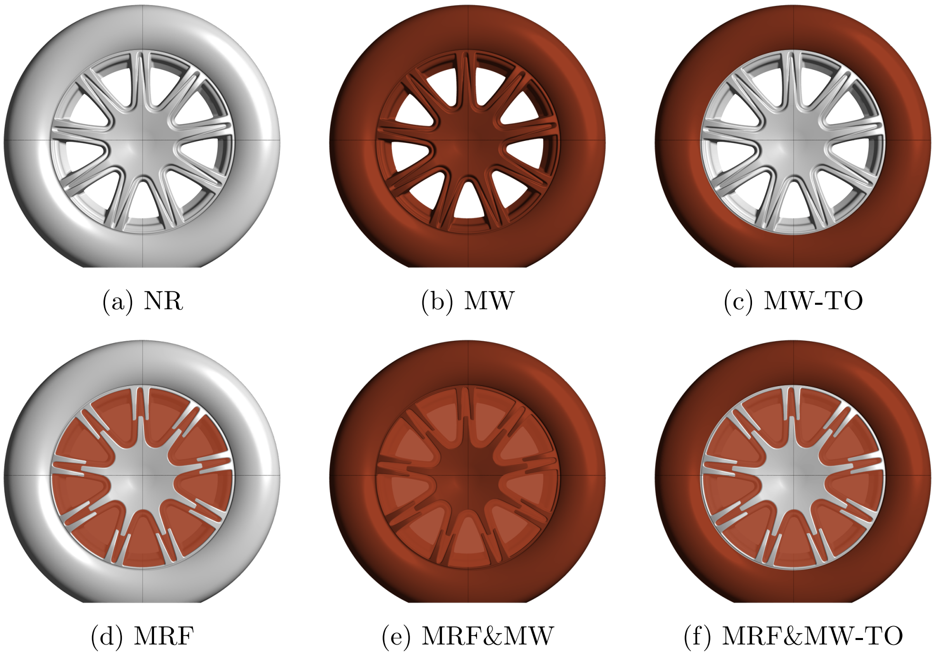
(a) NR (b) MW (c) MW-TO

(d) MRF (e) MRF&MW (f) MRF&MW-TO

Figure 3.20: Applied combinations of rotation methods. Gray-colored wheel parts represent stationarity, while red-colored components are in rotation.

Moving Wall at the tires only (*MW-TO*)

A rotational surface boundary is applied to the tires only, while the rims, as well as the *MRF* volumes, are not in rotation.

Rotating rim volumes (*MRF*)

Solely the volumes within the rim spokes are rotated by the *MRF* method. The surfaces of rims and tires are stationary and not rotating.

Moving Wall at the wheels & rotating rim volume (*MRF&MW*)

The wheels (tires and rims), as well as the *MRF* zone inside the rim spokes, are in rotation.

Moving Wall at the tires only & rotating rim volume (*MRF&MW-TO*)

The tires, as well as the *MRF* volumes inside the rim spokes, are in rotation, while the rim surfaces are stationary.

A summary of the applied velocities on the individual wheel zones is given in Table 3.2. Here v_{tires} and v_{rims} represent the surface velocities applied to the *MW* boundaries at tires and rims, and v_{MRF} represents the velocity applied to the *MRF* volume within the rim spoke zones. The angular rotation velocity of the tire and the rim, as well as the *MRF* volume, were calculated from the driving speed and the distance from the wheel axis of rotation to the ground in order to match the air velocity of 140 km/h.

Name	v_{tires} [km/h]	v_{rims} [km/h]	v_{MRF} [km/h]
NR	0	0	0
MW	140	140	0
MW-TO	140	0	0
MRF	0	0	140
MRF&MW	140	140	140
MRF&MW-TO	140	0	140

Table 3.2: Wheel rotation boundary conditions.

3.5.7 Porous media and cooling package

The heat exchangers of the cooling package (radiator and condenser) are included in the simulations, since their impacts on the air flow topology around the vehicle and through the engine compartment are important for the aerodynamic vehicle simulation. However, due to the large number and size of the channels through the heat exchangers, it is hardly possible to simulate the air flow through these narrow tubes in all details, which is why a simplified simulation model is utilized. For this purpose, the individual heat exchangers were modeled as uniform pentahedral volume cells, as shown in Fig. 3.21, and defined as porous media.

The mathematical approach to modeling porous media is based on the law of Darcy and Forchheimer and consists of an additional momentum source term in the momentum equation of the fluid [76, 84]. This term contributes to the pressure gradient in the porous cells and generates a pressure drop proportional to the fluid velocity or the fluid velocity squared. The source term thus consists of two parts: a viscous loss pressure and an inertia loss pressure. It can be represented for a simple, homogeneous medium as follows:

$$-\nabla p = \underbrace{\frac{\mu}{\alpha}\vec{u}}_{\text{viscous press.}} + \underbrace{\beta\,\rho\,|\vec{u}|\,\vec{u}}_{\text{inertia press.}} \tag{3.80}$$

where $-\nabla p$ represents the pressure gradient in the flow direction, μ is the dynamic viscosity of the fluid, α corresponds to the permeability of the porous medium and $\vec{u}$ is the velocity in the flow direction. $1/\alpha$ is also called the viscous resistance coefficient and β is the inertial resistance coefficient. Only at very low speeds, as it is the case in laminar flows, the viscous portion of this formula alone suffices. In case of turbulent flows, viscous and inertial effects cause a non-linear behavior, which is accounted for in the second term.

The heat exchangers are permeable in the direction of flow, which corresponds to the x-direction in this case, but impermeable in the other two spatial directions. This directivity is modeled by setting the loss coefficients for the local y- and z-directions to values three orders of magnitude higher than those in the main flux direction. Thus, any cross flow is suppressed.

The corresponding values for the viscous and the inertial resistance coefficients were determined experimentally and provided by the component supplier. The thermal component,

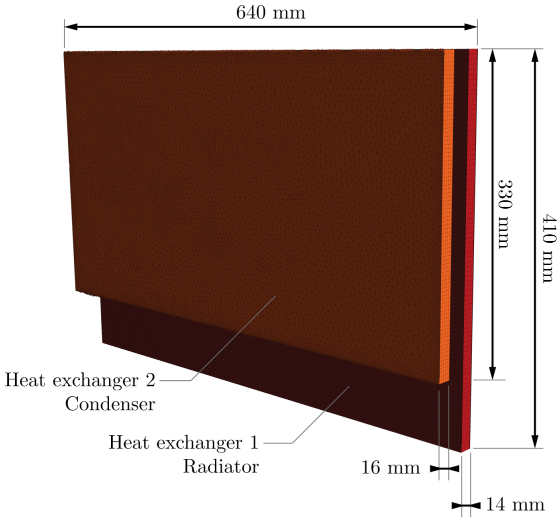

Figure 3.21: Cooling package - Porous media.

and therefore the energy equation, has been neglected for all simulations. The fan rotation velocity was set to zero (fixed-fan condition), since this setting can also be easily reproduced in the wind tunnel experiment.

3.5.8 Convergence criteria

The residues of the continuity and momentum equations, vehicle drag and lift, as well as transport equations of the turbulence model for k and ϵ were monitored throughout the simulations. The simulations were considered as converged, once the residuals of the continuity and momentum equations, as well as the fluctuations of vehicle drag and lift, had reached small values.

3.5.9 Post-processing and analysis

A variety of numerical evaluation processes and methods are identical to those of the experiment and will therefore not be discussed again in this chapter. However, the numerical simulations offer the possibility to perform additional investigations, as well as more detailed analyses, which would not be possible in the experiment without great effort. These methods are described subsequently in this section.

Forces and moments

The total force component along the direction of a specific unit vector $\vec{a}$ for a surface cell of a wall boundary is calculated by *Fluent* by summing the dot products of pressure and viscous forces with that specific vector according to the following equation [63]:

$$F_a = \vec{a} \cdot \vec{F}_p + \vec{a} \cdot \vec{F}_v \tag{3.81}$$

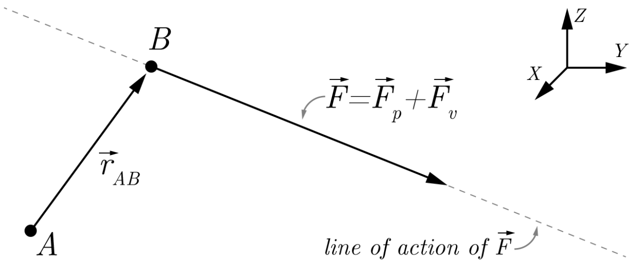

Figure 3.22: Moment about a defined center.

where F_a represents the total force, $\vec{a}$ is a specified unit vector, $\vec{F_p}$ is the pressure force vector and $\vec{F_v}$ is the viscous force vector. For $\vec{a}$ being a vector in x-direction, this results in drag, y-direction results in side forces and z-direction results in lift or down-force.

The complete vehicle force components are calculated through integration of the force components of all surface cells at the vehicle surface:

$$F_{a,tot} = \sum_{n=1}^{N} F_{a,n} \tag{3.82}$$

with $F_{a,tot}$ as the total force component of the complete vehicle along $\vec{a}$ and N as the number of cells of the vehicle surface.

The total moment vector $\vec{M_A}$ is the vector from a specified moment center A to the force origin B, as shown schematically in Fig. 3.22 [63]. It is calculated by summing the pressure and viscous force moments for each surface element. These are the cross products of the pressure and viscous force vectors with the moment vector $\vec{r}_{AB}$, according to:

$$\vec{M_A} = \vec{r}_{AB} \times \vec{F_p} + \vec{r}_{AB} \times \vec{F_v} \tag{3.83}$$

The integral complete-vehicle aerodynamic drag force $F_{D,\text{CV}}$, as well as the corresponding coefficients, are tracked throughout the simulation process. The aerodynamic force values in the analyses are always means of the values from the last 300 iterations, calculated according to

$$F_{D,\text{CV}} = \overline{F_{D,\text{CV}}} = \frac{1}{s} \sum_{i=N-s+1}^{N} F_{D,\text{CV}_i} \tag{3.84}$$

where F_{D,CV_i} corresponds to the vehicle drag force at the ith iteration, s is the number of last iterations about which the mean is computed, and N is the total number of iterations of the simulation.

Drag evolution

In the vehicle industry it is common to represent the aerodynamic drag coefficients $C_{D,\text{X,acc}}$, $C_{D,\text{Y,acc}}$ and $C_{D,\text{Z,acc}}$ accumulated along the vehicle axes x, y and z as auxiliary quantities for identifying aerodynamic loss areas. For this purpose, the aerodynamic drag force

$F_{D,\mathrm{acc}}$, which is the force component in the direction x of the flow velocity acting on a part A_{part} of the vehicle surface, is determined according to

$$F_{D,\mathrm{acc}} = \int\limits_{A_{\mathrm{part}}} \sum_{i=1}^{3} \sigma_{ix}\, n_i \,\mathrm{d}A \tag{3.85}$$

Here, σ_{ix} are the components of the stress tensor $\boldsymbol{\sigma}$ with regard to the momentum balance in the x direction. The stress is due to pressure and viscous friction. n_i are the components of the local normal unit vector of the individual vehicle surface element, and the indices i from 1 to 3 represent the three Cartesian directions x, y and z.

From Eq. (3.85) and Eq. (3.50) the accumulated drag coefficient $C_{D,\mathrm{acc}}$ can be derived as

$$C_{D,\mathrm{acc}} = \frac{1}{\frac{\rho}{2}\, u_\infty^2\, A_p} \int\limits_{A_{\mathrm{part}}} \sum_{i=1}^{3} \sigma_{ix}\, n_i \,\mathrm{d}A \tag{3.86}$$

The resulting drag is integrated over the vehicle surface, separately along the three vehicle main axes in the x, y, or z directions, yielding the corresponding accumulated vehicle drag coefficients $C_{D,\mathrm{X,acc}}$, $C_{D,\mathrm{Y,acc}}$ and $C_{D,\mathrm{Z,acc}}$. The integration areas $A_{\mathrm{part,X}}$, $A_{\mathrm{part,Y}}$ or $A_{\mathrm{part,Z}}$ are selected as follows:

$$\begin{aligned}
&A_{\mathrm{part,X}}:\\
&\qquad x_{\mathrm{min,CV}} \le x \le x_2\\
&\qquad y_{\mathrm{min,CV}} \le y \le y_{\mathrm{max,CV}}\\
&\qquad z_{\mathrm{min,CV}} \le z \le z_{\mathrm{max,CV}}\\
&A_{\mathrm{part,Y}}:\\
&\qquad x_{\mathrm{min,CV}} \le x \le x_{\mathrm{max,CV}}\\
&\qquad y_{\mathrm{min,CV}} \le y_2 \le 0 \text{ and } 0 \le y_2 \le y_{\mathrm{max,CV}}\\
&\qquad z_{\mathrm{min,CV}} \le z \le z_{\mathrm{max,CV}}\\
&A_{\mathrm{part,Z}}:\\
&\qquad x_{\mathrm{min,CV}} \le x \le x_{\mathrm{max,CV}}\\
&\qquad y_{\mathrm{min,CV}} \le y \le y_{\mathrm{max,CV}}\\
&\qquad z_{\mathrm{min,CV}} \le z \le z_2
\end{aligned} \tag{3.87}$$

where $(x, y, z)_{\mathrm{min,CV}}$ and $(x, y, z)_{\mathrm{max,CV}}$ are the minimum and maximum complete-vehicle dimensions in the x, y and z directions, respectively. x_2, y_2 and z_2 each represent variable upper limits to which the integration is carried along the x, y and z axes. $A_{\mathrm{part,Y}}$ is an exceptional case, where the integration starts from the vehicle central plane (y = 0) and extends from the left to the right side of the vehicle.

Accumulated drag coefficients are subsequently evaluated for the complete vehicle $C_{D,\mathrm{X/Y/Z,CV,acc}}$, the vehicle body $C_{D,\mathrm{X/Y/Z,BODY,acc}}$, and the wheels $C_{D,\mathrm{X/Y/Z,WHEELS,acc}}$.
To illustrate the aerodynamic drag development along the vehicle axis, these analyses were performed utilizing *ANSYS Fluent* and the self-developed software package *ASDAT* (described in Chapter 3.6). Furthermore, this approach was applied in this study to perform differential drag analyses between individual simulation cases.

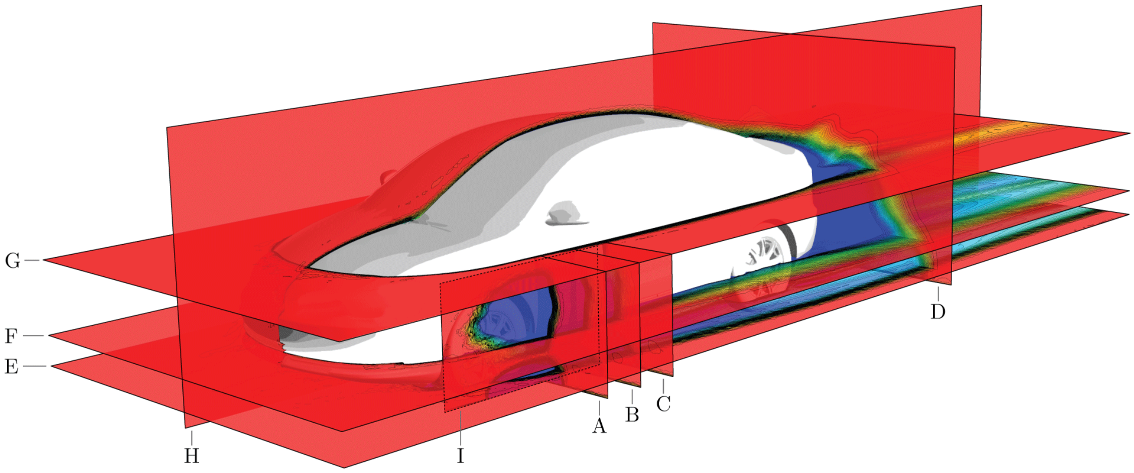

Figure 3.23: Analysis plane dimensions and positions.

Analysis planes

The evaluation and visualisation of the pressure situation in the defined analysis planes is analogue to the experiments described in Chapter 3.4.6. However, in the numerical case all available data points are used, which results in a higher data resolution than in the experiment.

In addition to the four previously discussed analysis planes for the experiment, six further planes have been defined for the evaluation of the numerical results. These are three horizontal z-planes, with *plane E* positioned between the vehicle underbody and the ground at a height of z = 100 mm, *plane F* at the wheel center at a height of z = 304 mm, and *plane G* above the wheel arches at a height of z = 800 mm. These planes have dimensions from x_1 = -3000 mm to x_2 = 5500 mm, and from y_1 = -1500 mm to y_2 = 1500 mm, covering the entire air flow and pressure situation around the vehicle. Furthermore, three y-planes have been defined, with *plane H* placed as the mid-plane of the vehicle in position y = 0 mm, with dimensions from x_1 = -3000 mm to x_2 = 5500 mm, and from z_1 = 0 mm to z_2 = 2000 mm. *Plane I* is located next to the left front wheel arch in position y = -950 mm with dimensions from x_1 = -1800 mm to x_2 = -700 mm and z_1 = 0 mm to z_2 = 800 mm, while *plane J* is positioned within the left front wheel arch at the center of the wheel at y = -780 mm with dimensions from x_1 = -1800 mm to x_2 = -800 mm and z_1 = 0 mm to z_2 = 750 mm. In addition, *plane D* in the wake area of the vehicle was extended to cover both halves of the vehicle and thus covers positions from y_1 = -1500 mm to y_2 = 1500 mm. An overview of all analysis planes (with the exception of *plane J*) used subsequently for the evaluation of the numerical results is shown in Fig. 3.23.

Surface pressure at the vehicle and within the wheel arch

The post-processing of the numerically obtained pressure data on the vehicle surface and at the wheel arch is analogous to the analysis process of the surface pressures for the hardware test described in Chapter 3.4.5. In contrast to the experiment, however, the pressure situation at the entire rear base, and not only at the left half of the vehicle, can

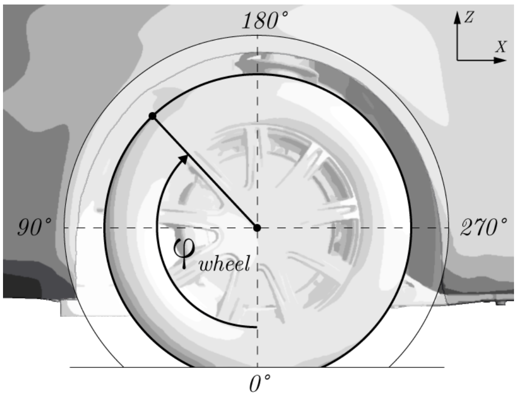

Figure 3.24: Angular notation at the tire surface.

be evaluated. Accordingly, the analysis area has been extended and covers an area from y_1 = -780 mm to y_2 = 780 mm.

In addition, the surface pressure at the tire tread can be investigated. The wheel house-fixed coordinate system described in Chapter 3.4.5 with the corresponding angular notation (Eq. (3.54)) and the angle φ_{wheel} is used to determine the positions at the tire surface, as shown in Fig. 3.24.

Surface pressure at the wheel

In contrast to the experiment, the numerical study offers the possibility to analyse the pressure situation at the tire tread. For this analysis, the surface pressure coefficient along a line in the middle of the left front wheel, at position y = -780 mm, is examined. Similar to the analysis process of surface pressure within the wheel arch, the results are plotted along the tire surface dependent on the angular position. The coordinate transformation was carried out according to the formula (3.54), where the position of the front axle was again selected as the origin of the coordinates and 0° or 360° are positioned below the axle on the wind tunnel floor.

Air mass flow rate

In order to determine the air mass flow rates, the simulation mesh must be prepared accordingly, and permeable analysis surfaces must be defined at the desired positions, at which these physical quantities can be evaluated. Accordingly, mass flow analyses at various surfaces were carried out in the subsequent investigations. For the investigations at the cooling grill, the mockup closing surfaces between the grills were used. Furthermore the front surfaces of the porous media at the heat exchangers of the cooling package, as well as the outer surfaces of the *MRF* boxes at the rims were utilized as analysis surfaces.

The air mass flow rate through a single surface element is defined as [63]:

$$\dot{m} = \rho \dot{V} = \rho A \vec{v} \cdot \vec{n} \tag{3.88}$$

where $\dot{m}$ is the air mass flow rate, ρ is the density of the fluid, $\dot{V}$ is the volume flow rate, $\vec{v}$ is the flow velocity of the mass elements, $\vec{n}$ is the cross-sectional surface unit normal vector, and A the surface.

Equation (3.88) is only valid for a flat, plane surface. In general, a surface integral, or the sum of the mass flow rates through all N surface elements of the investigated area, has to be used for the mass flow rate calculations:

$$\dot{m} = \int_A \rho \, d\dot{V} = \rho A \, \vec{v} \cdot \vec{n} = \sum_{i=1}^{N} \rho A \, \vec{v}_i \cdot \vec{n}_i \tag{3.89}$$

In this equation, index i indicates element i of the investigated surface.

The direction of flow through the evaluation areas are taken into account by means of signs on the basis of the surface cell normals. According to this, inflowing masses are rated positive, outflowing ones negative. Inflowing masses, in the case of the grill flows, are oriented into the engine compartment, and for the rims from the vehicle center to the outside. The resulting mass flow rate is therefore the difference between in- and outflowing air masses.

Mass flow rates through the individual porous media of the heat exchangers of the cooling package and through the cooling grill, as well as through the rims are tracked continuously during the simulation. The values used and shown in subsequent analyses are always mean values over the last 300 iterations and are calculated according to:

$$\dot{m} = \overline{\dot{m}} = \frac{1}{s} \sum_{i=N-s+1}^{N} \dot{m}_i \tag{3.90}$$

where s is the number of last iterations about which is averaged, and N is the total number of iterations of the simulation.

Streamlines

One way to study and visualize complex flow topologies is the use of streamlines. They are defined as curves that are tangent to the flow velocity vector at every point of the flow field at one moment in time [85]. Since there is no normal velocity component along their path, different streamlines within a stream do not overlap. In contrast, pathlines are trajectories of individual fluid particles. In steady flows, where the flow velocity field does not change over time, streamlines and pathlines coincide.

The equation of a streamlines can be derived from the definition being a curve tangent to the velocity vector in the flow field of the fluid:

$$\frac{d\vec{x}_S}{ds} \times \vec{u}(\vec{x}_S) = \vec{0} \tag{3.91}$$

where $\vec{x}_S(s)$ represents one streamline, which is parameterized by the variable s ($s \mapsto \vec{x}_S(s)$), and $\vec{u} = (u, v, w)$ is the velocity vector.

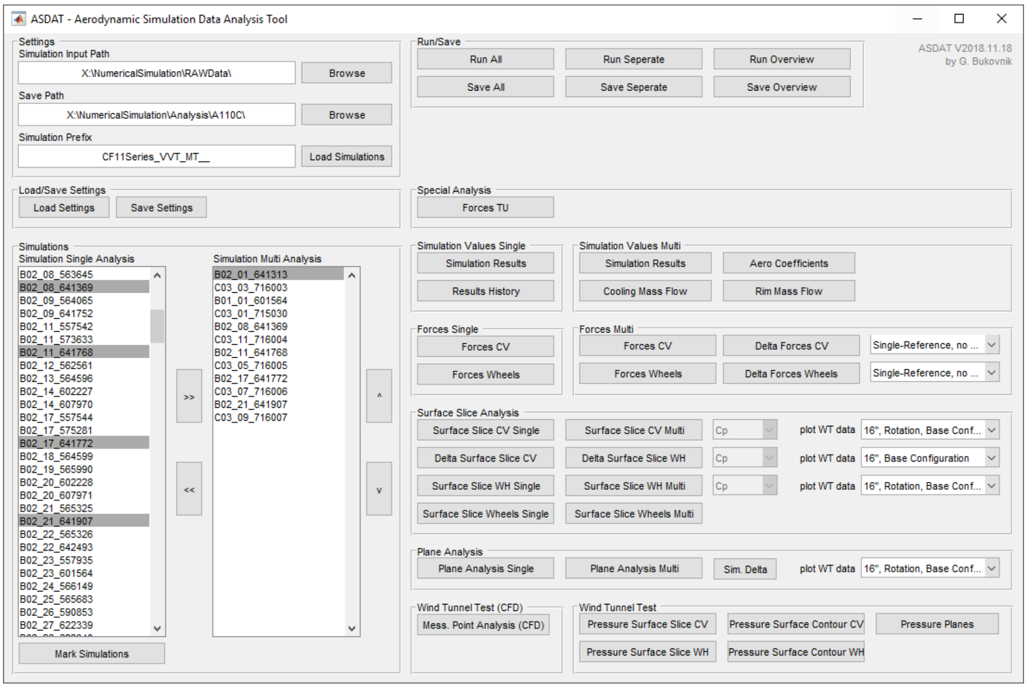

ASDAT - Aerodynamic Simulation Data Analysis Tool

Simulation Input Path: X:\NumericalSimulation\RAWData\

Save Path: X:\NumericalSimulation\Analysis\A110C\

Simulation Prefix: CF11Series_VVT_MT__

Forces Multi: Single-Reference, no ...

Forces Multi: Single-Reference, no ...

Surface Slice Analysis: Cp; plot WT data: 16", Rotation, Base Conf...

Surface Slice Analysis: Cp; plot WT data: 16", Base Configuration

Surface Slice Analysis: Cp; plot WT data: 16", Rotation, Base Conf...

Plane Analysis: plot WT data: 16", Rotation, Base Conf...

Figure 3.25: ASDAT - Graphical User Interface.

With the coordinates of points on a streamline $\vec{x}_S = (x_S, y_S, z_S)$, it can be concluded

$$\frac{dx_S}{u} = \frac{dy_S}{v} = \frac{dz_S}{w} \tag{3.92}$$

3.6 ASDAT - Aerodynamic Simulation Data Analysis Tool

In the scope of this work it was necessary to develop a custom post-processing tool in order to effectively manage, analyse and store the large number of simulation data generated during this study, and furthermore also due to limited hardware and software resources. The requirement for this analysis software was to enable time-optimized preparation, analysis and visualization of the simulation results. This concept was ultimately extended to manage and analyse the measurement data of the wind tunnel experiment also.

To meet these requirements, the software-suite *ASDAT - Aerodynamic Simulation Data Analysis Tool*) (Fig. 3.25) was developed. This software package contains database concepts to effectively store relevant simulation results, a variety of analysis processes developed especially for the evaluation of large amounts of data, and also visualization functions for the graphic processing of the computational and experimental results. The core of this tool forms an extensive software library based on the proprietary programming language *Matlab*. The required simulation data were extracted and provided to *ASDAT* for further processing utilizing scripts based on a combination of *Perl*, *Ansys Supersyntax* and *Powerscript*.

In this thesis, all analyses, evaluations and graphical representations of the numerical and experimental results were carried out with this analysis tool. Only visualizations of the simulation mesh and of three-dimensional streamlines were performed with tools like *ANSYS Fluent* and *CFD-Post*.

Chapter 4

Impact of rim geometry on vehicle aerodynamics experiments

Rim geometries affect the air flow situation in their proximity and have furthermore an impact on the integral aerodynamic forces of a vehicle, as shown by the studies of Mlinaric [29], Landström [40] and Schnepf [39], among others. This wheel characteristic is investigated in the context of this preliminary study for the test vehicle by means of wind tunnel experiments. Therefore, the influence of three production rims with different geometries and sizes on the aerodynamic behaviour of the test vehicle is subsequently examined. Furthermore, the results of these investigations serve to define the numerical load cases for the following studies and to provide experimental data for the correlation with the numerical results of the subsequent investigations. In this chapter, the test cases and the measuring program are presented first. Subsequently, the results of the experiment are discussed on the basis of flow topology and vehicle drag analyses.

4.1 Experimental test cases and measuring program

The test vehicle was prepared as accurately as possible to represent the CAD data in order to facilitate a validation between the experiment and the computational investigations. No additional modifications were applied during the experiments. The wind tunnel investigations were carried out with three series rims *Rim16*, *Rim17* and *Rim18*, where the ride height of the vehicle was kept constant for all measurements. Furthermore, the vehicle was measured in the mockup configuration, as well as with open cooling air intake and thus with enabled engine compartment flow (base configuration). Investigations were conducted with rotating and with stationary wheels. The wind tunnel boundary layer treatment was active for all test cases, which included active boundary layer suction, tangential blowing, and a moving center-belt.

Several vehicle configurations and boundary conditions were defined and combined with each other in order to process all topics efficiently within the limited test time. These presets resulted in the 16 test cases listed in Table 4.1. The case name consists of four parts separated by dots. The first part (WT) indicates that these are load cases of the wind tunnel experiment, while the second part indicates whether the engine compartment flow is disabled (A) or enabled (B). The third part indicates the tested rim geometry and

Test case	Rims	Cooling air inlet	Wheel rotation
WT.A.16.RT	*Rim16*	closed	yes
WT.B.16.RT	*Rim16*	open	yes
WT.A.16.NR	*Rim16*	closed	no
WT.B.16.NR	*Rim16*	open	no
WT.A.17.RT	*Rim17*	closed	yes
WT.B.17.RT	*Rim17*	open	yes
WT.A.17.NR	*Rim17*	closed	no
WT.B.17.NR	*Rim17*	open	no
WT.A.18.RT	*Rim18*	closed	yes
WT.B.18.RT	*Rim18*	open	yes
WT.A.18.NR	*Rim18*	closed	no
WT.B.18.NR	*Rim18*	open	no

Table 4.1: Experimental test cases

the last part shows whether the wheels were rotating (*RT*) or stationary (*NR*).

The integral aerodynamic forces and surface pressure measurements of the vehicle were performed for each test case. Due to limited test time, investigations of the flow topology by means of pressure plane measurements could only be conducted for test cases with rims *Rim16*.

4.2 Impact of rim geometry on vehicle flow topology

Flow topology examinations are subsequently performed based on surface pressure measurements on the vehicle, since flow field measurement data is only available for configurations with rims *Rim16*. Conclusions regarding the impact of rim geometries on the vehicle flow topology can also be made based on these data and are therefore performed by means of differential analysis of the surface pressure data. For this purpose, the pressure probes at the vehicle surface were distributed to four vehicle zones (see Section 3.4.5), which were evaluated individually.

The comparative analyses between the individual configurations are carried out on the basis of a representative differential value of the surface pressure coefficient for each of these zones. In order to assess the total surface pressure alterations between two cases, the absolute value of the differential pressure coefficient is computed for every probe. The sum of the results is formed in each surface zone and divided by the number of probes in this region. The calculations were performed according to the following formula, which bases on Eq. (3.56):

$$\overline{\mid \Delta C_P \mid} = \frac{1}{N} \sum_{i=1}^{N} \mid C_{P,A_i} - C_{P,B_i} \mid \tag{4.1}$$

where $\overline{\mid \Delta C_P \mid}$ is the absolute mean deviation of the surface pressure coefficient, C_{P,A_i} is the measured surface pressure coefficient for probe i for test case A, C_{P,B_i} is the corresponding reference value at the same position, and N is the number of probes in the

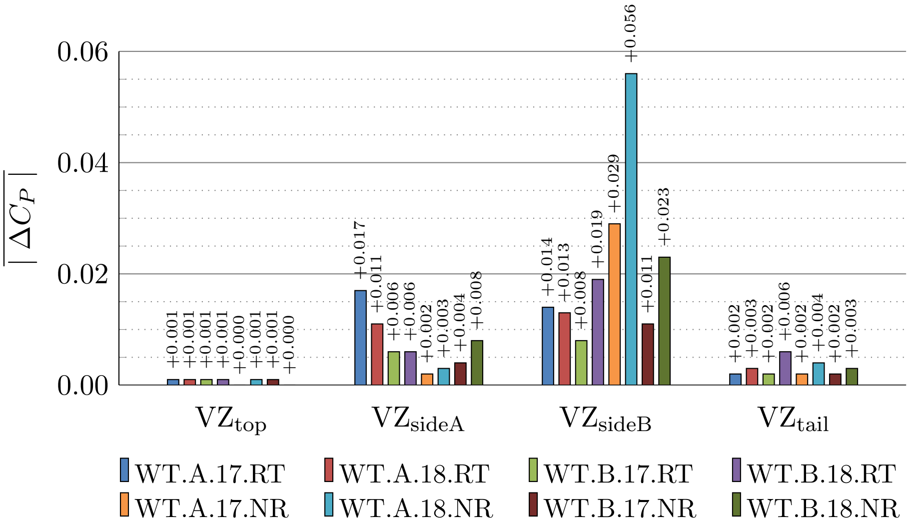

Figure 4.1: Mean absolute surface pressure coefficient differences for stationary and rotating wheels.

examined vehicle zone.

These investigations were conducted for various vehicle configurations, where in each case a vehicle configuration with the identical setup, but *Rim16* rims was used as the reference.

The results of the measured mean absolute surface pressure deviations are summarized in Fig. 4.1 and reveal a similar impact of the rim geometry on the flow topology of the vehicle for all tested configurations. The biggest surface pressure alterations are detected on the lateral surfaces $\mathrm{VZ}_{\mathrm{sideA}}$ and $\mathrm{VZ}_{\mathrm{sideB}}$. For rotating wheels, the impact on both zones is balanced. However, for stationary wheels, the impact downstream of the wheel arch at zone $\mathrm{VZ}_{\mathrm{sideB}}$ is more dominant than it is upstream for zone $\mathrm{VZ}_{\mathrm{sideA}}$. Along the vehicle centerline, in zone $\mathrm{VZ}_{\mathrm{top}}$, the differential values are close to zero, from which it can be concluded that the rim geometry has an insignificant impact on the flow topology in this region. Pressure distribution alterations are furthermore detected at the tail area $\mathrm{VZ}_{\mathrm{tail}}$, which suggests that individual rim geometries cause small, but nevertheless not negligible changes in the vehicle base pressure.

4.3 Impact of rim geometry on vehicle drag

The impact of rim geometries on the aerodynamic properties of the vehicle is examined by means of the integral vehicle resistance. For this purpose, two test cases with identical vehicle configurations (cooling air intake and wheel rotation), but various rims are considered, where always a setup with *Rim16* rims is used as reference. Differential drag values are calculated according to

$$\Delta C_{D,\mathrm{CV}} = C_{D,\mathrm{CV,A}} - C_{D,\mathrm{CV,ref}}, \tag{4.2}$$

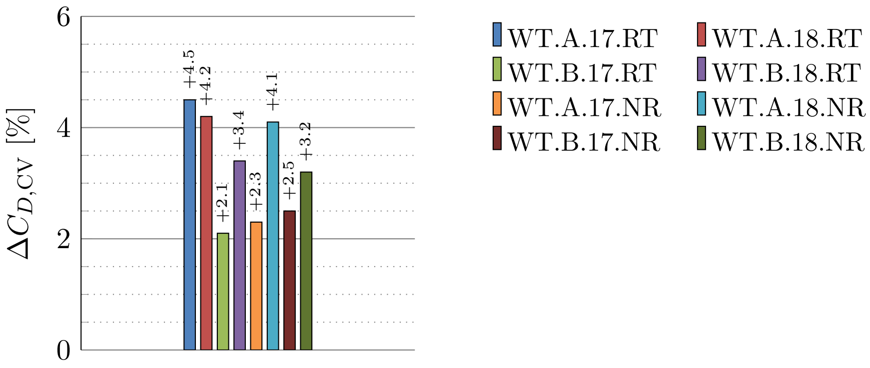

Figure 4.2: Vehicle drag differences $\Delta C_{D,\mathrm{CV}}$ for individual rim geometries, rotating and stationary wheels and engine compartment flow configurations.

where $\Delta C_{D,\mathrm{CV}}$ is the differential vehicle drag, $C_{D,\mathrm{CV,A}}$ is the measured vehicle drag of test case A and $C_{D,\mathrm{CV,ref}}$ is the corresponding value of the reference case.

The results are represented as percentages that each refer to the corresponding reference case and are shown in Fig. 4.2 for all vehicle configurations. The impact of the rim geometry on the drag coefficient of the vehicle is clearly demonstrated. Differential drag values and trends are different for all configurations and range from $\Delta C_D = 2.1\%$ to $\Delta C_D = 4.5\%$. Vehicle configurations with *Rim17* and *Rim18* show a higher drag value compared to the reference configuration with *Rim16*. This effect applies to all test cases, regardless of wheel rotation or cooling air configuration.

4.4 Synopsis

The results of the wind tunnel experiment reveal a clear impact of the rim geometry on the aerodynamic parameters of the vehicle. This effect depends on the rim geometry and boundary conditions, such as wheel rotation and engine compartment flow. The changes in the surface pressure distribution mainly affect the area up- and downstream of the wheel arch. Alterations of the pressure situation were also detected at the vehicle base, while the influence at the upper vehicle area is marginal.

However, the analysis of the integral forces on the vehicle reveals a not insignificant impact on the aerodynamic drag with changes up to 4.5% for this vehicle. A possible reason for this effect can be the trend towards decreasing geometric blockage of larger rims, which has a significant impact on its crossflow and the outflow behavior from the wheel arches into the main lateral flow, as well as on the air flow situation downstream of the wheel arch due to interference effects. This interpretation is consistent with the results of the surface pressure analysis at the lateral and base zones of the vehicle. Furthermore, the different aerodynamic quality of the three rim designs should be considered as a possible cause for their distinct effects on the aerodynamic parameters of the test vehicle.

These results confirm the findings from the experimental studies of Mlinaric [29], Landström et al. [41, 43, 45], Zhiling et al. [42] and Schnepf [39], as well as from the numerical investigations of Cederlund and Vikström [48] and Buscariolo and Karbon [46], who also observed an influence of diverse rim geometries on the aerodynamics of a vehicle. Based on this conclusion, and in order to be able to make the most comprehensive possible statement in the subsequent analyses, a part of the following studies will be carried out with three individual rim geometries.

Chapter 5

Impact of rim orientation on vehicle aerodynamics simulations

The numerical investigations in this thesis base on the steady-state *RANS* approach with the constraint of stationary rim geometry for the *MW* and *MRF* rotation methods, as well as the combinations of both. Applying these methods to simulate wheel rotation means that the rim and tire geometries of the computational mesh remain stationary, and the rotation is simulated using various mathematical models, as discussed in Chapter 3.5. This approach implies that the simulation can only provide results for one specific rim orientation. Since the wheel geometry does not rotate and remains motionless in its position, it seems likely that the geometric rim orientation could have an impact on the simulation results.

Due to this reason, a comprehensive sensitivity study on the impact of different rim orientations on the aerodynamic situation of the vehicle is initially performed on the basis of the flow topology analyses in the proximity of the left front wheel and the underbody region for the stationary case with fixed wheels. In a further phase of this study, the examinations are extended from the stationary case to all load cases with rotating wheels in order to analyse the range of the vehicle resistance between individual rim positions for each rotation method. These investigations are deliberately kept minimal, as the focus is on the analysis of the impact on the integral vehicle drag, which will be investigated subsequently in combination with its evolution along the vehicle's main axes. A detailed examination of the air flow situation in proximity of the wheels and the wheel arch, as well as the entire vehicle, will follow in the subsequent chapters. Based on these simulation results, the load cases for further numerical investigations are defined.

5.1 Simulation cases

The fully detailed computational test vehicle model will be used in the following study. Since the cooling air has a non negligible effect on the air flow situation in proximity of the front wheels [86, 87], subsequent investigations are carried out for the mockup configuration, in comparison to vehicle configurations with enabled engine compartment flow. Furthermore, stationary load cases, i.e. with fixed wheels, are considered to study the aerodynamic effects of individual rim orientations on simulations without influences from a wheel rotation method. All available rotation methods are applied to simulate wheel rotation, i.e. *MW*, *MW-TO* and *MRF*, as well as the combinations *MRF&MW* and *MRF&MW-TO*. According to the results and conclusions regarding rim geometry from Chapter 4, the following examinations are carried out for rims *Rim16*, *Rim17* and *Rim18*.

In order to investigate the impact of individual rim orientations, two initial rotation positions were defined for each of the three rim geometries. The rims were symmetrically rotated by the angle φ on the left and right side of the vehicle. This corresponds to an anti-clockwise rotation on the left side or a clockwise rotation on the right side of the vehicle. In the following, position α corresponds to the construction position of the rims, while position β represents the additional, rotated position. The rotation angle φ between rim position α and β was chosen for each rim geometry separately and in a way that the maximum change of spoke blockage inside the wheels was achieved. The resulting values are listed in Table 5.1, while Fig. 5.1 shows positions α and β for all rim geometries.

Rims	φ
Rim16	18°
Rim17	20°
Rim18	25°

Table 5.1: Rotation angles between the spoke positions α and β for each rim geometry.

An additional set of six simulation meshes was created through combination of the rotated rim geometries with the vehicle mesh. A full list of all the load cases is shown in Table 5.2 the mockup, and in Table 5.3 for the base configuration. The notation of these setups consists of three parts, separated by dots. The first letter indicates the rim orientation and engine air flow configuration, where *A* and *C* represent the cooling mockup with rim positions α and β, and *B* and *D* are the corresponding simulation cases with enabled engine compartment flow. The second part of the notation corresponds to the rim size, and the third section to the applied wheel rotation method.

5.2 Impact of rim orientation and wheel rotation methods on the simulated vehicle flow topology

In order to understand the influence of the rim position on the aerodynamics of the vehicle, its impact on the flow topology in relevant vehicle areas is examined. The flow situation in the region of the front wheel on the left side is examined in analysis *plane A*, which is positioned downstream from the front wheel house, as well as in *plane I*, positioned next to this wheel arch (see Fig. 3.23). In addition to the pressure distribution, the projected streamlines are also shown in *plane A*. The impact on the flow topology along the vehicle is analysed in *plane E*. To identify and visualize the air flow alterations, the corresponding pressure coefficients are computed in these planes according to Eq. (3.49), and the results are displayed as contour plots.

The results of the flow topology analysis in the area of the left front wheel in *plane A* and *plane I* are shown in Fig. 5.2. The results of the analysis in the underbody area are

Case	Rims	Cooling air inlet area	Tire rotation method	Rim rotation method	Rim position
A.16.NR	*Rim16*	closed	-	-	α
A.16.MW	*Rim16*	closed	MW	MW	α
A.16.MW-TO	*Rim16*	closed	MW	-	α
A.16.MRF	*Rim16*	closed	-	MRF	α
A.16.MRF&MW	*Rim16*	closed	MW	MRF&MW	α
A.16.MRF&MW-TO	*Rim16*	closed	MW	MRF	α
C.16.NR	*Rim16*	closed	-	-	β
C.16.MW	*Rim16*	closed	MW	MW	β
C.16.MW-TO	*Rim16*	closed	MW	-	β
C.16.MRF	*Rim16*	closed	-	MRF	β
C.16.MRF&MW	*Rim16*	closed	MW	MRF&MW	β
C.16.MRF&MW-TO	*Rim16*	closed	MW	MRF	β
A.17.NR	*Rim17*	closed	-	-	α
A.17.MW	*Rim17*	closed	MW	MW	α
A.17.MW-TO	*Rim17*	closed	MW	-	α
A.17.MRF	*Rim17*	closed	-	MRF	α
A.17.MRF&MW	*Rim17*	closed	MW	MRF&MW	α
A.17.MRF&MW-TO	*Rim17*	closed	MW	MRF	α
C.17.NR	*Rim17*	closed	-	-	β
C.17.MW	*Rim17*	closed	MW	MW	β
C.17.MW-TO	*Rim17*	closed	MW	-	β
C.17.MRF	*Rim17*	closed	-	MRF	β
C.17.MRF&MW	*Rim17*	closed	MW	MRF&MW	β
C.17.MRF&MW-TO	*Rim17*	closed	MW	MRF	β
A.18.NR	*Rim18*	closed	-	-	α
A.18.MW	*Rim18*	closed	MW	MW	α
A.18.MW-TO	*Rim18*	closed	MW	-	α
A.18.MRF	*Rim18*	closed	-	MRF	α
A.18.MRF&MW	*Rim18*	closed	MW	MRF&MW	α
A.18.MRF&MW-TO	*Rim18*	closed	MW	MRF	α
C.18.NR	*Rim18*	closed	-	-	β
C.18.MW	*Rim18*	closed	MW	MW	β
C.18.MW-TO	*Rim18*	closed	MW	-	β
C.18.MRF	*Rim18*	closed	-	MRF	β
C.18.MRF&MW	*Rim18*	closed	MW	MRF&MW	β
C.18.MRF&MW-TO	*Rim18*	closed	MW	MRF	β

Table 5.2: Simulation load cases with mockup configuration.

Case	Rims	Cooling air inlet area	Tire rotation method	Rim rotation method	Rim position
B.16.NR	*Rim16*	open	-	-	α
B.16.MW	*Rim16*	open	MW	MW	α
B.16.MW-TO	*Rim16*	open	MW	-	α
B.16.MRF	*Rim16*	open	-	MRF	α
B.16.MRF&MW	*Rim16*	open	MW	MRF&MW	α
B.16.MRF&MW-TO	*Rim16*	open	MW	MRF	α
D.16.NR	*Rim16*	open	-	-	β
D.16.MW	*Rim16*	open	MW	MW	β
D.16.MW-TO	*Rim16*	open	MW	-	β
D.16.MRF	*Rim16*	open	-	MRF	β
D.16.MRF&MW	*Rim16*	open	MW	MRF&MW	β
D.16.MRF&MW-TO	*Rim16*	open	MW	MRF	β
B.17.NR	*Rim17*	open	-	-	α
B.17.MW	*Rim17*	open	MW	MW	α
B.17.MW-TO	*Rim17*	open	MW	-	α
B.17.MRF	*Rim17*	open	-	MRF	α
B.17.MRF&MW	*Rim17*	open	MW	MRF&MW	α
B.17.MRF&MW-TO	*Rim17*	open	MW	MRF	α
D.17.NR	*Rim17*	open	-	-	β
D.17.MW	*Rim17*	open	MW	MW	β
D.17.MW-TO	*Rim17*	open	MW	-	β
D.17.MRF	*Rim17*	open	-	MRF	β
D.17.MRF&MW	*Rim17*	open	MW	MRF&MW	β
D.17.MRF&MW-TO	*Rim17*	open	MW	MRF	β
B.18.NR	*Rim18*	open	-	-	α
B.18.MW	*Rim18*	open	MW	MW	α
B.18.MW-TO	*Rim18*	open	MW	-	α
B.18.MRF	*Rim18*	open	-	MRF	α
B.18.MRF&MW	*Rim18*	open	MW	MRF&MW	α
B.18.MRF&MW-TO	*Rim18*	open	MW	MRF	α
D.18.NR	*Rim18*	open	-	-	β
D.18.MW	*Rim18*	open	MW	MW	β
D.18.MW-TO	*Rim18*	open	MW	-	β
D.18.MRF	*Rim18*	open	-	MRF	β
D.18.MRF&MW	*Rim18*	open	MW	MRF&MW	β
D.18.MRF&MW-TO	*Rim18*	open	MW	MRF	β

Table 5.3: Simulation load cases with enabled engine compartment flow.

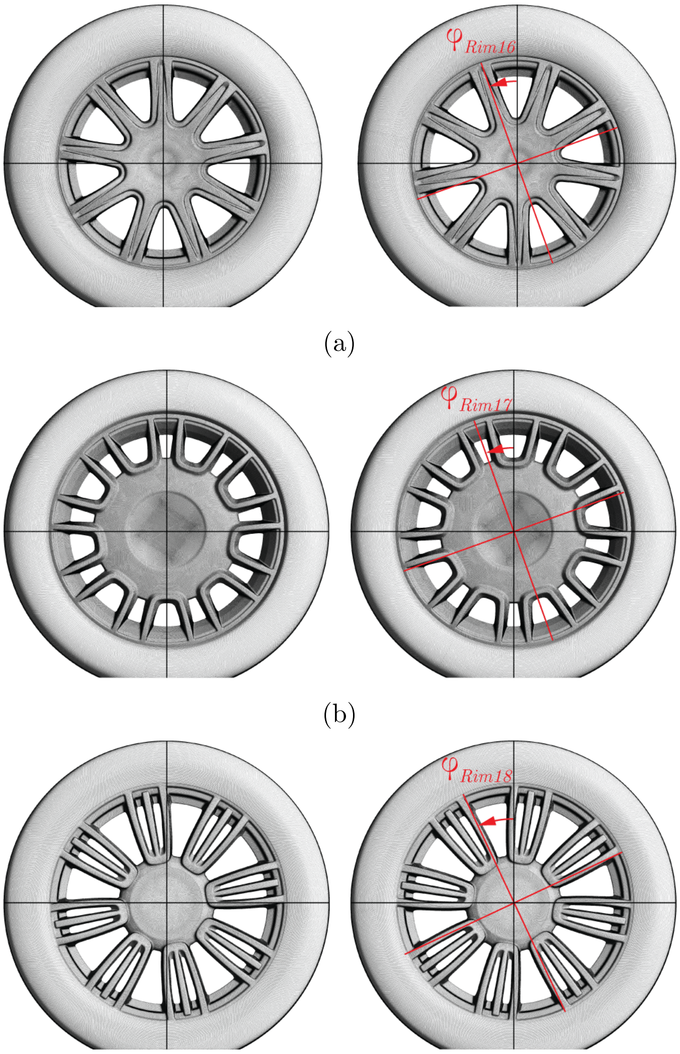

(a)

(b)

(c)

Figure 5.1: *Rim16* (top), *Rim17* (center) and *Rim18* (bottom) with simplified tire geometry in rim positions α (left) and β (right).

displayed in Fig. 5.3. Since the flow structure alterations between the two rim positions are small, a differential analysis of the surface pressure coefficients was carried out additionally, defining the pressure coefficient difference as

$$\Delta C_P = C_{P,\beta} - C_{P,\alpha} \tag{5.1}$$

where $C_{P,\alpha}$ is the pressure coefficient with the rims in position α, and $C_{P,\beta}$ corresponds to position β. ΔC_P is visualized in Figs. 5.2e, 5.2f and 5.3c, where data were scaled to highlight the air flow alterations as well as possible. The setup with rims in position α was selected as the reference case for this analysis. Corresponding plots for simulation cases with *Rim17* and *Rim18* can be found in Appendix A.

The flow analysis in the stationary case reveals that the rim orientation has a significant impact on the flow topology close to the front wheels and, consequently, on the flow sit-

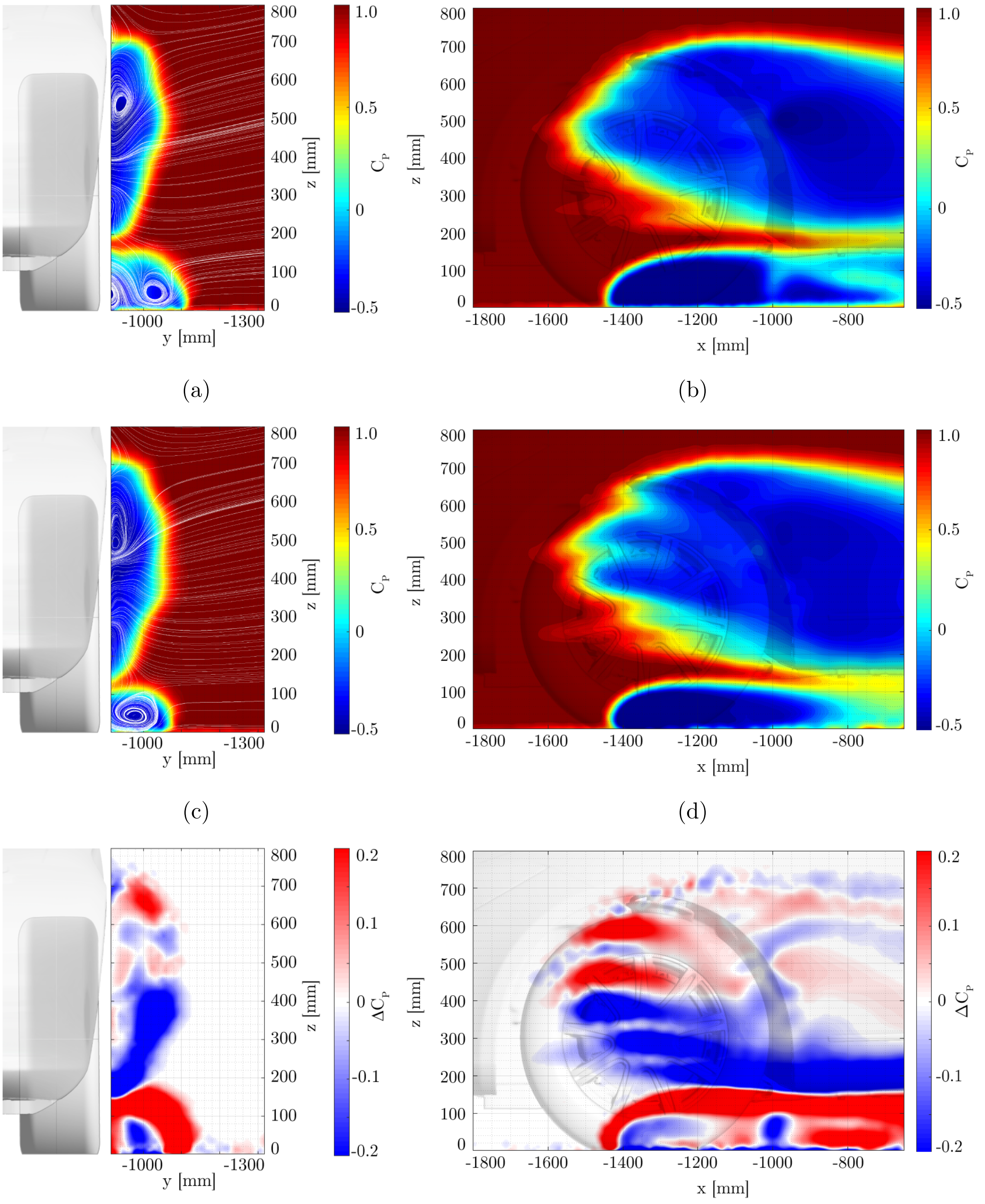

(a) (b)

(c) (d)

(e) (f)

Figure 5.2: Pressure coefficient C_P downstream of the wheel arch for the stationary simulation case with rims *Rim16*. Rim orientation α (*B.16.NR*) (top), β (*D.16.NR*) (center), and the differential analysis ΔC_P between both cases (bottom) at *plane A* with projected streamlines (left) and *plane I* (right).

uation around the entire vehicle. The investigated air flow situation near the wheel arch is subsequently interpreted and discussed based on the findings of the studies by Wäschle [37] and the thermology introduced in this work.

Major alterations of the air flow topology are identifiable in the area of the front wheels (Figs. 5.2a, 5.2c and 5.2e), where a slight shift downwards of the vortex structure can be recognized in the rotated case. The near-ground vortex is less developed, while the upper vortex has increased in size. Through comparison of the wheel vortices with the underlying rims, a correlation between the rim geometries and the flow topologies becomes apparent. The influence on the flow field in this region can therefore be attributed to crossflow through the rims and wheel arches, since the venting behavior of the wheel houses strongly depends on the blockage by the spokes. Since the spoke orientation varies between the two simulation cases, the air streams at different positions through the rims and outward from the wheel arch, affecting the main air flow. This alteration is readily apparent through comparison of the pressure differences adjacent to the front wheels along the vehicle (Figs. 5.2b, 5.2d and 5.2f). Air venting occurs at different locations for these two rim positions, which directly affects the vortex formation in this area.

The analysis of the underbody air flow situation in *plane E* (Figs. 5.3a and 5.3b), as well as the analysis of the pressure difference in this area (Fig. 5.3c) confirms this interpretation. An apparent alteration of the flow topology, originating from the front wheels and propagating downstream to the tail and beyond, can be recognized. In addition, the outflow of cooling air into the underbody region is also affected, which can be attributed to the altered pressure situation within the wheel arches and at the underbody. Therefore it can be concluded that this pressure difference also determines the outflow behavior of the cooling air from the engine compartment, and thus the rate of air entering the wheel arches and the underbody.

5.3 Impact of rim orientation and wheel rotation methods on the simulated vehicle drag

In the previous section, the focus has been on examining the effects of rim orientation and wheel rotation methods on the simulated flow topology of the vehicle. The determined changes in the flow topology and the resulting interference effects must eventually influence the integral aerodynamic vehicle forces. Therefore, the impact of rim orientation on the aerodynamic drag will be investigated subsequently.

Drag development

The origin and development of the total aerodynamic drag differences $\Delta C_{D,\text{CV}}$ between the two cases with rim orientation positions α and β can be identified through an analysis of the accumulated vehicle drag coefficient difference $\Delta C_{D,\text{CV,acc}}$. For this purpose, $C_{D,\text{CV,acc}}$ is determined for both load cases, according to the analysis process described in Chapter 3.5.9. Subsequently, the accumulated vehicle drag coefficient difference is calcu-

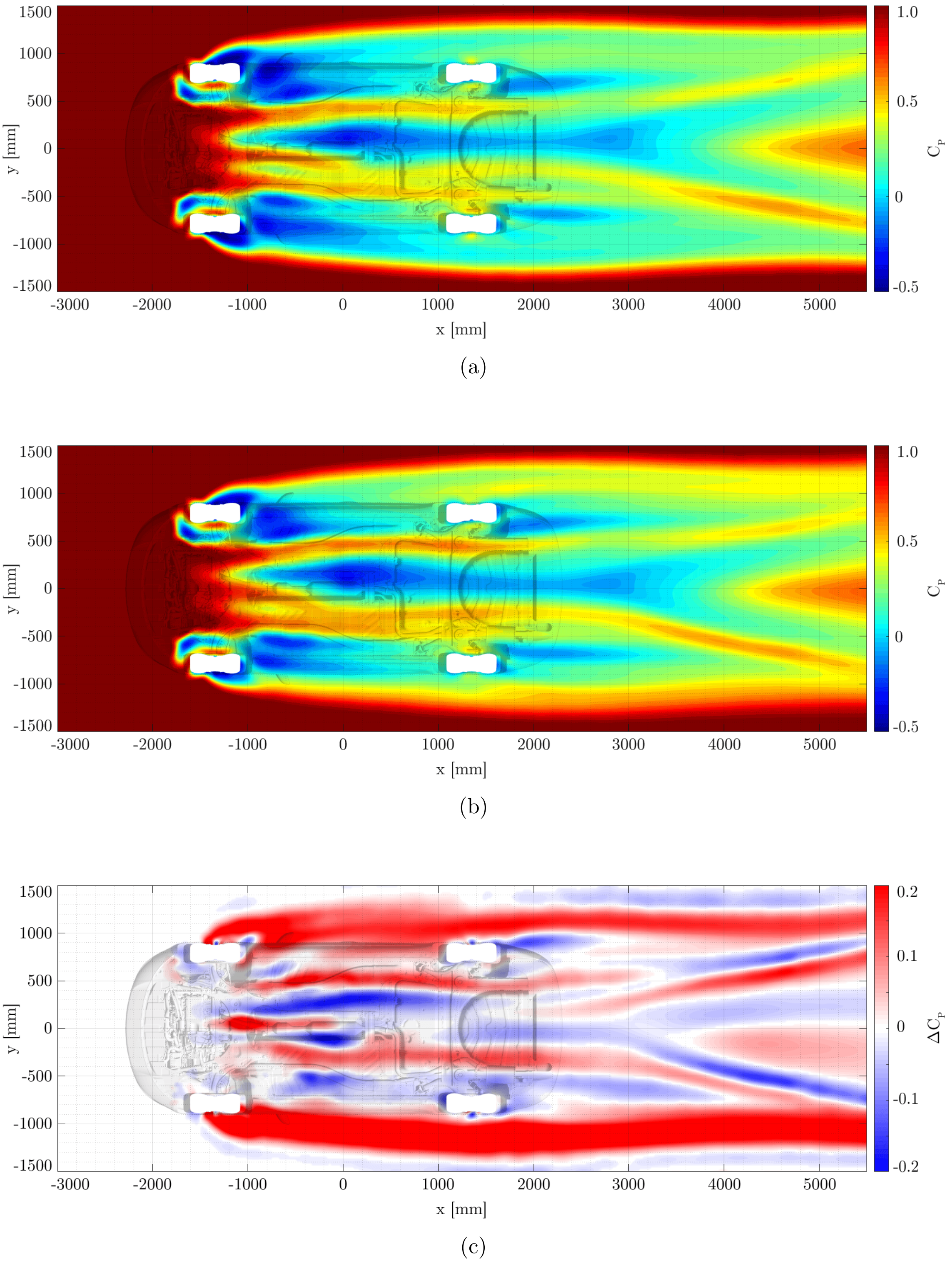

(a)

(b)

(c)

Figure 5.3: Pressure coefficient C_P at the underbody in *plane E* for the stationary simulation case with *Rim16*. Rim orientation α (*B.16.NR*) (top), β (*D.16.NR*) (center), and the differential analysis ΔC_P between both cases (bottom).

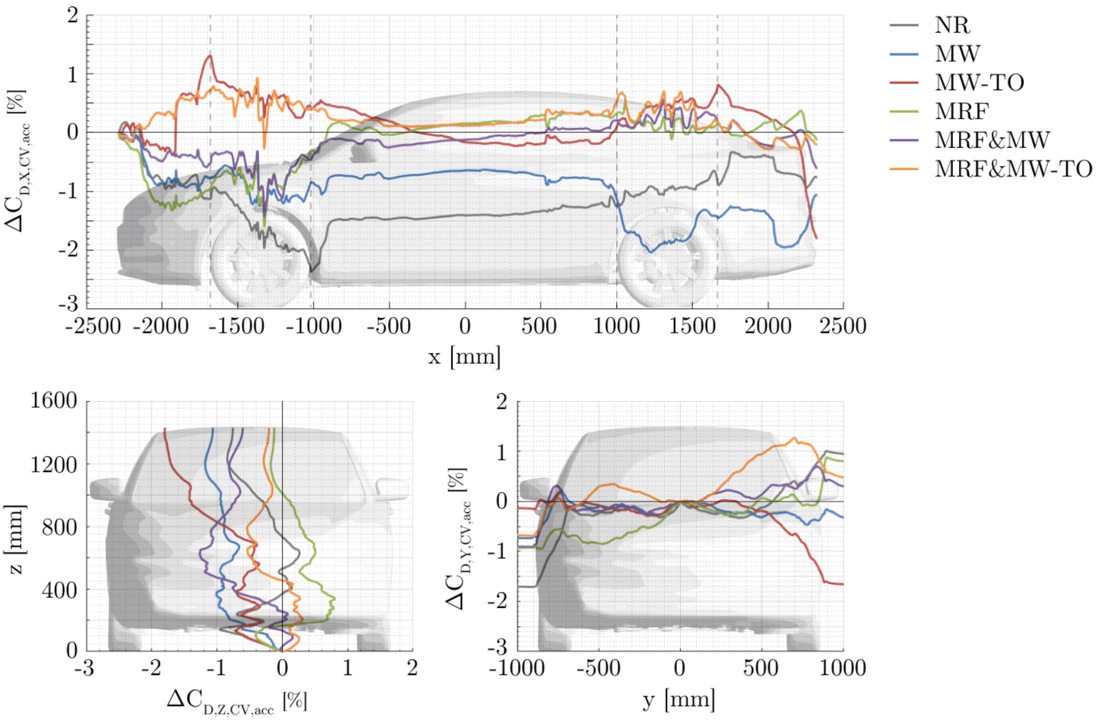

Figure 5.4: Development of the accumulated vehicle drag coefficient difference $\Delta C_{D,\text{CV}}$ along the vehicle axes for *Rim16*. Simulation cases *D.16.*-B.16.**.

lated through

$$\Delta C_{D,\text{CV,acc}} = C_{D,\text{CV,acc},\beta} - C_{D,\text{CV,acc},\alpha} \tag{5.2}$$

and the results are displayed along the vehicle's main axes. In Eq. (5.2), $C_{D,\text{CV,acc},\alpha}$ is the accumulated vehicle drag coefficient for rim orientation α, while $C_{D,\text{CV,acc},\beta}$ corresponds to rim orientation β.

This investigation is performed for the stationary case, as well as for all simulation cases with applied wheel rotation methods. In addition to the vehicle drag, the separate evolutions of the vehicle body drag $\Delta C_{D,\text{BODY,acc}}$ and the wheel drag $\Delta C_{D,\text{WHEELS,acc}}$ are investigated as well. $\Delta C_{D,\text{WHEELS,acc}}$ considers the drag value of all tires and rims, while $\Delta C_{D,\text{BODY,acc}}$ includes all remaining components of the vehicle. The results are displayed in percent, with the vehicle drag coefficient for rim position α as the reference value. The outcomes for *Rim16* are shown in Fig. 5.4 for the vehicle, in Fig. 5.5 for the body and in Fig. 5.6 for the wheels. Accordingly, the results for *Rim17* and *Rim18*, as well as for all mockup configurations are shown in Appendix A.

The results reveal an apparent impact of the rim orientation on the entire drag situation of the vehicle. Effects are recognizable also in regions upstream from the zone of the actual geometric change, i.e. at the vehicle front. Major alterations of the vehicle drag coefficient can be detected at the front end and in the region of the front and rear wheel arches, as well as in the tail area (Fig. 5.4). The analysis of drag changes at the body (Fig. 5.5) and the wheels (Fig. 5.6) reveals that these alterations can be equally divided between the two groups. However, the proportions of body and wheel drag changes do not necessarily have

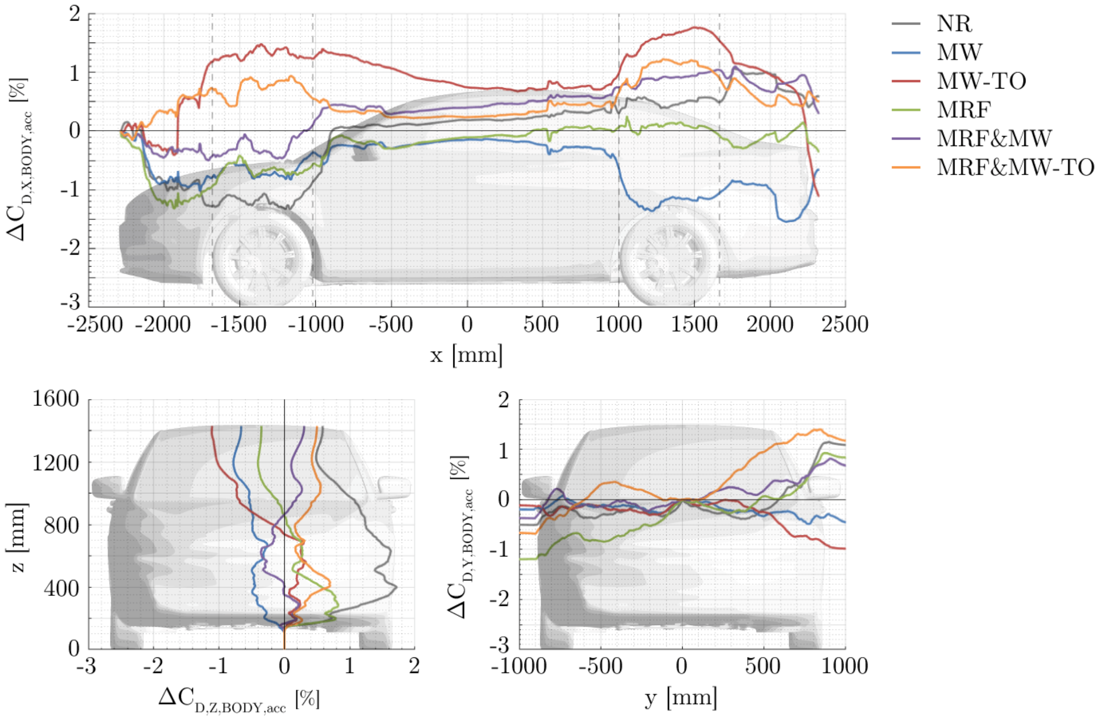

Figure 5.5: Development of the accumulated body drag coefficient difference $\Delta C_{D,\mathrm{BODY}}$ along the vehicle axes for *Rim16*. Simulation cases *D.16.*-B.16.**.

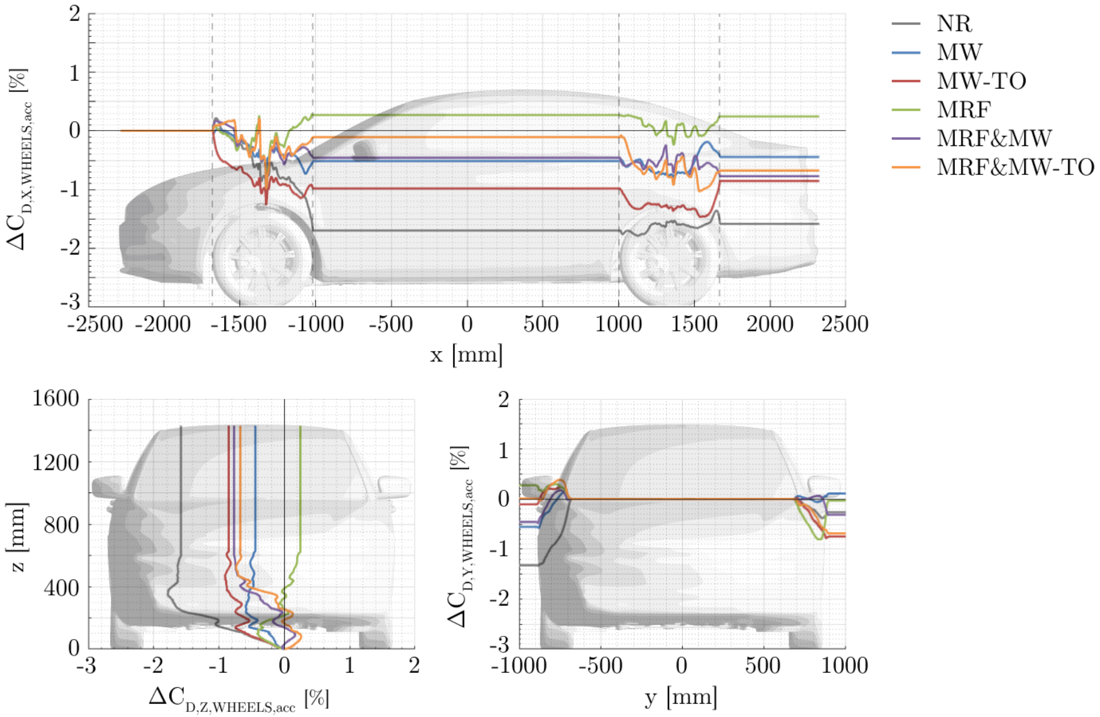

Figure 5.6: Development of the accumulated wheel drag coefficient difference $\Delta C_{D,\mathrm{WHEELS}}$ along the vehicle axes for *Rim16*. Simulation cases *D.16.*-B.16.**.

the same tendencies, which results either in an overall increase, in a reduction or even in a cancellation of the resulting vehicle resistance difference, as shown by the example of *MRF* in Fig. 5.5 and Fig. 5.6.

The evolution of the drag along the three vehicle axes is analysed subsequently. As previously mentioned, a major alteration in vehicle drag can be recognized at the vehicle front end already. This impact can be attributed to a change of the engine compartment flow, as well as the outflow behavior of the cooling air into the wheel arches and the underbody, which is also revealed by the flow topology analyses in this area (Fig. 5.3c). Furthermore, drag changes occur in the front wheel arch region, which are of a similar magnitude as those at the vehicle front end. These effects can be attributed to the altered cross flow situation through the rims and the venting behavior of the wheel arches. The stationary case shows the biggest drag differences between the two rim positions in this area, which results directly from drag alterations at the wheels. The central vehicle region, between the front and the rear wheel arches, shows only marginal vehicle drag alterations. However, interference effects are noticeable, which change the air flow situation around various vehicle parts, such as near the fuel tank around $x = 500$ mm for *Rim17* (Fig. A.8). Drag changes at the rear wheel arches are similar to those at the front wheel houses. However, the tail section shows a large proportion of the drag alterations for *MW-TO* and *MW*. The impact for *MRF*, *MRF&MW*, as well as *MRF&MW-TO*, is low in this area. These results demonstrate that large drag alterations may occur locally, but they may also vanish downstream along the vehicle, finally resulting in a minor impact on the total vehicle drag, as shown for the example of the *MRF* (Fig. 5.4). Conversely, the flow field can be altered in such a way that, although only small local drag changes occur along the vehicle, these finally turn into major alterations in the rear area. This effect is evident for *MW-TO*, where a drag increase eventually develops into a strong drag decrease at the vehicle tail. From these observations it can be concluded that those changes of the flow structure are not just a local phenomenon. They rather change the global flow topology of the vehicle due to interference effects.

The analysis of the drag coefficient difference along the y axis (Fig. 5.4) yields a disparate evolution for the left and right sides of the vehicle, as shown, e.g., for the *MRF* simulation case, where the impact in drag on the driver side is positive, while it is largely negative on the passenger side. The drag analysis along the x axis revealed that these differences finally cancel out at the rear. A possible explanation for this phenomenon are the asymmetric vehicle geometry and the asymmetric engine compartment flow, as well as non-left/right handed wheel rim geometries, which results in an unbalanced underbody flow and affects the cross flow through the rims. Drag changes in the y direction can be detected mainly on the sides of the vehicle, which can be attributed to the impact from the wheels.

The drag analysis along the z axis reveals that the main alterations are located in the lower half of the vehicle, especially for the stationary case, which can be attributed particularly to the proportion of the wheels. Through cross-comparison with the analysis results along the x axis, the effects can be limited to the underbody, the lower part of the front wheels and the tail.

The observed effects between mockup (Figs. A.5, A.6 and A.7) and vehicle configurations with enabled cooling air flow are comparable to a great extent (Figs. 5.4, 5.5, 5.6, A.8 and A.9). However, less vehicle drag alterations occur for the mockup in the area of the engine compartment due to the absence of underhood air flow.

Integral vehicle drag

The effects of rim orientation on the integral aerodynamic vehicle drag are analysed by differences between simulation results for different rim positions. The vehicle drag difference is calculated based on the drag coefficients according to

$$\Delta C_{D,\mathrm{CV}} = C_{D,\mathrm{CV},\beta} - C_{D,\mathrm{CV},\alpha} \tag{5.3}$$

where $C_{D,\mathrm{CV},\alpha}$ is the vehicle drag coefficient for rim orientation α, and $C_{D,\mathrm{CV},\beta}$ corresponds to rim orientation β. The results are expressed in percent, with the vehicle drag coefficient for rim orientation α as the reference. The results are shown in Fig. 5.7 for the mockup and Fig. 5.8 for configurations with enabled engine compartment flow.

The magnitude of the differences depends on rim geometry, applied rotation method and cooling air configuration. For the stationary case, the drag differences show values up to 1.7% for the mockup and up to 0.8% for configurations with engine compartment flow. The application of rotation methods may enhance or reduce this effect, depending on the rim geometry and cooling air configuration. For rotating wheels, the difference in magnitude in total vehicle drag between the two rim positions is up to 2.7% for the cooling mockup and up to 4.1% for the setup with enabled cooling air flow. However, a trend for the individual wheel rotation methods is not recognizable.

5.4 Synopsis

The studies demonstrated that the rim orientation and spoke position alter the flow topology of the vehicle for stationary and rotating wheels, regardless of the applied rotation method. Minor changes in the rim geometry greatly affect the air flow situation at the complete vehicle, and consequently also the vehicle drag. The flow topology is altered, and thus the pressure distribution in the area of the front wheels. Since the latter affects the cross flow through the rims, as well as the outflow behavior of cooling air from the engine compartment into the wheel arches and to the underbody, this may be a possible explanation for this effect.

The modified air flow topology results furthermore in altered local drag evolutions along the vehicle, with the greatest alterations at the front end, in the region of the front and rear wheel arches, the underbody, as well as at the tail. The effects from the vehicle body and wheels are about the same in magnitude, however they may have different tendencies, resulting either in an overall increase, reduction, or even cancellation of the resulting vehicle drag difference. The impact on the integral vehicle resistance depends on the applied wheel rotation method as well as the rim geometry and can make up to 4.1% of the vehicle drag value. However, a trend between the individual rotation approaches could not be determined. These findings correlate with the results and extend the study of Landström

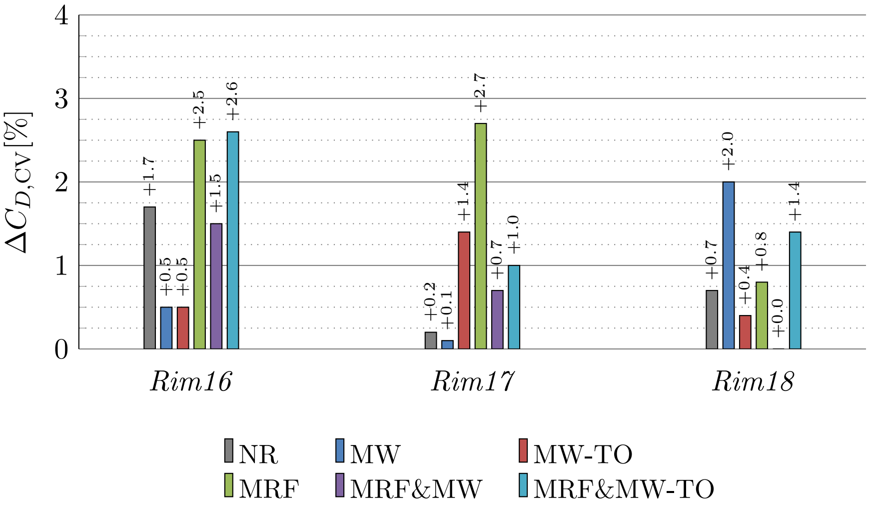

Figure 5.7: Differences in the vehicle drag coefficient for two rim orientations with cooling mockup configuration.

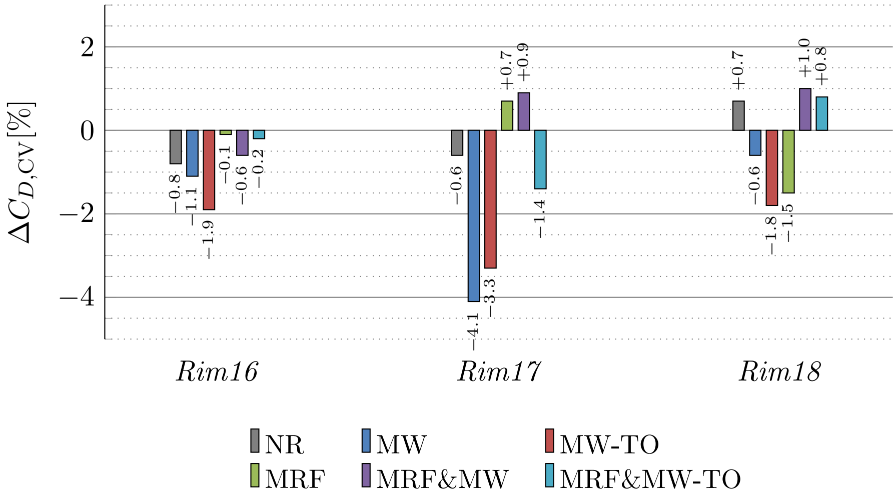

Figure 5.8: Differences in the vehicle drag coefficient for two rim orientations with enabled engine compartment flow.

et al. [47], who considered the *MRF* and the *SM* methods in their research.

Due to the great impact of the rim orientation on the aerodynamic behavior of the vehicle, it is recommended to account for this impact generally in numerical simulations in which the tire and rim geometries cannot be rotated, such as for the *RANS* approach. In these cases, various relevant rim orientations should be examined in order to quantify the uncertainty of its influence on the integral vehicle drag. Some of the subsequent analyses in this study will therefore be carried out for two rim orientations.

Chapter 6

Impact of wheel rotation methods on wheel arch aerodynamics

The air flow situation within the wheel arch and the impact of the rotating wheel on the aerodynamic situation in this region must be understood in order to conceive the effects of wheel rotation on the aerodynamic behaviour of the vehicle. Therefore, the impact of wheel rotation on the air flow situation within the wheel arch, as well as in the wake area of the front wheel, is analysed in this chapter by means of flow field examinations. These results are completed by analyses of the surface pressure situation at the wheel house shell and at the tire tread. The numerical results are discussed and validated with the findings from the wind tunnel experiments and the literature, with focus on the possibilities of individual numerical wheel rotation methods to predict the examined air flow alterations. The results of these studies serve as the basis for the investigations in the following chapters. For this study, experimental investigations in the wind tunnel, as well as numerical simulations are carried out. The content of this chapter is structured accordingly. In the first part, the experimental and simulation test cases are presented. Subsequently, the results of the experiment and the numerical investigations are discussed.

6.1 Experimental test cases and measuring program

The wind tunnel experiments were performed with the test vehicle for three series rims *Rim16*, *Rim17* and *Rim18*, constant vehicle ride height and enabled engine compartment flow. Furthermore, all measurements were carried out with stationary, as well as with rotating wheels. The ground simulation system was active for each test, by means of boundary layer suction and moving center belt. In the following analyses, the reference cases will each be a vehicle configuration with non-rotating wheels and fixed wheel drive units. Further details of the preparations of the test vehicle and the test cases, as well as the wind-tunnel boundary conditions, correspond to those presented in Chapter 4 and will therefore not be repeated and discussed again at this point. The resulting vehicle configurations are also consistent with those described in Chapter 4 and are listed in table 4.1. For each test case, the integral aerodynamic forces were examined, and surface pressure measurements within the wheel arch were conducted.

6.2 Simulation cases

The computational studies are performed using fully detailed simulation models of the test vehicle with enabled engine compartment flow. Again, all available rotation methods are used to simulate wheel rotation, i.e. *MW*, *MW-TO* and *MRF* and the combinations *MRF&MW* and *MRF&MW-TO*. In accordance to the findings from Chapter 4, the simulations are carried out for rims *Rim16*, *Rim17* and *Rim18*. However, mainly the simulation results of *Rim16* are presented in this chapter. Further analysis results of load cases with rims *Rim17* and *Rim18* can be found in Appendix B. A complete list of all load cases and setups used for the numerical investigations of this chapter is shown in Table 5.3.

6.3 Impact of wheel rotation on the flow topology inside the wheel arch

In order to understand the flow situation and the effective aerodynamic mechanisms within the wheel house and the effects of the wheel rotation on them, the flow topology is initially examined in close proximity of the left front wheel, as well as in its wake. Detailed studies are carried out on the basis of pressure-based flow field analyses and through investigation of the surface pressure situation at the tire tread and at the wheel arch surface.

Flow topology studies in the proximity of the wheel are performed based on numerical results, since experimental flow field data was not available. For this purpose, the air flow situation is investigated in various analysis planes, where the pressure situation in these planes is represented as contour plots of the dimensionless pressure coefficient. These studies are subsequently extended by experimental and numerical surface pressure analyses at the wheel arch and at the tire tread, where the results are visualized as contour plots. In order to quantify the deviations between the individual load cases, averaged pressure coefficients are calculated for various sections of the wheel arch, in accordance with the evaluation process described in Chapter 3.4.5. The alterations of the pressure distribution at the tire tread are investigated and discussed through pressure evaluations along the center line of the wheel. The flow field of the vehicle is affected, inter alia, by the outflow behavior from the wheel arch through the rim into the lateral main flow [40]. For this reason, the influence of the wheel rotation on the air mass flow rate through the free surfaces of the rim geometry is numerically analysed, which is carried out according to the process outlined in Chapter 3.5.9.

In the following sections, the results of the experiment are discussed initially, by means of the examination of the surface pressure situation at the wheel arch surface. Subsequently, the results of the computational studies are presented. Eventually, the numerical results are validated with the findings of the experiment and from the literature.

6.3.1 Experimental results

The measured pressures at the wheel arch surface are shown in Fig. 6.1 in form of C_P for load cases with rims *Rim16*, *Rim17* and *Rim18*. In this analysis, a strip of the complex, three-dimensional curved wheel arch surface is represented as a planar area, and the corresponding surface pressures therein as a contour plot. The plane is oriented as if the vehicle was viewed from below. The lower edge of the plot thus corresponds to the edge, formed by the wheel arch and the vehicle underbody upstream of the tire. Accordingly, the upper line represents the edge between the wheel arch and underbody downstream of the wheel. The negative y coordinate axis corresponds to the vehicle exterior, which implies that the left side of the plot points outwards and the right side into the vehicle. The white area between $\varphi = 170°$ and $\varphi = 200°$ corresponds to the notch in the wheel arch geometry due to the implementation of shock absorber and spring. For each configuration, the stationary case is illustrated in the left column, and the according case with rotating wheels in the middle column. In addition, differential pressure analyses between these two cases have been performed for each configuration according to Eq. (3.55) and the results are visualized in the right column. The setups with stationary wheels were defined as reference case B for this analysis.

In order to quantify and compare the results of the individual load cases with each other, the wheel house surface is divided into six even angular sections, each with an angular range of $\Delta\varphi = 36.67°$, as described in Chapter 3.4.5. For each of these segments, the mean deviation of the surface pressure coefficient $\overline{\Delta C_P}$ was calculated according to Eq. (3.56) between load cases with stationary and rotating wheels. The results are presented in Fig. 6.2 for all rim geometries.

The results of the experiment reveal that rotating wheels alter the surface pressure situation and reduce the pressure for large areas of the wheel arch liner in reference to the stationary cases. This effect is obvious for all rim configurations, particularly in the area $90° \leq \varphi \leq 240°$ (Fig. 6.1) and for the corresponding areas WH_B, WH_C and WH_D (Fig. 6.2).

Noteworthy are the two wheel house areas near the opening to the underbody region, located up- and downstream of the wheel at $\varphi < 90°$ and $\varphi > 260°$, i.e. area $\mathrm{WH_A}$ and $\mathrm{WH_F}$, where localized pressure increases can be detected. This phenomenon occurs most likely due to the fact that an air flow is oriented against the wheel arch surface in this area due to the rotating wheel.

6.3.2 Numerical investigations

In contrast to the experiment, it is possible to carry out detailed investigations of the air flow situation within the wheel house with the aid of numerical simulations. Therefore, detailed flow field studies and analyses of the tire surface pressure will be discussed in the following in addition to the examinations of the surface pressure situation of the wheel arch.

The computational examinations are performed for all wheel rotation methods. In contrast to the experiment, where the measurement of the flow field was only possible for rims *Rim16*, the numerical simulations are carried out for the three rim geometries *Rim16*, *Rim17* and *Rim18*. For this study, several different analysis methods are used to describe the flow effects for the individual simulation cases. These methods are described below in the sections in which they are applied.

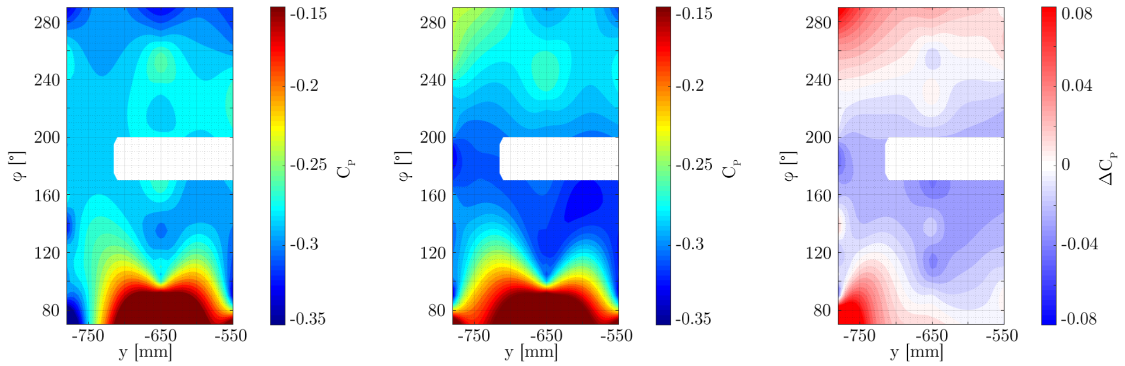

(a) *Rim16*

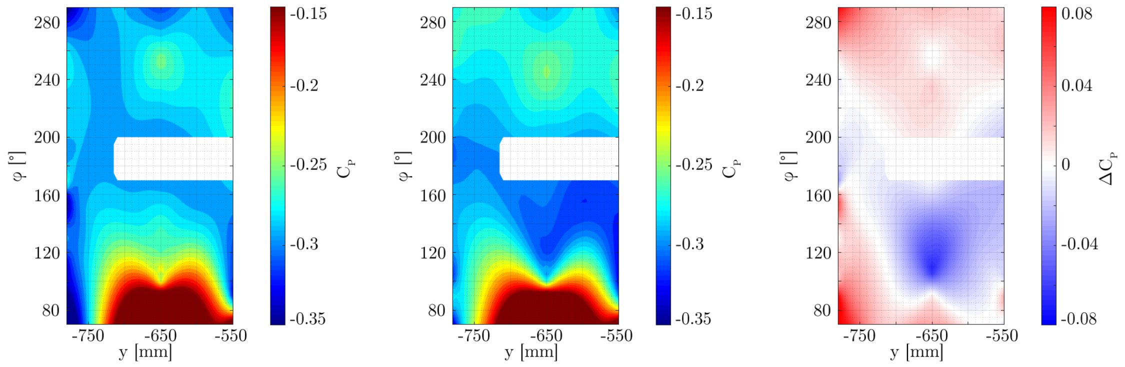

(b) *Rim17*

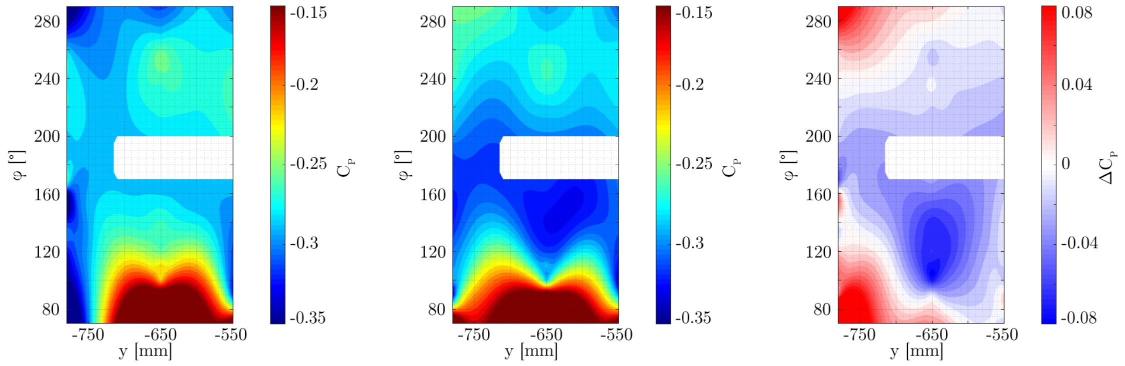

(c) *Rim18*

Figure 6.1: Pressure coefficient C_P at the wheel arch surface for *Rim16* (top), *Rim17* (center), *Rim18* (bottom). Stationary case (*WT.B.16/17/18.NR*) (left column), rotating wheels (*WT.B.16/17/18.RT*) (center column), and the differential analysis ΔC_P between both cases (right column).

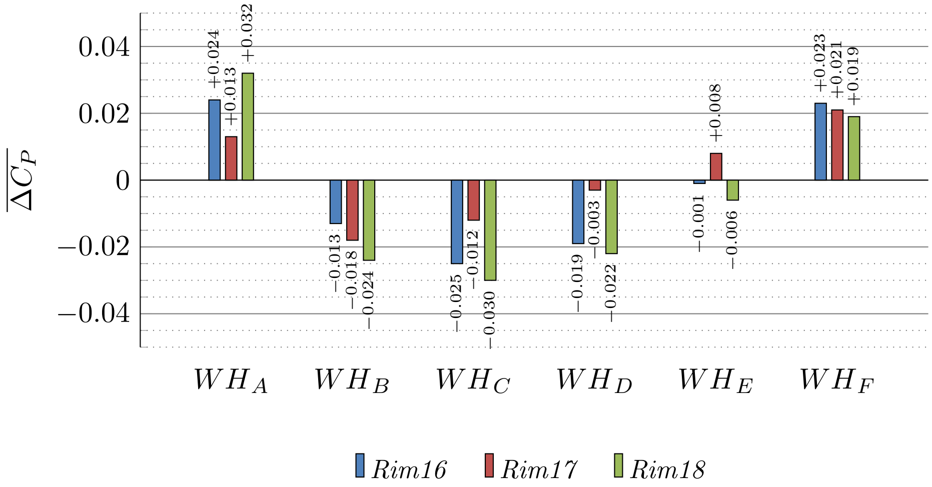

Figure 6.2: Mean deviation of the surface pressure coefficient $\overline{\Delta C_P}$ between stationary (*WT.B.16/17/18.NR*) and rotating wheels (*WT.B.16/17/18.RT*) for various sections of the wheel arch.

In the following, the highly complex air flow situation and the flow phenomena in the immediate vicinity of the wheel and within the wheel arch are presented, and the flow effects in the individual areas along the tire tread and the corresponding sections in the wheel arch are discussed. From an aerodynamic point of view, the region in proximity of the wheel can be divided into a lower section, outside of the wheel house, and an upper section, within the wheel arch. In the first part the air flow situation in the underbody region in close proximity to the wheel is analysed. These investigations consider the wheel section located between the vehicle underbody and the road, where the wheel is hit directly by the main flow, as well as the wake area downstream of the wheel. In the second part of this section, the air flow situation within the wheel arch is discussed. Finally, the results are validated with the findings of the experiment and other studies.

Air flow topology in the underbody region

In the following, visualization of the air flow topology and the surface pressure situation at the tire tread serves as a basis for the analysis of the flow topology in the underbody region and within the wheel arch. The complex flow situation is therefore illustrated by means of three-dimensional streamlines. The results are shown in Fig. 6.3, where the left column shows the wheel arch diagonally from the front, and the right column diagonally from behind. Tire and rim, as well as chassis and brake system geometries, are also considered, while the vehicle is rendered transparent. To allow for a more detailed analysis of the flow situation within the wheel arch, surface streamlines were calculated in *plane J*, which is positioned at the centerline of the wheel, i.e. at y = -780 mm (Fig. 6.4). The streamlines in both analyses are colored using the magnitude of the dimensionless velocity (Eq. (3.32)).

The surface pressure distribution on the tire tread is examined by means of a pressure study along the centerline of the tire surface. The applied analyses processes follow the methods described in Chapter 3.4.5. The results of this investigation are shown in Fig.

6.5, while the corresponding differential analysis between the individual rotation methods and the reference case with stationary wheels can be seen in Fig. 6.6. The corresponding results for simulation cases with Rim17 and Rim18 rims can be found in Appendix B.

To detail the impact of wheel rotation on the air flow situation in close proximity to the lower part of the wheel, the pressure distribution is investigated and discussed in a localized section of *plane E*, as well as in *plane J*. The analyses in *plane E* serve not only to characterize the flow situation within the wheel arch, but also to investigate the influence of wheel rotation on the wheel yaw angle, and furthermore the wake area of the front wheel. To illustrate the impact of wheel rotation on the air flow situation and to point out flow topology alterations in this area, differential analyses are performed on the results of both analysis planes, where the simulation case with stationary wheels serves as the reference. The results of the pressure distribution study in *plane E* are presented in Fig. 6.7, while the results of the differential pressure analysis are shown in Fig. 6.8. The respective stationary reference case is presented in Fig. 6.8a. The remaining figures illustrate the differential studies of the respective rotation methods. The results of the differential analysis in *plane J* are shown in Fig. 6.9, while the reference case is presented in Fig. 6.9a. Accordingly, the remaining figures illustrate the analyses for the individual wheel rotation methods. The representation of the pressure distribution in *plane J* has been omitted, since the changes in the flow topology are small and therefore hardly recognizable in this type of visualization.

The analysis results of the air flow topology within the wheel arch (Fig. 6.3) reveal that the frontal wheel surface is hit directly by the main flow from the gap between the road and the vehicle at a certain yaw angle due to displacement effects of the vehicle's front bumper geometry [21, 32]. As a result, the flow is divided into several partial flows, which are either directed around the wheel or up into the wheel arch. The parts of the air stream diverted to the sides of the wheel detach at the tire edges due to boundary layer separation and form two separation bubbles. These bubbles are stretched by the underbody flow and form two open, longitudinal vortices, the so-called *horseshoe ground vortex*, which extends downstream into the underbody region and the wake area of the vehicle [24, 37]. The effects of this flow phenomenon on the aerodynamic situation of the vehicle will be discussed in detail in Chapter 7.

In the surface pressure analysis of the tire tread (Fig. 6.5), the region of the tire surface hit directly by the mainstream in the underfloor gap corresponds to the angular range from $\varphi_{\text{wheel}} = 24°$, where the contact line of tire and road is located, to $\varphi_{\text{wheel}} = 60°$, from where the tire is covered by the wheel spoiler and the wheel arch. A pressure coefficient of $C_P = 1$ results for the stationary case at the contact line. This corresponds to the highest possible value of the pressure coefficient the vehicle surface without further energy input. However, the differential pressure analysis (Fig. 6.6) reveals that this value is higher by 0.05 for rotation methods that apply the *MW* approach to the tire tread than for the stationary reference case or *MRF*. However, detailed pressure investigations reveal a stagnation area with even higher pressure values of $C_P \simeq 2$ in localized region at the contact line with its center positioned slightly beside the tire centerline at y = -765 mm. A surface pressure coefficient greater than 1 results since the surfaces of the tire and the ground move toward each other and cause the air flow to accelerate in that direction, thus

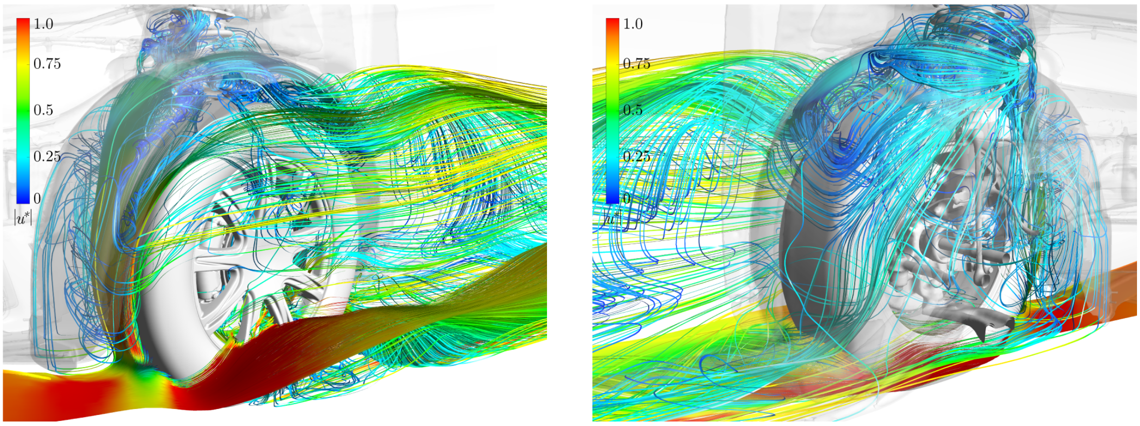

(a) NR

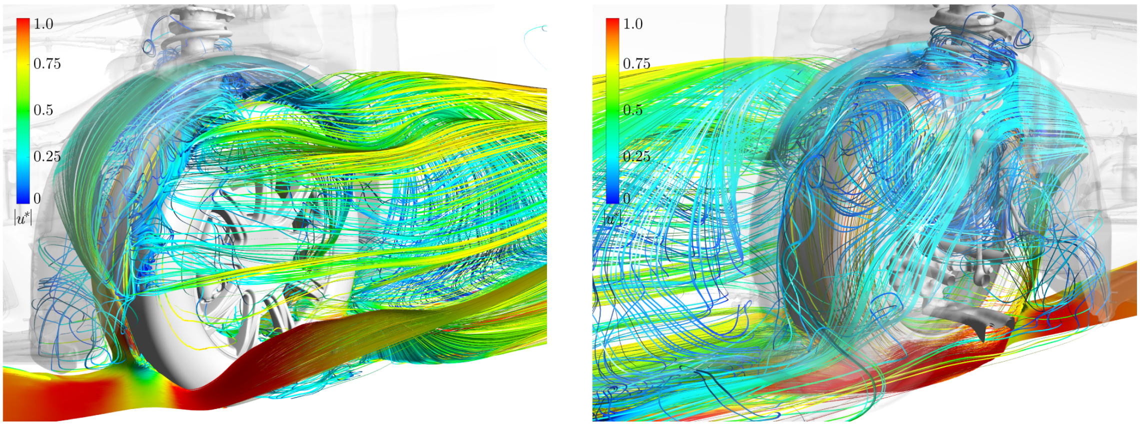

(b) MW

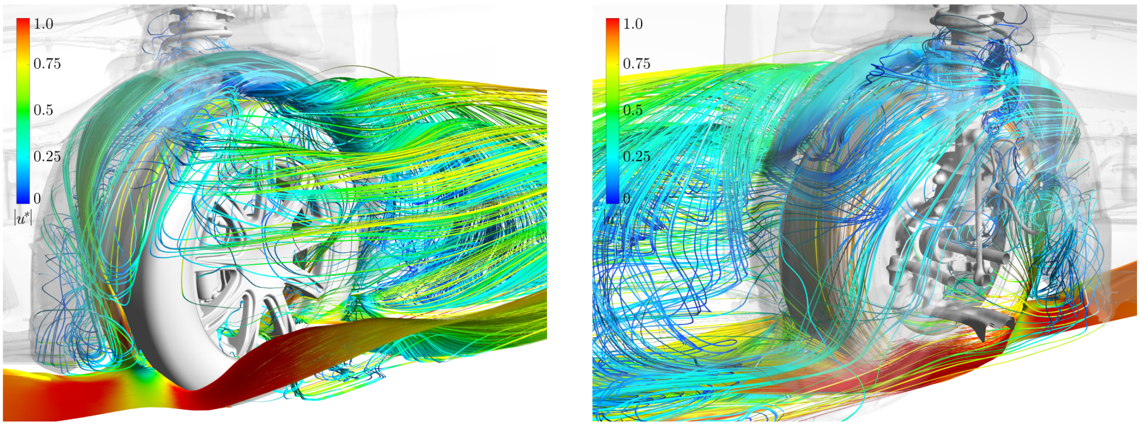

(c) MW-TO

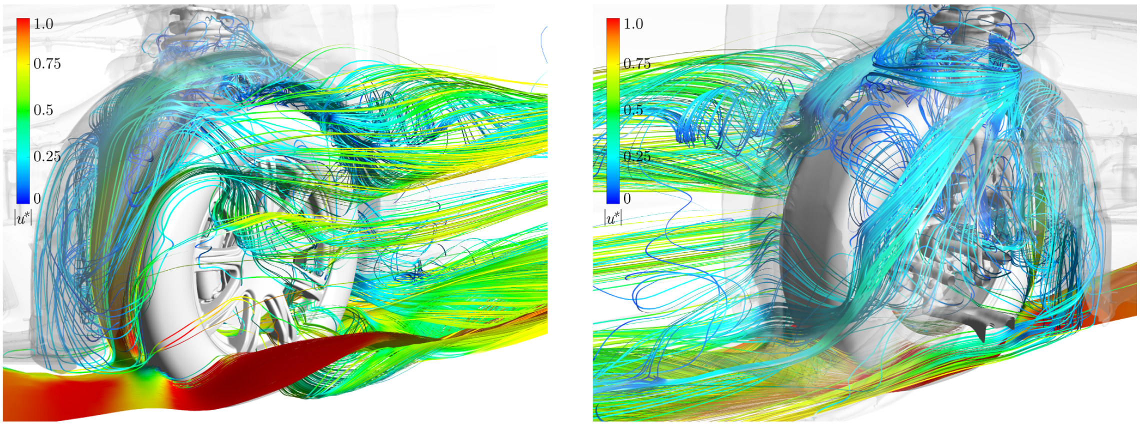

(d) MRF

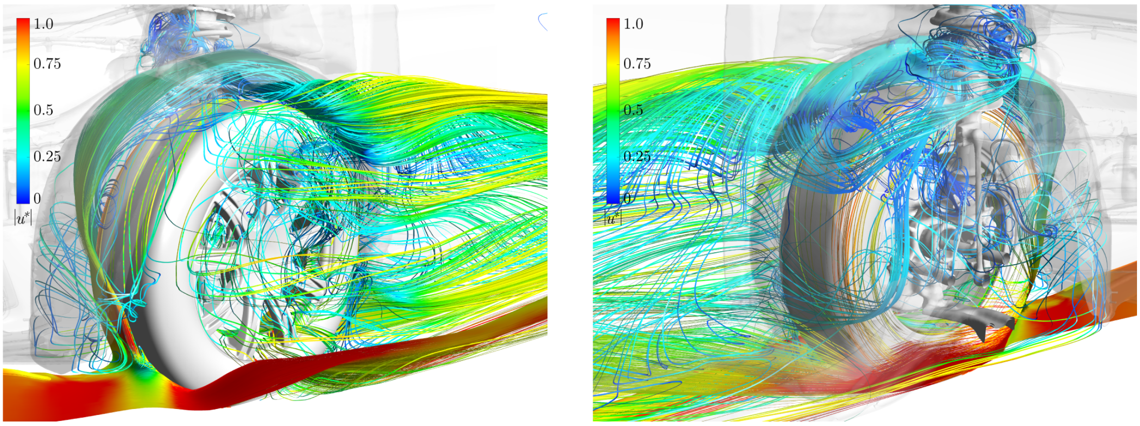

(e) MRF&MW

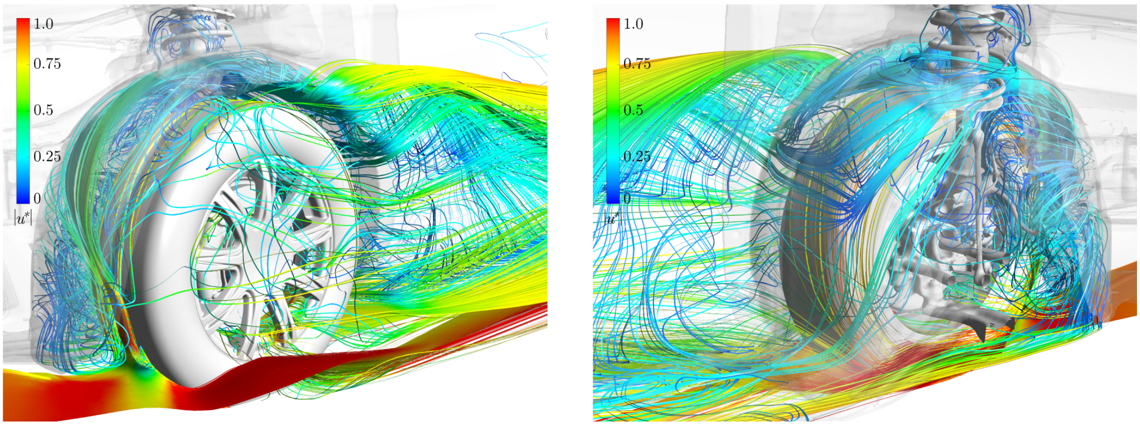

(f) MRF&MW-TO

Figure 6.3: Air flow topology within the wheel arch from front (left) and rear (right). Simulation cases *B.16.**.

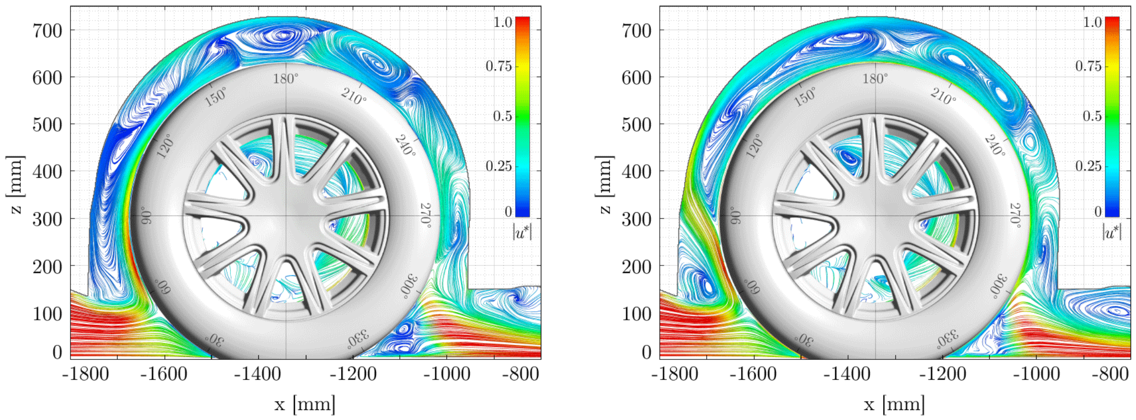

(a) NR (b) MW

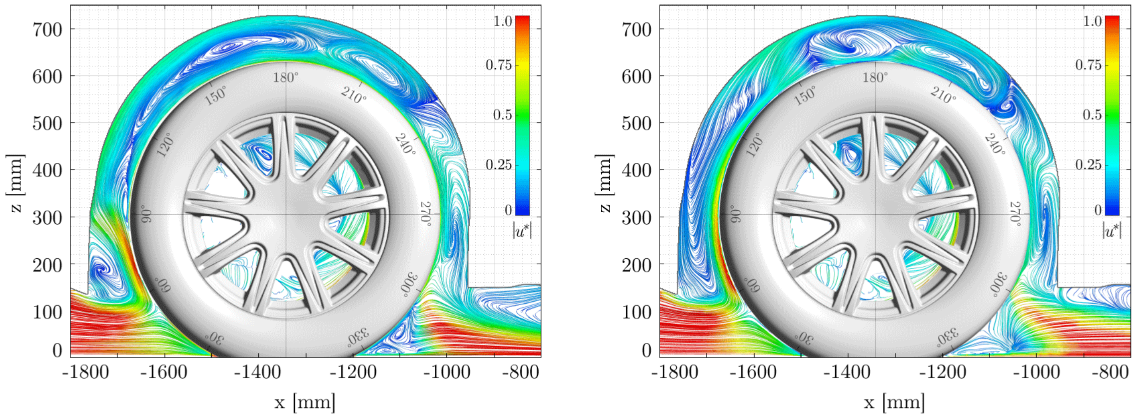

(c) MW-TO (d) MRF

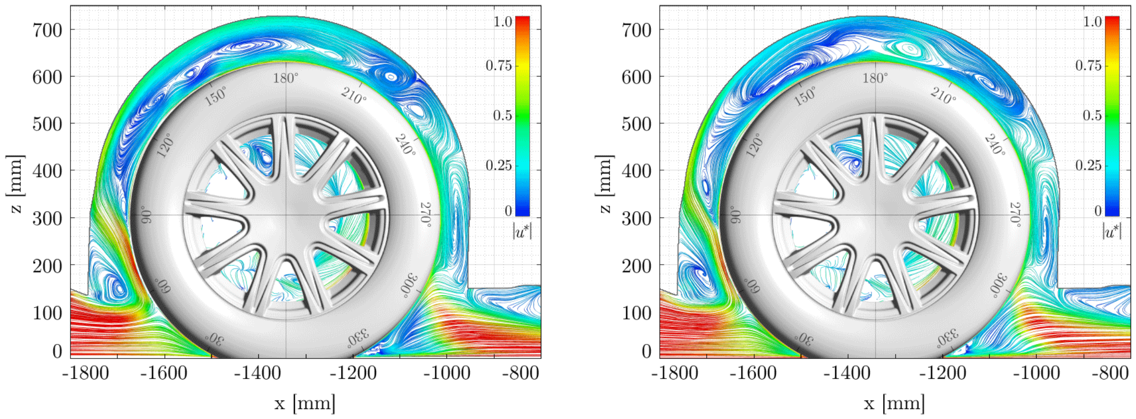

(e) MRF&MW (f) MRF&MW-TO

Figure 6.4: Air flow topology within the wheel arch in *plane J*. Simulation cases *B.16.**.

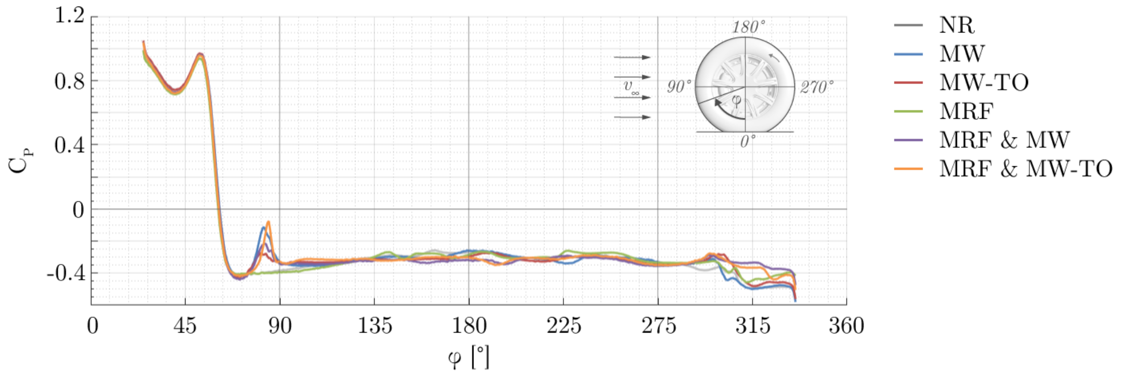

Figure 6.5: Pressure coefficient C_P at the tire tread along the centerline of the wheel. Simulation cases *B.16.**.

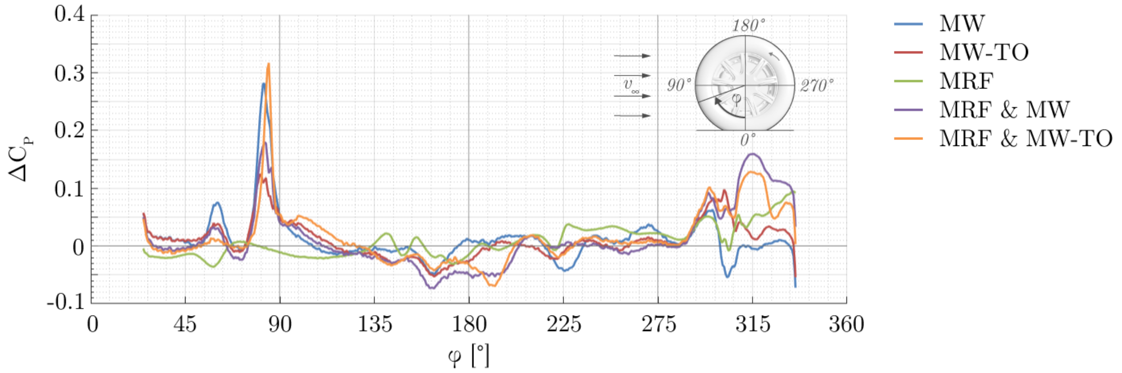

Figure 6.6: Pressure coefficient differences ΔC_P at the tire tread along the centerline of the wheel. Simulation cases *B.16.*-B.16.NR*.

introducing energy into this system and resulting in a total energy in this area that is higher than that of the free stream. These two flows collide at the contact line between the rotating tire and the moving road, greatly increasing the pressure locally in this region and forcing the air to a sudden lateral evasion. Due to this effect, the highest pressure coefficient values are detected at the contact line of tire and ground. This phenomenon, referred to as *jetting*, was postulated by Fackrell and Harvey [10].

Starting from the contact line between the wheel and the road, the pressure coefficient decreases for all simulation cases with increasing angle and reaches a local minimum with a value of 0.7 at $\varphi_{\text{wheel}} = 40°$, which is caused by air flow separation effects due to the inclined flow of the tire. At $\varphi_{\text{wheel}} = 55°$, a second local surface pressure maximum is approached. This point corresponds to the stagnation point of the free underbody flow at the tire surface, as can be seen in Fig. 6.4. The underbody air flow hits the surface obliquely at a certain yaw angle at this point, which results in a pressure coefficient slightly less than 1. The air flow approaching the tire above the stagnation point is deflected at high speed upwards into the wheel arch. In combination with the coverage of the wheels by wheel housing and spoiler, that prevent the direct approach of the free flow, this causes

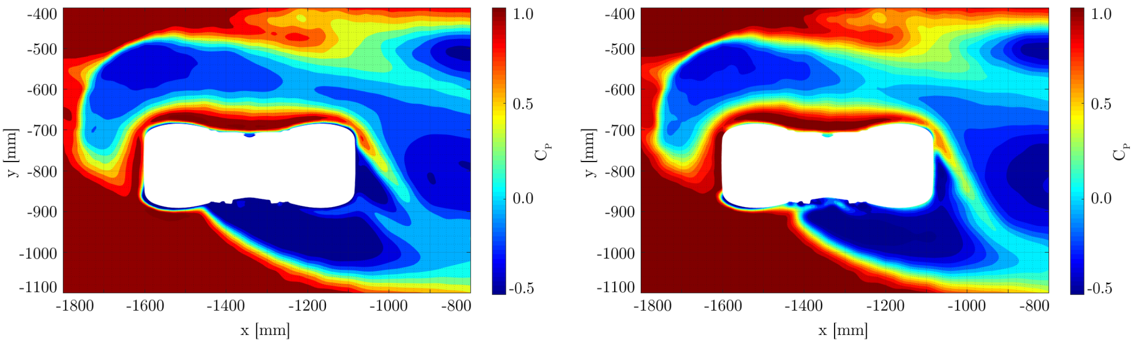

(a) NR

(b) MW

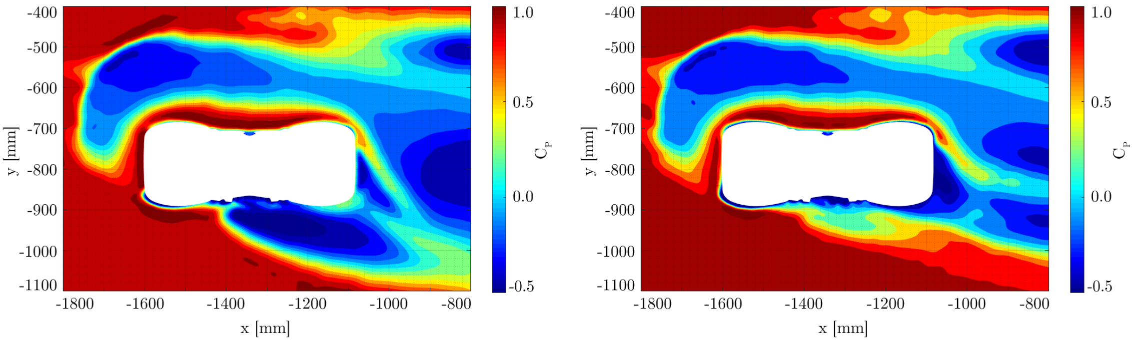

(c) MW-TO

(d) MRF

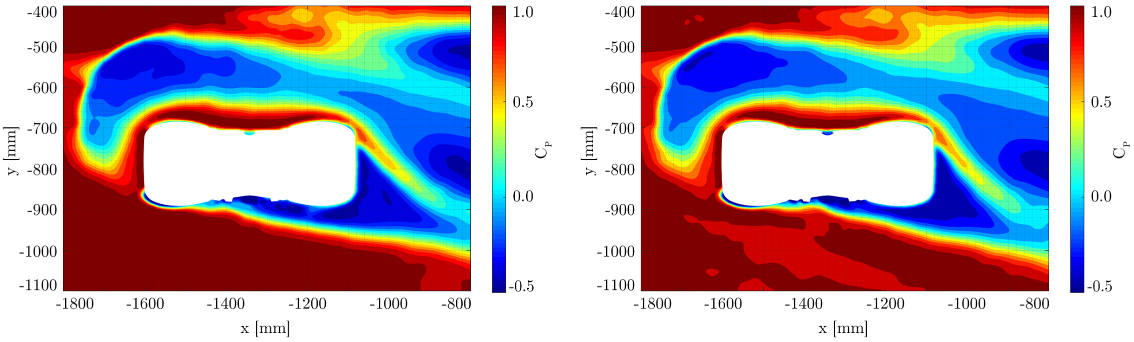

(e) MRF&MW

(f) MRF&MW-TO

Figure 6.7: Pressure coefficient C_P in the vicinity of the front wheel in *plane E*. Simulation cases *B.16.**.

a sharp drop of C_P to values below zero across the tire surface for angles higher than $\varphi_{\text{wheel}} = 55^\circ$ to a minimum at $\varphi\text{wheel} = 60^\circ$ for all rotation methods (Fig. 6.5).

Within the wake of the wheel i.e. in the gap between vehicle and the ground, starting at $\varphi_{\text{wheel}} = 290^\circ$, the tire surface pressure differential analysis (Fig. 6.6) reveals a pressure increase at the tire tread for all rotation methods in comparison to the stationary reference case. This observation implies flow topology alterations and, furthermore, a reduction of the detachment area due to wheel rotation.

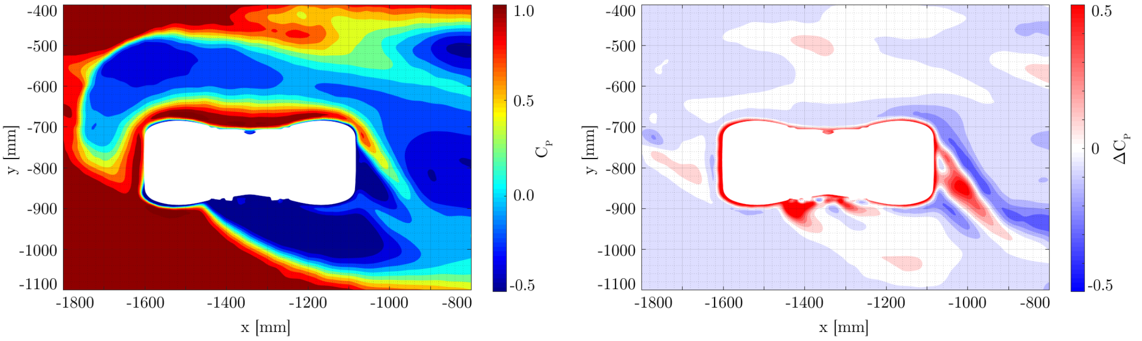

(a) NR

(b) MW

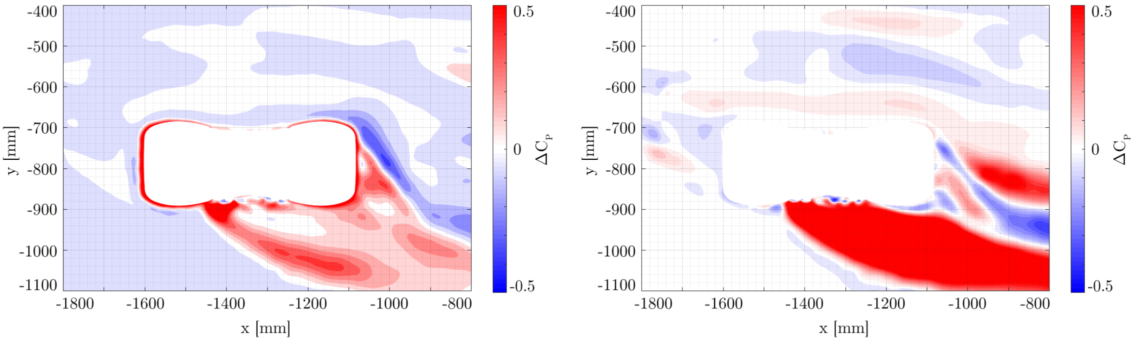

(c) MW-TO

(d) MRF

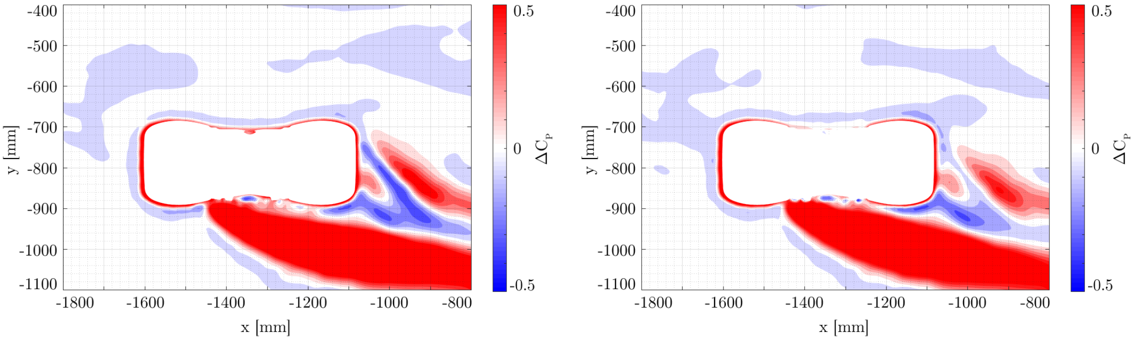

(e) MRF&MW

(f) MRF&MW-TO

Figure 6.8: Pressure coefficient differences ΔC_P against the stationary case (*B.16.**-*B.16.NR*) in the vicinity of the front wheel in *plane E*.

The analysis results of the wheel wake region in *plane E* (Fig. 6.8) and *plane J* (Fig. 6.9) confirm this assumption and reveal that the yaw angle of the air flow at the front wheel and thus the structure of the wake region laterally and downstream of the wheel has been modified in relation to the reference case due to rotating wheels. For *MW* (Fig. 6.7b), minor changes of the separation bubble structure occur, while with *MW-TO* (Fig. 6.7c) a reduction in the wake region is already evident. An increase in pressure directly behind the wheel can be detected for both methods through the differential analysis (Fig. 6.8). However, for load cases using the *MRF* approach, i.e. *MRF* (Fig. 6.7d), *MRF&MW* (Fig. 6.7e), as well as *MRF&MW-TO* (Fig. 6.7f), alterations of the wheel wake structure are

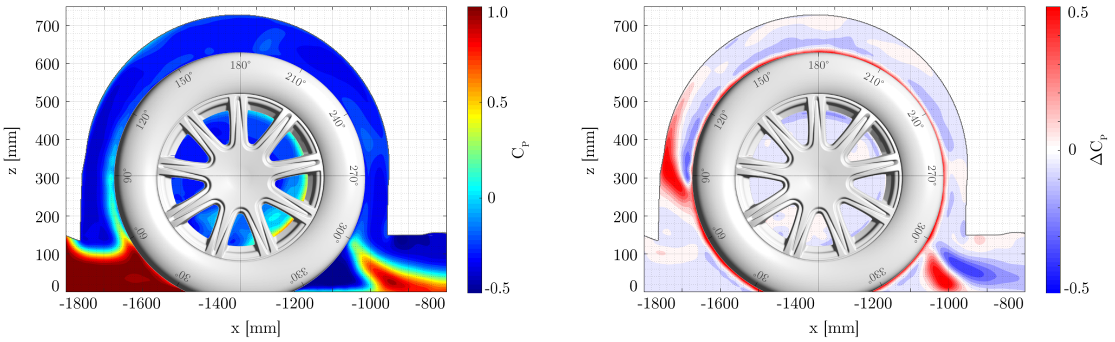

(a) NR

(b) MW

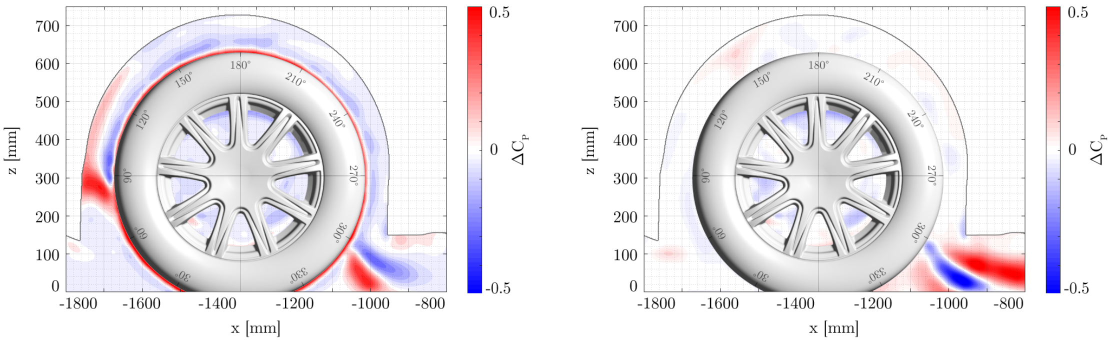

(c) MW-TO

(d) MRF

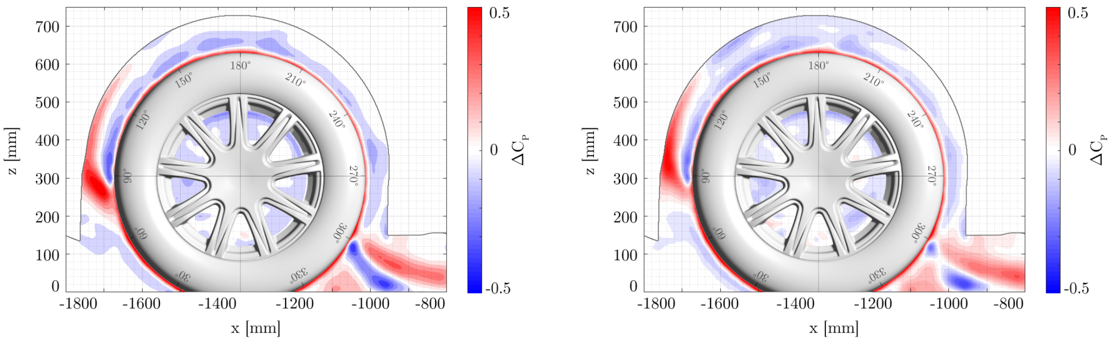

(e) MRF&MW

(f) MRF&MW-TO

Figure 6.9: Pressure coefficient differences ΔC_P against the stationary case (*B.16.*-B.16.NR*) within the wheel arch in *plane J*.

evident. For these three load cases, the detachment area has shifted from the wheel side to the area downstream the wheel, and has also decreased in size. In particular *MRF* shows a significantly reduced low pressure area downstream of the rotating wheel. The impact between the individual rotation methods becomes obvious through comparison of the resulting flow fields of *MW* and *MRF* and reveal that the detachment area for *MW* shows many more similarities to the stationary case than *MRF*. On the basis of the results it is possible to conclude on a flatter yaw angle relative to the vehicle center line in y-direction for rotating wheels in comparison to the stationary case, in particular for the *MRF* approach and both combined rotation methods *MRF&MW* and *MRF&MW-TO*. Depending on the applied rotation method, rotating wheels therefore have a decisive impact on the wheel yaw angle, and thus on the separation area and the pressure situation, as well as the flow topology in the vicinity of the wheel.

At $\varphi_{\text{wheel}} = 295°$ (Fig. 6.5), a pressure peak can be detected for all simulation cases, which is followed by fluctuations and raised surface pressure as the angle increases. These observations are indicative of the structural alteration in the wheel wake topology. The results of the differential pressure analyses in Fig. 6.8 and Fig. 6.9 support this finding and reveal a shift in the wake area due to an altered outflow behavior of the underbody flow downstream of the wheel into the main flow next to the vehicle. These changes are apparent for *MW* and *MRF*-based rotation methods. With increasing angles up to $\varphi_{\text{wheel}} = 315°$, the pressure at the wheel surface rises due to the changed flow topology and the resulting reduction of the wheel wake structure, especially for *MRF*-based rotation methods.

At the rear contact line between the wheel and the ground, at $\varphi_{\text{wheel}} = 336°$, a strong negative pressure gradient is noticeable for all *MW*-based rotation methods. At this position, the pressure coefficient drops sharply and likewise represents the global minimum at the tire tread. This alteration corresponds to the *rear jetting* phenomenon [10, 11, 14] and can be attributed to the rotational movement of the tire tread that accelerates air from the contact area along the rotation direction of the wheel, reducing the pressure in this region. Due to the lack of a rotating tire surface for *MRF*, this effect cannot be determined for this approach.

The two combined rotation methods *MRF&MW* and *MRF&MW-TO* show flow phenomena that were observed either for *MW* or *MRF*. Thus, the *MW* typical local pressure increase at the contact line of tire and road upstream of the wheel, as well as a negative pressure peak downstream of the wheel can be recognized. However, the wake area of the wheels corresponds to that of the *MRF* simulation case.

Air flow topology within the wheel arch

In the previous section it was shown that a part of the air stream resulting from the separation at the front tire surface is directed up into the wheel arch. Subsequently, this sub-stream will be investigated, and the flow situation within the wheel house will be discussed for various wheel rotation approaches. This study is primarily based on the analysis of the air flow topology through three-dimensional streamlines and the surface pressure distribution at the tire tread and at the wheel house shell, as well as on the analysis of the pressure situation in the gap between tire tread and wheel arch surface. To examine the pressure situation at the tire surface, the results of the pressure distribution along the center-line of the tire tread (Fig. 6.5) and the corresponding differential analysis (Fig. 6.6) from the previous section are used. The surface pressure distributions at the wheel arch are shown as contour plots in Fig. 6.10, while the results of the associated differential analysis are illustrated in Fig. 6.11. Fig. 6.11a corresponds to the reference case with stationary wheels, and the remaining lots represent the results of the differential analysis of the respective wheel rotation methods.

Due to the effects and flow phenomena within the wheel arch, the rotation methods can be classified into two groups. On the one hand, these are the methods which apply the

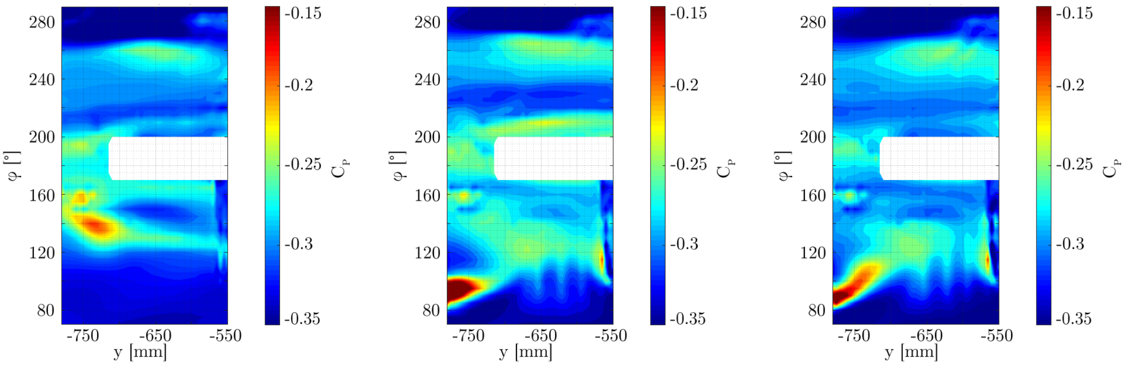

(a) NR (b) MW (c) MW-TO

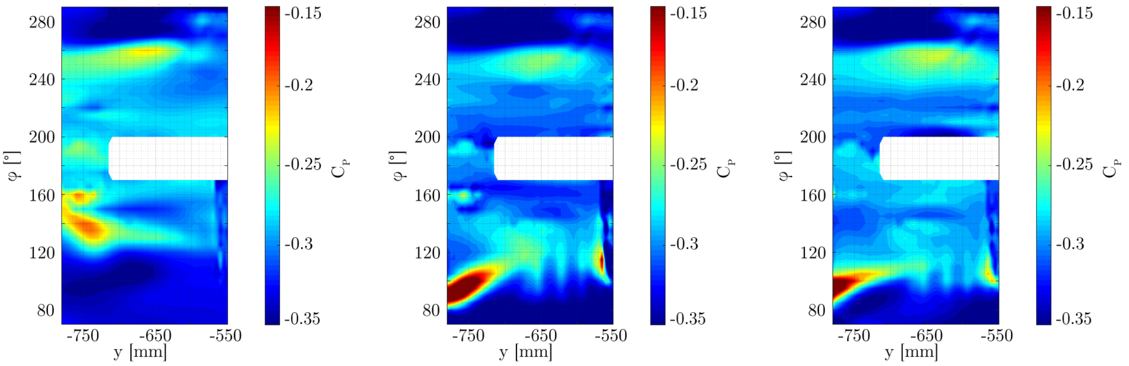

(d) MRF (e) MRF&MW (f) MRF&MW-TO

Figure 6.10: Pressure coefficient C_P at the wheel arch surface. Simulation cases *B.16.**.

MW approach to the tire tread, and, on the other hand, those methods that do not, which pertains to the stationary reference case and the *MRF* method. Accordingly, the flow situation of these two groups will be discussed seperately below. The two combined rotation methods, i.e. *MRF&MW* and *MRF&MW-TO*, are examined at the end of this section.

The analysis of the flow topology (Fig. 6.3 and Fig. 6.4) reveals for simulation cases with stationary tire surface, i.e. the reference case and *MRF*, that the upward-directed portion of the air flow centrifugally detaches due to inertia effects from the tire treat in the upper part of the wheel at approximately $\varphi_{\text{wheel}} = 130°$ and eventually hits the wheel arch surface. This is indicated by two localized pressure peaks at the wheel arch between $\varphi_{\text{WH}} = 140°$ and $\varphi_{\text{WH}} = 160°$ (Fig. 6.10a and Fig. 6.10d).

In contrast, the analysis of the flow topology for the second group, that are all rotation methods rotating the tire tread by means of the *MW* approach, reveals an altered detachment behavior from the tire surface. These simulations predict an earlier separation of the flow from the rotating tire tread than it is the case for the stationary one, as shown in Fig. 6.3b representative for the *MW* case. The air flow separation phenomenon can be attributed to the rotational movement of the tire tread through the *MW* method, which accelerates the air according to the running direction forward into the anterior region of

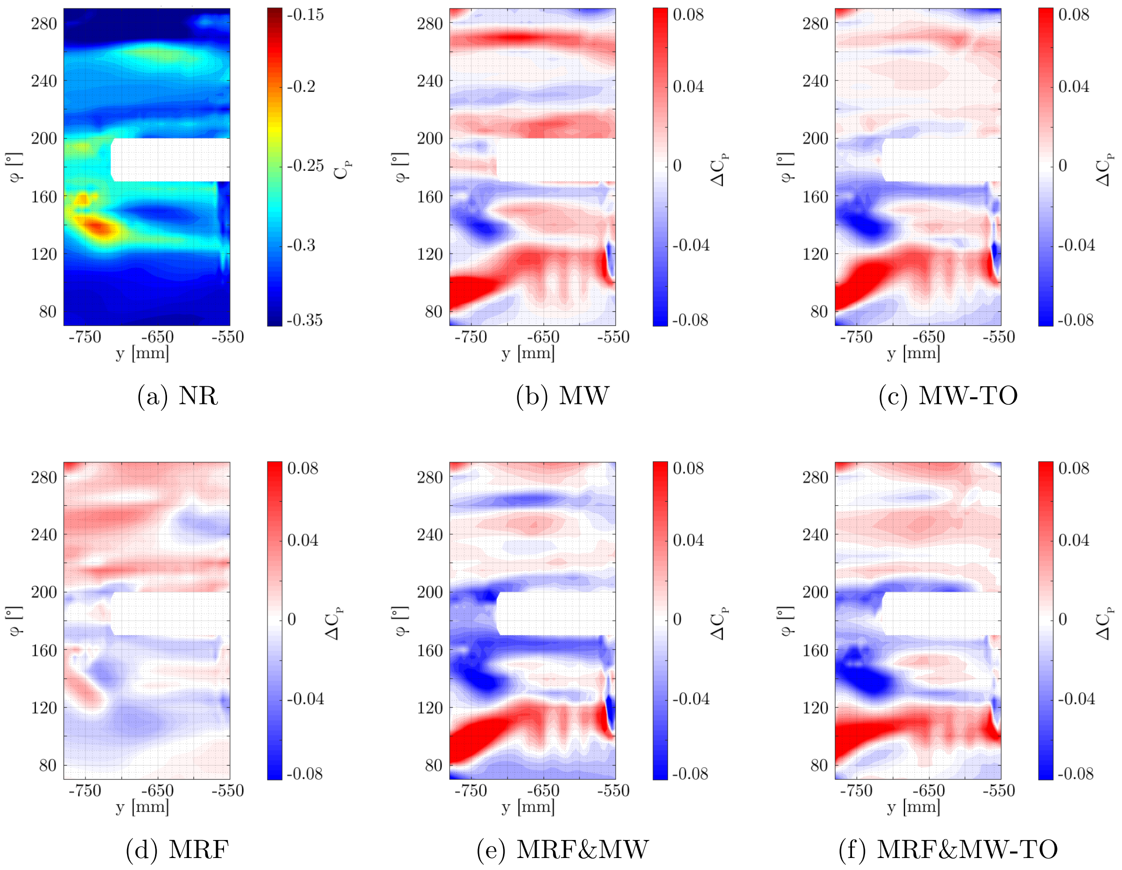

(a) NR (b) MW (c) MW-TO

(d) MRF (e) MRF&MW (f) MRF&MW-TO

Figure 6.11: Pressure coefficient differences ΔC_P at the wheel arch surface. Simulation cases *B.16.*-B.16.NR*.

the wheel arch. As a result, the forward accelerated air from the top of the wheel arch hits the incoming air stream from the underbody in front of the wheel at $\varphi_{\text{wheel}} = 80°$ (Fig. 6.4b). For this reason the surface pressure analysis on the tire tread (Fig. 6.5 and Fig. 6.6) shows a pressure peak at $\varphi_{\text{wheel}} = 80°$, in contrast to the *MRF* method and the stationary case. This is the contact area between the upward deflected main flow and that air flow which is accelerated by the wheel against it, resulting in the formation of a strong shear layer. The upward orientated air stream loses momentum and separates from the rotating wheel surface, consequently lowering the local surface pressure for increasing angles. This type of flow separation is referred to as *Moore-Rott-Sear* (MRS) separation [88]. The analysis of the pressure situation in close proximity to the wheel in *plane J* (Fig. 6.9), as well as the visualization by streamlines (Fig. 6.3 and 6.4) reveal that the separated flow is eventually accelerated against the front wheel arch wall. A region with locally increased pressure can be detected in front of the wheel arch between $\varphi_{\text{WH}} = 80°$ and $\varphi_{\text{WH}} = 120°$ (Fig. 6.10 and Fig. 6.11). Furthermore, in the region between the upward-directed air flow and the front surface of the wheel housing shell, a low-pressure recirculation area, the so called *spoiler tip vortex*, can be observed, which arises due to the flow separation at the lower edge of the spoiler at the wheel arch liner. In consequence of the altered flow separation at the tire tread, the structure of this vortex is affected, and its size is reduced.

Since the tire rotation is not taken into account for the *MRF* method, the effect of early flow separation and the consequent structural change of the spoiler tip vortex is not recognizable for this simulation approach.

Continuing along the top and back of the tire tread, for angles between $\varphi_{\text{wheel}} = 90°$ and $\varphi_{\text{wheel}} = 270°$ (Fig. 6.5), the pressure coefficient remains negative for all rotation methods and the stationary case and fluctuates around $C_P = -0.3$. Due to the lack of flow separation, the surface pressure at *MRF* is higher over large parts of the wheel than in the case of rotating methods with moving tire tread. The uniform surface pressure distribution in the upper part of the tire can be attributed to the influence of the wheel spoiler on the underbody flow, which directs the air flow towards the centerline of the vehicle. Therefore, the air is not caught in the wheel arch, which results in this negative, evenly distributed pressure coefficient [28].

The analysis of the stream lines in *plane J* (Fig. 6.4) reveals that the air flow, which separates from the tire surface and is directed into the upper wheel house region, streams in clockwise direction along the wheel arch surface into the rear area of the wheel house for all rotational methods and the stationary case.

For *MW*-based simulation cases, a thin layer of air is recognizable in close proximity to the wheel, which is accelerated according to the tire surface rotation counterclockwise in the forward region of the wheel arch. Due to the interaction of these two oppositely oriented flows, several vortex structures are detected in the area between both streams, especially in the angular range between $\varphi_{\text{wheel}} = 100°$ and $\varphi_{\text{wheel}} = 230°$. This vortex formation results due to flow velocity deviations and the resulting shear layer at the interface of the two divergent accelerated air currents (*Kelvin-Helmholtz Instability* [89, 90]). The interaction of the flow with the counter-rotating tire tread, which introduces kinetic energy into this system, results in a pressure increase in close proximity to the tire surface, as shown through the differential pressure analysis in *plane J* (Fig. 6.9).

Multiple vortex structures can be recognized along the area between the tire tread and the wheel arch for both the *MRF* method and the stationary reference case (Figs. 6.4d and 6.4a). These structures develop also due to shearing movements at the interface between the backward accelerated air flow and the stagnant air layer near the stationary tire surface against which it is being accelerated. These vortex structures have larger geometrical dimensions than those in simulation cases with rotating tire tread, since no air flow exists that streams along the tire surface into the front wheel house region. Further differences of the vortex structure between MW-based rotation methods and approaches with stationary tire surface can be detected in the front area due to the different separation point of the flow from the tire surface which affects the shape of the spoiler tip vortex.

For the stationary case, the wheel arch vents into the underbody (Fig. 6.4a), as well as laterally into the main flow next to the vehicle. The latter happens from the gap between the vehicle and the tire surface along the entire wheel arch, i.e. in the front as well as in the rear area (Fig. 6.3a).

For *MW*-based rotation approaches, air ventilation occurs at the rear portion of the wheel arch into the underbody (Fig. 6.4b and 6.4c), as well as at the upper rear area laterally into the main flow (Figs. 6.3b and 6.3c). An outflow from the frontal region of the wheel arch into the underbody or in the lateral mainstream could not be observed.

The outflow behavior of the *MRF* method resembles the stationary case and takes place in the front and in the rear area of the wheel house sideways into the main flow (Fig. 6.3d) and also from the rear area into the underbody (Fig. 6.4d). Due to the lack of surface rotation of the tire, outflow from the rear can be observed closer to the floor than it is the case for rotating tire tread. Furthermore, a part of the air ventilating into the underbody is deflected downstream of the wheel into the main lateral flow.

The two combinations *MRF&MW* and *MRF&MW-TO* show again the individual flow phenomena characteristic of both *MW* and *MRF*. The resulting air flow topologies for *MRF&MW* (Figs. 6.3e and 6.4e) and *MRF&MW-TO* (Figs. 6.3f and 6.4f) are similar to that of *MW* (Figs. 6.3b and 6.4b) or *MW-TO* (Figs. 6.3c and 6.4c), but resemble also that of *MRF* (Figs. 6.3d and 6.4d), especially downstream of the wheel in its wake area. The pressure increase in the front region between $\varphi_{\text{wheel}} = 50°$ and $\varphi_{\text{wheel}} = 120°$ (Fig. 6.5), that is typical for *MW* and *MW-TO* and which is caused by early flow separation, becomes apparent for both, *MRF&MW* and *MRF&MW-TO*. The presence of this effect is furthermore confirmed by the surface pressure analysis of the wheel arch liner (Fig. 6.10 and Fig. 6.11). In addition, the significant increase in pressure over wide areas of the rear wheel surface at $\varphi_{\text{wheel}} > 250°$, which could only be detected for the *MRF* method, can also be observed. Furthermore, the differential pressure analysis in *plane J* (Fig. 6.9) shows the *MW*-distinctive pressure increase in close proximity to the tire tread over a wider area of the upper wheel surface. From these observations it can be concluded that the flow phenomena caused by the two rotation groups *MW* and *MRF* are additive to a large extent and can therefore be observed with both combined rotation methods *MRF&MW* and *MRF&MW-TO*.

The numerical results are validated with the experiment on the basis of the surface pressure data of the wheel arch liner (Fig. 6.1 and Figs. 6.10, 6.11), since only these experimental data is available. However, this examination is challenging, since the geometrical resolution of the experimental data is lower due to the limited number of pressure probes than it is for the simulations, where the pressure values at every single cell of the surface mesh can be considered for the analysis.

In the experiment, a pressure increase in the front, outer area of the wheel arch shell was detected at approximately $\varphi_{\text{WH}} = 90°$ and y = -780 mm, which indicates an early detachment of the upward directed flow from the rotating tire tread, and, consequently the impact of this stream on the wheel arch liner surface at this location. However, the measurement results indicate a larger area with increased pressure and not a local pressure peak, as the simulations predicted. Since the simulations have shown that this is a very localized effect, it is possible that this pressure peak is present, but could not be resolved due to the limited geometric resolution capacity of the probes in this area.

Furthermore, all rotation approaches predict a surface pressure reduction over large areas in the upper region of the wheel arch liner, in accordance with the results of the experiment. The numerical results also reveal that these regions are pervaded by small areas of increased pressure. This observation could not be confirmed in the experiment, which in turn could be attributed again to the low resolution capacity.

Finally, an increase in pressure in the rear of the wheel arch liner, downstream of the wheel, could be detected for all rotation methods, which thus corresponds to the results of the measurement. This pressure increase is most noticeable for the *MRF* method. The pressure areas contain also small, local areas with reduced pressure, which could not be located in the experiment.

6.4 Impact of wheel rotation on rim air mass flow

In the previous sections, the flow topology in the wheel house was investigated, and the differences between *MW* and *MRF* were discussed. Finally, in this part of the chapter, the impact of individual wheel rotation approaches on the flow behavior through the rims is investigated. For this purpose, the mass flow rates through front and rear rims are first examined. Based on these results, differential analyses are performed subsequently and alterations to the stationary reference case are presented.

The calculation of the total air mass flow rates through the rims, i.e. between the spokes, were accomplished through integration of the mass flux over the open surface area of each rim, according to the process described in Chapter 3.5.9. Since the rims have different geometries, and therefore also different open areas, an additional variable is introduced in order to achieve a better comparability between individual rims. For this purpose, the measured air mass-flow rate was normalized by the open surface area between the spokes of each rim according to

$$\dot{m}'_{RIM} = \frac{\dot{m}}{A_{RIM}} \tag{6.1}$$

where $\dot{m}'$ is the rim air mass flux and A_{RIM} is the open rim area.

The open area was measured for each rim using CAD data and the results are shown in Table 6.1.

Rim	A_{RIM} $[m^2]$
Rim16	0.1286
Rim17	0.1529
Rim18	0.1690

Table 6.1: Open area between the spokes of the individual rim geometries.

In order to quantify the mass flux alterations, differential values were calculated according to the following equation, using the stationary case as a reference:

$$\Delta\dot{m}'_{RIM} = \dot{m}'_{RIM,rot} - \dot{m}'_{RIM,stat} \tag{6.2}$$

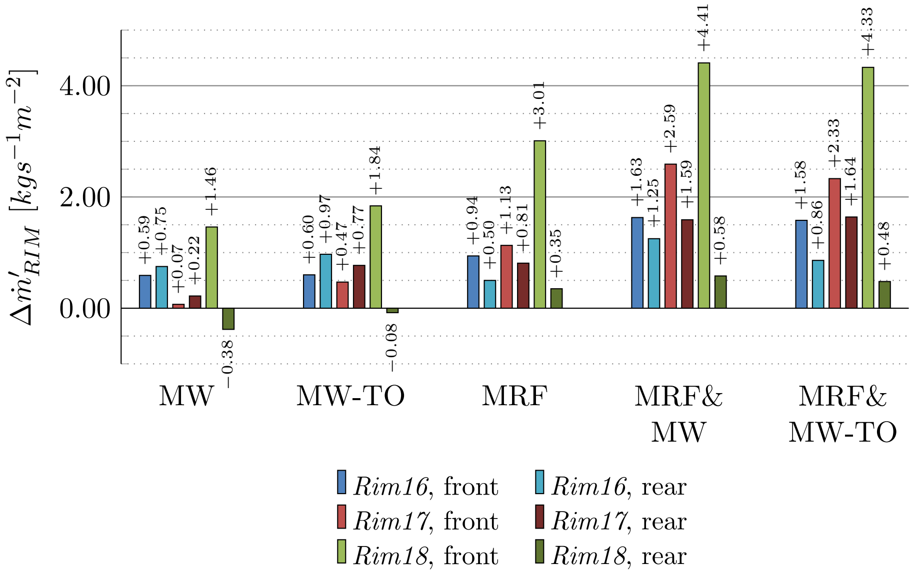

Figure 6.12: Rim air mass flux differences $\Delta\dot{m}'_{RIM}$. Simulation cases B.16.*-B.16.NR.

where $\dot{m}'_{RIM,rot}$ represents the rim air mass flux for a setup with rotating wheels, and $\dot{m}'_{RIM,stat}$ is the reference case with stationary wheels.

The differential analysis is carried out separately for the two front and rear rims, and the results are summed for each wheel group. The resulting air masses are shown in Fig. 6.12.

The analysis results reveal that all rotation methods affect the air mass flux through front and rear rims. The magnitude of these alterations depends on the rim geometry, and therefore also on the open rim area. By applying wheel rotation boundary conditions to the front wheels, air mass-flow rates are always increased into outward direction, independent of the rotation method. The impact of this effect is stronger for the *MRF*-based rotation methods, i.e. *MRF*, *MRF&MW* and *MRF&MW-TO*. The most significant impact on the air mass-flow rates show the combinations *MRF&MW* and *MRF&MW-TO*. The mass-flow rates through the rear rims are also increased into outward direction for most simulation cases. However, exceptions are the *MW* and *MW-TO* configurations of *Rim18*, where the mass flow rate is slightly decreased against to the stationary case. It was furthermore observed that the *MRF* approach increases the air mass flow rate through the front wheels more than through the rear wheels.

6.5 Synopsis

In this study, the impact of rotating wheels on the aerodynamic situation within the wheel arch and in the wake of the front wheel were examined experimentally and numerically for the test vehicle. For this purpose, the flow topology in the vicinity of the wheel, as well as the surface pressure distribution at the tire tread and at the wheel arch, were investigated.

In the first part of this study, experiments were carried out in the wind tunnel to analyse the effects of the rotating wheels on the air flow behavior in the wheel house, and to generate reliable measurement data for the validation of the numerical results. The analysis of the surface pressure situation in the wheel arch shell shows pressure increases close to the underbody gap in the frontal and the rear areas, which occurs most likely due to the rotating wheels that accelerate air against these wheel arch surface regions. These results are consistent with observations from the experiments made by Landström et al. [38], who also observed a pressure increase at these wheel house regions. Furthermore, pressure reductions over large parts of the upper wheel arch region could be detected in accordance with the experiment and also with the results of Landström et al. [38] and Wäschle [37].

Subsequently, the effects of the individual rotation methods on the flow situation within the wheel arch were numerically investigated. The computational results revealed alterations of the flow topology in the underbody gap between the vehicle and the road, as well as in close proximity to the wheel in the entire wheel arch, in comparison to the stationary reference case. In particular affected by rotating wheels was the flow situation in the ground-level region of the wheels, including the wheel wake structure along with the ventilation behavior of the wheel arch into the lateral mainstream and into the underbody flow. The origin of these changes could be attributed, on the one hand, to the different yaw angle of the air flow at the front wheel, as well as the altered separation behavior of the flow along the moving tire tread, in particular in the frontal region of the tire. On the basis of the observed flow effects, the individual wheel rotation methods can be divided into three groups, which are the *MW*-based methods (*MW* and *MW-TO*), the *MRF* method, as well as the two methods that use a combination of the first two groups (*MRF&MW* and *MRF&MW-TO*). Furthermore, a distinction was made between the area in the underbody gap and that within the wheel house.

Underbody region and wheel wake area

The analysis of the flow situation in the underbody gap between the vehicle and the road has revealed the following findings.

- The main flow that hits the frontal tire tread directly is split into three sub-flows, where two streams are directed laterally around the wheel and the third part is deflected along the tire surface upwards into the wheel arch.
- A rotating tire surface is required in order to correctly reproduce the *front and rear jetting* phenomena, which emerge as a positive pressure peak with $C_P > 1$ upstream and as a negative peak downstream of the wheel at the contact line of the tire with the ground in accordance with the predictions and results by Fackrell and Harvey, among others [10, 13, 15, 16, 19, 20, 28]. A moving tired tread is only considered numerically through application of the *MW* approach (*MW* or *MW-TO*) to the tire surface.
- The structure of the wake region of the front wheel is affected by all rotational methods, where a distinction could be made between the two groups of *MW*- and *MRF*-based rotation methods. This impact can be attributed to the changed flatter yaw angle of the air stream on the tire, and thus also to the altered flow direction of the underbody stream into the lateral main flow, as well as to the resulting outflow

and venting behavior from the wheel arch. These results correlate with the findings of Wiedemann [32], who measured experimentally both a reduction of the front wheel yawing angle due to wheel rotation, and furthermore an increase in pressure in the wake of the front wheels.

- A local pressure increase in the wake region close to the wheel could be observed for all rotation methods, which corresponds to the statements of Mercker et al. [5], Wiedemann [32] and Elofsson and Bannister [34].

Wheel arch

The studies on the impact of the rotating wheels on the flow topology within the wheel arch has led to the following findings.

- The portion of the main flow hitting the tire and is directed upwards into the wheel house detaches tangentially from the curved tire tread in the upper region of the wheel arch due to inertial effects and consequently impacts at the wheel arch liner surface for the stationary reference case. This separation behavior of the flow from the tire tread is identical to the *MRF* method. For *MW*-based rotation methods, however, this air flow meets those air masses which are accelerated forward from the rear and top of the wheel arch by the rotational movement of the tires which yields the formation of a strong shear layer. Due to the resulting loss of momentum, the flow detaches from the tire tread (*MRS* detachment [88]) and, unlike the stationary case, is accelerated against the front and not against the upper wheel house wall, resulting in a local pressure increase in this area. Due to the altered flow direction a pressure reduction in a localized region in the upper wheel house occurs. It can be concluded that the tire rotation has a decisive impact on the separation behavior of the flow from the tire surface. These observations corroborate the findings of Fackrell and Harvey [11] or Régert and Lajos [24], who were able to detect earlier flow separation on the tire tread of an isolated wheel due to its rotational motion.
- The air flow is directed along the wheel arch surface further into the upper and rear area of the wheel house, regardless of the applied rotation method. In this area the flow approaches a stream which is either accelerated in the opposite direction due to the rotation of the tire tread (in the case of *MW*-based rotation methods), or which is at rest due to a stationary tire surface (in case of *MRF* or the stationary reference). In both cases several vortex structures develop in the gap between the tire and the wheel housing shell due to the velocity divergence of these two flows and the resulting shear layer at their interface (*Kelvin-Helmholtz Instability* [89, 90]).
- The rotational movement of the tire surface results in flow separations along the entire tire tread for *MW*- and *MW-TO*-based simulation cases.
- The surface pressure increase in the frontal wheel house area and the corresponding pressure reduction in the upper region, which results from the altered separation location of the air flow from the tire tread for *MW*-based simulation cases, was also detected experimentally. However, the measurement results indicate a larger area with increased pressure, not a local pressure peak, as the simulations predicted. This divergence may be attributed to a low spatial resolution of the measurement probes in the experiment.

- Pressure reductions over large regions of the upper part of the wheel arch shell, as well as pressure increases in the rear area were observed for all rotation methods and thus correspond to the results of the experimental findings of Dimitriou and Klussmann [28]. However, these pressure alterations are less developed for the *MRF* approach, which surface pressure distribution resembles in many areas those of the stationary case, than of *MW*-based simulation cases.

Further observations

In addition, the following findings were obtained from the results.

- Both combined rotation methods, *MRF&MW* and *MRF&MW-TO*, show the flow effects predicted by *MW*- and *MRF*-based simulations. The for *MW* typical phenomena of early flow separation, especially at the front tire tread and along the entire tire surface, as well as similar structural alterations of the wheel wake region as predicted by *MRF*, were observed. From these results it can be concluded that the occurring flow effects of *MRF* and *MW* are additive to a certain extent.

- The tire surface pressure distribution shows great consistency between the stationary case and the *MRF* approach, from which follows that the pressure distribution at the tire tread depends strongly on the moving tire tread. The measured pressure curves on the tire surface are consistent with those numerically determined by Axon et al. [16], as well as with the experimental results of Dimitriou and Klussmann [28].

- In summary, different effects of individual rotation methods were determined, above all, on the yaw angle at which the underbody flow approaches the wheels, the structure of the wheel wake region, the separation behavior of the upward deflected air flow and the outflow situation from the wheel arch.

Chapter 7

Impact of wheel rotation on vehicle aerodynamics

The ability of each numerical rotation method to predict the effects of rotating wheels on the aerodynamic behaviour of the vehicle is examined in this chapter. These investigations therefore extend the studies of the wheel and the wheel arch from Chapter 6 to the entire vehicle. The aim is to determine experimentally and numerically the impact of wheel rotation on the aerodynamic situation of the vehicle, with focus on the investigation and evaluation of the quality and the capability of the individual numerical rotation methods to simulate the effects of rotating wheels detected in the experiment.

In the first section of this chapter, the air flow situation is examined in order to describe the impact of rotating wheels on the flow topology of the test vehicle. This is achieved by means of flow field investigations in the vicinity of the front wheel arch, as well as in the underbody and the vehicle's wake region. The studies are completed by an analysis of the surface pressure situation in various vehicle areas, such as at the side, underbody, top or base. Subsequently, the evolution and magnitude of the integral aerodynamic drag of the vehicle and the share of body and wheels are analysed and discussed. In the final section, the investigations are extended to the impact of the front and rear wheel rotation on the aerodynamic properties of the vehicle.

Experiments as well as numerical investigations are carried out for this study. The hardware tests in the wind tunnel were performed to investigate the influence of wheel rotation on the aerodynamic behavior of this particular test vehicle. Furthermore, the experiments serve to confirm and reproduce results and basic findings from previous studies [5, 31, 34, 37, 40, 87] in order to ensure a reliable and well-founded experimental database for the validation of the numerical results. The gained data is used during the further procedures as a reconciliation dataset for all computational investigations. In the numerical sections, *CFD* simulation results are analysed and furthermore validated with the outcomes and findings of the wind tunnel experiment. The subsequently discussed topics are accordingly divided into an experimental and a numerical part. Both, the experimental and numerical test cases are presented and discussed below.

7.1 Experimental test cases and measuring program

The test cases as well as the measuring program of the wind tunnel experiments performed for this study correspond to those discussed in Chapter 4 and 6. The test vehicle was measured in mockup configuration and also with enabled engine compartment flow, where three series rim geometries *Rim16*, *Rim17* and *Rim18* were used in accordance with the results and conclusions from chapters 4 and 5. The vehicle riding height was kept constant during all tests. Furthermore, measurements were performed with stationary as well as with rotating wheels. However, the ground simulation system was active for each test case in terms of boundary layer suction and moving center belt. Vehicle configurations with stationary wheels and non-moving wheel drive units, but active ground simulation, will each be used in the following as the reference cases.

Details of the test vehicle, as well as the wind tunnel boundary conditions are listed in Chapter 4 and will therefore not be repeated at this point. A list of the examined load cases is shown in Table 4.1.

For the experimental study, the integral aerodynamic forces and the surface pressure in various regions of the test vehicle were determined for each load case. However, due to limited test time, measurements of the flow topology by means of pressure examinations in the previously defined analysis planes are performed only for test cases with rims *Rim16*.

7.2 Simulation cases

Most computational load cases correspond to those of Chapter 6. Subsequent investigations were performed with the detailed simulation models of the test vehicle, using both cooling mockup configurations as well as setups with enabled engine compartment flow. Various rotation methods and combinations of rotation methods are considered to simulate wheel rotation, i.e. *MW*, *MW-TO*, *MRF*, as well as *MRF&MW* and *MRF&MW-TO*, where simulation cases with stationary wheels serve as a reference in the following. The rim variants *Rim16*, *Rim17* and *Rim18* were each examined for two rim orientations α and β in accordance with the findings regarding the impact of rim orientation from Chapter 5. A complete list containing all simulation cases and setups that were investigated for this numerical study is shown in Table 5.3 and Table 5.2. However, the focus of the examinations in this chapter was placed on load cases with *Rim16* and enabled engine compartment flow. The most important corresponding simulation results for load cases considering rims *Rim17* or *Rim18* are listed in Appendix C. In order to minimize the number of analyses to a manageable amount, simulation cases with rim orientation β or in cooling mockup configuration are only considered for studies of the integral vehicle drag.

7.3 Impact of wheel rotation on the vehicle flow topology

In order to understand the flow topology and the aerodynamic mechanisms acting on the wheel and on the vehicle, the air flow situation in various individual vehicle areas is investigated. For this purpose, regions are selected in which major air flow alterations due to wheel rotation are expected, as well as areas which are particularly interesting with respect to the development of vehicle drag. These are regions in close proximity of the front wheel arch on the driver's side and lateral downstream of the front wheel, as well as at the underbody, at the tail and at the wake region of the vehicle. Detailed investigations were carried out by means of pressure-induced air flow analyses and surface pressure measurements with the test vehicle in the wind tunnel. The same and further investigations were performed numerically with its virtual counterpart.

The pressure-based flow field measurements are carried out at different measurement planes located at the individual vehicle areas, where the pressure situation is visualized by means of contour plots of the pressure coefficient in order to identify flow structures and patterns. Numerical flow topology studies are performed with all rim geometries. However, the validation with the experiment is performed utilizing the case with *Rim16* rims, as experimental data is only available for this configuration.

To detail the complex flow topology further, the surface pressure distribution is examined in the defined vehicle regions, and the results of the air flow investigations are supplemented by this data. The measurement results are visualized in the following as contour plots. In order to quantify the results and the alterations between individual load cases, a representative surface pressure quantity is calculated based on this data in accordance with the evaluation process described in Chapter 3.4.5. The surface pressure analyses were carried out for three rim geometries, since the required experimental data was available for all vehicle configurations, in contrast to the flow topology study.

For most parts, the results of the measurements and analyses of the individual vehicle areas are presented and discussed separately. Both the experimental and the numerical part of this chapter are therefore subdivided according to the individual vehicle regions.

7.3.1 Experimental results

Wheel arch vicinity

First, the air flow topology and the impact of wheel rotation on it are analysed in close proximity to the front wheel arch. For this purpose, the pressure situation is investigated in *planes A*, *B* and *C*, that are located alongside to the vehicle and downstream of the wheel arch on the driver's side.

For the experimental part, vehicle configurations with *Rim16* rims and enabled engine compartment flow for setups with stationary (test case *WT.B.16.NR*) and rotating wheels (test case *WT.B.16.RT*) are considered. The pressure distributions in *planes A*, *B* and *C* are shown in Fig. 7.1, where the left column corresponds to the stationary case, and the right one to the load case with rotating wheels. The surface pressure distribution at the vehicle side, downstream of the front left wheel arch ($\mathrm{VZ_{sideB}}$), are shown in Fig. 7.2, where Fig. 7.2a corresponds to the stationary case and Fig. 7.2b to the setup with rotating wheels. The results of the differential pressure analysis are plotted additionally to highlight the differences between the two load cases (Fig. 7.2c).

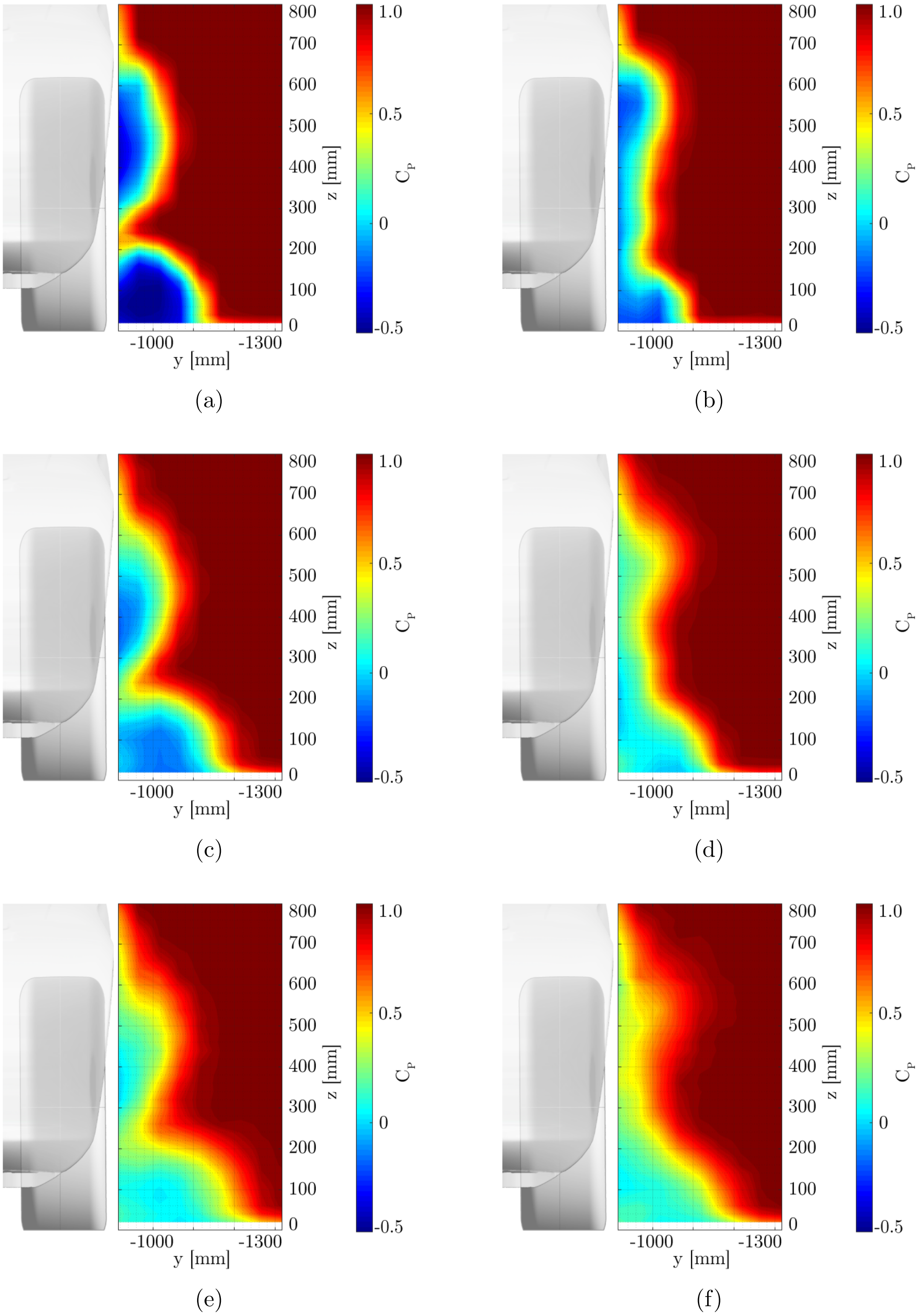

(a) (b) (c) (d) (e) (f)

Figure 7.1: Pressure coefficient C_P from measurements downstream of the wheel arch in *plane A* (top), *plane B* (center) and *plane C* (bottom) for *Rim16*. Stationary wheels (*WT.B.16.NR*) (left column) and rotating wheels (*WT.B.16.RT*) (right column).

The results of Chapter 6 have revealed that rotating wheels affect the highly complex flow situation within the wheel arch, and consequently its vicinity. Therefore, this region is used as a starting point for the following analyses to study the impact of rotating wheels on the flow topology of the vehicle. The investigated air flow situation in proximity of the wheel arch is subsequently interpreted and discussed based on the findings of the studies by Wäschle [37] and the thermology introduced in this work. Through comparison of the pressure distribution in *plane A* between the stationary case (Fig. 7.1a) and the case with rotating wheels (Fig. 7.1b), alterations in the flow situation can be identified.

For the stationary case, two distinct low pressure areas can clearly be identified, where the upper one can be attributed to the *rim vortex* in the form of a horseshoe, which arises due to flow separation at the rim hub and is fed by air from the gap between the wheel and the upper half of the wheel arch. However, for rotating wheels the size of the upper negative pressure area decreases, but gains in height and is noticeably flattened. This flow structure alteration is caused by air mass leaking from the wheel arch, reducing the strength of the upper rim vortices. Additionally, the air adjacent to the upper half of the wheel arch is accelerated against the main flow direction by the rotating tire and rim surfaces, causing a reverse flow area at the upper front of the tire that also weakens the vortex intensity.

This countercurrent against the main flow induces a rotation resulting in the additional *side vortex* between the upper and lower vortices, which merges the two clearly distinguishable low pressure areas to a large negative pressure region for rotating wheels.

The low pressure area near the ground originates also partly due to this horseshoe-shaped *rim vortex* and is fed by the air flow through the rims, which is therefore heavily dependent on the rim geometry, as discussed in Chapter 4. This portion of the lower vortex typically arises for both stationary and rotating wheels. The other part of the near-ground low pressure area emerges due to the *wheel squash vortex*, which originates because of air flow separations at the outer shoulder of the front wheel. Rotating wheels introduce energy into this vortex, resulting in a shift of the separation point from the tire contact patch downstream, causing a smaller *wheel squash vortex* structure than in the stationary case. The *jetting phenomenon* must also be taken into account in the case of rotating wheels. Due to two converging boundary layers, which in this case applies to the moving floor and the front of the rotating tire, a strong high pressure area develops in front of the contact patch. This high pressure region results in two jets laterally directed away from the pressure maximum, and deflected downstream by the main flow, creating a horse shoe vortex around the contact patch. The measurement results for the stationary case reveal that both vortex regions have a pressure coefficient well below zero, which indicates high energy losses. For rotating wheels, the pressure coefficient in both areas is also negative, but not as much as in the case of stationary wheels, which suggests lower vortex losses and supports previous explanations.

The investigation of flow topology development downstream of the wheel arch in planes *B* and *C* (Figs. 7.1c-7.1f) reveal also distinctive vortex structures. However, the strength of the low pressure areas decreases constantly downstream, with simultaneous broadening of its structure, in particular for the ground-level vortex, which suggests that the eddies begin

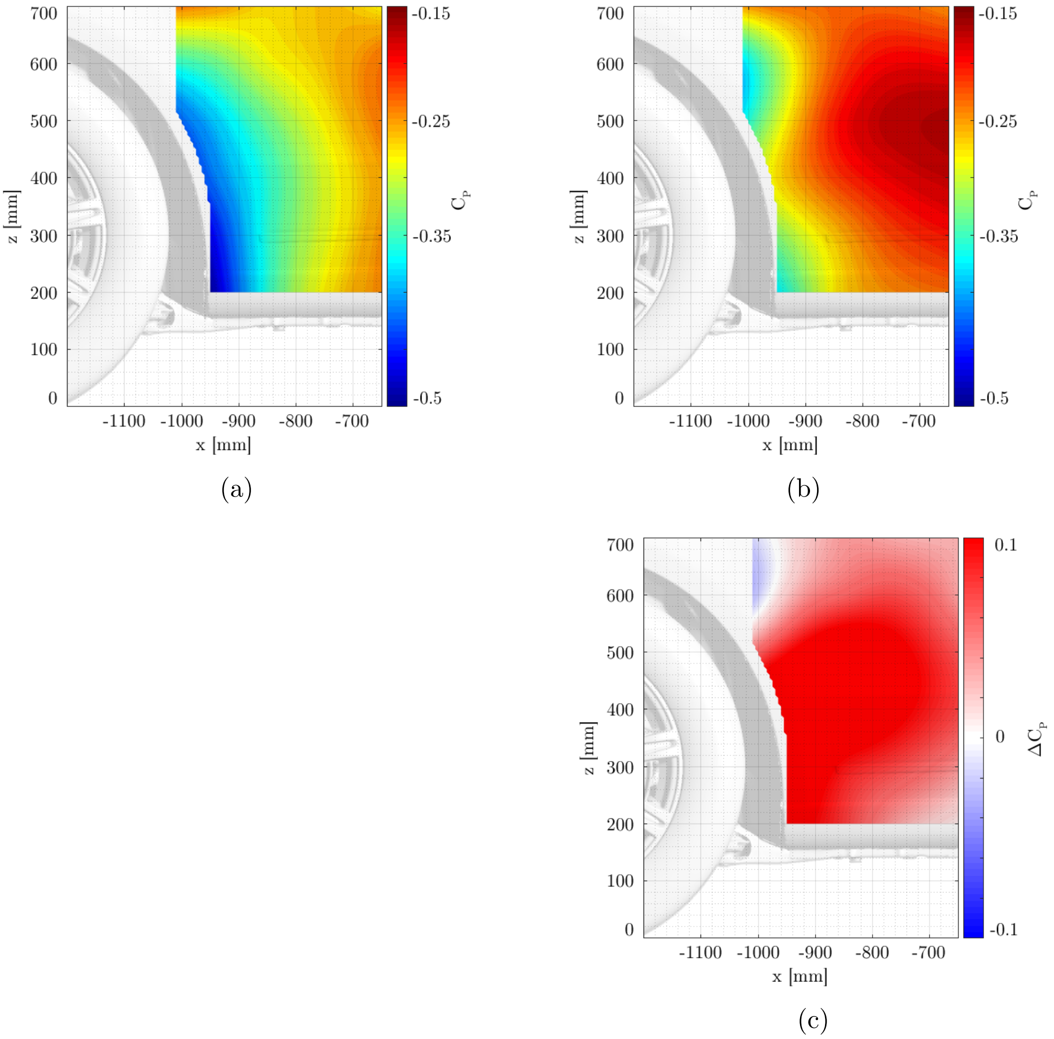

Figure 7.2: Pressure coefficient C_P from measurements at the vehicle surface at $\mathrm{VZ}_{\mathrm{sideB}}$ for *Rim16*. Stationary case (*WT.B.16.NR*) (top left), rotating wheels (*WT.B.16.RT*) (top right), and the differential analysis ΔC_P between both cases (bottom right).

to dissolve. Another effect to be considered is the formation of a ground-level boundary layer due to the stationary wind tunnel floor next to the vehicle, which merges with the *wheel squash vortex* and spreads it additionally. Furthermore, a slight downward shift of the vortices is seen through comparison of the z-position of both vortex centers downstream between *plane A*, *B* and *C* for stationary and for rotating wheels.

The investigations of the surface pressure situation at the lateral area of the vehicle yield that wheel rotation leads to an increase in pressure in the entire area of the vehicle surface downstream of the wheel arch (Fig. 7.2). These findings support the results of the flow topology investigation, which show a reduction of the upper *rim vortex* and the near-ground *wheel squash vortex*, in the wake of the front wheel arch, and thus a less developed low pressure area at the vehicle wall. The increase in pressure is particularly distinctive at a height of $z = 400$ mm, where the *side vortex* has formed due to the rotation of the

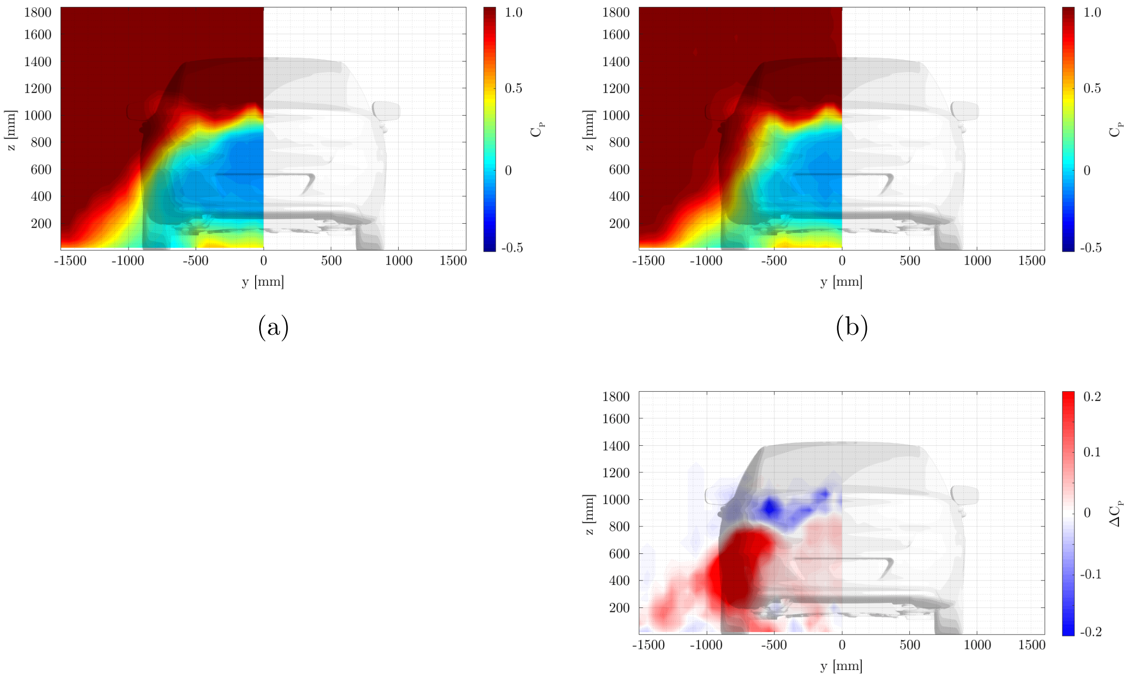

(a) (b)

(c)

Figure 7.3: Pressure coefficient C_P from measurements at the vehicle wake in *plane D* for *Rim16*. Stationary case (*WT.B.16.NR*) (top left), rotating wheels (*WT.B.16.RT*) (top right), and the differential analysis ΔC_P between both cases (bottom right).

wheel, and the low pressure area between the *rim* and the *wheel squash vortex* increases. This effect applies to all vehicle configurations and will be discussed in Chapter 7.3.

Vehicle tail and wake area

The air flow topology at the rear of the vehicle will be analysed and discussed in this section. Therefore, the flow situation is examined by means of pressure measurements in *plane D*, which is located in the vehicle's wake area at position $x = 2800$ mm. The analysis results of the measured pressure distribution are shown for stationary wheels in Fig. 7.3a and for rotating wheels in Fig. 7.3b. The differential flow field between these test cases is shown in Fig. 7.3c in order to facilitate the comparison of these results and to visualize the impact of wheel rotation on the wake structure of the vehicle.

The results reveal remarkable alterations of the air flow topology downstream of the vehicle. Major pressure increases are detected at the lateral areas of the wake structure and furthermore at the center of the vehicle's rear, as well as near the ground behind and besides the vehicle, which, however, show a lower strength than the lateral region. This phenomenon can be attributed to energy additionally introduced into the flow due to tire rotation, thereby reducing the range of high energy losses in the wake [37]. In contrast, pressure reductions can be identified in the upper third of the tail area. These results suggest that wheel rotation has a significant impact on the base wake structure and therefore

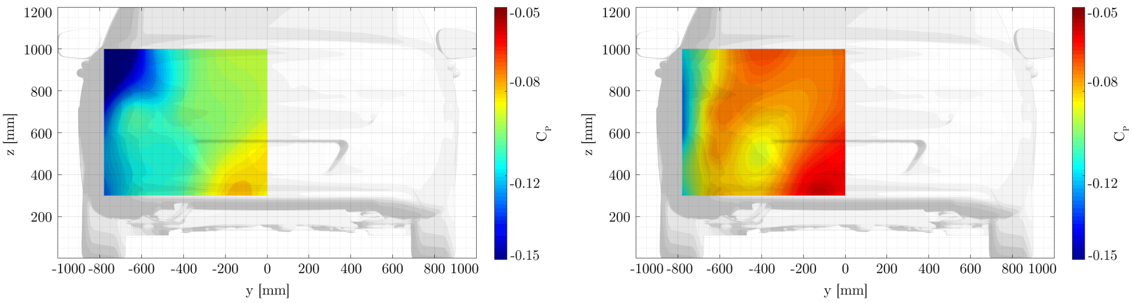

(a) Stationary wheels (*WT.B.16.NR*).

(b) Rotating wheels (*WT.B.16.RT*).

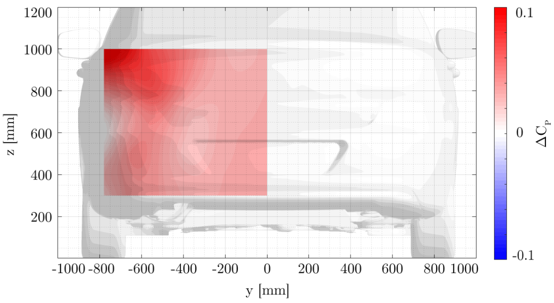

(c) Differential analysis.

Figure 7.4: Pressure coefficient C_P from measurements at the vehicle tail surface at $\mathrm{VZ}_{\mathrm{tail}}$ for *Rim16*. Stationary case (*WT.B.16.NR*) (top left), rotating wheels (*WT.B.16.RT*) (top right), and the differential analysis ΔC_P between both cases (bottom right).

not only change the local air flow situation at the wheel arch area, but also the global air flow topology of the vehicle.

This assumption is supported by the analysis of the surface pressure situation (Fig. 7.4), which demonstrates that alterations of the flow situation in the vehicle's vicinity affect the surface pressure distribution at the vehicle base, as the outcomes of the flow topology measurements of the vehicle wake area already suggested. A pressure increase is recognizable at the entire rear of the vehicle, and in particular in the lateral region above the tail light. These effects were reproduced and demonstrated for all rim geometries, as well as engine compartment flow and mockup configurations, and correlate with the findings of previous experimental studies [34, 37, 40].

Summary of the surface pressure situation

In the previous sections, the measured surface pressure alterations were discussed separately for individual vehicle zones, i.e. at the vehicle side and at the tail. In this section, the effects of wheel rotation on the surface pressure situation of the entire vehicle will be considered together for all examined surface regions. Therefore, previously discussed pressure analyses of vehicle zones $\mathrm{VZ}_{\mathrm{sideB}}$ and $\mathrm{VZ}_{\mathrm{tail}}$ are supplemented and completed by the measurement results of the surface pressure distribution in the region upstream of the wheel arch, at $\mathrm{VZ}_{\mathrm{sideA}}$, and at the upper vehicle area, at $\mathrm{VZ}_{\mathrm{top}}$. To quantify these

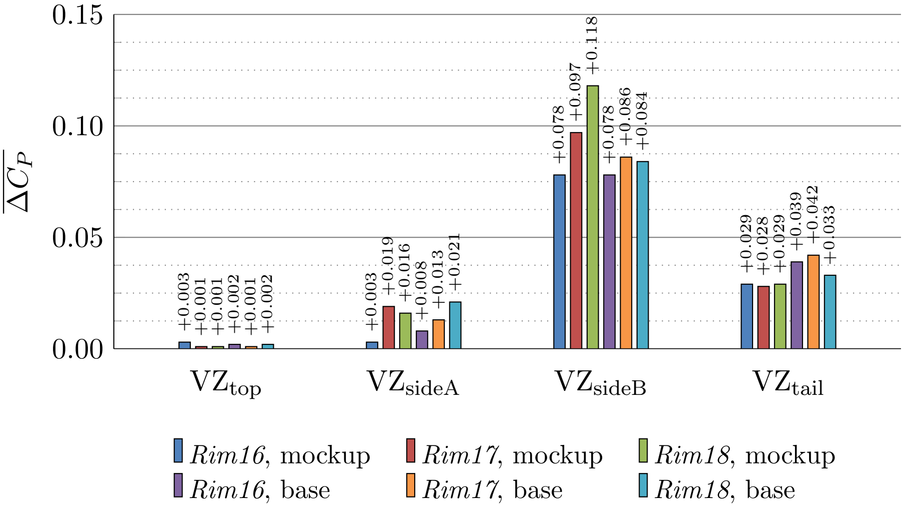

Figure 7.5: Mean deviation of the surface pressure coefficient $\overline{\Delta C_P}$ between stationary (*WT.A/B.16/17/18.NR*) and rotating wheels (*WT.A/B.16/17/18.RT*) for various vehicle zones.

results the mean deviation of the surface pressure coefficient is calculated for each vehicle surface zone according to Eq. (3.56) between load cases with stationary and with rotating wheels, but otherwise the same same vehicle configuration. The outcomes of this analysis are shown in Fig. 7.5 for all vehicle configurations.

The differential analysis reveals that wheel rotation alters the surface pressure situation in all examined regions, which, however, vary in magnitude. The measured value ranges and trends show great similarities for all vehicle configurations. The most noticeable impact on the pressure distribution is detected at the lateral area $\mathrm{VZ_{sideB}}$. In this region, the surface pressure increases over a large area due to the effects of the altered and weakened lateral vortex structures, as discussed in the previous section. In contrast, the pressure alterations in the region upstream of the wheel house at $\mathrm{VZ_{sideA}}$ are comparatively small, which suggests minor modifications of the air flow situation at the front bumper sides. Furthermore, the effects along the centerline at the top of the vehicle $\mathrm{VZ_{top}}$ are marginal, suggesting that the flow situation in the upper part of the vehicle is hardly affected by rotating wheels. At the vehicle base $\mathrm{VZ_{tail}}$, wheel rotation causes an increase in the surface pressure, which nevertheless is relatively low compared to lateral region $\mathrm{VZ_{sideB}}$. However, this altered pressure distribution has a decisive effect on the aerodynamic drag coefficient of the vehicle due to the size and orientation of this vehicle surface, which will be discussed in subsequent sections of this chapter.

7.3.2 Numerical investigations

In this section, the flow topology of the vehicle is studied by means of computational methods. For this purpose, the air flow situation is analysed in the vicinity of the wheel arch, the underbody region, as well as the rear area of the vehicle. The results of the numerical examinations are discussed below and furthermore validated with the results of the experimental studies. Contrary to the experiment, where only rim *Rim16* could be used for the flow field measurements, the numerical investigations are performed for all rim geometries. However, mainly the simulation results of *Rim16* are presented in this chapter.

Wheel arch vicinity

The flow topology studies in close proximity to the front wheel arch are performed according to the experiment in the region alongside to the vehicle and downstream of the wheel arch on the driver's side, in analysis *plane A*. In addition to the pressure distribution, the projected streamlines are also shown. In order to detail these results, further examinations of the air flow situation are carried out within *plane I*, which is located next to the left front wheel arch and depicts the development of the flow structure downstream.

The simulation results of the pressure distribution in *plane A* are shown in Fig. 7.6, where the reference case with stationary wheels is shown in Fig. 7.6a. The remaining diagrams represent the results of load cases with applied rotation methods. The pressure distribution in *plane I* is visualized in Fig. 7.7, where the reference case is shown in Fig. 7.7a and the simulation results of load cases with rotating wheels in the remnant diagrams. The illustrated simulation results in *plane A* and *plane I* are discussed collectively below.

The analysis of the flow topology of the stationary case (Figs. 7.6a and 7.7a) reveals flow structures characterized by two separate areas with negative pressure coefficients. The upper area can be assigned to the *rim vortex* and the ground level area to the *wheel squash vortex*, according to the previously discussed experimental examinations. A good structural consistency with the results of the wind tunnel experiment (Fig. 7.1a) is determined. However, the upper vortex is overestimated in the simulation, and the separation between the two negative pressure areas is therefore shifted towards the floor. For this reason, the ground-level pressure area is predicted smaller than it is in the experiment. No rotational wheel boundary conditions were applied for this simulation setup, so that the simulated air flow could be validated by the wind-tunnel data of the test case with stationary wheels. For that reason, a possible explanation for this flow structure deviation might be deviating surface geometries between the simplified tire simulation model and the fully detailed and deformed tire in reality. Furthermore, deviations that result from different floor simulation approaches may also be considered.

The *MW* (Figs. 7.6b and 7.7b), as well as the *MW-TO* (Figs. 7.6c and 7.7c) method predict two distinct regions with negative pressure coefficients next to the wheel, with structures similar to those of the stationary case. However, in comparison to the stationary case, the simulation results of *MW* show marginal weakening of the upper and lower vortex, resulting in a reduced negative pressure area. For *MW-TO*, the lower vortex is even less developed than for *MW*, and thus the upper vortex is slightly shifted downwards. The validation of the numerical results with the experiment indicated that the decrease of the upper and lower pressure areas are accurately predicted by both rotation approaches. However, contrary to the experiment, both methods anticipate two isolated vortices next to the rotating wheel, which suggests the absence of the *side vortex.* The flow topology analyses in *plane I* (Figs. 7.7b and 7.7c) confirm this conclusion and demonstrate that both rotation methods fail to reproduce this proportion of the lateral flow structure.

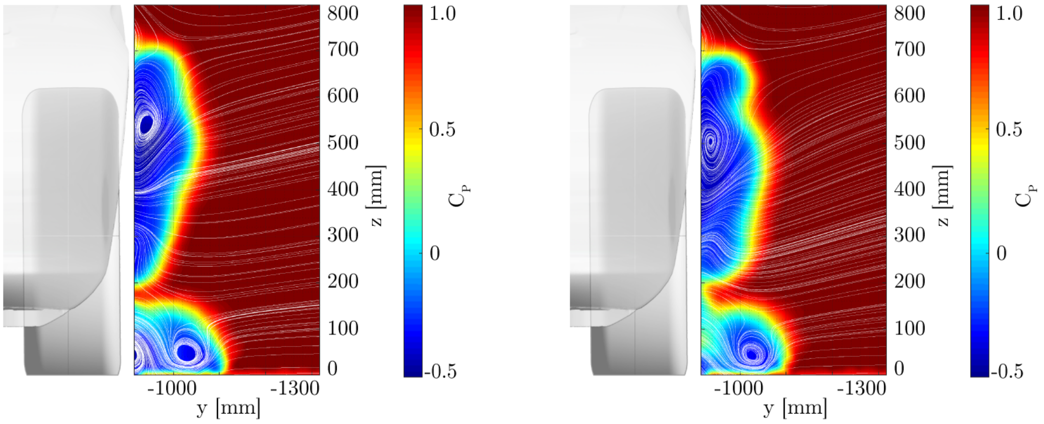

(a) NR

(b) MW

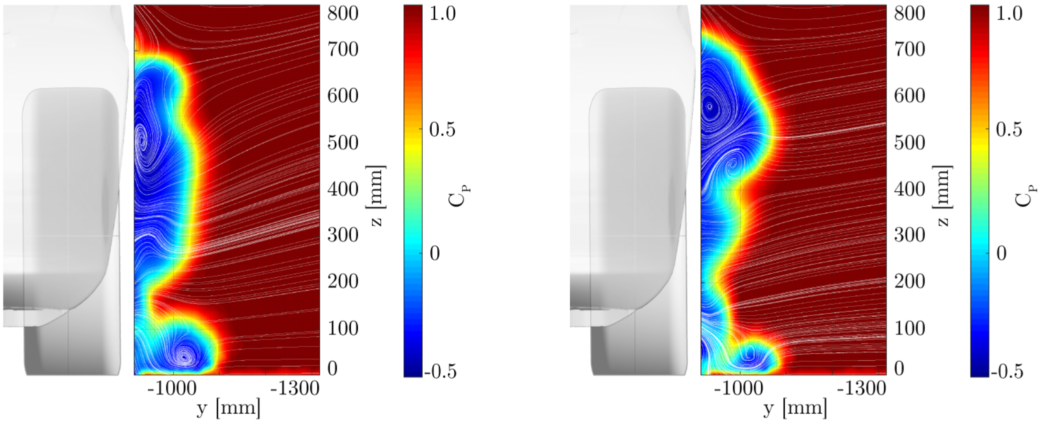

(c) MW-TO

(d) MRF

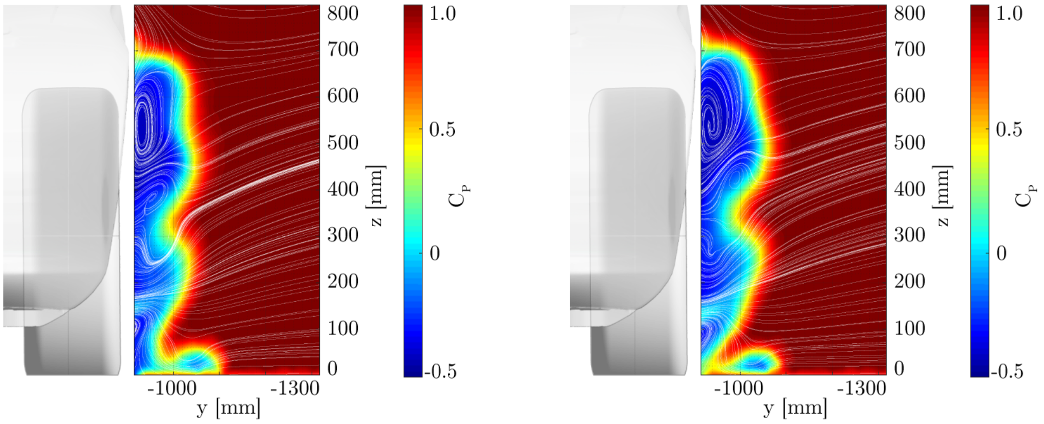

(e) MRF&MW

(f) MRF&MW-TO

Figure 7.6: Pressure coefficient C_P with projected streamlines downstream of the wheel arch in *plane A* for *Rim16*. Simulation cases *B.16.**.

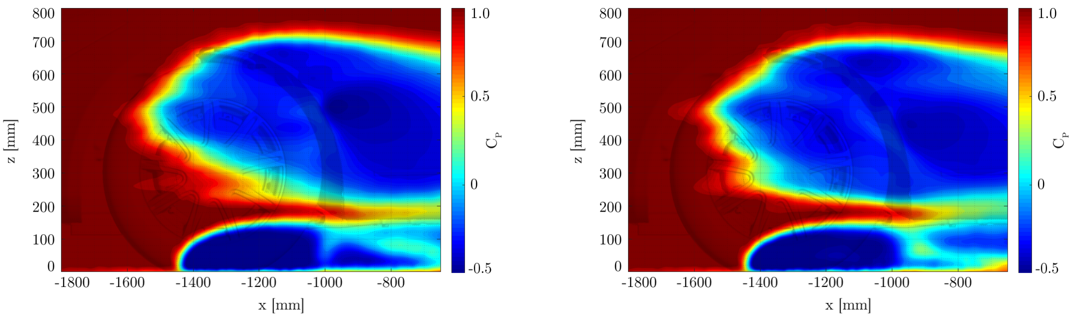

(a) NR

(b) MW

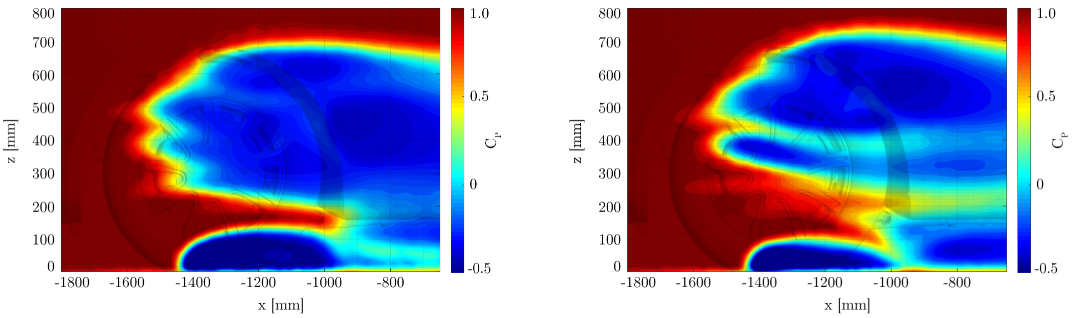

(c) MW-TO

(d) MRF

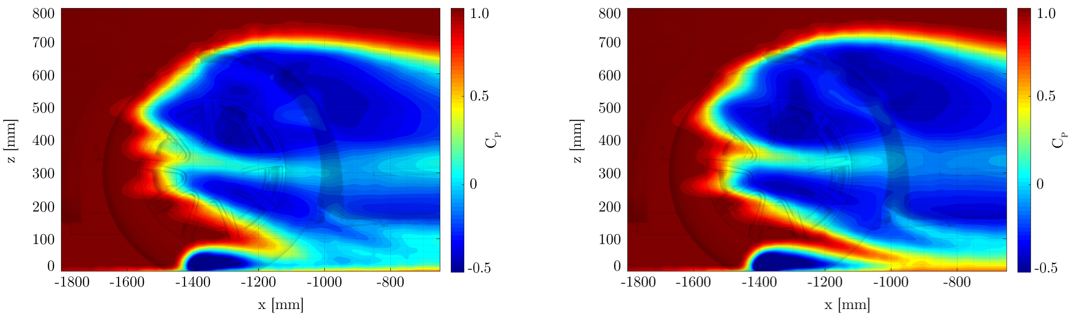

(e) MRF&MW

(f) MRF&MW-TO

Figure 7.7: Pressure coefficient C_P next to the front wheel arch in *plane I* for *Rim16*. Simulation cases *B.16.**.

The *MRF* method (Fig. 7.6d) predicts significant alterations of the flow topology in comparison to *MW* and *MW-TO* or the stationary case. Instead of two distinct areas with negative pressure coefficients, one large region is formed, with its center shifted away from the vehicle. These results indicate the existence of the *side vortex*, which is confirmed through the flow topology analysis in *plane I* (Fig. 7.7d), that reveals a third vortex structure in the center of the rim in addition to the *rim vortex* and the *wheel squash vortex*, which was not observed for *MW* or *MW-TO*. This is the *side vortex*.

The flow topology investigations of *MRF&MW* (Fig. 7.6e) and *MRF&MW-TO* (Fig. 7.6f) reveal one connected low pressure area. The analysis of resulting flow structures for both approaches yield an attenuated upper vortex and a more developed *side vortex*, while the ground-level vortex is weakened in comparison to *MRF* (Fig. 7.7d). Furthermore, the air flow investigations of both simulation cases in *plane I* (Figs. 7.7e and 7.7f) confirm the existence of the *side vortex*.

The simulation results of the *MRF*-based methods, i.e. *MRF*, *MRF&MW* and *MRF&MW-TO*, show great structural similarities of the lateral flow topology with the experiment. For those approaches, three separate vortices are clearly recognizable next to the wheel. However, especially *MRF&MW* and *MRF&MW-TO* under-predict the strength of the ground-level vortex. Although both methods predict a contiguous low pressure region near the ground, a small vortex structure can be identified, which separates from the main vortex. This flow structure alteration could not be detected in the experiment, where one coherent area was measured at this position. Nevertheless, the *MRF* method shows best structural correlation with the experiment of all applied rotation methods.

In order to detail the flow topology studies, surface pressure investigation were carried out at the lateral vehicle zone $\mathrm{VZ}_{\mathrm{sideB}}$. The results are shown in Fig. 7.8 for the stationary reference case as well as for the rotation methods.

The evaluation of the surface pressures distribution of the stationary case (Fig. 7.8a) reveals large areas with negative surface pressure coefficients, which result from the lateral separation vortices of the wheel arch and the consequently formed separation bubbles. The lowest values are located near the upper part of the wheel arch, which, however, dissolves downstream. The impact of the lateral vortices and detachment areas on the surface pressure situation in this region is clearly visible. The horizontally orientated low-pressure structure at z = 420 mm originates from the door kink at which the air flow separates.

An increase of the surface pressure over to the stationary case is predicted by all rotation methods (Figs. 7.8b-7.8f). For *MW* and *MW-TO*, pressure increases can be detected especially in the upper half of the examined area, while, for *MRF* and the combinations *MRF&MW* and *MRF&MW-TO*, these alterations are evident over a wide range of the lateral surface region. Furthermore, the pressure increase in the upper regions at x = -950 mm and z = 500 mm indicates a size reduction of the upper vortex structure and further an alteration of the air flow situation in this region due to rotating wheels, in accordance with the conclusions of the flow topology study.

The validation of the simulation results with the wind tunnel tests is challenging, due to the reduced geometrical resolution of the experimental data in consequence of the limited number of pressure probes, in contrast to the simulation, where the pressure values at every single surface cell can be considered for the analysis. For this reason, not all flow phenomena might be captured in detail in the experiment. Therefore, the comparative analysis is limited mainly to general statements about the pressure change and does not include detailed comparisons of the differential surface pressure structure. Anyhow, the experimentally determined pressure distribution at $\mathrm{VZ}_{\mathrm{sideB}}$ for stationary and rotating wheels are essentially reproduced numerically. Both, the results from the simulation and the experiment reveal regions with negative pressure coefficients. Furthermore, the surface pressure is increased in comparison to the stationary case for all rotation methods, in good agreement with the findings of the experiment. Especially *MRF*, *MRF&MW*,

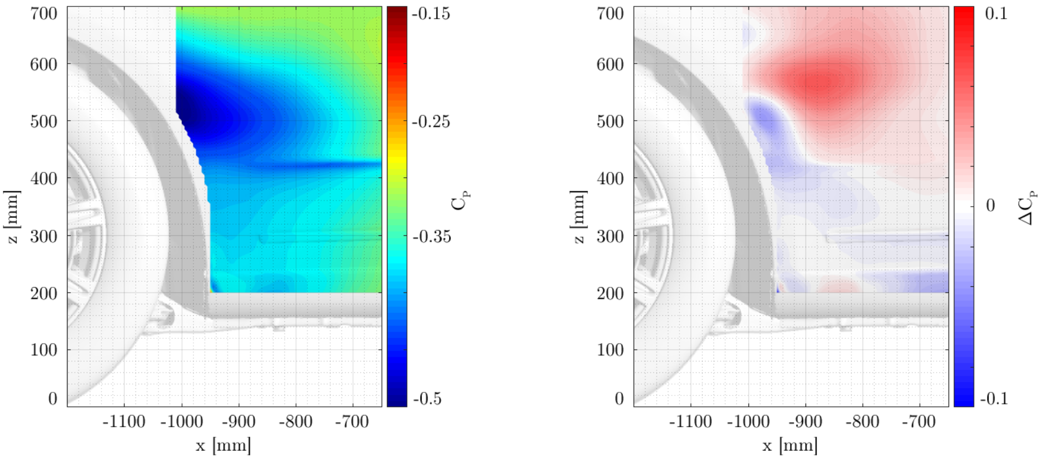

(a) NR (b) MW

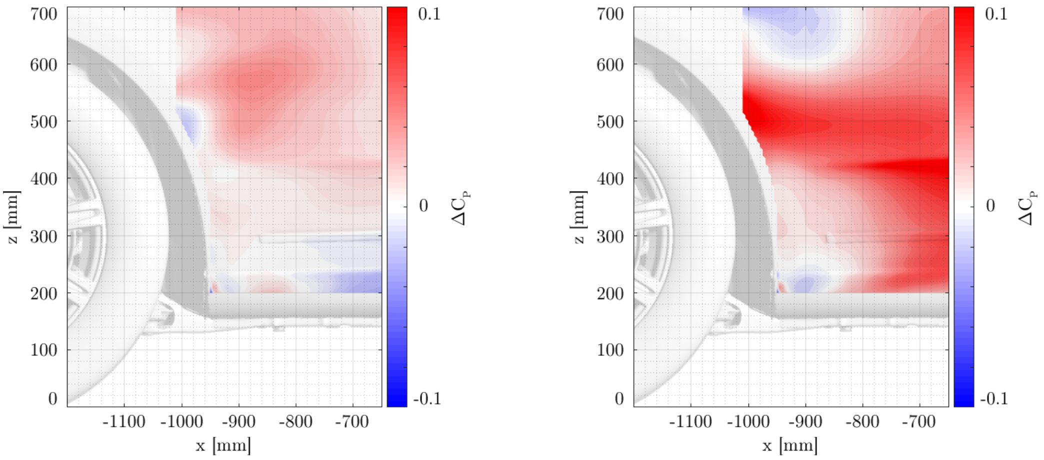

(c) MW-TO (d) MRF

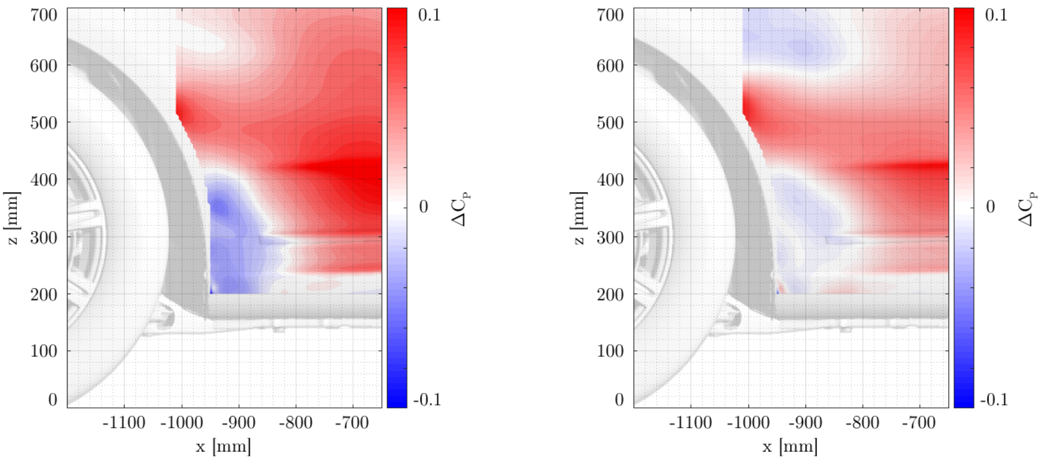

(e) MRF&MW (f) MRF&MW-TO

Figure 7.8: Pressure coefficient differences ΔC_P at the vehicle surface at $\mathrm{VZ}_{\mathrm{sideB}}$ for *Rim16*. Simulation cases *B.16.*-B.16.NR*.

and *MRF&MW-TO* show good agreement between the predicted pressure increase and the results of the wind tunnel measurements. However, the local flow phenomenon at the door kink could not be detected in the experiment, which might be due to the limited resolution of the experimental data.

Underbody region

The flow topology in the underbody region, from the front wheel arches downstream to the rear of the vehicle, is examined in analysis *plane E* that is positioned between the underbody and the floor, as well as in *plane F* which is located at the height level of the wheel center. Flow pattern studies are furthermore performed in *plane G* which is placed in a z-position above the wheel arches. To illustrate the impact of rotating wheels on the flow topology, differential pressure analyses are performed for these planes, and the results are visualized as contour plots, wherefore the stationary load case is used as the reference. The results are shown in Fig. 7.9 for *plane E*, Fig. 7.10 for *plane F* and Fig. 7.11 for *plane G*. The stationary reference case is shown in the first sub-figures (Figs. 7.9a, 7.10a and 7.11a), while the other figures display the results of the differential analysis for the respective rotation methods. In order to simplify the localization of flow patterns, the test vehicle is also illustrated in these diagrams. For the evaluation of the underbody flow in *plane E*, the vehicle's geometry was mirrored at the vehicle center plane at $y = 0$ mm to ensure comparability with the other planes, as all analyses are top views. Characteristic differences are especially expected for the fundamentally distinct wheel rotation methods *MW* and *MW-TO*, as well as *MRF*, *MRF&MW* and *MRF&MW-TO*, according to the results of the previous section. Therefore, the following investigations focus especially on those two distinctive rotation approaches.

The results reveal that the altered air flow situation within the wheel arch and the associated outflow behaviour, as well as the flatter yaw angle of the front wheels, affect the flow topology of the vehicle. The differential pressure analysis in the underbody region in *plane E* (Fig. 7.9) reveals major alterations of the flow situation due to rotating wheels. Two distinct effects are identified and roughly assigned to the group of *MW*-based rotation methods (*MW* and *MW-TO*) or to *MRF*. Left and right from the vehicle center, two main flow regions with increased pressure are detected that propagate downstream from the front wheels to the rear of the vehicle. These pressure alterations represent a shift in the underfloor flow, which raises the pressure downstream to the lateral tail areas. The origin of these two flows suggests that they correspond to an altered outflow from the engine compartment. This effect occurs for *MW* (Fig. 7.9b), *MW-TO* (Fig. 7.9c) and *MRF* (Fig. 7.9d), but is especially distinct for *MW* and *MW-TO*. Furthermore, the variation of the front wheel's air separation structures results in two regions with increased pressure, starting laterally at the front wheels and propagating downstream along the vehicle sides. Through cross comparison with the flow topology alterations next to and downstream of the front wheel arch in *plane A* (Fig. 7.6) and *plane I* (Fig. 7.7) it is apparent that these high pressure regions correspond to the weakening and decrease of the size of the ground-level *wheel squash vortex* and therefore to the reduction of the detachment area of the wheel arches. This effect is especially evident for the *MRF* method (Fig. 7.9d). Both the *MW* and the *MW-TO* methods predict also slight increases in pressure at the regions lateral downstream of the front wheels, which, however, disappear until the vehicle

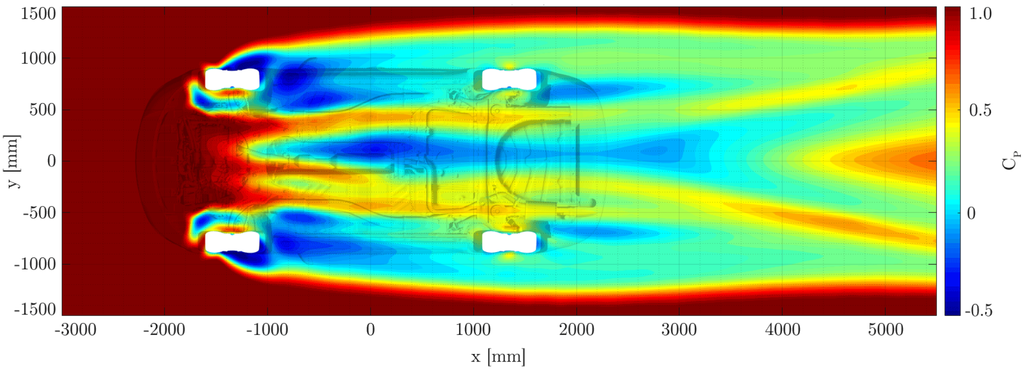

(a) NR

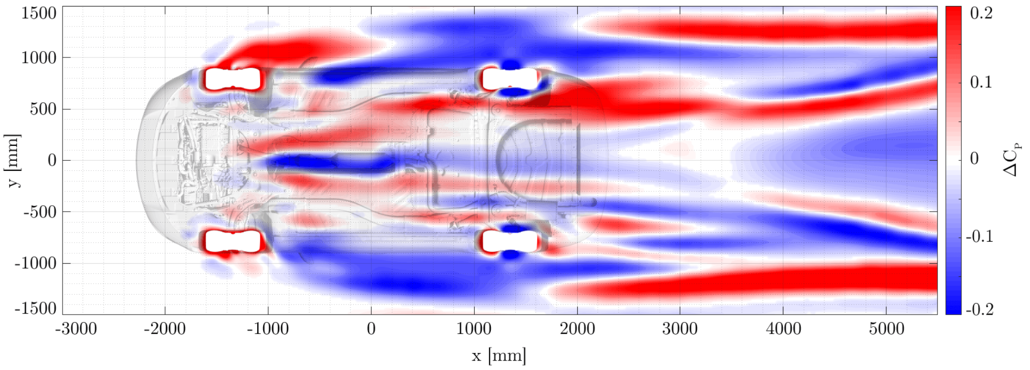

(b) MW

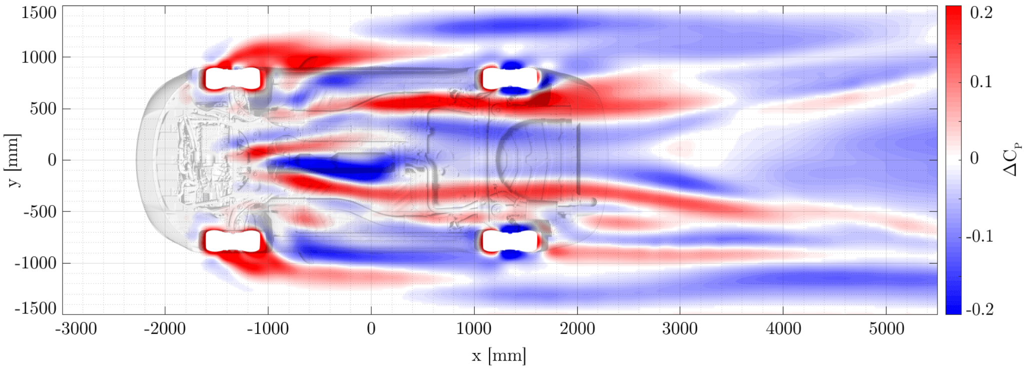

(c) MW-TO

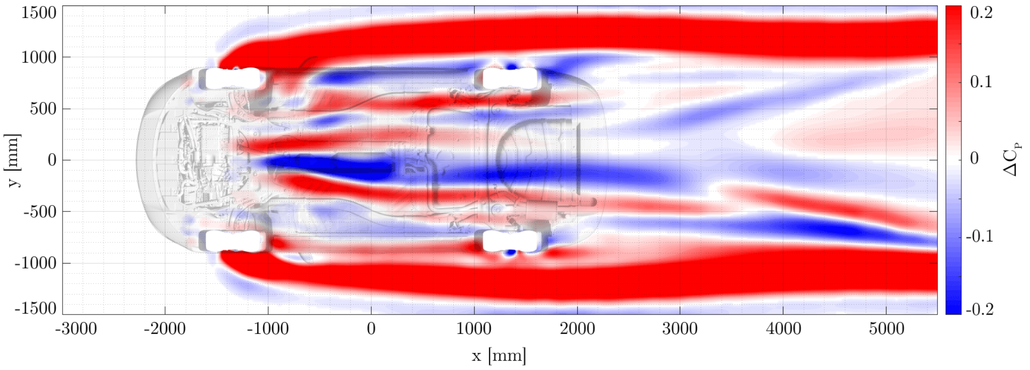

(d) MRF

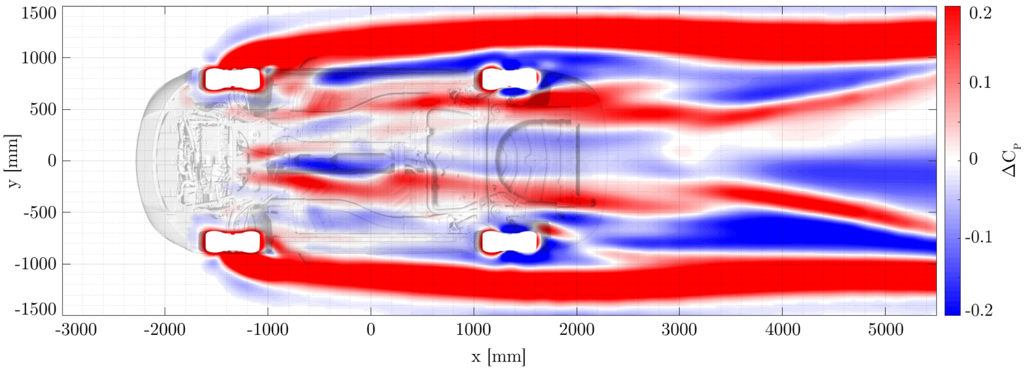

(e) MRF&MW

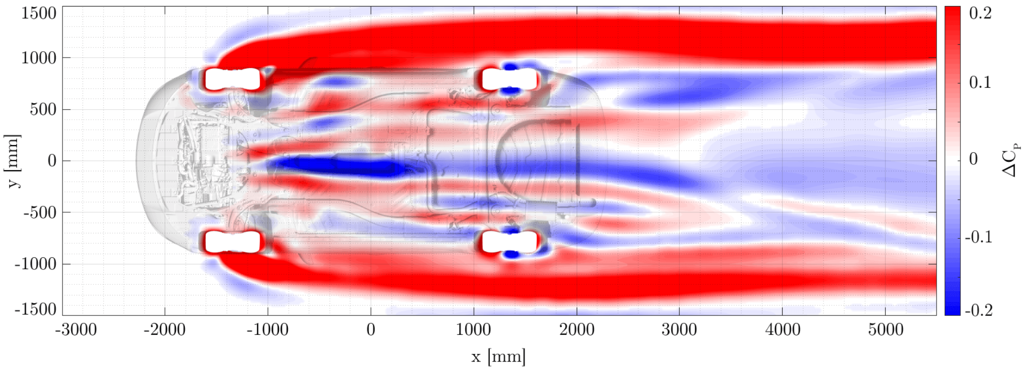

(f) MRF&MW-TO

Figure 7.9: Pressure coefficient differences ΔC_P at the underbody in *plane E* for *Rim16*. Simulation cases *B.16.*-B.16.NR*.

center. For the combined rotation methods *MRF&MW* (Fig. 7.9e) and *MRF&MW-TO* (Fig. 7.9f) flows, with increased pressure can be detected underneath the vehicles, as well as its sides, wherefore it can be concluded that these two effects are additive to some extent.

The flow topology analysis at the level of the wheel center in *plane F* (Fig. 7.10) reveals a large pressure reduction area, and thus a widening of the wheel arch separation bubble, which originates at the front wheel houses and forms downstream along the vehicle for all rotation methods. These air flow alterations occur due to the displacement and broadening of the upper wheel vortex for *MW* and *MW-TO*, respectively due to the formation of the rim vortex for *MRF*, *MRF&MW*, and *MRF&MW-TO* (Fig. 7.6), as demonstrated in the previous section. However, pressure increases in extensive areas are detected at the rear of the vehicle, especially in the area downstream of the wheel arches, at the side drawers and the rear base, which consequently suggests a narrowing of the vehicle wake area. The occurrence of this effect can be attributed to the altered outflow behaviour of the wheel houses and furthermore to the modified underbody air flow, that provides more air mass to the lateral tail areas and thus supports the pressure recovery at the rear of the vehicle. These air flow alterations are predicted by all rotation methods, but the pressure gain downstream of the vehicle base is in particular pronounced for *MW* and *MW-TO*.

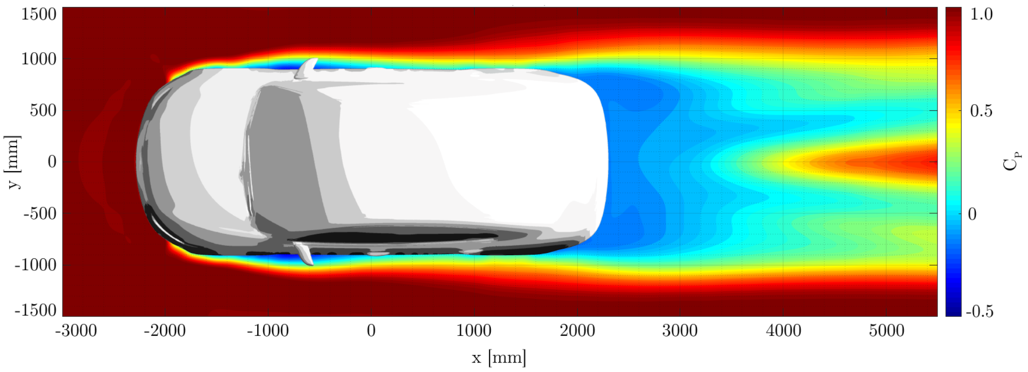

(a) NR

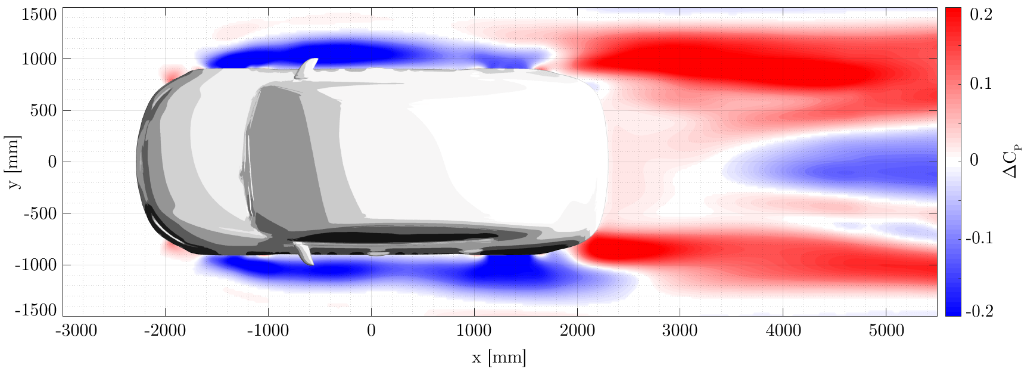

(b) MW

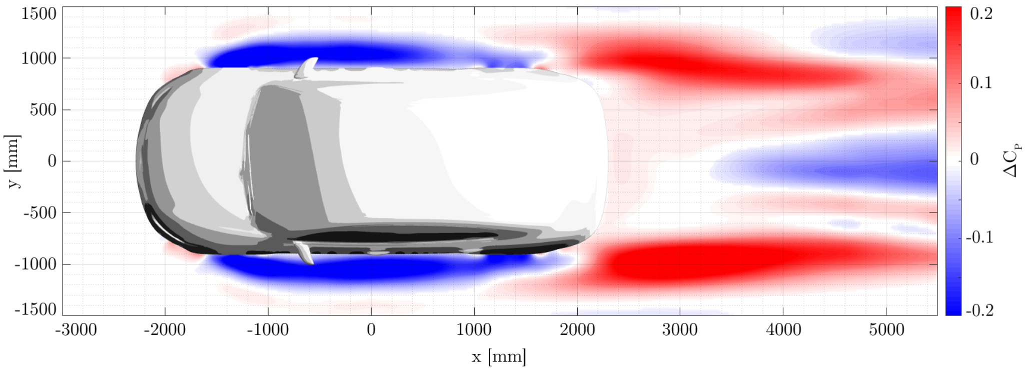

(c) MW-TO

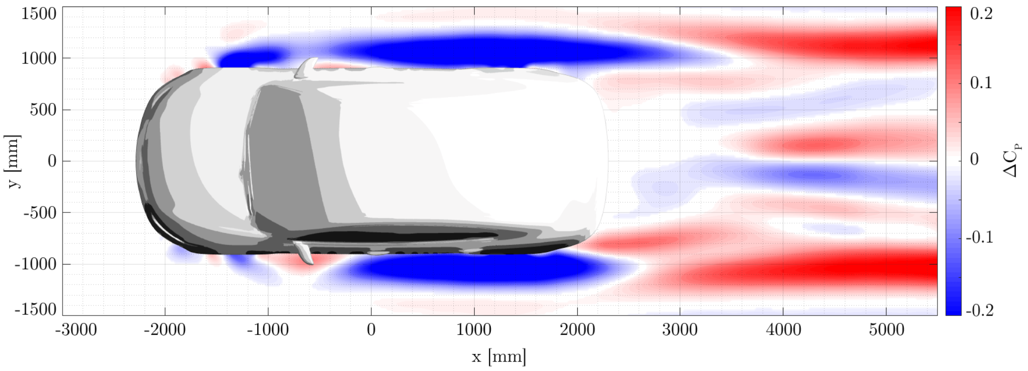

(d) MRF

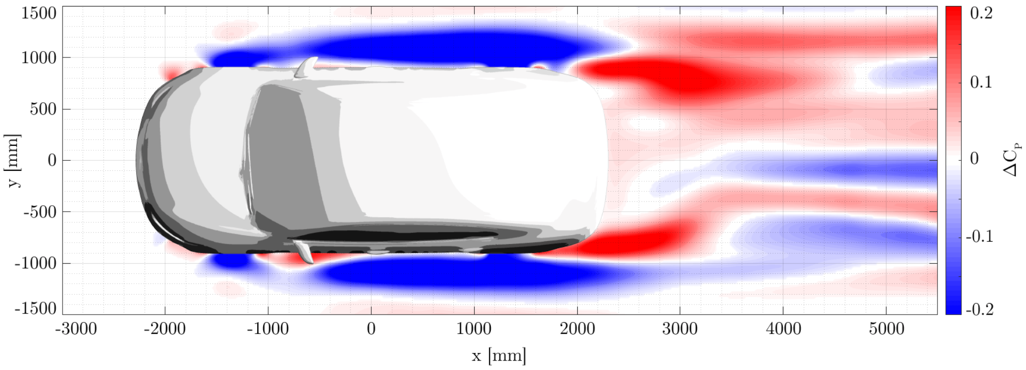

(e) MRF&MW

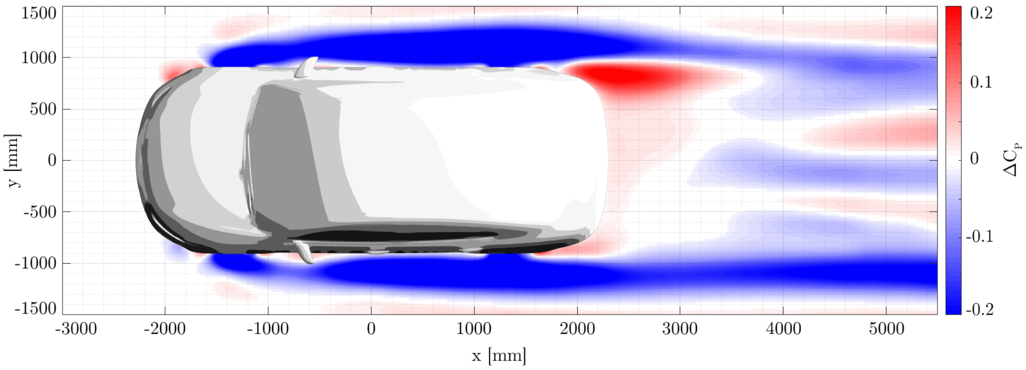

(f) MRF&MW-TO

Figure 7.10: Pressure coefficient differences ΔC_P downstream the vehicle in *plane F* for *Rim16*. Simulation cases *B.16.*-B.16.NR*.

The air flow alterations adjacent to the vehicle are limited to the lower sections, as no effects in this range can be detected for the upper regions in *plane G* (Fig. 7.11). However, pressure increases are evident at the lateral tail regions, and at the vehicle wake for all rotation methods. For the *MRF* method, these pressure regions are greatly attenuated and can only be recognized in proximity of the vehicle base and on the right side of the tail.

Vehicle tail and wake area

The flow topology in the vehicle wake is examined in analysis *plane H*, which is located at the centerline of the car, as well as in *plane D*, which is positioned 460 mm downstream from the rearmost point of the vehicle. The results of the pressure analyses in *plane H* and *plane D* are shown in Fig. 7.12 and in Fig. 7.13, respectively. In order to investigate the effects on the vehicle itself and to detail the results of the flow analyses, the surface pressure situation at the vehicle base is examined, and the results are presented in Fig. 7.14. Differential pressure analyses are carried out for all load cases in comparison to the stationary reference setup in order to visualize the impact of the individual wheel rotation methods on the flow topology and the surface pressure situation in this vehicle region. Therefore, Figs. 7.13a and 7.12a, as well as Fig. 7.14a show the reference case, and the remaining figures show the load cases with the individual wheel rotation methods.

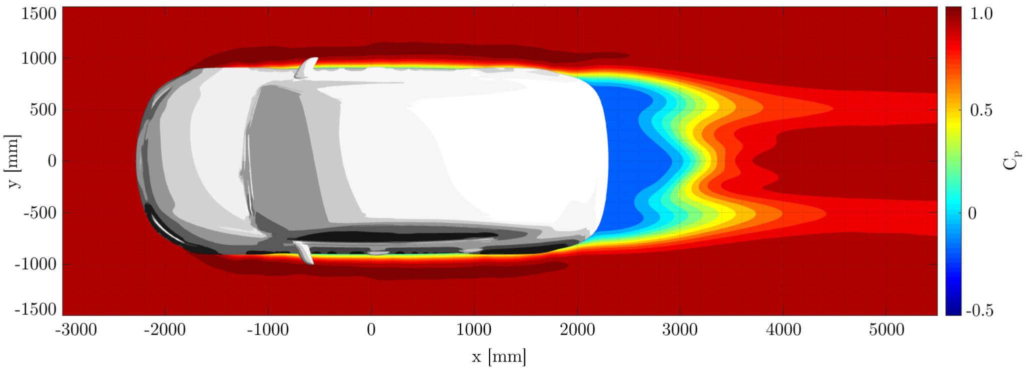

(a) NR

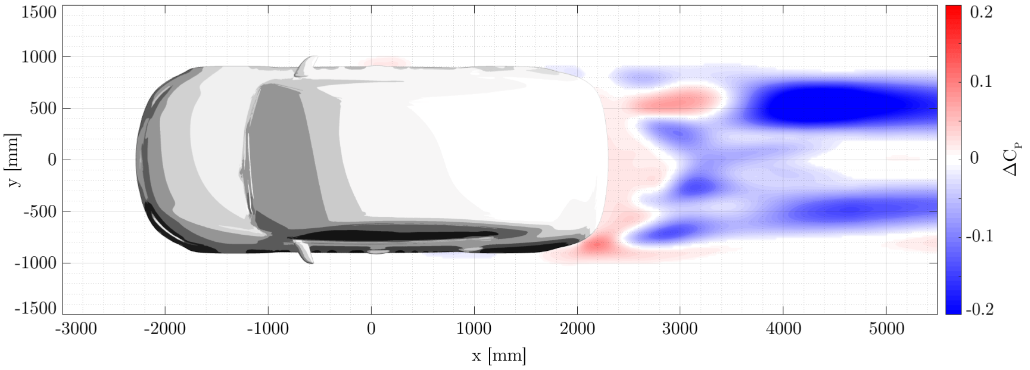

(b) MW

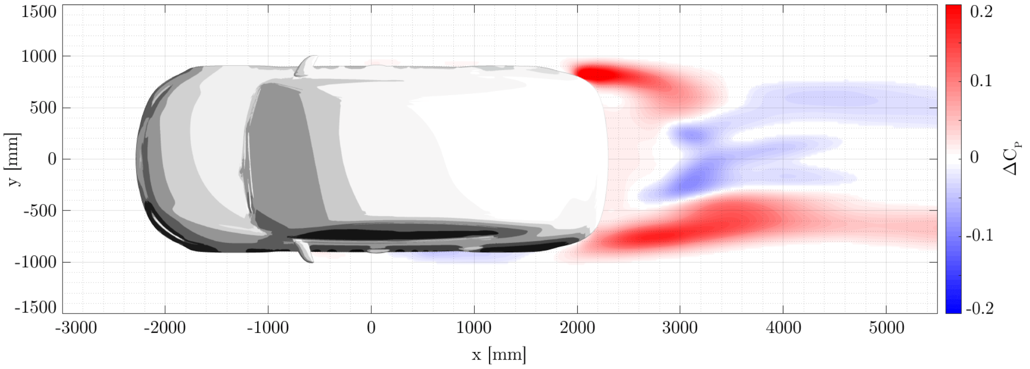

(c) MW-TO

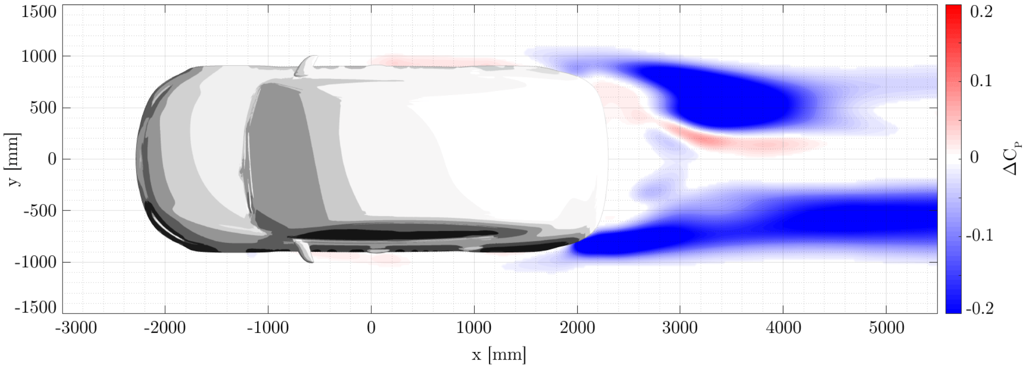

(d) MRF

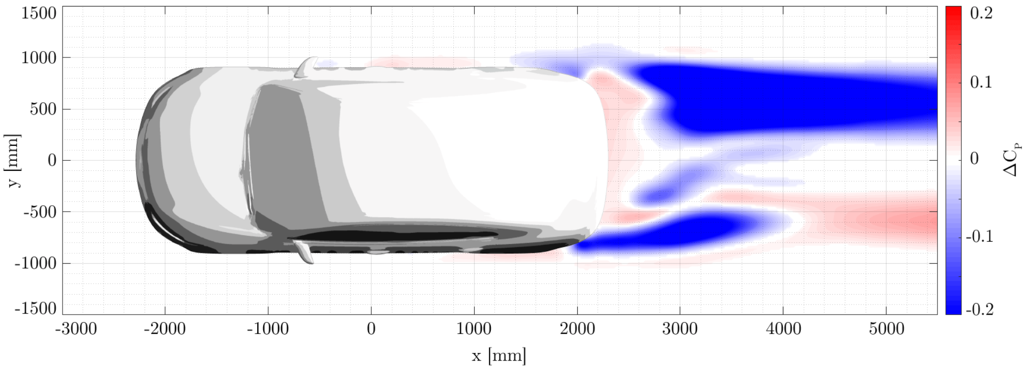

(e) MRF&MW

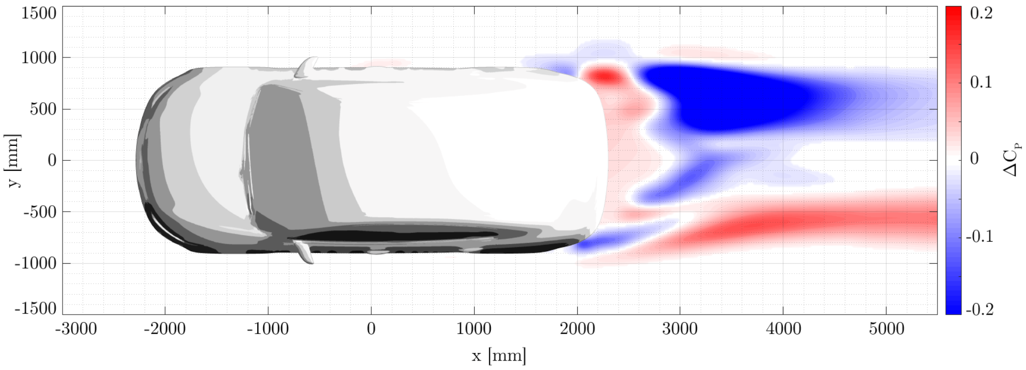

(f) MRF&MW-TO

Figure 7.11: Pressure coefficient differences ΔC_P downstream of the vehicle in *plane G* for *Rim16*. Simulation cases *B.16.*-B.16.NR*.

The analysis results of the tail area in *plane H* (Fig. 7.12) reveal an increase of the pressure downstream the center plane of the vehicle in close proximity to the rear surface. This effect occurs in all rotation methods, but the pressure increase is comparatively low for the *MRF* approach, in a value range of $\Delta C_P < 0.01$.

The modified flow situation of the vehicle results in complex structural alterations of the wake topology, especially at the peripheral areas of the dead water region (Fig. 7.13). Similarities between the individual load cases with rotating wheels are determined by means of pressure increases at the lower lateral sides and pressure reductions downstream of the boot lid separation edge, as well as near the ground at the center of the vehicle. The two high pressure areas bounding this central low pressure region laterally are the two high pressure underbody streams that were discussed in the previous section. The streams are recognizable for all rotation approaches, but for *MRF* in a weakened form. The pressure alteration fluctuations in this region, together with the flow topology analysis at the underbody (Fig. 7.9), indicate a shifted air flow topology that originates from the altered flow situation at the underbody, and in further consequence, from the modified rear wheel wake structures. The pressure situation downstream of the rear lights and the lateral areas below is affected by the individual rotation methods in different ways. While

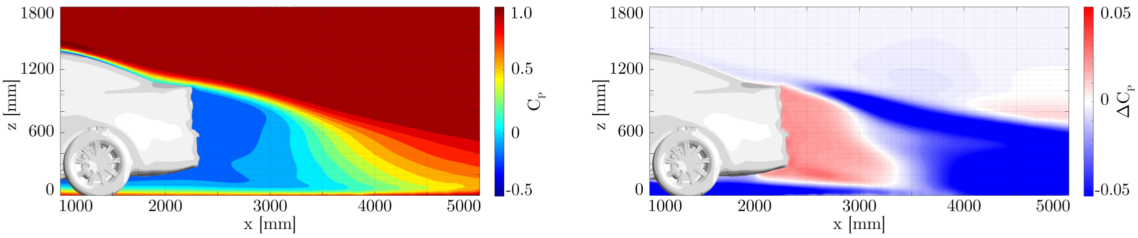

(a) NR

(b) MW

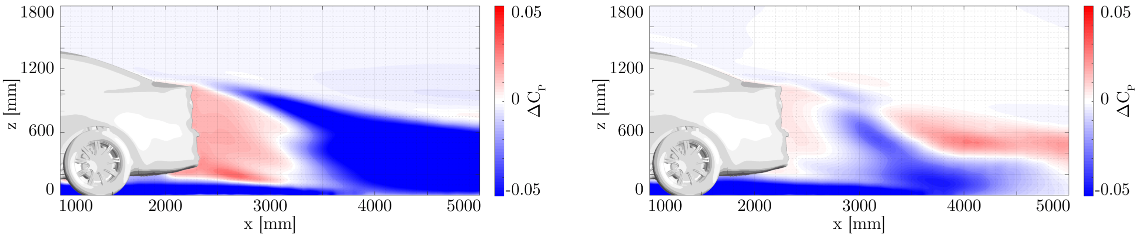

(c) MW-TO

(d) MRF

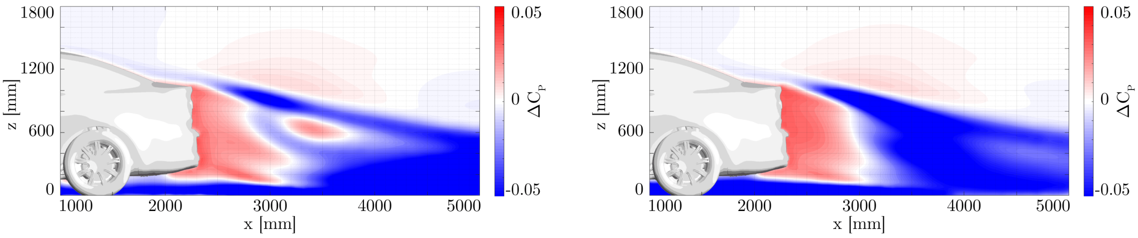

(e) MRF&MW

(f) MRF&MW-TO

Figure 7.12: Pressure coefficient differences ΔC_P at the vehicle wake in *plane H* for *Rim16*. Simulation cases *B.16.*-B.16.NR.*

MW and *MW-TO* predict positive and negative pressure changes, *MRF* reveals an area of massive pressure reduction. A slight increase in pressure can be detected over large areas at the center of the rear base for *MW* and *MW-TO*, but not for *MRF*, due to its small extent in the x-direction in this case. However, its existence is apparent in *plane H* (Fig. 7.12d). The results of this study yield that *MRF&MW* and *MRF&MW-TO* predict the wake structure alterations of *MW* or *MW-TO* and *MRF*, respectively.

The effects of the vehicle's wake alterations on the vehicle itself can be determined through evaluation of the surface pressure situation at its base area. The results of this study are shown in Fig. 7.14 and reveal pressure increases for all rotational methods in comparison to the stationary case. This also applies to the *MRF* method, where an increase in pressure was hardly detectable by previous analyses in this region. Furthermore, the pressure alteration structures show asymmetric behavior, especially for *MW* and *MRF*, which can be attributed to the unsymmetric nature of the vehicle geometry, and thus to the unequal alterations of the flow field. The strongest pressure gains are predicted by both combined wheel rotation approaches *MRF&MW* and *MRF&MW-TO*.

The numerical results show good qualitative correlation with the results of the wind tunnel experiment for the flow topology alterations in the wake area (Fig. 7.3) and for the

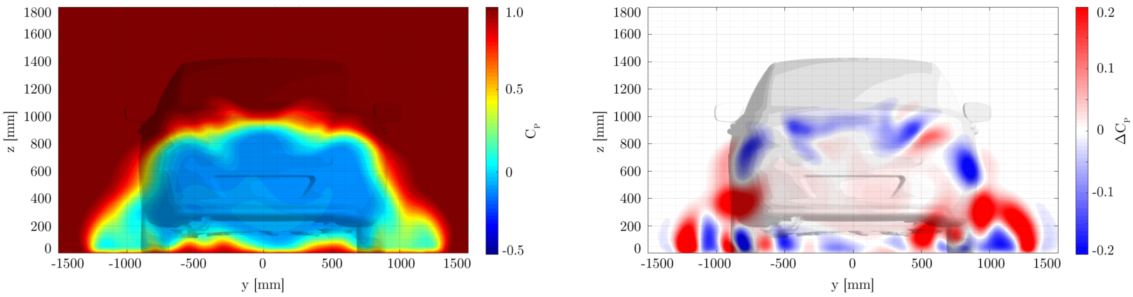

(a) NR

(b) MW

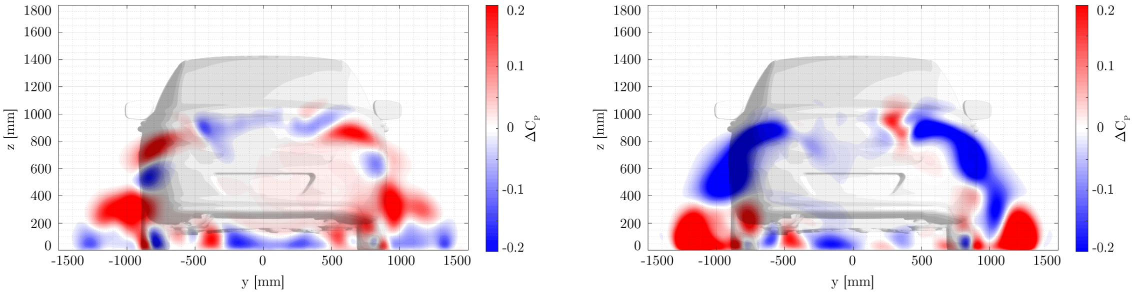

(c) MW-TO

(d) MRF

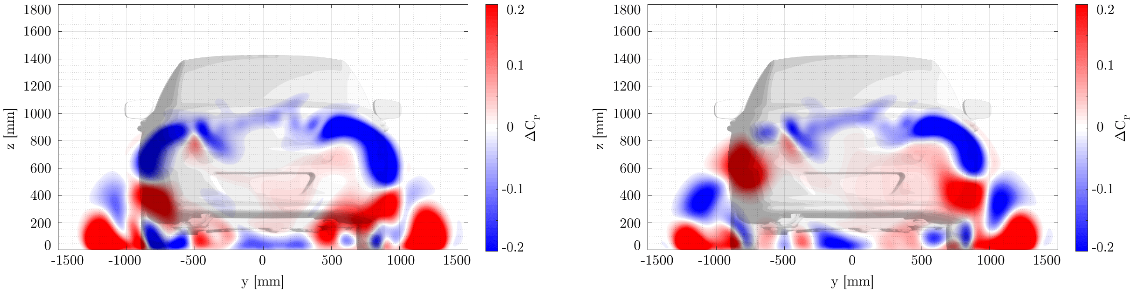

(e) MRF&MW

(f) MRF&MW-TO

Figure 7.13: Pressure coefficient differences ΔC_P at the vehicle wake in *plane D* for *Rim16*. Simulation cases *B.16.*-B.16.NR*.

surface pressure changes at the rear of the vehicle (Fig. 7.4). The general pressure increase of the vehicle's wake region, and thus also over wide areas of the vehicle's base surface, could be reproduced by all rotation methods. However, the structural alterations in the wake area are predicted with different accuracy by the individual rotation methods. The pressure reduction regions downstream of the trunklid separation edge were reproduced by all simulations. Nevertheless, the reductions were underestimated by *MW-TO* at the sidewise border areas. The pressure increases downstream of the lateral tail surfaces were reproduced over large ranges by *MW* and *MW-TO*, but not by *MRF*. The experimentally measured pressure increase near the ground, at the sides of the vehicle, were correctly predicted by all rotation methods. However, although a rise in pressure is predicted by *MW* and *MW-TO*, the simulation results of these rotation methods also reveal additional pressure reduction zones that were not detected in the experiment. Although *MW*, *MW-TO*, and *MRF* were able to reproduce some of the observed effects of the wind tunnel experiments, they fail to predict others. However, all investigated effects could be simulated by

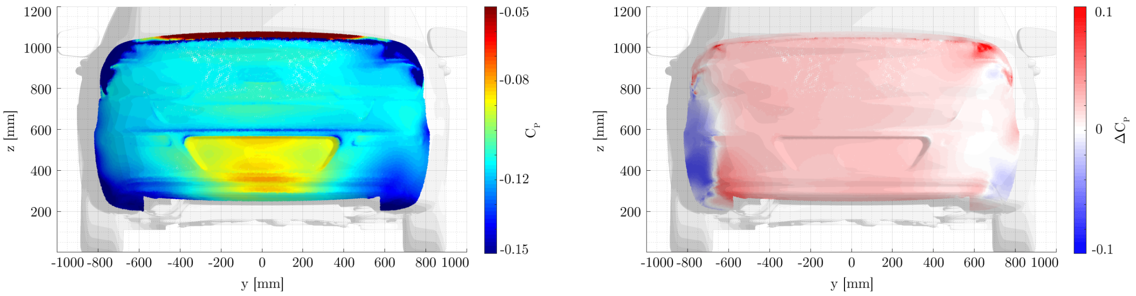

(a) NR

(b) MW

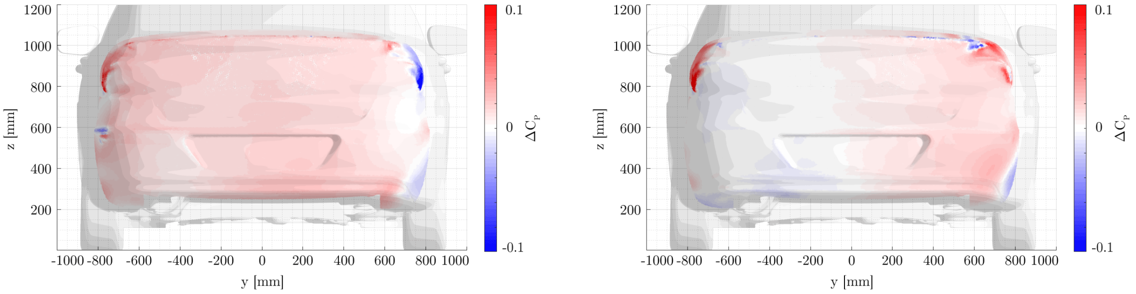

(c) MW-TO

(d) MRF

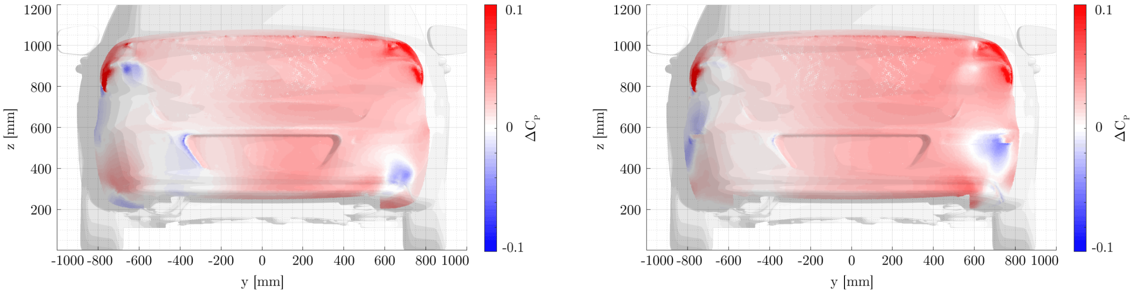

(e) MRF&MW

(f) MRF&MW-TO

Figure 7.14: Pressure coefficient differences ΔC_P at the vehicle tail surface for *Rim16*. Simulation cases *B.16.*-B.16.NR*.

the combinations *MRF&MW* and *MRF&MW-TO*, wherefore, the greatest similarities of the alterations of the wake structure and the surface pressure situation in the rear area of the vehicle could be observed with these two approaches.

Summary of the surface pressure situation

In order to study the impact of rotating wheels on the air flow situation of the vehicle, the surface pressure distribution in four vehicle zones is evaluated. In addition to the previously discussed surface pressure situation up- and downstream of the wheel arch ($\mathrm{VZ}_{\mathrm{sideA}}$, $\mathrm{VZ}_{\mathrm{sideB}}$) and at the rear ($\mathrm{VZ}_{\mathrm{tail}}$), the surface pressure at the upper vehicle area along the vehicle's centerline ($\mathrm{VZ}_{\mathrm{top}}$) is also examined. As these results have not yet been presented, they will be discussed first below. The studies of the differential surface pressure at $\mathrm{VZ}_{\mathrm{top}}$ are supplemented by the outcomes of the differential analysis, between stationary and

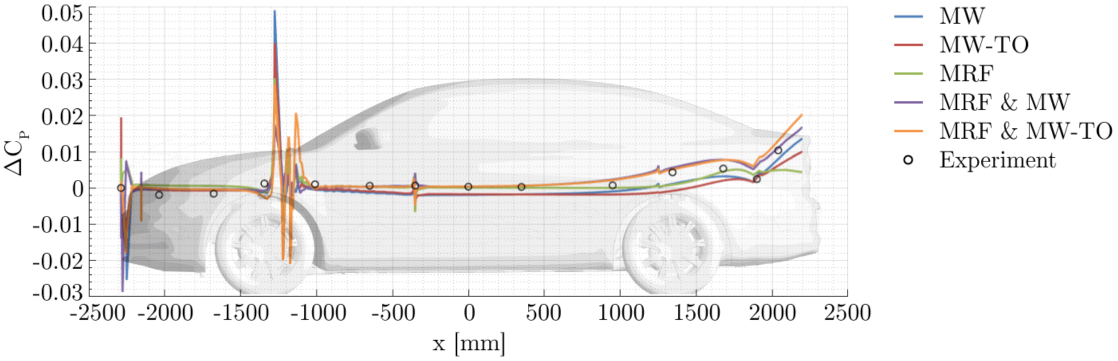

Figure 7.15: Pressure coefficient differences ΔC_P at the upper vehicle surface along centerline of the vehicle. Simulation cases *B.16.*-B.16.NR* and experimental test case *WT.B.16.RT-WT.B.16.NR*.

rotating wheels, of the wind tunnel experiment and are shown in Fig. 7.15.

The surface pressure analysis at VZ_{top} reveals a similar pressure evolution downstream of the vehicle for all simulation methods. The pressure changes remain in a small value range of $| \Delta C_P | < 0.01$ for the major part of the vehicle, which suggests marginal flow topology alterations in the upper vehicle area due to rotating wheels. The resulting differences in pressure are negligible at the hood, but increase downstream towards the tail area, which correlates with the pressure increase detected at the vehicle rear in the previous section of this chapter. Major surface pressure alterations on the roof are detected in the area of the front grill and at the windscreen wipers in the region of the windshield root, where a positive differential pressure peak is followed by a negative one, and vice versa. Furthermore, differential pressure peaks are detected in the area of the roof joints at the windscreen and the rear window, as well as the parting line between the tail and trunk lid. These effects can be explained by the fact that even small pressure alterations can lead to displaced flow separations at the component edges in these regions, and thus to measurable pressure changes. It is evident that the results of the numerical investigation correlate with the results of the wind tunnel experiment, since both the minor flow topology alterations and the pressure increase in the rear are reproduced by all rotation methods. However, in the experiment, due to the limited number of measuring points only pressure losses at the parting line between the rear and the boot lid are detected.

In order to analyse the effects of rotating wheels on the surface pressure distribution of the complete vehicle, the mean deviation of the surface pressure coefficient is calculated for each surface zone between load cases with stationary and with rotating wheels. The computations for regions VZ_{top}, VZ_{sideA}, VZ_{sideB} and VZ_{rear} were carried out according to Eq. (3.56), and the corresponding results are shown in Fig. 7.16 for all simulation cases.

The outcomes of this analysis along the center-line of the vehicle (VZ_{top}) reveal a marginal or even no impact of rotating wheels on the pressure distribution in the upper area of the vehicle with values of $\overline{\Delta C_P} \leq 0.003$. Likewise, the impact on the surface pressures upstream of the front wheel arch (VZ_{sideA}) is low and shows pressure reductions for all rotation methods, except for *MRF&MW-TO*. An increase in surface pressure is detected

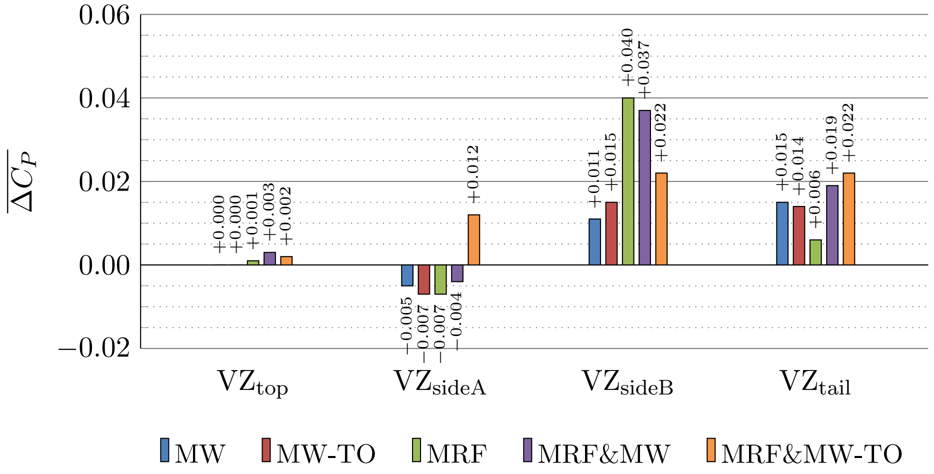

Figure 7.16: Mean deviation of the surface pressure coefficient $\overline{\Delta C_P}$ between stationary (*B.16.NR*) and rotating wheels (_B.16.*_) for *Rim16* at various vehicle zones.

at VZ_{sideB}, downstream of the wheel house, for all rotational methods, with the strongest raise for *MRF* and in the combinations of *MRF&MW* and *MRF&MW-TO*, indicating the biggest air flow deviations. The analysis results at VZ_{tail} yield an increase of pressure for all simulation methods in accordance with to the surface pressure analysis in this area (Fig. 7.14). However, this pressure reduction is low for the *MRF* method in comparison to the results of other rotation methods, which has already been discussed earlier in this chapter.

The validation of the numerical results with the outcomes of the wind tunnel experiment for the test case with *Rim16* and enabled engine compartment flow (Fig. 7.5) reveals that all rotation approaches underestimate the surface pressure alterations on the vehicle and show correspondingly lower values of the mean pressure coefficient differences, especially at VZ_{sideB} and the VZ_{tail} area. A possible explanation for this deviation may be the limited number of pressure sensors, and therefore the restricted measurement resolution and the resulting constraints to detect and identify local pressure gradients. The marginal impact of rotating wheels on the pressure situation at VZ_{top}, as well as the pressure increase at VZ_{tail} and downstream of the wheel arch at VZ_{sideB}, are reproduced by all rotational methods. Furthermore, the wind tunnel measurements reveal a slight pressure increase at VZ_{sideA}, upstream of the front wheel arch, which is also predicted by the *MRF&MW-TO* method, while all other rotation methods show a slight pressure decrease in this area. However, the magnitude of these pressure alterations is comparatively low in contrast to the outcomes of the wind tunnel test, especially for *MW* and *MW-TO*. In summary, it can be stated that the simulation results of *MRF&MW* and *MRF&MW-TO*, as well as *MRF*, show the highest correlations with the results of the experiment.

7.4 Impact of wheel rotation on vehicle drag

The focus has so far been on the study of the effects of wheel rotation on the local and global air flow situation of the vehicle. However, the determined flow topology alterations and the resulting interference effects must ultimately affect the integral aerodynamic vehicle forces. Therefore, the effects of rotating wheels on the aerodynamic drag will be examined in this section. For this purpose, initially the development of the vehicle, body and wheel drag along the vehicle axes is investigated based on numerical results. The integral drag quantities offer a simple but effective possibility to validate the simulation results with the experiment. Therefore, the impact of rotating wheels on the integral vehicle drag coefficient will be discussed subsequently by means of experimental and numerical data.

Development of vehicle, body and wheel drag differences

The origin and development of the total aerodynamic drag differences $\Delta C_{D,\mathrm{CV}}$ between all load cases with rotating wheels and the stationary reference case can be identified through an analysis of the accumulated vehicle drag coefficient difference $\Delta C_{D,\mathrm{CV,acc}}$. For this purpose, $C_{D,\mathrm{CV,acc}}$ is determined for all load cases according to the analysis described in Chapter 3.5.9. The accumulated vehicle drag coefficient difference is calculated through

$$\Delta C_{D,\mathrm{CV,acc}} = C_{D,\mathrm{CV,acc,stat}} - C_{D,\mathrm{CV,acc,rot}} \tag{7.1}$$

and the results are displayed along the vehicle's main axes. In Eq. (7.1), $C_{D,\mathrm{CV,acc,stat}}$ is the accumulated vehicle drag coefficient for the case with stationary wheels, while $C_{D,\mathrm{CV,acc,rot}}$ corresponds to the cases with rotating wheels.

In addition to the vehicle drag, the separate evolutions of the vehicle body drag $\Delta C_{D,\mathrm{BODY,acc}}$ and the wheel drag $\Delta C_{D,\mathrm{WHEELS,acc}}$ are investigated as well. $\Delta C_{D,\mathrm{WHEELS,acc}}$ considers the drag of all tires and rims, while $\Delta C_{D,\mathrm{BODY,acc}}$ includes all remaining components of the vehicle. The results are displayed in percent, with the vehicle drag coefficient for stationary wheels as the reference value. The results for load cases with rims *Rim16* and enabled engine compartment flow are shown in Figs. 7.17, 7.18 and 7.19. Corresponding analyses for *Rim17* and *Rim18* can be found in Appendix C.

The analysis results reveal that drag alterations occur all over the vehicle independent of the applied rotation methods, which correlates with the flow topology analyses from the previous section. Based on these findings it can be concluded that rotating wheels affect not only the air flow situation in proximity of tires and rims, but the flow topology in vicinity of the whole vehicle - starting already upstream of the front wheels and developing downstream until the tail.

The major vehicle drag changes occur especially at the wheel and wheel house regions and at the tail (Fig. 7.17), where the front wheel arch and especially the tail are mainly responsible for drag reduction. The analyses of the drag development for the vehicle body (Fig. 7.18) and the wheels (Fig. 7.19) demonstrate that the body is responsible for the majority of the aerodynamic drag changes, where the main part originates from the vehicle tail. The wheel drag study reveals that especially the front wheels contribute to the

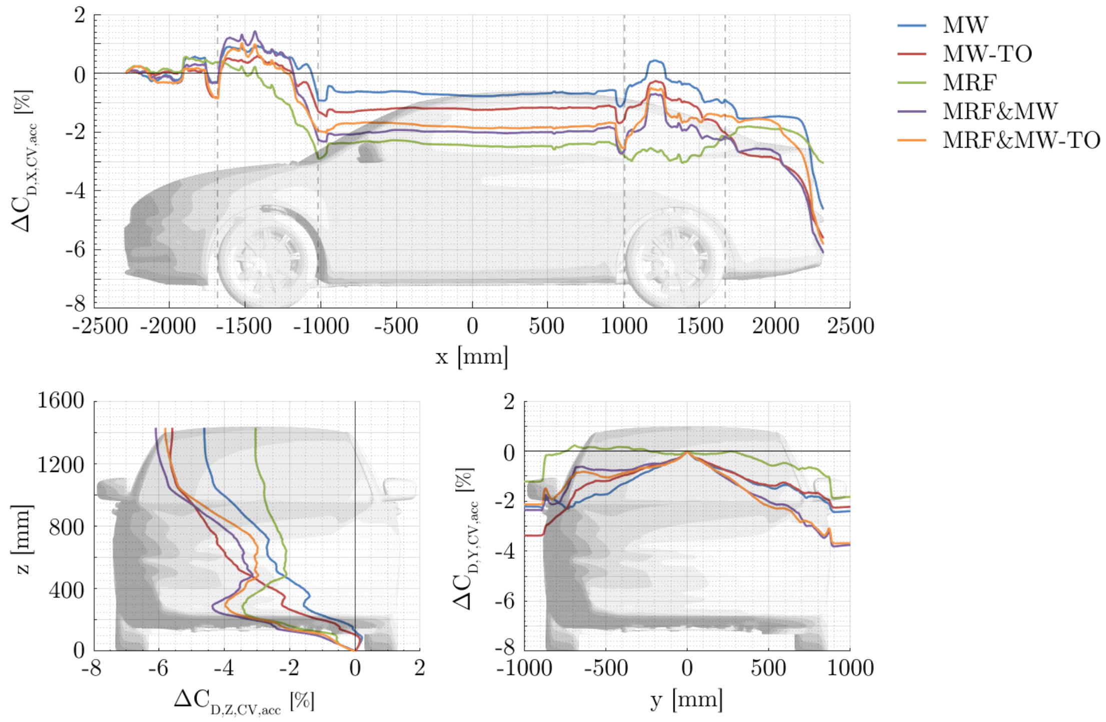

Figure 7.17: Development of the accumulated vehicle drag coefficient differences $\Delta C_{D,\mathrm{CV}}$ along the vehicle axes for *Rim16*. Simulation cases *B.16.*-B.16.NR*.

resistance reduction, while the rear wheels have the opposite effect, which counteracts the reduction and almost eliminates it. This applies to all rotation methods, except *MRF*, where the influence of the front wheels is far greater than that of the rear wheels.

The differential drag analyses along the x axis, from the front of the vehicle downstream to the tail area (Fig. 7.17), reveals minor drag alterations already at the front end and at the engine compartment. However, significant changes occur in the area of the front wheel arches and the front wheels. These effects can be explained by the fact that the wheel rotation causes pressure increases in the frontal and rear section of the wheel houses surface (Fig. 6.11) and the tire tread (Fig. 6.6). A strong reduction of drag can be recognized at the front wall of the wheel arch (Fig. 7.18) due to the positive pressure difference that acts on this backward aligned surface. This tendency is the opposite for the wheels (Fig. 7.19), since their surfaces are oriented in the forward direction, wherefrom the subsequent increase in drag results. This effect is predicted by all rotation methods, except for *MRF*, suggesting that *MW* causes this phenomenon. This assumption correlates with the conclusions from Chapter 6, where surface pressure increases at the front wheel arch surface was demonstrated through early flow separation caused by the *MW* approach at the tire tread. The opposite phenomenon is observed downstream of the front wheels, where the increased pressure in the wheel wake reduces the drag, while the resistance of the vehicle body increases due to the positive differential pressure on the forward oriented rear wall of the wheel arch. However, in total a drag reduction for the front wheel arch area is predicted by all rotation methods, since the drag reduction in the front half of the wheel arch is greater than the drag increase in the rear half. The *MRF* method reveals the

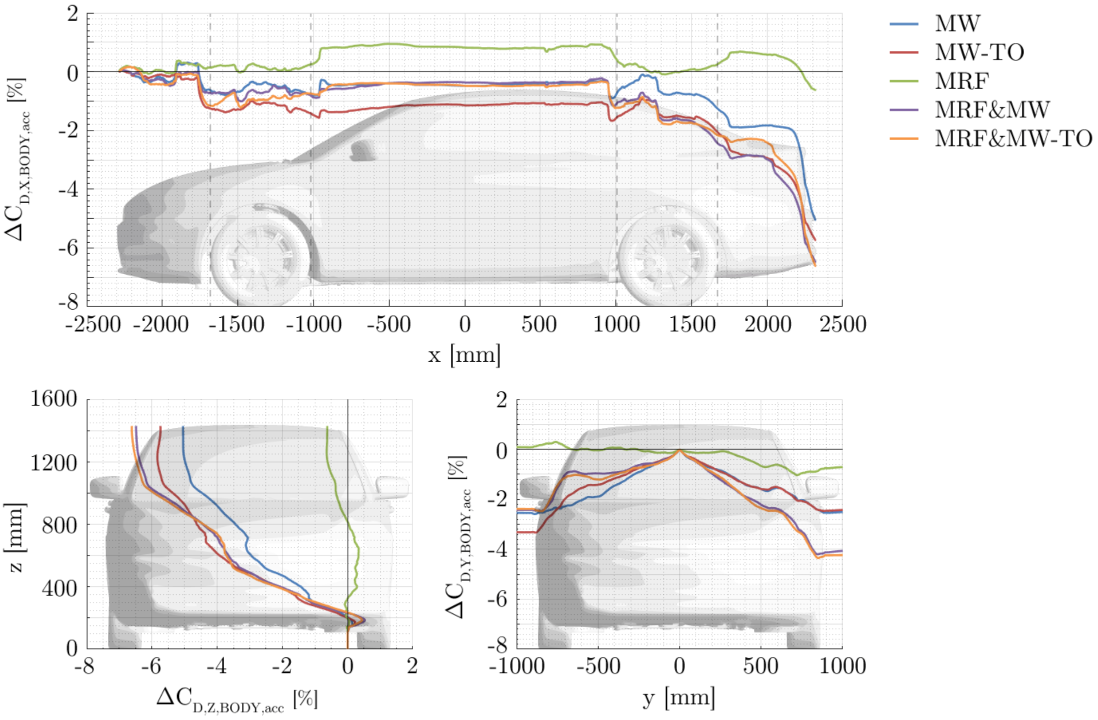

Figure 7.18: Development of the accumulated body drag coefficient differences $\Delta C_{D,\mathrm{BODY}}$ along the vehicle axes for *Rim16*. Simulation cases *B.16.*-B.16.NR*.

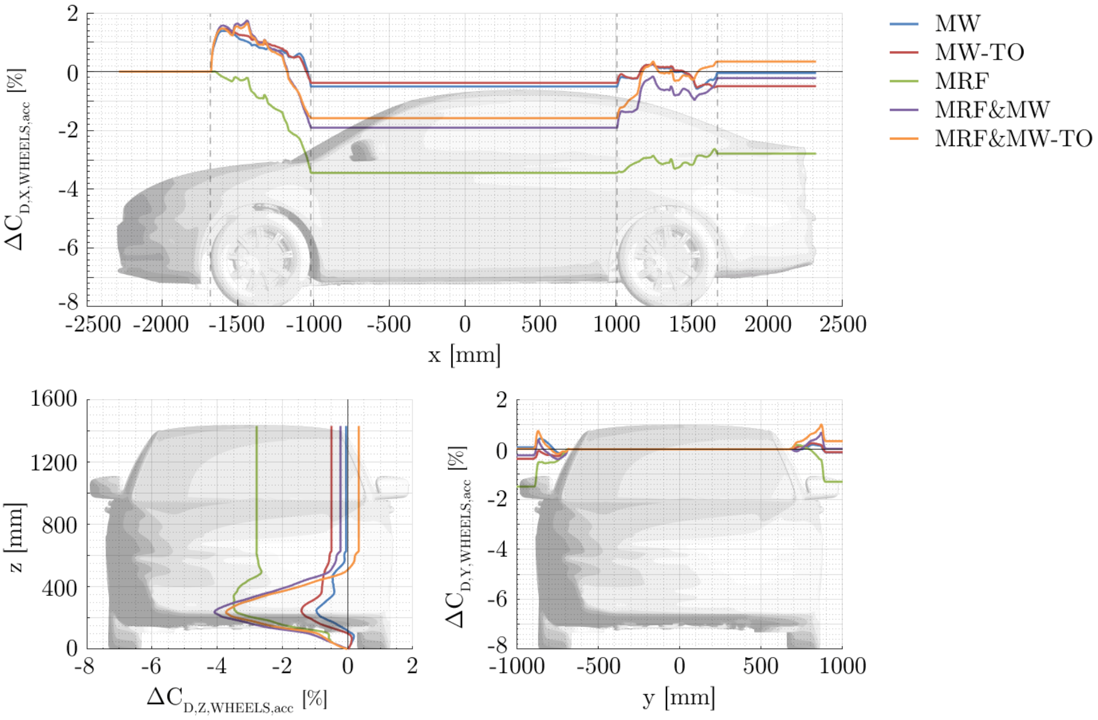

Figure 7.19: Development of the accumulated wheel drag coefficient differences $\Delta C_{D,\mathrm{WHEELS}}$ along the vehicle axes for *Rim16*. Simulation cases *B.16.*-B.16.NR*.

greatest drag reduction due to the lack of wheel resistance in the front and the resulting strong integral drag reduction of the wheels, which even compensates the drag increase in the rear of the wheel house. *MRF&MW-TO* predicts an increase in resistance due to the wheels, which is compensated by the drag reduction caused at the vehicle body, resulting in a reduced total vehicle drag. The influence of *MRF&MW* and *MRF&MW-TO* on the drag of the vehicle body, and the total vehicle is greater than the respective influences of *MW*, *MW-TO* and *MRF*, suggesting that the effects of *MW/MW-TO* and *MRF* are to some extent additive. The drag development of different rotation methods at the middle of the vehicle is similar for all cases and shows no significant changes. At the rear wheel arches, the tires cause an increase in resistance in the front half of the wheel arch, which is similar, but not as strong as at the front wheel arch. A pressure recovery in the wake of the wheels is not recognizable, wherefore the rear wheels in total make a positive contribution to the total vehicle drag. In contrast to the front wheels, this also applies to the *MRF* method. On the vehicle body, a massive drag reduction develops from the area of the rear wheel arch downstream to the tail of the vehicle. This phenomenon can be attributed to the altered flow topology in the rear area and the resulting surface pressure increase at the vehicle base, which supports the pressure recovery in this area and thus reduces the drag value.

Proceeding from the center of the y axis and following the two strains to the left and right sides of the vehicle (Fig. 7.17), it is noticeable that the differences in drag development is not equal for both lateral surfaces, which was already recognized through the flow topology study and can be ascribed to the unsymmetric geometry of the vehicle. Major changes occur at the wheel and wheel house area, and especially at the vehicle sides.

The drag development along the z axis (Fig. 7.17) reveals that the major drag alterations can be narrowed to a range up to tail height at around $z = 1000$ mm, i.e. the lower part of the vehicle. The vehicle drag evolution above this level is similar for all rotational methods, and small compared to the lower regions, indicating that upper vehicle areas play a minor role in aerodynamic resistance development due to wheel rotation, in accordance with the respective surface pressure analysis at $\mathrm{VZ}_{\mathrm{top}}$ (Fig. 7.16).

The analysis of the drag evolution of the wheels in y- and in z-directions (Fig. 7.19) yields a drag increase from the inside to the outside, which finally abruptly drops. Based on the position of this effect, this sudden decrease can be attributed especially to the spokes. It is revealed that drag reduction occurs in the lower region of the rims, which is eventually compensated for the most part by an increase in the upper rim area. Here, a difference between the two groups of rotation approaches based on *MW* and *MRF* can be determined, with the effect more pronounced for the second group.

The investigations of the drag development on the vehicle show similar results for all rotation methods. Both the characteristic resistance development in the area of the wheel arches and the distinctive drag reduction in the rear area are predicted. However, *MRF* (with rims *Rim16*) is an exception and reveals flow structures in the region of the front wheels, that result in a strong reduction of resistance. As a result, the biggest changes in resistance are caused by wheels and body, and not by the body alone.

Vehicle drag - Experimental results

The impact of wheel rotation on the integral aerodynamic vehicle drag is determined by means of differential analyses between cases with rotating and with stationary wheels. Analyses are carried out for load cases with mockup configuration and with enabled engine compartment flow. Differential values of the vehicle drag $\Delta C_{D,\mathrm{CV}}$ are calculated according to

$$\Delta C_{D,\mathrm{CV}} = C_{D,\mathrm{CV,rot}} - C_{D,\mathrm{CV,stat}} \tag{7.2}$$

where $C_{D,\mathrm{CV,rot}}$ corresponds to the vehicle drag for a setup with rotating wheels and $C_{D,\mathrm{CV,stat}}$ represents the reference case with stationary wheels.

The results are expressed as percentage values to allow the comparison of various vehicle configurations and rim geometries. The reference case is always the setup with stationary wheels. The results of the experimental study are listed in Table 7.1 for vehicle mockup configurations and in Table 7.2 for vehicles with enabled engine compartment flow and are subsequently discussed, while the numerical results are presented in the next section.

Case	$\Delta C_{D,\mathrm{CV}}[\%]$
Rim16	-9.1
Rim17	-7.1
Rim18	-9.0

Table 7.1: Differences in the vehicle drag coefficient $\Delta C_{D,\mathrm{CV}}$ between stationary and rotating wheels for mockup configurations.

Case	$\Delta C_{D,\mathrm{CV}}[\%]$
Rim16	-7.5
Rim17	-7.9
Rim18	-7.4

Table 7.2: Differences in the vehicle drag coefficient $\Delta C_{D,\mathrm{CV}}$ between stationary and rotating wheels with enabled engine compartment flow.

The analysis results demonstrate a significant impact of rotating wheels on the vehicle drag for all configurations. Drag values are reduced by similar amounts, which suggests that this effect is largely independent of the rim geometry or engine compartment flow for this test vehicle. The decrease of the total drag correlates with the results of the wake topology alteration and the resulting pressure increase at the rear of the vehicle discussed in previous sections. The flow topology alterations within the wheel arch caused by the wheel rotation thus affect the flow situation in the vicinity of the entire vehicle, which results in a modified surface pressure situation, and ultimately affects the integral drag value of the vehicle.

Vehicle drag - Numerical investigations

As in the experimental investigations, the impact of rotating wheels is evaluated numerically by a differential analysis of the integral vehicle drag for simulation cases with rotating wheels in relation to the corresponding stationary reference cases. This examination is carried out for all wheel rotation methods applied at three rim variants, as well as for the mockup configuration and for enabled engine compartment flow. Furthermore, these investigations are performed for both rim orientations of each geometry. The calculation of the differential drag values are performed according to Eq. (7.2). The results for the mockup and enabled engine compartment flow are shown in Fig. 7.20 and Fig. 7.21, respectively.

The analysis results reveal that all applied wheel rotation methods affect the vehicle drag and reduce it against the stationary case. This effect applies to all rim geometries and orientations, as well as to the mockup and simulation cases with engine compartment flow. However, for the mockup case with rims *Rim17*, the rotation methods *MW* and *MW-TO* yield no impact on the total vehicle drag. Deviations of the vehicle drag between rotating wheels and stationary wheels yield values of up to -10.2% for the mockup and up to -7.9% with enabled engine compartment flow. The greatest reduction in resistance is achieved by applying combinations of *MRF&MW* and *MRF&MW-TO* on tires and rims. Furthermore, the drag reducing effect is lower for the *MW* rotation method than for *MW-TO*. These trends are similar and comparable for all rim variants. The analysis of rim orientations α and β reveals alterations of the integral vehicle drag, thus demonstrating the importance of rim orientations for numerical simulations, as stated and discussed in Chapter 5.

Finally the results of the numerical investigations are validated with the outcomes of the wind tunnel experiment to determine the prediction accuracy of each rotation approach. For this purpose, a differential analysis between the changes of the total vehicle drag coefficient for rotating versus stationary wheels is performed between numerical and experimental data. This approach ensures that only the impact of wheel rotation is evaluated and no other factors are considered in the analysis. Thus, the differences in drag change between the numerical and experimental results are calculated according to

$$\Delta\left(\Delta C_{D,\mathrm{CV}}\right) = \Delta C_{D,\mathrm{CV,sim}} - \Delta C_{D,\mathrm{CV,exp}} \tag{7.3}$$

where $\Delta C_{D,\mathrm{CV,sim}}$ is the difference in drag of the simulation and $\Delta C_{D,\mathrm{CV,exp}}$ represents the corresponding reference value of the experiment.

This analysis is carried out for the mockup configuration, as well as with engine compartment flow, where the differential values are represented as percentage deviations of the reference value from the experiment. The results are presented in Fig. 7.22 for the mockup configurations and in Fig. 7.23 for engine compartment flow configurations.

The investigations yield deviations in the prediction of the impact of rotating wheels on the total vehicle drag between simulation and experiment. The magnitudes of the differences are in a value range of -1.1% to $+7.5\%$ and depend on the rotation method, engine compartment flow configuration, as well as tire geometry and rim orientation.

The simulations predict the vehicle drag for the mockup and variants with engine compartment flow with comparable accuracy, although minor differences between the two configurations can be detected. The deviations between simulation and experiment are in a range of -1.1% to $+7.5\%$ for the mockup, whereas this range is narrower for enabled engine compartment flow with deviations between $+0.1\%$ and $+5.9\%$.

The combinations *MRF&MW* and *MRF&MW-TO* show the best agreement with the experiment with an absolute average prediction accuracy $\overline{\left|\Delta\left(\Delta C_{D,\mathrm{CV}}\right)\right|} \leq 1.2\%$ for the

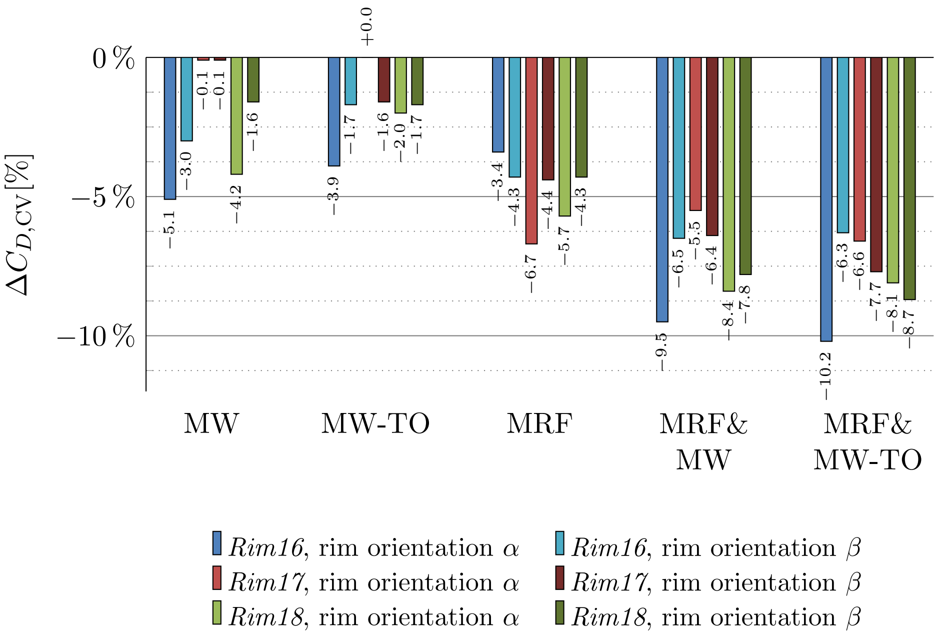

Figure 7.20: Differences in the vehicle drag coefficient $\Delta C_{D,\mathrm{CV}}$ between stationary and rotating wheels for two rim orientations and mockup configuration. Simulation cases *A/C.16/17/18.*-A/C.16/17/18.NR.*

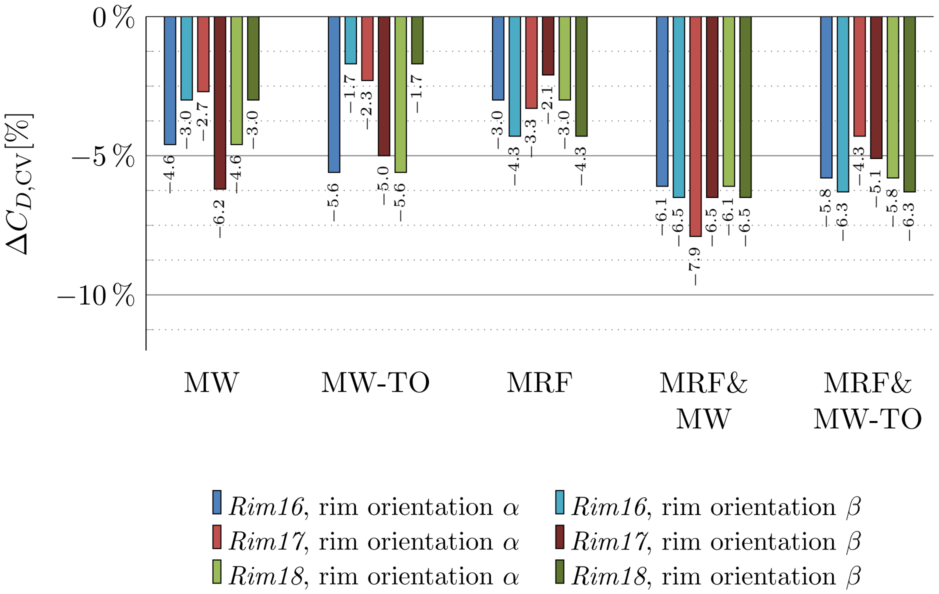

Figure 7.21: Differences in the vehicle drag coefficient $\Delta C_{D,\mathrm{CV}}$ between stationary and rotating wheels for two rim orientations and enabled engine compartment flow. Simulation cases *B/D.16/17/18.*-B/D.16/17/18.NR.*

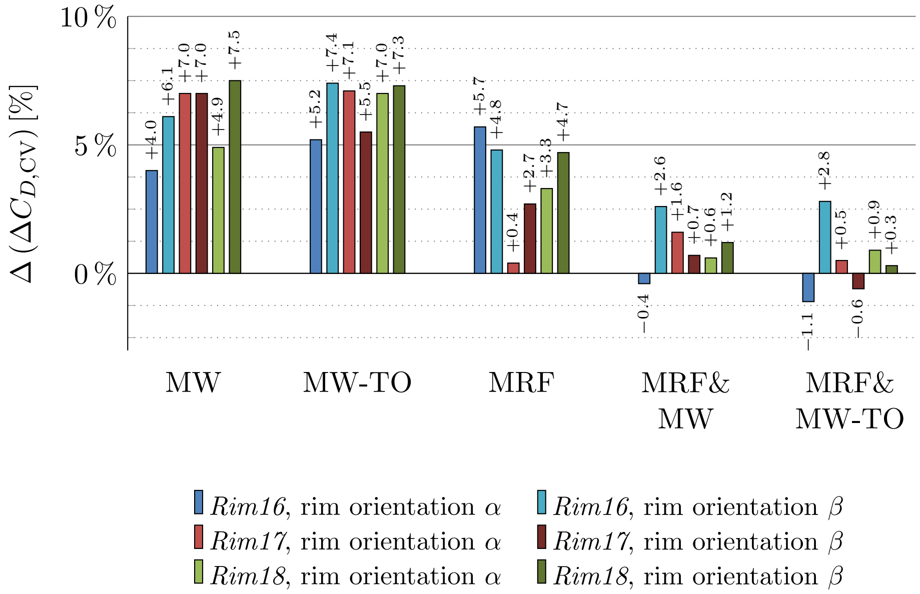

Figure 7.22: Deviation of the simulated vehicle drag coefficient from the experiment for individual wheel rotation methods for two rim orientations and for the mockup configuration. Simulation and experimental test cases *A/C.16/17/18.*-WT.A.16/17/18.RT*.

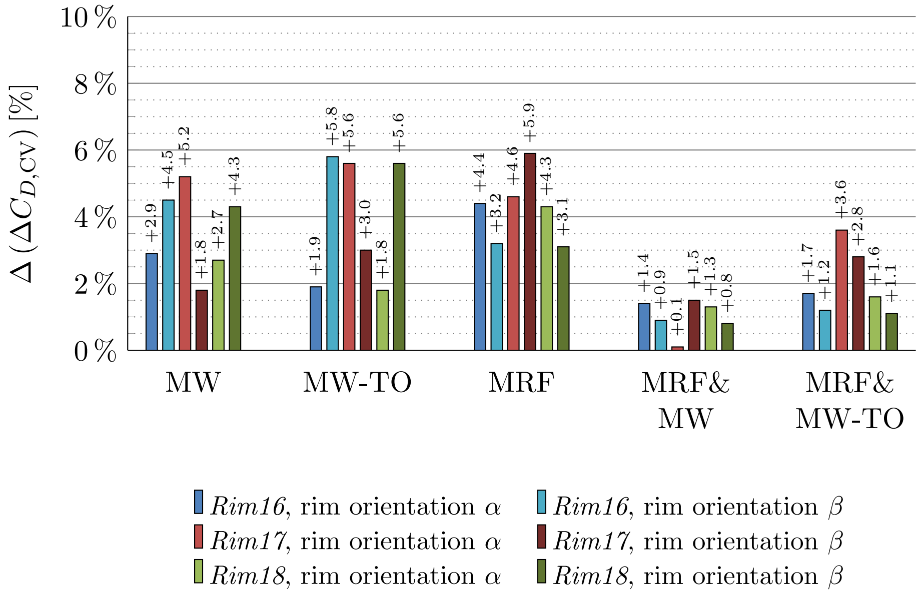

Figure 7.23: Deviation of the simulated vehicle drag coefficient from the experiment for individual wheel rotation methods for two rim orientations and enabled engine compartment flow. Simulation and experimental test cases *B/D.16/17/18.*-WT.B.16/17/18.RT*.

mockup and $\overline{|\Delta\left(\Delta C_{D,\mathrm{CV}}\right)|} \leq 2.0\%$ with enabled engine compartment flow. Only one simulation case misses an accuracy of $< 3\%$. Although both methods show a similarly good prediction accuracy, *MRF&MW* is slightly more precise than *MRF&MW-TO*. The biggest deviations between simulation and experiment yield *MW*, *MW-TO* and *MRF* with average deviations from 3.4% to 6.4% for the mockup and 3.6% to 4.3% with engine compartment flow. These three rotation methods tend to underpredict the impact of wheel rotation on the overall vehicle drag.

Remarkable, and by no means negligible, is the impact of the rim orientation on the accuracy of the simulation results. There are alterations up to 3.9% between rims in orientations α and β, on which the same wheel rotation method is applied. Furthermore, the deviation tendencies of simulation cases with identical wheel rotation methods and the same rim geometries in different orientations versus the experimental reference values are not the same for all cases. The example of the mockup simulation with applied *MRF&MW-TO* method and rim geometry *Rim16* shows that the case using rim orientation α underestimates the drag reduction by 1.1%, whereas the case using rim orientation β over predicts it by 2.8%.

7.5 Impact of wheel rotation on vehicle-body, wheel, tire and rim drag

The study of drag development along the vehicle axes revealed that large parts of the drag alterations are caused by the vehicle body and that the wheels only make a small contribution. In order to quantify these alterations, the distribution of drag changes is subsequently analysed between vehicle body and wheels, where it is distinguished between the front and rear wheel groups. Furthermore, the proportions of tires and rims will be split and examined separately. These studies are carried out on the basis of simulation cases for rim geometries *Rim16*, *Rim17* and *Rim18* and enabled engine compartment flow. The percentage shares of body and wheels of the vehicle drag alterations are shown in Fig. 7.24, while the resulting proportions between front and rear wheels are visualized in Fig. 7.25. The differential analysis of the total wheel drag distribution across all four wheels between tires and rims is shown in Fig. 7.26 for the stationary case, as well as for all rotational methods. Percentage values are used for comparison between the vehicle configurations. The reference in each case is the drag value of the total wheel of the respective vehicle configuration.

The results reveal that the majority of vehicle drag results from the vehicle body (Fig. 7.24), in accordance with the findings of the previous section. The proportion of the body drag is always reduced due to rotating wheels, having a reducing effect on the total vehicle drag. In contrast, the proportion of wheels can also be positive and thus raise the drag. The proportion of the vehicle body varies in a range between -9.0% and -1.4% for the individual rotation methods and rim geometries, while the proportion of the wheels is comparably small with values between -1.9% and $+1.9\%$.

The contribution of the front wheels to the total vehicle drag alteration is negative for all simulation cases (Fig. 7.25), while the proportion of the rear wheels is positive. The front

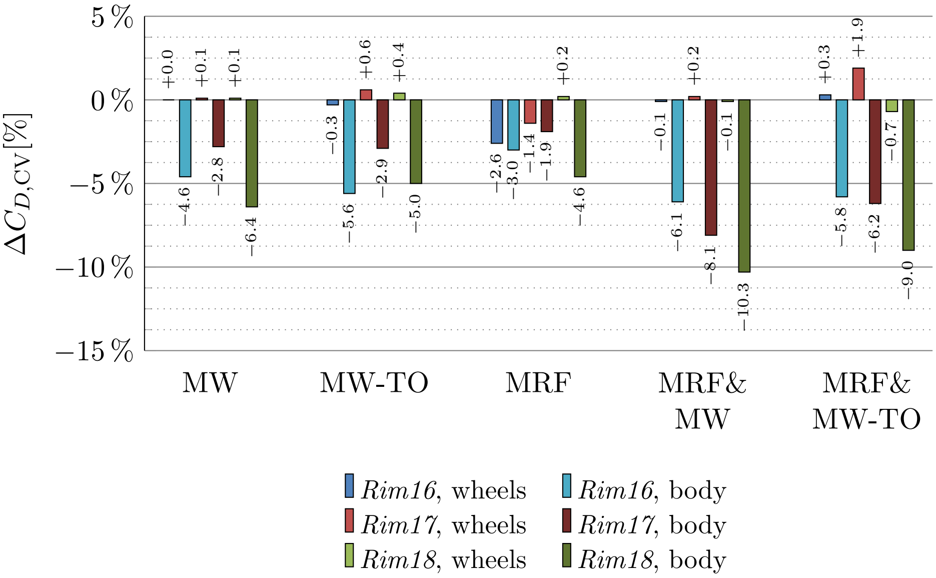

Figure 7.24: Percentage shares of vehicle body and wheels of the vehicle drag alterations due to wheel rotation. Simulation cases *B.16/17/18.*-B.16/17/18.NR*.

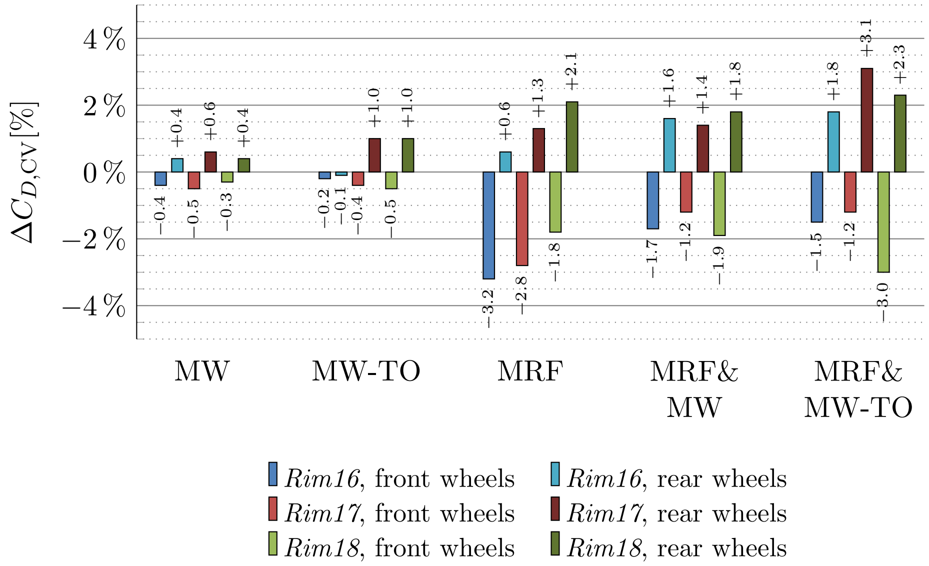

Figure 7.25: Percentage shares of front and rear wheels of the vehicle drag alterations due to wheel rotation. Simulation cases *B.16/17/18.*-B.16/17/18.NR*.

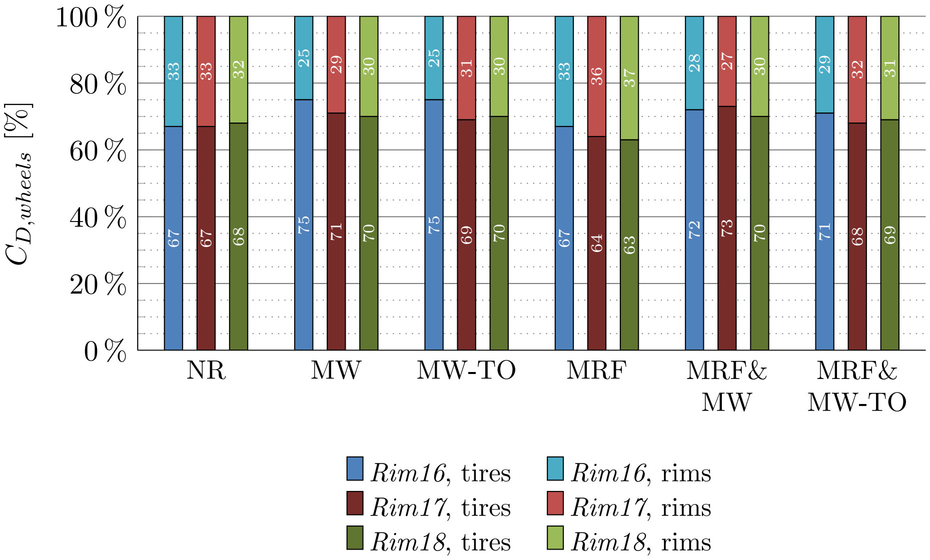

Figure 7.26: Percentage share of tires and rims of the wheel drag. Simulation cases *B.16/17/18.**.

wheels thus contribute to a reduction in drag, while the rear wheels tend to increase it. Since the percentage shares of front and rear wheels have the same order of magnitude, the total impact of all four wheels on the vehicle drag is significantly reduced or even extinguished. The simulation setup with *MW-TO* and rims *Rim16* represents an exception to this, with a minor negative contribution of the rear wheels.

The proportions of rims and tires are comparable for all rim geometries and demonstrate that the major part of the drag alteration is contributed by the tires (Fig. 7.26). The results of the stationary cases reveal an average share of the tires of 67% and 33% for the rims. For simulation cases with rotating tire tread, i.e. *MW*, *MW-TO*, as well as *MRF&MW* and *MRF&MW-TO*, an increase in the impact of the tires and a corresponding decrease of the rims is detected, which yields a marginally higher contribution of 70% for the tires and 30% for the rims. Furthermore, the results reveal that the ratio between tires and rims for the simulation case with *MRF* is similar to those with stationary wheels (*NR*), as both cases predict the least proportion of the tires to the total wheel drag. These findings suggest that the proportions of rims and tires on the total wheel drag depend on the rotating tire tread. Furthermore, wheel rotation increases the percentage share of the tires on the wheel drag.

7.6 Impact of front and rear wheel rotation on vehicle aerodynamics

In the previous studies, various rotation methods were applied collectively on both front and rear wheels. In order to detail these analyses and to understand the effects of front and rear wheel rotation and their impact on the aerodynamic behaviour of the vehicle, these are subsequently examined separately. For this purpose, the individual rotation methods are applied to the two front or rear wheels, while the other wheels remain stationary. The impact on the vehicle air flow topology and on the aerodynamic drag is analysed and compared to the stationary case, i.e. with four stationary wheels, as well as to the respective simulation case with four rotating wheels through application of the same rotation method. Furthermore, the results of front and rear wheel rotation are compared, and differences are discussed. The outcomes are correlated with studies of others, such as Wickern and Lindener [33], Elofsson and Bannister [34], as well as Koitrand and Rehnberg [35], since no measurement results from the experiment are available for these setups.

In accordance with the analyses of previous studies with four rotating wheels, the alterations of the flow topology of the entire vehicle are initially examined. Subsequently, the impact of rotating wheels on the vehicle drag, as well as the contributions of individual vehicle areas, and the origin and evolution of these alterations, are analysed and discussed.

Simulation cases

Additional simulation load cases, which consider the separate application of wheel rotation methods on front and rear wheels, had to be defined for this study. The rotation methods were applied separately on the two wheel groups, where the other group was set to remain stationary. According to the previous investigations, these examinations were carried out considering three rim geometries *Rim16*, *Rim17* and *Rim18* with enabled engine compartment flow. These configurations yield thirty additional simulation cases, which are presented in Table 7.3.

7.6.1 Impact of front and rear wheel rotation on vehicle flow topology

First, the effects of front and rear wheel rotation on the vehicle's air flow topology are analysed. For this purpose, the pressure situation is investigated in *plane F*, at the height of the wheel center, as well as in *plane D* in the wake area of the vehicle. Furthermore, the surface pressure situation at the tail is examined to illustrate the effects of flow topology alterations on the vehicle itself. Differential pressure analyses are performed, using the stationary case as the reference. The results are shown in Fig. 7.27 for *plane E*, Fig. 7.28 for *plane F* and in Fig. 7.29 for *plane D*, while the outcomes of the surface pressure analysis at the rear are presented in Fig. 7.30. Each row of these figures corresponds to the results for a certain rotation method, where the application of this method for the front wheels is shown in the left column, while the right column illustrates the results of the application to the rear wheels.

Front wheel rotation

The application of front wheel rotation results in a change of the flow structure along the entire underbody area of the vehicle (Fig. 7.27). A good agreement with the resulting pressure distributions of simulation cases with four rotating wheels are found. Both the shift in the underbody flow and the pressure increases next to the vehicle (from the front wheel arches and along to the rear and further downstream) are observed. The formation

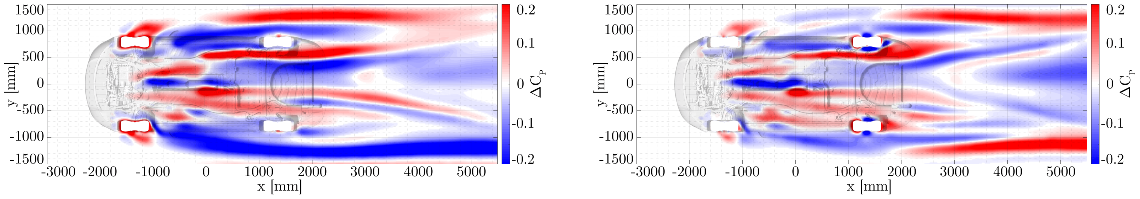

(a) MW, front wheels rotating (b) MW, rear wheels rotating

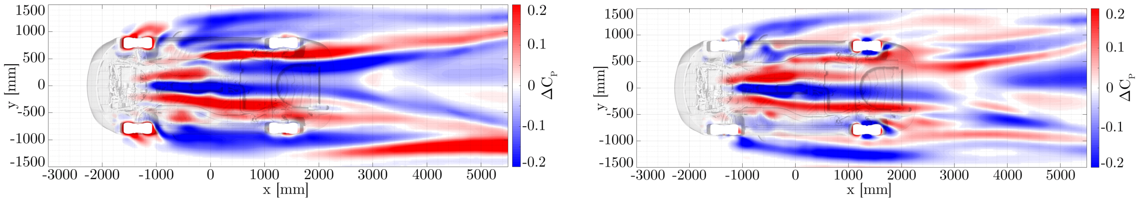

(c) MW-TO, front wheels rotating (d) MW-TO, rear wheels rotating

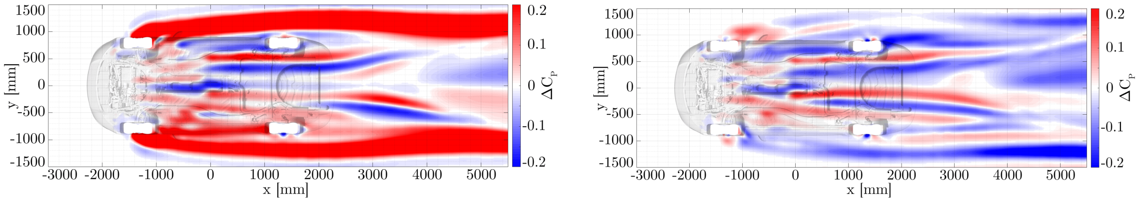

(e) MRF, front wheels rotating (f) MRF, rear wheels rotating

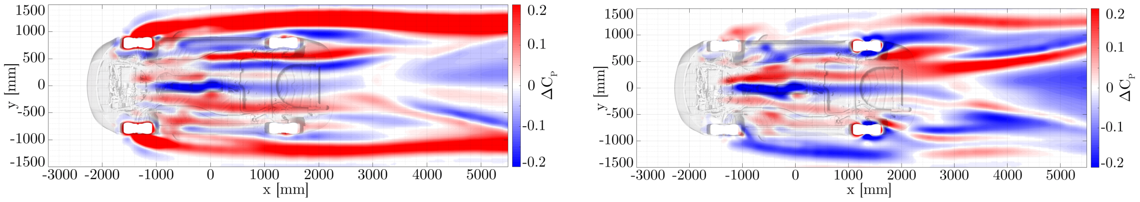

(g) MRF&MW, front wheels rotating (h) MRF&MW, rear wheels rotating

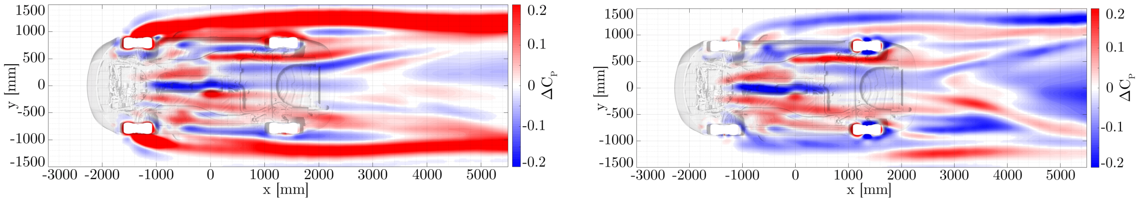

(i) MRF&MW-TO, front wheels rotating (j) MRF&MW-TO, rear wheels rotating

Figure 7.27: Pressure coefficient differences ΔC_P against stationary wheels (*B.16.NR*) due to rotating front wheels (*B.16.*.FR*) (left column) or rear wheels (*B.16.*.RR*) (right column) downstream the vehicle in *plane E* for *Rim16*.

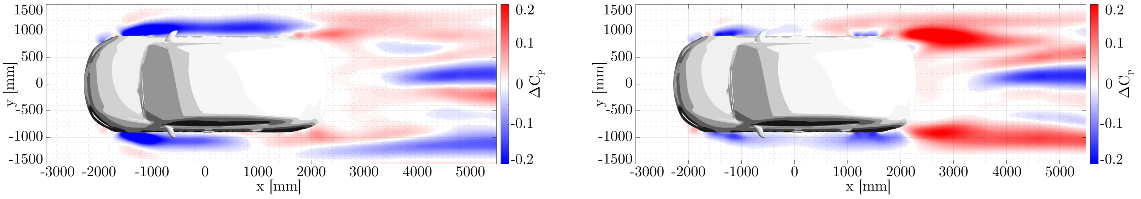

(a) MW, front wheels rotating

(b) MW, rear wheels rotating

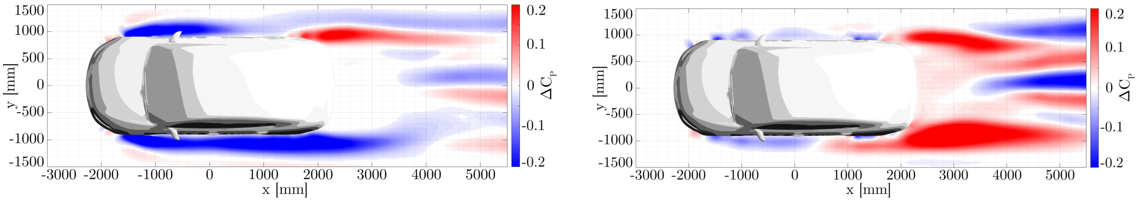

(c) MW-TO, front wheels rotating

(d) MW-TO, rear wheels rotating

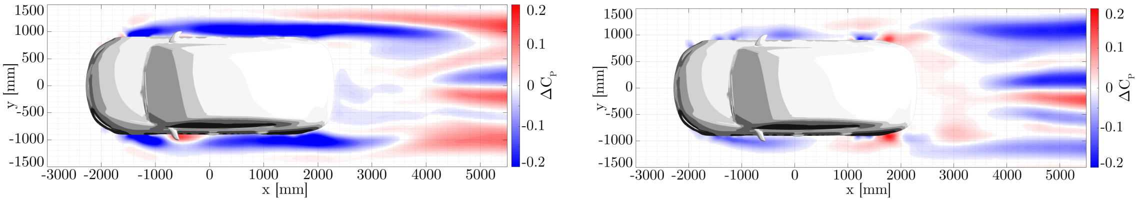

(e) MRF, front wheels rotating

(f) MRF, rear wheels rotating

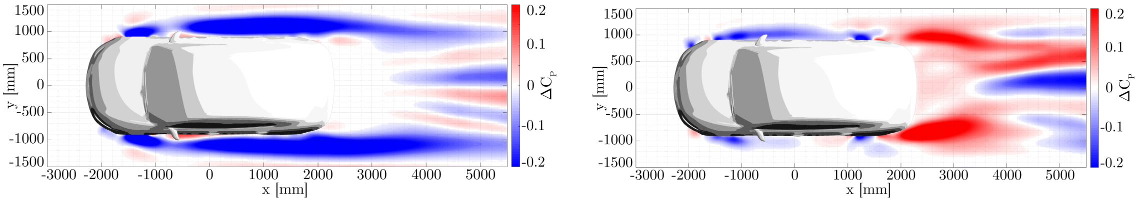

(g) MRF&MW, front wheels rotating

(h) MRF&MW, rear wheels rotating

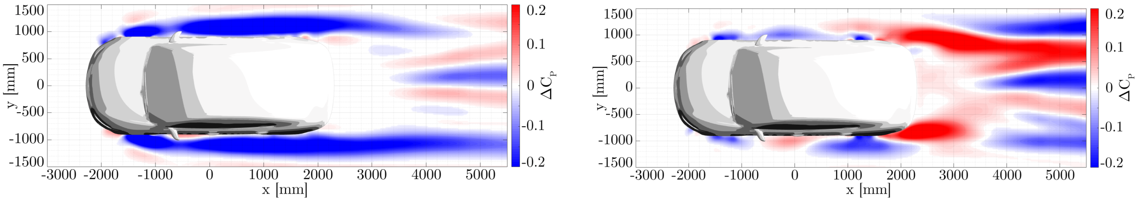

(i) MRF&MW-TO, front wheels rotating

(j) MRF&MW-TO, rear wheels rotating

Figure 7.28: Pressure coefficient differences ΔC_P against stationary wheels (*B.16.NR*) due to rotating front wheels (*B.16.*.FR*) (left column) or rear wheels (*B.16.*.RR*) (right column) downstream the vehicle in *plane F* for *Rim16*.

Case	Rims	Cooling air inlet area	Front tire rotation method	Front rim rotation method	Rear tire rotation method	Rear rim rotation method
B.16.MW.FR	*Rim16*	open	MW	MW	-	-
B.16.MW.RR	*Rim16*	open	-	-	MW	MW
B.16.MW-TO.FR	*Rim16*	open	MW	-	-	-
B.16.MW-TO.RR	*Rim16*	open	-	-	MW	-
B.16.MRF.FR	*Rim16*	open	-	MRF	-	-
B.16.MRF.RR	*Rim16*	open	-	-	-	MRF
B.16.MRF&MW.FR	*Rim16*	open	MW	MRF & MW	-	-
B.16.MRF&MW.RR	*Rim16*	open	-	-	MW	MRF & MW
B.16.MRF&MW-TO.FR	*Rim16*	open	MW	MRF	-	-
B.16.MRF&MW-TO.RR	*Rim16*	open	-	-	MW	MRF
B.17.MW.FR	*Rim17*	open	MW	MW	-	-
B.17.MW.RR	*Rim17*	open	-	-	MW	MW
B.17.MW-TO.FR	*Rim17*	open	MW	-	-	-
B.17.MW-TO.RR	*Rim17*	open	-	-	MW	-
B.17.MRF.FR	*Rim17*	open	-	MRF	-	-
B.17.MRF.RR	*Rim17*	open	-	-	-	MRF
B.17.MRF&MW.FR	*Rim17*	open	MW	MRF & MW	-	-
B.17.MRF&MW.RR	*Rim17*	open	-	-	MW	MRF & MW
B.17.MRF&MW-TO.FR	*Rim17*	open	MW	MRF	-	-
B.17.MRF&MW-TO.RR	*Rim17*	open	-	-	MW	MRF
B.18.MW.FR	*Rim18*	open	MW	MW	-	-
B.18.MW.RR	*Rim18*	open	-	-	MW	MW
B.18.MW-TO.FR	*Rim18*	open	MW	-	-	-
B.18.MW-TO.RR	*Rim18*	open	-	-	MW	-
B.18.MRF.FR	*Rim18*	open	-	MRF	-	-
B.18.MRF.RR	*Rim18*	open	-	-	-	MRF
B.18.MRF&MW.FR	*Rim18*	open	MW	MRF & MW	-	-
B.18.MRF&MW.RR	*Rim18*	open	-	-	MW	MRF & MW
B.18.MRF&MW-TO.FR	*Rim18*	open	MW	MRF	-	-
B.18.MRF&MW-TO.RR	*Rim18*	open	-	-	MW	MRF

Table 7.3: Simulation cases for the study of front- and rear wheel rotation.

of the pressure areas and the vehicle are particularly evident for rotation methods that utilize *MRF* (Figs. 7.27e, 7.27g and 7.27i). As discussed in the previous chapter, these alterations indicate a change in the separation behavior at the front wheels.

Rotating front wheels furthermore result in an increase of low pressure vortex regions in vicinity of the front wheel arches, which extend downstream along the vehicle (Fig. 7.28). For *MW* (Fig. 7.28a) and *MW-TO* (Fig. 7.28c), this flow field alteration yields areas with increased pressure at the rear wheel arch region and the lateral surfaces of the tail. Areas with increased pressure are identifiable on both vehicle sides for *MW*, and on one side for *MW-TO*. Furthermore, the base wake structure of the vehicle is altered due to interference effects, causing a pressure increase at the tail. Applying rotation methods *MRF* (Fig. 7.28e), *MRF&MW* (Fig. 7.28g) or *MRF&MW-TO* (Fig. 7.28i) results in a wide and longer separation area originating at the front wheel arches and extending downstream along the vehicle to the tail and beyond. However, regions with increased pressure could not be observed at the rear area for these rotation methods.

Considering the effects of front wheel rotation on the flow topology in the vehicle wake (Fig. 7.29), areas with increased pressure at the upper half of the vehicle sides are predicted by *MW* (Fig. 7.29a), *MW-TO* (Fig. 7.29c), as well as by *MRF&MW* (Fig. 7.29g) and *MRF&MW-TO* (Fig. 7.29i). For *MW*, this effect applies to the entire vehicle side. In contrast, *MRF* (Fig. 7.29e) predicts extensive pressure losses next to the vehicle. Both combined rotation methods, *MRF&MW*, as well as *MRF&MW-TO*, show a pressure situ-

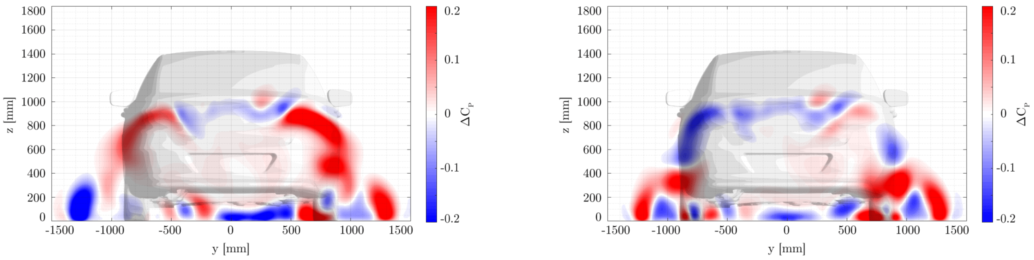

(a) MW, front wheels rotating (b) MW, rear wheels rotating

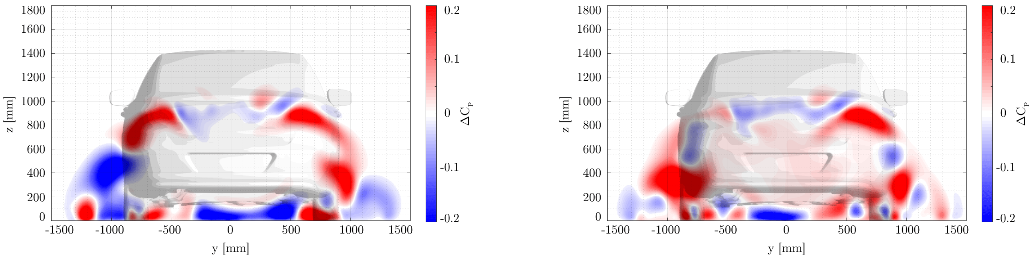

(c) MW-TO, front wheels rotating (d) MW-TO, rear wheels rotating

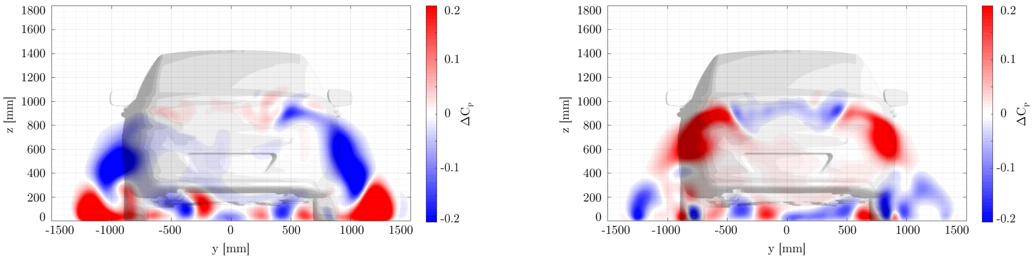

(e) MRF, front wheels rotating (f) MRF, rear wheels rotating

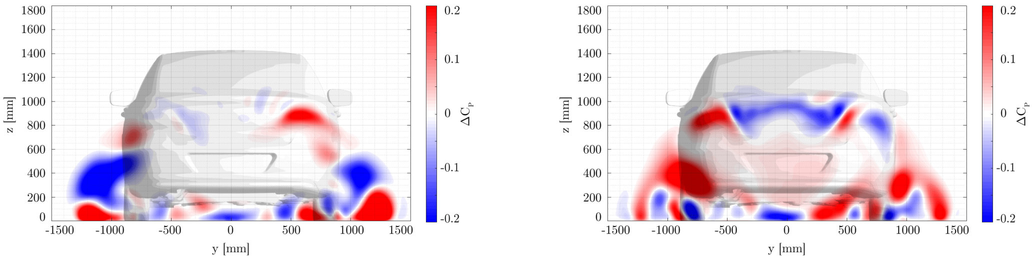

(g) MRF&MW, front wheels rotating (h) MRF&MW, rear wheels rotating

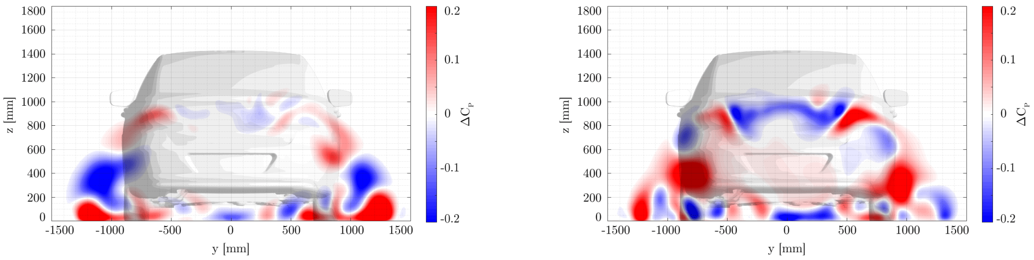

(i) MRF&MW-TO, front wheels rotating (j) MRF&MW-TO, rear wheels rotating

Figure 7.29: Pressure coefficient differences ΔC_P against stationary wheels (*B.16.NR*) due to rotating front wheels (*B.16.*.FR*) (left column) or rear wheels (*B.16.*.RR*) (right column) at the vehicle wake in *plane D* for *Rim16*.

ation similar to *MRF*. However, the lateral pressure loss regions are limited by areas with increased pressure in the top area downstream of the rear lights. An increase in pressure at the rear base is only detected for the *MW* method, while the other rotation methods predict extensive regions with reduced pressure.

Rear wheel rotation

Rotating rear wheels result in alterations of the pressure distribution in the entire underbody area, which already appear at the front wheel arches and extend further downstream to the vehicle tail and beyond (Fig. 7.29). These results are remarkable, since they demonstrate that rotating rear wheels also affect the flow in front section of the vehicle. However, the observed pressure changes are not as distinct as for simulation cases with rotating front wheels. Accordingly, only minor alterations of the flow and the detachment behavior at the front wheels can be detected.

Furthermore, rear wheel rotation causes pressure increases in the lateral areas of the rear wheel arch, especially for simulation cases that utilize *MW* (Fig. 7.28b), *MW-TO* (Fig. 7.28d), *MRF&MW* (Fig. 7.28h) or *MRF&MW-TO* (Fig. 7.28j) as the rotation method. This effect is also predicted by *MRF* (Fig. 7.28f), albeit in a weaker form than with the other rotation methods. An explanation for this flow topology alteration may be the reduction in the lateral air outflow from the rear wheel arch due to rotating tire surfaces. The acceleration of the air towards the rotating tire surface results in a back-flow that reduces the side venting, especially in the rear region of the wheel arch [34]. Due to the stationary tire surfaces for the *MRF* method, this effect can only be observed in a reduced form with this approach. The pressure gain at the rear wheel arch extends downstream along the vehicle via the lateral tail surfaces, where it causes pressure increases for all simulation cases in further consequence. Moreover, the analysis results demonstrate that rotating rear wheels not only reduce the detachment areas at the rear wheel arches, but also affect the wake of the front wheel houses. Although the front wheels are stationary in this setup, meaning that the boundary conditions for these wheels are identical to the reference case, a pressure increase is also observable in this region, which reduces the lateral wake area of the front wheel arches. The alteration of the flow topology due to the rear wheel rotation thus affects the air flow situation upstream at the front wheels, and consequently alters the air flow situation of the entire vehicle.

The differential analysis of the wake area (Fig. 7.29) demonstrates pressure increasing effects at the vehicle base for all wheel rotation methods, especially at the lateral regions of the tail and downstream of the rear wheel arches, which results in a narrowing of the wake. For the *MRF* method (fig. 7.29f), this area covers the top half of the tail. Furthermore, rear wheel rotation causes a pressure drop in the upper rear area, downstream of the separation edge of the boot lid, for all rotation methods. Investigations of the near-ground region reveal a pressure reduction in the central area, which is limited to the sides by regions of increased pressure. This result suggests a shift of the flow topology of the underbody area, as previously discussed for simulation cases with four rotating wheels. The analysis results of the differential pressure situation in *plane D* and *plane F* demonstrate that the local flow situation of the rear wheels and wheel arches interferes with the flow topology of the vehicle tail, causing a pressure increase in the lateral regions of the wake area and thus narrowing the base wake structure. These effects were detected with varying intensity for all rotation methods.

Surface pressure situation

The flow topology alterations of the vehicle wake affect the surface pressure situation of the vehicle, especially at the tail region. The comparison of the left and right columns in Fig. 7.30 reveals that the altered air flow situation causes a higher increase of the surface pressure at the vehicle tail for rear wheel rotation than for rotating front wheels, independently of the applied rotation method. Since only rear wheel rotation predicts pressure increases, and furthermore narrowing effects on the wake region, it is obvious to see this as cause for the reduction of the rear pressure. In contrast, rotating front wheels affect the surface pressure situation marginally and may even predict surface pressure reduction for individual rotation methods.

Comparison to four rotating wheels

The comparison with the results of the flow topology studies with four rotating wheels in *plane F* (Fig. 7.10) reveals that the frontal vehicle flow situation closely resembles the results of simulation cases with rotating front wheels (Fig. 7.28). The same applies to the flow topology in the rear of the vehicle and load cases with rotating rear wheels. This conclusion is confirmed by the results of the differential pressure analysis in the vehicle wake, which reveals good agreement between simulations with four rotating wheels (Fig. 7.13) and load cases with rotating rear wheels (Fig. 7.29).

On the basis of these observations it can be assumed that a distinction can be made between the impact of front and rear wheel rotation on the flow topology of the vehicle. The front wheel rotation significantly shapes the vehicle flow from the front end to the rear wheel arch, and the rotating rear wheels dominate the flow topology alterations downstream of the rear wheel arch to the tail. Thus, the rotation of the rear wheels represents an important factor of impact on the aerodynamic situation of the entire vehicle due to its influence on the flow topology of the tail, and thus on the surface pressure at the rear base. An exception to this is the *MRF* approach, where the analysis has a more dominant effect on the flow topology alterations of the entire vehicle than the rear wheel rotation.

7.6.2 Impact of front and rear wheel rotation on vehicle drag

In this section, the effects of the front and rear wheel rotation on the vehicle drag are examined separately from each other. Therefore, the evolution of vehicle drag alterations and the impact on integral vehicle drag are investigated. For this purpose, the drag deviations between the stationary reference case and the simulation cases with front or rear wheel rotation are accumulated along the vehicle axes. This analysis is performed separately for the entire vehicle, as well as vehicle body and wheels. The results are shown below for front wheel rotation in Figs. 7.31, 7.32 and 7.33, while the results for rear wheel

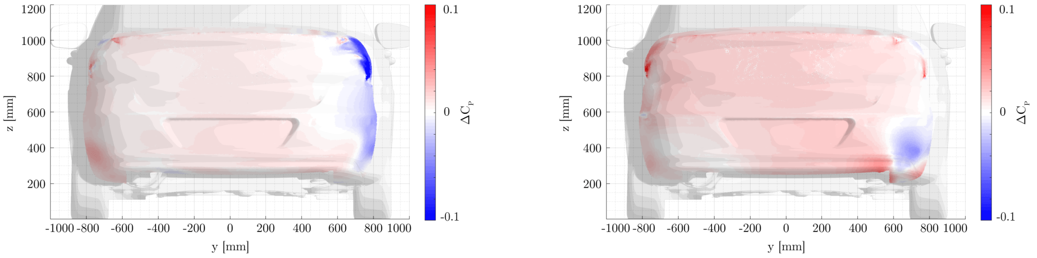

(a) MW, front wheels rotating (b) MW, rear wheels rotating

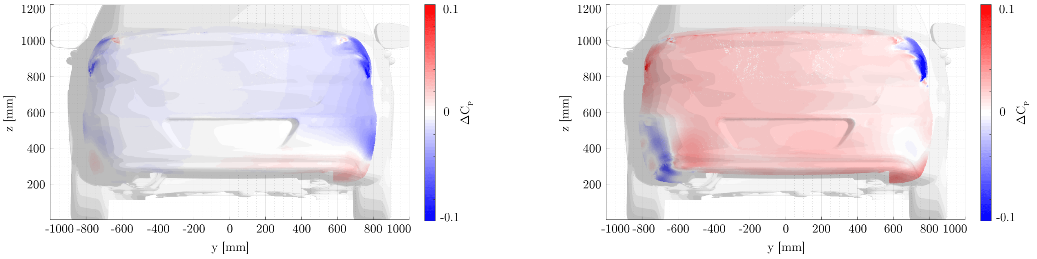

(c) MW-TO, front wheels rotating (d) MW-TO, rear wheels rotating

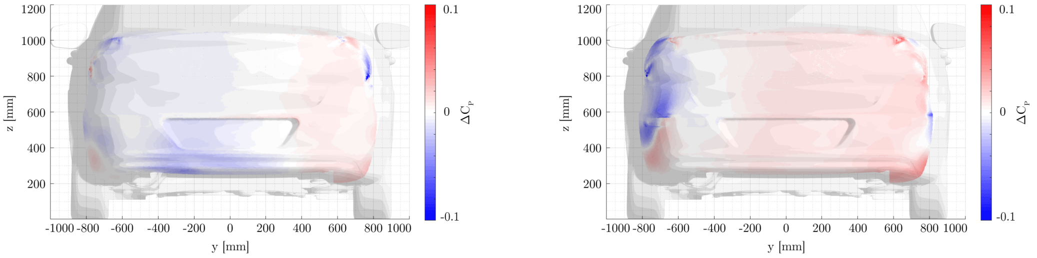

(e) MRF, front wheels rotating (f) MRF, rear wheels rotating

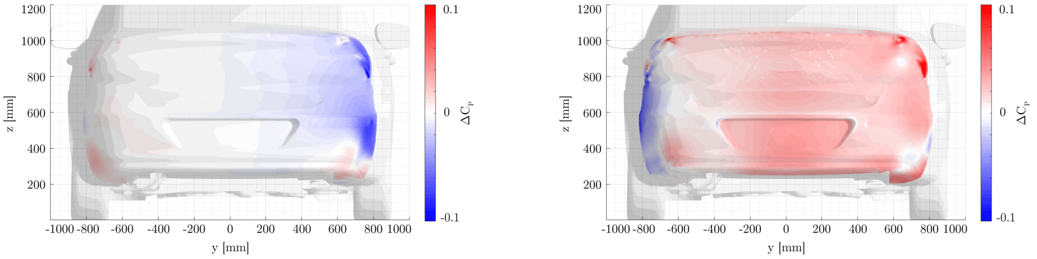

(g) MRF&MW, front wheels rotating (h) MRF&MW, rear wheels rotating

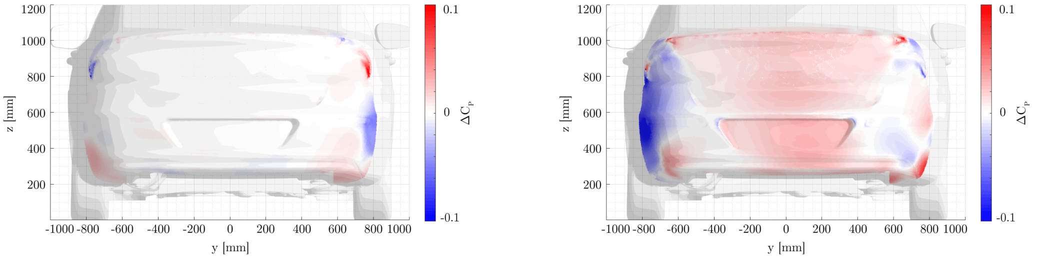

(i) MRF&MW-TO, front wheels rotating (j) MRF&MW-TO, rear wheels rotating

Figure 7.30: Pressure coefficient differences ΔC_P against stationary wheels (*B.16.NR*) due to rotating front wheels (*B.16.*.FR*) (left column) or rear wheels (*B.16.*.RR*) (right column) at the vehicle tail surface for *Rim16*.

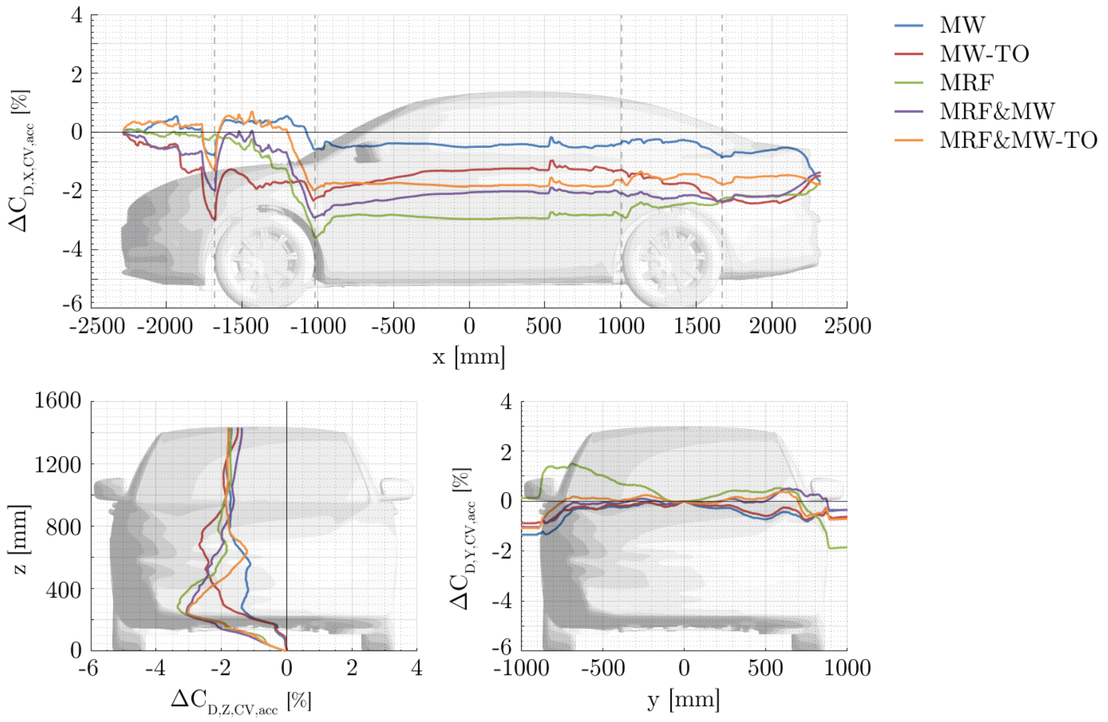

Figure 7.31: Development of the accumulated vehicle drag coefficient differences $\Delta C_{D,\mathrm{CV}}$ against the stationary case (*B.16.NR*) along the vehicle axes for *Rim16* with rotating front wheels (*B.16.*.FR*). Rear wheels are stationary.

rotation are visualized in Figs. 7.34, 7.35 and 7.36.

Front wheel rotation

The development of vehicle drag along the x axis (Fig. 7.31, 7.32 and 7.33) show good agreement with the simulation cases with four rotating wheels (Figs. 7.17, 7.18 and 7.19).

Small drag alterations in the front region of the vehicle, as well as a negative peak in the front half and a drag decrease in the rear part of the front wheel arch are revealed. This peak is observable for all rotation methods, except *MRF*, and consists of a negative component, which results from the vehicle body (Fig. 7.32), and a positive component whose origin can be attributed to the wheels (Fig. 7.33), as previously discussed for simulation cases with four rotating wheels. The reduction in drag at the rear part of the wheel house originates also from the wheels. Finally, these effects result in major drag reduction for all rotation methods in the front wheel arch area.

In the region between front and rear wheel arch, the total drag remains constant for the greater part for all rotation methods. However, minor peaks in differential drag are detected, which can be attributed to the change in flow in proximity of attachment parts in the underbody, such as the tank or the rear axle.

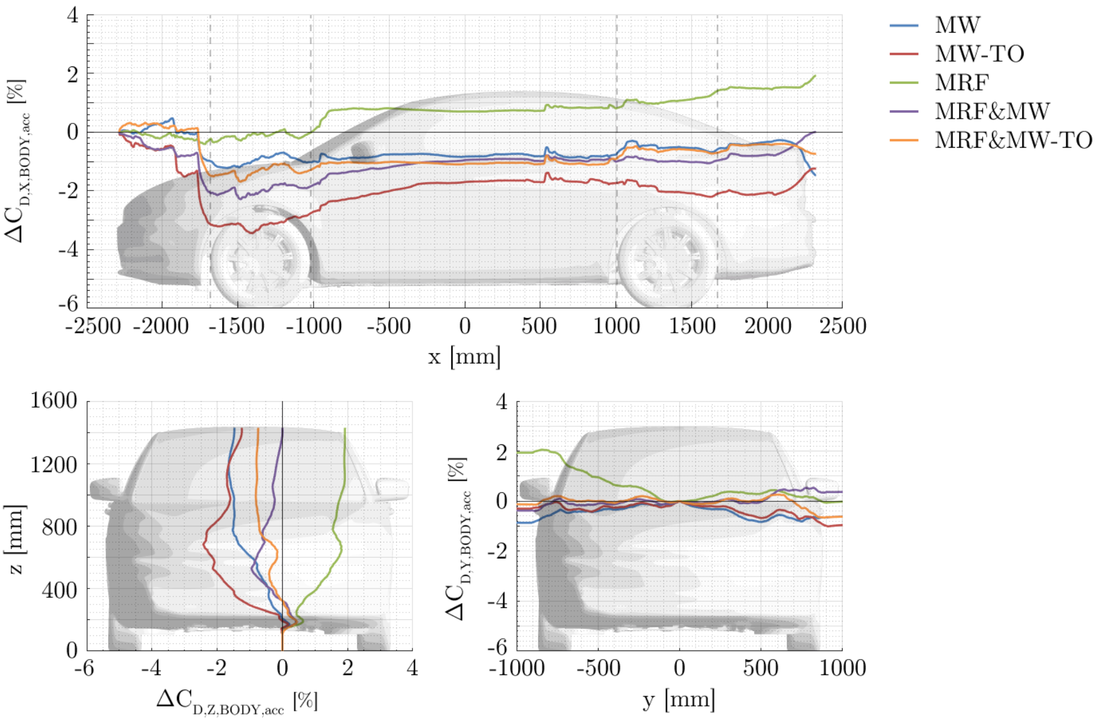

Figure 7.32: Development of the accumulated body drag coefficient differences $\Delta C_{D,\text{BODY}}$ against the stationary case (*B.16.NR*) along the vehicle axes for *Rim16* with rotating front wheels (*B.16.*.FR*). Rear wheels are stationary.

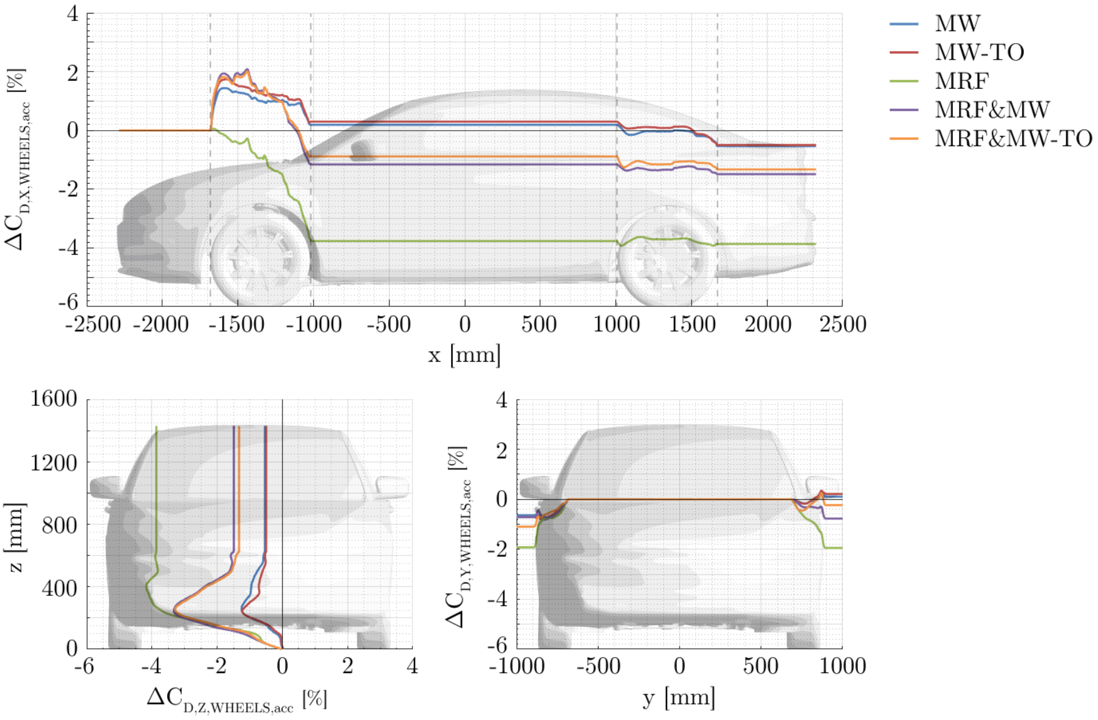

Figure 7.33: Development of the accumulated wheel drag coefficient differences $\Delta C_{D,\text{WHEELS}}$ against the stationary case (*B.16.NR*) along the vehicle axes for *Rim16* with rotating front wheels (*B.16.*.FR*). Rear wheels are stationary.

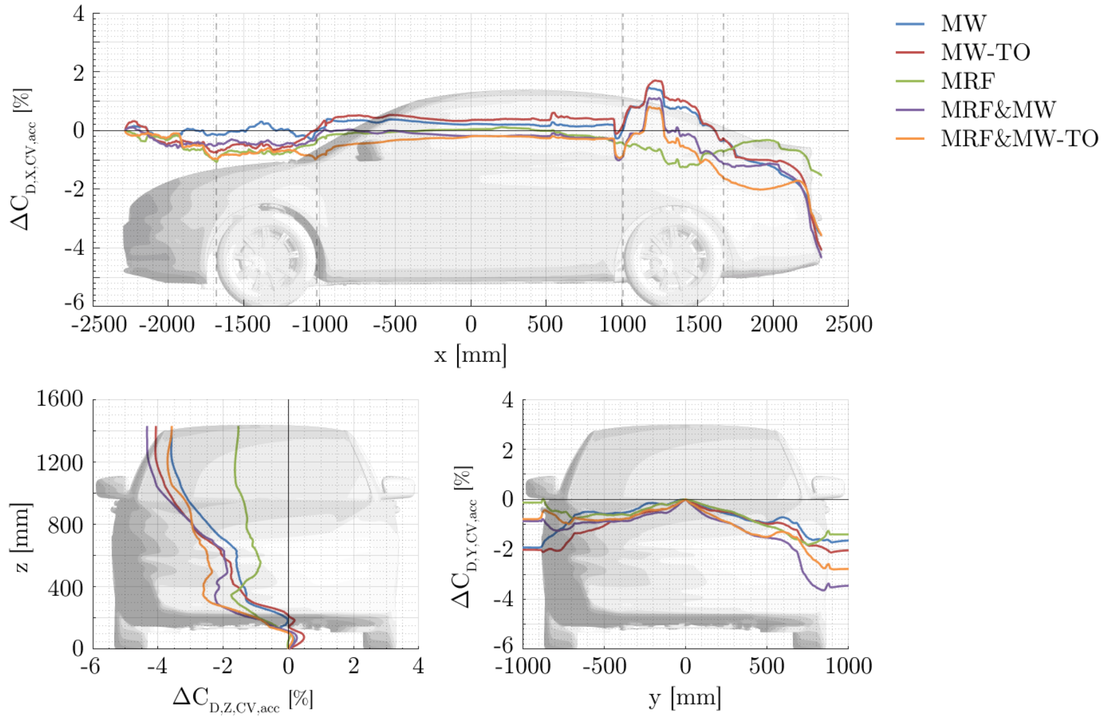

Figure 7.34: Development of the accumulated vehicle drag coefficient differences $\Delta C_{D,\mathrm{CV}}$ against the stationary case (*B.16.NR*) along the vehicle axes for *Rim16* with rotating rear wheels (*B.16.*.RR*). Front wheels are stationary.

The rear wheel arch reveals almost no drag alterations in comparison to the stationary case and contributes in total only a slight reduction to the drag, which therefore plays only a subordinate role in this setup. However, the contribution of the tail area to the vehicle drag depends on the applied rotation method and can either be positive or negative. Accordingly, *MW-TO* and *MRF&MW-TO* reduce the drag at the vehicle tail, while it increases for the other rotation methods. Thus it can be seen that, although the front wheel arch region causes a major reduction of the vehicle resistance, this reduction may decrease downstream due to local increases in drag and interference effects.

The integral changes in vehicle drag are equally divided between vehicle body and wheels for *MW*, *MW-TO* and *MRF&MW-TO*, while *MRF&MW* provides no impact of the vehicle body on the total vehicle drag. The *MRF* method alters the flow topology at the vehicle body in a way that it provides a positive contribution to the drag, which is, however, compensated by the negative portion of the wheels and ultimately results in a reduction of the integral vehicle resistance.

Rear wheel rotation

Simulation cases with rotating rear and stationary front wheels (Fig. 7.34) reveal marginal alterations of vehicle drag development from its front end to the rear wheel arch area in comparison to the stationary case. However, remarkable are drag changes at the front

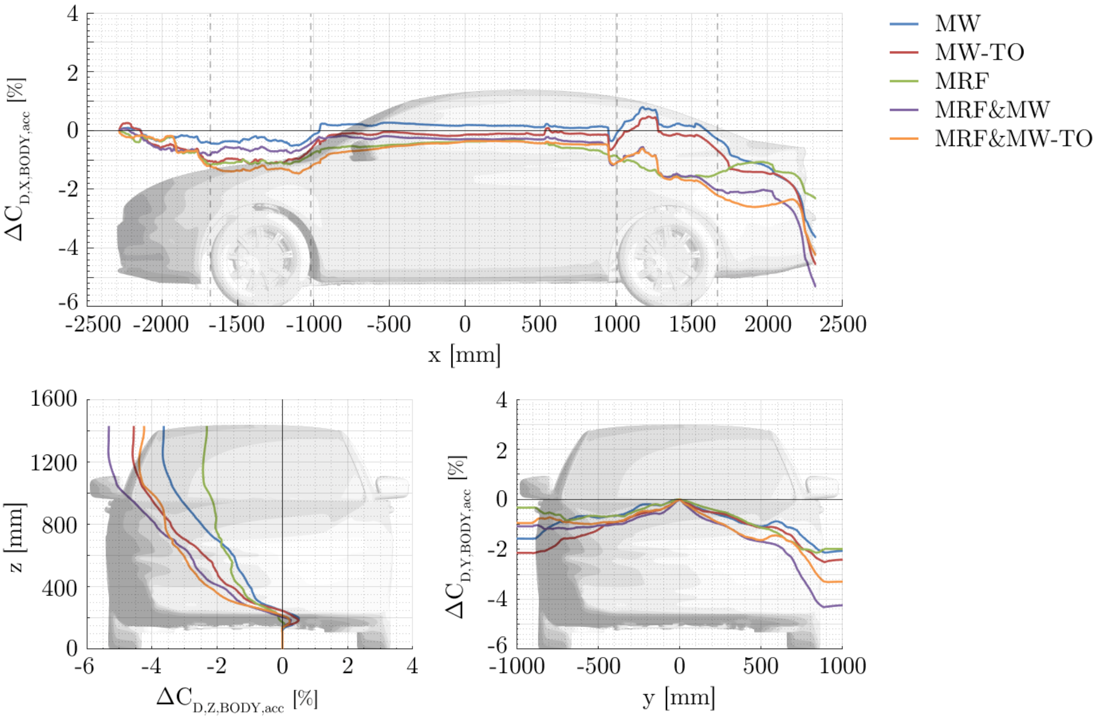

Figure 7.35: Development of the accumulated body drag coefficient differences $\Delta C_{D,\mathrm{BODY}}$ against the stationary case (*B.16.NR*) along the vehicle axes for *Rim16* with rotating rear wheels (*B.16.*.RR*). Front wheels are stationary.

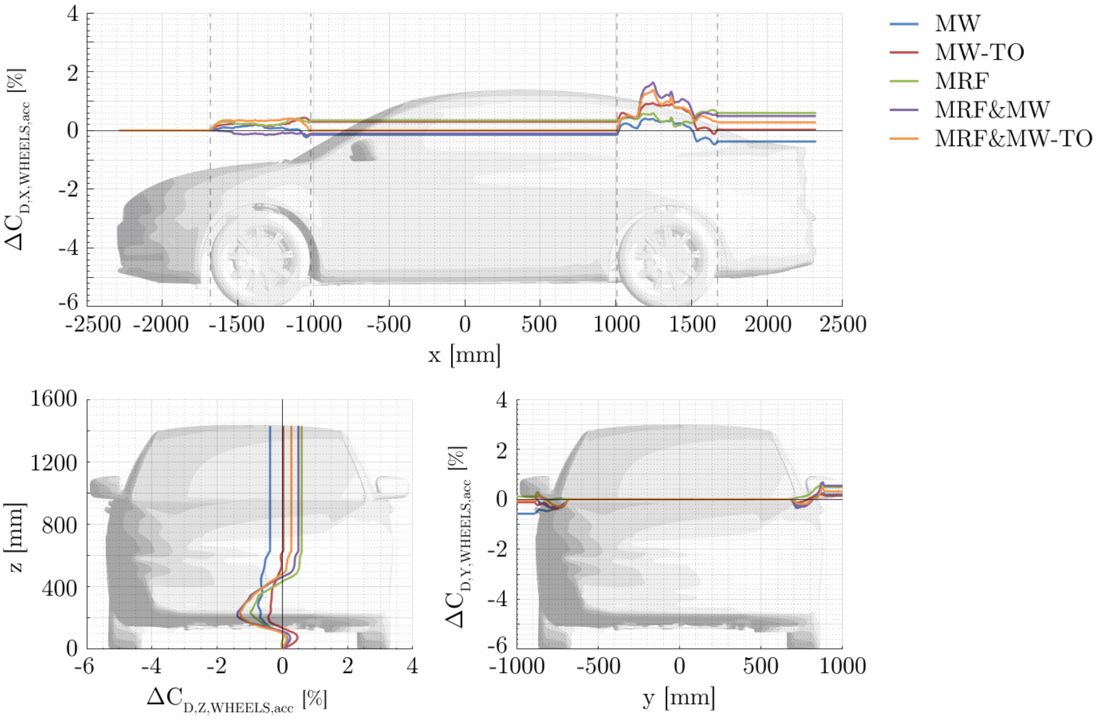

Figure 7.36: Development of the accumulated wheel drag coefficient differences $\Delta C_{D,\mathrm{WHEELS}}$ against the stationary case (*B.16.NR*) along the vehicle axes for *Rim16* with rotating rear wheels (*B.16.*.RR*). Front wheels are stationary.

wheel arch, which demonstrate that rotating rear wheels affect the underbody flow situation also in this region. This effect has already been indicated on the basis of the flow analyses in the previous section. The rear wheel rotation affects the flow topology downstream of the rear wheel arches considerably and causes a significant pressure increase at the tail, especially on the right side of the rear base (Fig. 7.30), which supports the pressure recovery at the base and thus reduces the integral vehicle drag. Most of the drag changes occur at the rear of the vehicle body, and not on the wheels themselves (Figs. 7.35 and 7.36), as it is the case for simulation setups with rotating front wheels or four rotating wheels.

The drag evolution analysis of rotating front and rear wheels (Figs. 7.31 and 7.34) demonstrate that both boundary conditions affect the aerodynamic drag situation of the entire vehicle, and not only at the proximity of the wheels, which also corresponds to the observed effect with four rotating wheels.

In conclusion it can be stated that the major impact on the integral vehicle drag is caused by the altered air flow situation at the tail area through rear wheel rotation. Front wheel rotation also affects the pressure situation at the rear, and therefore also the vehicle drag, however, this impact is small compared to the impact of rotating rear wheels.

Vehicle drag

The impact of the rotating front and rear wheels on the vehicle drag is eventually evaluated through differential analyses of simulation results with rotating front or rear wheels to the stationary reference case. This analysis is carried out for all rim geometries *Rim16*, *Rim17* and *Rim18*, considering engine compartment air flow. The differential vehicle drag is calculated according to Eq. (7.2), and the results are shown subsequently in Fig. 7.37.

The analysis results reveal that both front and rear wheel rotation affect the vehicle drag, whereas the rotation methods applied to the front wheels are far less effective than the application on the rear wheels, as the results from the previous section suggested. All rear wheel rotation methods reduce the drag of the vehicle in a range of −8.1% to −1.4%. This tendency also applies to the front wheel rotation with three exceptions that marginally increase the drag of the vehicle. These are the *MW* method with *Rim17* and *Rim18*, as well as the *MRF&MW-TO* approach with *Rim17*. The vehicle drag alterations with rotating front wheels are in a range of −2.9% to +0.5%, which indicates that pure front wheel rotation can either increase or decrease the total resistance, depending on the vehicle configuration. Accordingly, the results show that the impact of front and rear wheel rotation generally depends on rim geometry and the rotation method applied.

A comparison of the results of the integral differential drag analysis (Fig. 7.37) with the results of the difference analysis of the four rotating wheel simulations (Fig. 7.21) reveals that the sum of drag alterations of front and rear wheel rotation corresponds to the total differential values of the rotation methods applied to all four wheels. Therefore it can be deduced that the effects of front and rear wheel rotation are additive. The analysis results of flow topology alterations (Fig. 7.28) supports this conclusion.

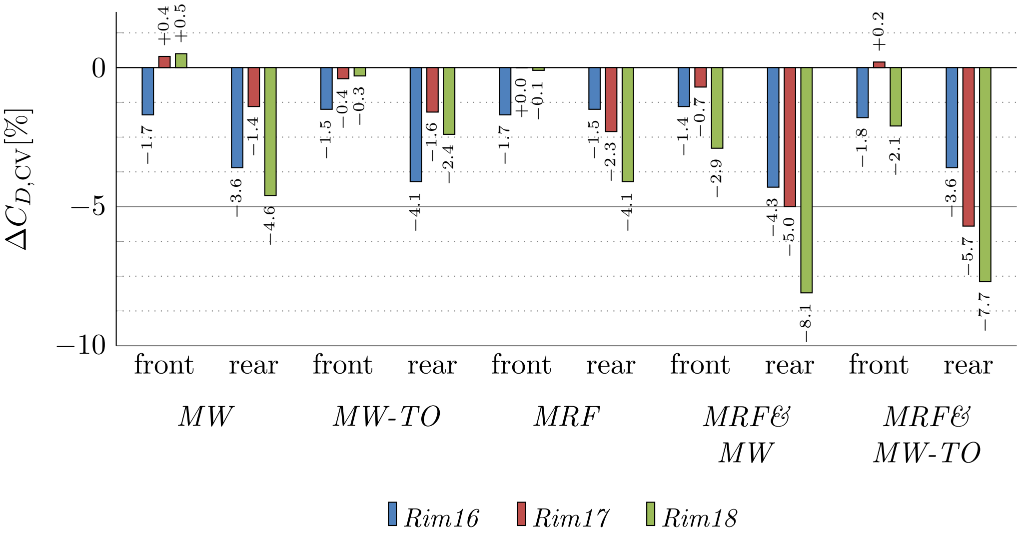

Figure 7.37: Differences in the vehicle drag coefficient $\Delta C_{D,\mathrm{CV}}$ between the stationary case (*B.16.NR*) and cases with various wheel rotation methods applied separately on front (*B.16.*.FR*) or rear wheels (*B.16.*.RR*).

7.7 Synopsis

Analyses on experimental and numerical basis were carried out to investigate the effects of rotating wheels on the aerodynamic situation of the entire vehicle. The examinations include the flow topology, the surface pressure distribution, as well as the integral vehicle drag and the respective proportions of the vehicle body, the wheels, as well as tires and rims. Both the impact of four rotating wheels, and also of wheel rotation methods applied separately to the front and rear wheel groups were evaluated.

7.7.1 Air flow topology

Initially, wind tunnel experiments were carried out to determine and analyse the aerodynamic behavior of the test vehicle. These investigations included analyses of the flow field and the surface pressure situation, as well as the integral drag of the vehicle. The results were validated with the findings of other experimental studies to ensure the reliability of this data which was used subsequently as a basis for further comparisons with the numerical results. The wind tunnel measurement results and analyses of the flow topology in vicinity of the left front wheel and in the wake of the test vehicle, as well as the surface pressure in various vehicle zones reproduced and confirmed the experimental findings of previous studies by Elofsson and Bannister [34], Wäschle [37] and Landström [40] for stationary and rotating wheel test cases, as well as the aerodynamic alterations between these setups.

For the subsequent numerical investigations, a reference case with four stationary wheels was simulated, and the flow topology of the experiment was successfully reproduced. The numerical results revealed two distinct low pressure regions downstream of the front wheel arch, which can be attributed to the upper *rim vortex* and the lower *wheel squash vortex*. Small deviations of the eddy structures between measurement result and simulation can be attributed to the simplified tire geometry or the moving road simulation [37].

Wheel arch and wheel wake area

The effects of the individual wheel rotation methods on the aerodynamic situation of the vehicle were examined in relation to the stationary reference case, with the following findings.

- The application of rotation methods significantly alters the flow topology in proximity of the entire vehicle, regardless of the utilized method. The flow topology alterations that result from rotating wheels may be reflected by individual wheel rotation methods with varying degrees of accuracy.
- The resulting pressure regions and the associated vortex structures in the front wheel area are comparable for all rotational methods. Two distinct low pressure areas are identified - on the one hand, a wheel house pressure area, which results from the ventilation of the wheel arch from the area between the tire and the wheel house, as well as the outflow through the rims, and, on the other hand, a floor pressure area that originates from the jetting phenomenon and the resulting horseshoe vortex near the ground. However, depending on the applied rotation method, these pressure regions consist of one or more vortices, which interact with each other.
- The shape and structure of these low pressure vortex areas depend on the rim geometry, as well as the chosen rotation method. A distinction can be made especially between methods based on *MW* or *MRF*.
- *MW* and *MW-TO* predict only minor alterations of the air flow situation in proximity of the wheel compared to the stationary case and show therefore only limited agreement with the outcomes of the wind tunnel experiment.
- In contrast, the *MRF* method and both combined wheel rotation approaches *MRF&MW* and *MRF&MW-TO* predict the formation of a third eddy structure, the *side vortex*, which is located alongside the rim between the lower and upper vertices, in accordance with the observations of the experiment and the findings of Wäschle [37]. These results suggest that *MRF* makes an important contribution to the realistic simulation of the flow topology in vicinity of the wheel and can therefore not be neglected for the correct simulation of rotating wheels.
- The surface pressure analysis of the lateral area downstream of the front wheel arch yields similar tendencies and supports these findings. All rotation methods were able to reproduce the surface pressure rise determined in the experiment over wide areas of the vehicle sides.
- A slight downward shift of the lateral vortex structures was detected for all rotation methods in flow direction downstream of the vehicle, in agreement with the observations of Wäschle [37].

- It can be stated that *MRF&MW*, *MRF&MW-TO* and especially *MRF* show best structural correlation with the experiment in these vehicle areas.

Underbody region

The flow topology in the underbody area is significantly affected by wheel rotation, since rotating boundaries alter the air flow situation within the wheel arch and the associated outflow, as well as the yaw angle of the approaching flow at the wheels and thereby affect the structure of its wake region. All these effects can roughly be attributed to the two rotation approaches *MW* or *MW-TO* and *MRF*.

- Applying *MW* or *MW-TO* raises the pressure in the underbody area due to two main high pressure flows located to the left and right of the vehicle centerline. These streams extend downstream to the vehicle's tail and the wake region of the rear wheels. *MRF* also predicts these two high-pressure areas, but in a weakened form.

- For *MRF*, the *wheel squash vortex* is weakened, which raises the pressure downstream along the sides of the vehicle to the lateral rear areas. *MW* and *MW-TO* predict also a slight pressure increase at these regions, which, however, vanish until the vehicle center.

- The discussed effects are additive, wherefore all of them are recognizable for those rotation methods that use a combination of the *MRF* and the *MW* approach, i.e. for *MRF&MW* and *MRF&MW-TO*.

Vehicle tail and wake area

- The modified flow topology in the underbody and at the vehicle sides affects the structure of the vehicle wake due to interference effects for all rotation methods, as was assumed by Elofsson and Bannister [34] and predicted by Wäschle [37].

- As in the experiment, the largest structural alterations are detected in the center and the peripheral wake regions. A distinction can be made between the effects of *MW* and *MRF*-based rotation methods. Especially in the lateral areas, *MW*-based methods show a pressure increase, in contrast to *MRF*, which predicts pressure reduction.

- These flow topology alterations lead to an increase in pressure over large areas in the vehicle wake, especially at the centre, which can be detected for all rotation methods and confirms the results of the wind tunnel experiment, as well as the findings of previous studies [34]. Worth mentioning is that the *MRF* method predicts a smaller pressure increase in this area than the other methods.

- The pressure increase in the vehicle wake supports the pressure recovery at the tail, which results in an increase in the surface pressure at large parts of the tail. This pressure rise can be detected in a similar form for all applied rotation methods, confirming the results from the experiment and other studies [34, 38]. This effect is particularly distinct for the combined approaches *MRF&MW*, and *MRF&MW-TO*.

- Although the *MW*, *MW-TO*, and *MRF* approaches can predict some of the discussed flow topology alterations, they fail to estimate others, where differences between the *MW*- and *MRF*-based approaches are detected. However, *MRF&MW* as well as *MRF&MW-TO* predict all observed structural flow topology alterations, such as the narrowing effects at the tail, and therefore show the best agreement with the experiment and also with previous examinations [34].

Front and rear wheel rotation

- The effects of rotating wheels on the flow topology of the vehicle can be divided between the impact of the front and the rear wheel groups. However, both groups affect the entire flow field around the vehicle even if the other group remains stationary.
- The alterations of the flow situation in the region from the front end to the rear wheel house are largely dominated by rotating front wheels, which enlarge the lateral low pressure vortex areas downstream of the front wheel arches.
- In contrast, the changes downstream of the rear wheel arch are significantly affected by the rear wheel rotation, which has a narrowing effect on the wake area and is mainly responsible for the pressure increase at the tail, especially at the center region and at the outer lateral boundaries, which further influence the vehicle drag. Therefore, the interference between the flow situation of the rear wheels and their wheel arches with the wake area of the vehicle and the narrowing effect on the latter can be considered as the main cause for the drag reduction due to the wheel rotation. This confirms the results of the investigations of Wickern and Lindener [33], Elofsson and Bannister [34], Wäschle [37] and Zhiling et al. [42].
- Furthermore, the investigations have shown that the effects of wheel rotation on the flow topology of the two wheel groups are additive to a large extent, which corresponds to the statements of the studies of Elofsson and Bannister [34], as well as Koitrand and Rehnberg [35].
- The discussed and presented effects concerning front and rear wheel rotation were reproduced by all wheel rotation methods.

7.7.2 Surface pressure distribution

The evaluation of the surface pressure situation at various areas of the vehicle reveals that pressure changes, and thus also flow topology alterations, occur especially in the rear area, as well as downstream of the front wheel arch. In contrast, the flow situation in the upper area of the vehicle is only marginally affected. Again, the rotation methods *MRF&MW* and *MRF&MW-TO*, as well as *MRF*, show the best agreement with the results of the surface pressure distribution investigations from the experiment.

7.7.3 Vehicle drag

The alteration of the flow topology of the vehicle due to the wheel rotation has eventually an impact on the integral vehicle drag.

Experimental results

The wind tunnel experiments revealed the following findings:

- The experiment yields a reduction of the overall vehicle drag due to wheel rotation, thus confirming the positive impact of the rotating wheels on the vehicle resistance. These outcomes match the experimental findings of e.g. Mercker et al. [5], Wickern and Lindener [33], Wäschle [37] was well as Landström and co-workers [38, 40, 41], among others.

- However, the drag decrease is largely independent of the rim geometry or engine compartment flow configuration for the examined test vehicle. Therefore, no distinguishable trend in drag reduction could be determined due to the rim designs.

Numerical results

The numerical investigations of the impact of rotating wheels on the integral vehicle drag have revealed the following:

- All investigated wheel rotation methods have an impact on the vehicle drag and tend to reduce it.

- The drag reducing effect correlates not only with the results of the experiment, but also with the findings of other studies, such as [5, 33, 34, 37, 40, 46], among others.

- Drag alterations occur throughout the entire vehicle and show a similar development for all rotational methods.

- The magnitude of the impact of the wheel rotation on the total vehicle resistance depends on the applied rotation method and the rim geometry, as well as the rim orientation, and is in a range of 0% to −10.2% for the mockup and −2.1% to −7.9% for configurations with enabled engine compartment flow. These findings correspond to the results of the experiment, as well as to the statement by Schnepf [39].

- Both front and rear wheel rotation tends to reduce the integral vehicle drag. However, three exceptions were determined that predicted a minor drag increase of up to +0.5% for front wheel rotation.

- The drag reducing effects are largely caused by rotating rear wheels, regardless of the applied rotation method and used rim geometry. These findings are in accordance with the experimental studies of others [34, 37]. The impact on drag is in a range of −2.9% to +0.5% for front wheel rotation and −8.4% to −1.4% for rear wheel rotation.

- Front wheel rotation can either reduce or increase the total vehicle resistance, depending on the vehicle configuration and the utilized rotation method. This confirms the results of Elofsson and Bannister [34], who assumed that a reduced front wheel wake results in a larger rear wheel wake through interference effects, which consequently interferes with the wake of the vehicle.

- The local drag changes in the front wheel arch region due to front wheel rotation reveal large decreases with values up to -5.0%. However, this impact may decrease due to local drag increases downstream to the rear of the vehicle, resulting in a small contribution to the integral vehicle drag alteration, which confirms the findings of [34].

- The discussed aerodynamic effects of the two wheel groups are largely additive with regard to the impact on the total vehicle resistance, in accordance with the findings of the flow topology investigations. This conclusion was also made in other studies [34, 35].

- The findings of the numerical investigations of the front and rear wheel rotation correlate with the outcomes from experimental studies of Wickern and Lindener [33], Elofsson and Bannister [34], as well as Koitrand and Rehnberg [35]. All wheel rotation methods predicted the discussed effects on the vehicle drag, as well as the dominant influence of the rotating rear wheels in comparison to the front wheels. Furthermore, the determined value ranges of the total vehicle resistance change, as well as the increase in drag due to the front wheel rotation for some vehicle configurations, could be confirmed.

- A detailed analysis of the drag development of the different vehicle areas, and separately for body and wheels, demonstrated that the major vehicle drag alterations do not result from the forces acting on the wheels, but especially from those acting on the body, which confirms the findings of Wäschle [37]. In particular the rear area reduces the integral vehicle resistance. This applies to all rotation methods, however, for *MRF* the difference between wheels and body for simulation cases with rims *Rim16* and *Rim17* is much lower than for the other methods, due to an altered air flow situation within the front wheel house geometry and the resulting share on the total vehicle drag.

- Rotating front wheels (with stationary rear wheels) tend to reduce the total wheel drag, while rotating rear wheels (with stationary front wheels) tend to increase it. However, rotation of both front and rear wheels influences only slightly the total wheel drag. This is an indication of the additivity of the influence of the front and rear wheel rotation on the wheel drag, which ultimately cancel each other out.

- It can be deduced from these findings that, although the wheel rotation does not affect the local wheel drag, the modified flow situation in vicinity of the vehicle results in an altered pressure situation on the vehicle body, which ultimately leads to a vehicle drag reduction. The decreasing effect can be especially attributed to the surface pressure increase at the rear of the vehicle.

- Through analysis of the drag prediction accuracy between experiment and simulation, it was revealed that the most precise rotation methods to simulate the impact of the wheel rotation on the total vehicle drag are the combinations *MRF&MW* and *MRF&MW-TO* with an absolute average accuracy $\overline{|\Delta\left(\Delta C_{D,\mathrm{CV}}\right)|} \leq 1.2\%$ for the mockup and $\overline{|\Delta\left(\Delta C_{D,\mathrm{CV}}\right)|} \leq 2.0\%$ for configurations with engine compartment flow.

- Different rim orientations can cause differences in the integral vehicle drag of up to 4.1% of the reference case (rim position α). The orientation of the rim geometry thus has a significant impact on the air resistance of the vehicle and must not be neglected. A similar effect was also detected in numerical studies by Landström et al. [47].
- The wheel drag can be divided into shares of rims and tires, where the investigations demonstrated that the tires contribute the greater part to the wheel drag. The ratio of rim and tire drags is comparable for all rotation methods, except for *MRF*, which shows a similar division ratio as the stationary case. These results suggest that the rotating tire surface has an important effect on the distribution of wheel resistance between tires and rims.

Chapter 8

Discussion and conclusion

The results and conclusions of this work are summarized and discussed in this chapter. It should be noted that these findings apply especially to the present test vehicle, which suggests that they could not be universally valid. However, based on the results of similar investigations, the author assumes that these findings are, to a certain extent, valid for all passenger cars.

As a part of an initial preliminary study, the impact of the rim geometry on the aerodynamic behaviour of the test vehicle was investigated experimentally in the wind tunnel for three production rims. It was demonstrated that the rim design affects the flow topology of the vehicle, and thus also the integral vehicle drag. This impact depends on the tire rotation, as well as the cooling air configuration, and can be between 2.1% and 4.5% of the drag value. A reason for this effect may be the trend towards decreasing geometric blockage of larger rim geometries, which furthermore has an impact on the crossflow through the rims and on the outflow behavior of the air from the wheel arches into the main lateral flow. The results of the surface pressure analysis at the lateral and base zones of the vehicle revealed that the flow situation downstream of the wheel arch and at the vehicle base are also affected by interference effects. Furthermore, the aerodynamic quality of the rims should be considered as a possible cause for those alterations. Due to these results, and in order to be able to make the most comprehensive possible statement in the following analyses, a part of the subsequent studies of this thesis were carried out for those three rim geometries.

Due to the limitations of the applied simulation methods concerning geometric rotation of tires and rims, the impact of the rim orientation on the flow topology and on the integral vehicle drag was numerically investigated for various vehicle configurations within the scope of a second preliminary study. For this purpose, additional rotation positions were separately defined for each of the three rim geometries in a way to achieve a maximum change of the spoke position. These investigations demonstrated that the geometric rim orientation alterations represent a not negligible impact on the aerodynamic behaviour of the vehicle. The individual rim orientations not only significantly affect the air flow situation in vicinity of the entire vehicle, they also alter eventually the integral vehicle drag. These alterations depend on the applied wheel rotation method, rim geometry, as well as engine compartment flow configuration, and can be up to 4.1% of the vehicle resistance between two investigated rim positions. In order to increase the resulting simulation accuracy for simulation approaches where the rim geometries cannot be rotated, such as for the *RANS* method, it is therefore recommended to investigate two or more orientations with different rim blockages in order to be able to determine an appropriate value range of the total vehicle drag. Due to these findings, some of the subsequent investigations were performed utilizing two rim orientations.

In the first phase of the project, the effects of rotating wheels on the aerodynamic parameters of the test vehicle were determined by means of wind tunnel experiments. The air flow topology in vicinity of the front wheel and within the wheel arch, as well as in the wake area of the vehicle, was examined and the integral vehicle drag was determined. These tests were carried out for the stationary reference case as well as for rotating wheels with three different rim geometries and two cooling air configurations. The results were validated with previous studies to ensure to utilize a reliable and well-founded experimental database for the validation of the numerical results.

In the following project phase, computational studies were carried out with the virtual test vehicle, and the impact of the individual wheel rotation approaches on the flow topology and the surface pressure distribution within the wheel house, as well as for the entire test vehicle and furthermore the integral vehicle drag, were analysed. For this purpose, all four wheels, as well as the front and rear wheel groups separately, were set in rotation in order to assign the aerodynamic effects to the two wheel groups. The investigations were carried out for the same load cases as in the wind tunnel experiment, and the numerical results were validated with these data and the literature.

It has been shown that each of the investigated numerical wheel rotation methods predicts certain aerodynamic effects found in the experiment or in other studies, but fail to reproduce others. Due to the effects on the aerodynamic behaviour of the vehicle, the utilized rotation approaches can be divided into three individual groups. These are methods based on the *MW* or the *MRF* approach, or combinations of these two.

The two rotation methods of the first group, *MW* and *MW-TO*, are similar in many of the studied aspects. It was demonstrated that this group, or the application of the *MW* approach on the tire tread, is essential for the realistic simulation of the flow situation in close proximity of the wheel, since only they predict the development of the pressure situation at the tire surface in accordance with other studies, including the pressure increase to $C_P > 1$ upstream of the wheel at the contact line between tire and road. Furthermore this approach yields early flow separation at the tire tread and accordingly altered flow patterns within the wheel arch. However, both methods fail to predict the formation of the *rim vortex* laterally adjacent to the tire.

The second group, the *MRF* approach, predicts a flow topology within the wheel arch that is in many aspects similar to the stationary reference case, which does not result in an early flow detachment at the tire tread and thus also not in the associated air flow alterations, due to the lack of tire surface rotation. However, the *MRF* method reveals an alteration of the yaw angle of the approaching underbody flow on the wheel and significantly affects the outflow behavior from the wheel arch into the underbody region and into the main lateral flow. Consequently, these effects lead to the correct reproduction and formation of the rim vortex, and subsequently to the structural changes in the wake of the vehicle.

Despite the differences in these rotation approaches, both groups reproduce the surface pressure situation within the wheel arch and in the wake of the wheel according to the experiment or the measurement results of others.

It has been demonstrated that the effects of these rotation methods on the flow topology, as well as on the integral vehicle drag, are for the most part additive. Since some effects are exclusively predicted by *MW*, while others are only shown by *MRF*, it is not surprising that the numerical results of the third group, in particular namely the combinations of the first two approaches *MRF&MW*, as well as *MRF&MW-TO*, predict the aerodynamic effects of both, *MW* and *MRF*, and therefore have the greatest similarities with the experiment and the literature in terms of flow topology. By applying these two rotation methods, the air flow situation in proximity of the front wheel and within the wheel arch, as well as in the vehicle wake, are predicted in accordance with the experiment.

Front and rear wheel rotation, regardless of the applied rotation approach, cause alterations of the flow situation throughout the entire vehicle. Due to interference effects those lead to structural alterations and pressure increases in the vehicle wake region, and thus also at the surface of the rear base, eventually having a direct impact on the integral vehicle drag. The magnitude of the drag alteration depends on the applied rotation method.

The analysis results demonstrated that all of the studied rotation methods correctly reproduced the drag reducing effects of rotating wheels. However, the most accurate methods to predict the impact of rotating wheels on the total resistance of the vehicle are *MRF&MW* and *MRF&MW-TO*, with an average absolute predictive accuracy of $\leq 1.2\%$ for the mockup and $\leq 2.0\%$ for configurations with enabled engine compartment flow.

Considering the boundary conditions and constraints of this thesis, it is therefore recommended to utilize the *MRF&MW* or *MRF&MW-TO* method to model rotating wheels in steady-state *RANS* simulations, as both approaches demonstrated having the largest correlation with the determined air flow topology alterations, as well as the best predictive accuracy of the integral vehicle drag with the experiment.

Chapter 9

Further work and recommendations

The investigated aerodynamic effects of rotating wheels on the air flow topology, the surface pressure and the integral drag of the vehicle could be reproduced in the simulation with sufficient quality. However, none of the investigated rotation methods could predict all the effects observed in the experiment with high accuracy. These findings suggest that there are aerodynamic phenomena of rotating wheels, which are currently not reproduced through the utilized numerical simulation approaches. The aerodynamic development of the vehicle industry has the ambition to define precise simulation methods with negligible deviations from the experiment. However, since the current computational simulation methods applied in this study represent only simplified approximations of the reality for various reasons, this requirement can currently not be met. To improve the predictive quality further, various topics are therefore recommended for subsequent studies on the simulation of wheel rotation effects on the vehicle.

The knowledge gained during this study should be extended to other vehicle types, as well as additional rim geometries and sizes in order to confirm and generalize these findings. The realistic deformation of the tire geometry due to the vehicle weight, as well as due to centrifugal forces, was neglected in this research. Furthermore, the formation of the contact patch of the tire with the road has been simplified. These geometric alterations are located at an aerodynamically sensitive area, wherefore it can be assumed that they represent an influential factor on the flow situation in the proximity of the wheels. For this reason, further works should consider these geometric alterations and study the effects on the aerodynamic behaviour of the vehicle.

Furthermore, the consideration of detailed tire treads, including longitudinal and transverse grooves, would further improve the predictive accuracy of the simulation. The consideration of realistic deformed and detailed tire surfaces in combination with the findings from the presented study would therefore be convenient. However, this approach requires the application of appropriate rotation methods, such as *Sliding Mesh*, that could not be considered in this study because of the restriction to steady-state *RANS* simulations.

Therefore, the application of transient simulation methods would be advisable, since not only transient effects would be taken into account, but also a dynamic geometric modification of the simulation mesh would be possible. This would allow the actual rotation of tire and rim geometries of the virtual model.

A simulation approach taking into account the dynamic deformation of detailed tire treads would then represent the final step to a highly realistic wheel rotation method.

References

[1] European Federation for Transport and Environment, “Mind the gap 2016,” 2016. `https://www.transportenvironment.org/publications/mind-gap-2016-report`.

[2] U. Tietge, S. Díaz, P. Mock, A. Bandivadekar, J. Dornoff, and N. Ligterink, “From laboratory to road: A 2018 update,” 2019. `https://theicct.org/publications/laboratory-road-2018-update`.

[3] Council of European Union, “Comission regulation (EU) no 2017/1151,” 2017. `https://eur-lex.europa.eu/legal-content/EN/TXT/PDF/?uri=CELEX:32017R1151&from=EN`.

[4] Council of European Union, “Comission regulation (EU) no 2009/443,” 2009. `https://eur-lex.europa.eu/legal-content/EN/TXT/PDF/?uri=CELEX:32009R0443&from=EN`.

[5] E. Mercker, N. Breuer, H. Berneburg, and H. J. Emmelmann, “On the aerodynamic interference due to the rolling wheels of passenger cars,” in *International Congress & Exposition*, SAE International, 1991.

[6] A. Klemin, “A belt method of representing the ground,” *Journal of the Aeronautical Sciences*, vol. 1, pp. 198–199, 1934.

[7] A. Morelli, “Aerodynamic actions on an automobile wheel,” in *Road Vehicle Aerodynamics-Proceedings of the First Symposium on Road Vehicle Aerodynamics, City University, London, edited by AJ Scibor-Rylski*, 1969.

[8] A. Morelli, “Aerodynamic Effects of an Automobile Wheel,” in *Technical Report Trans 47/69, MIRA*, 1969.

[9] W. R. Stapleford and G. W. Carr, *Aerodynamic characteristics of exposed rotating wheels*. Lindley [England]: Motor Industry Research Association, 1970.

[10] J. Fackrell and J. Harvey, “The flow field and pressure distribution of an isolated road wheel,” *Advances in Road Vehicle Aerodynamics*, 1973.

[11] J. Fackrell and J. Harvey, “The aerodynamics of an isolated road wheel,” *Aerodynamics of Sports and Competition Automobiles*, vol. 16, 1974.

[12] A. Cogotti, “Aerodynamic characteristics of car wheels,” *International Journal of Vehicle Design*, pp. 173–196, 1983.

[13] A. P. Mears, R. G. Dominy, and D. B. Sims-Williams, "The air flow about an exposed racing wheel," in *Motorsports Engineering Conference & Exhibition*, SAE International, 2002.

[14] A. P. Mears and R. G. Dominy, "Racing car wheel aerodynamics – comparisons between experimental and cfd derived flow-field data," in *Motorsports Engineering Conference & Exposition*, SAE International, 2004.

[15] L. Axon, K. Garry, and J. Howell, "An evaluation of cfd for modelling the flow around stationary and rotating isolated wheels," in *International Congress & Exposition*, SAE International, 1998.

[16] L. Axon, K. Garry, and J. Howell, "The influence of ground condition on the flow around a wheel located within a wheelhouse cavity," in *International Congress & Exposition*, SAE International, 1999.

[17] J. McManus and X. Zhang, "A computational study of the flow around an isolated wheel in contact with ground," *ASME. J. Fluids Eng.*, vol. 128, no. May 2006, pp. 520–530, 2006.

[18] A. Wäschle, S. Cyr, T. Kuthada, and J. Wiedemann, "Flow around an isolated wheel - experimental and numerical comparison of two cfd codes," in *SAE 2004 World Congress & Exhibition*, SAE International, 2004.

[19] E. Croner, H. Bézard, C. Sicot, and G. Mothay, "Aerodynamic characterization of the wake of an isolated rolling wheel," *International Journal of Heat and Fluid Flow*, vol. 43, pp. 233 – 243, 2013. 7th International Symposium on Turbulence Heat & Mass Transfer (THMT-7), Palermo Conference on Modelling Fluid Flow (CMFF'12).

[20] F. Gérardin, C. Gentric, and N. Midoux, "Particle dispersion in the near-wake of an isolated rotating wheel: Experimental and cfd study," *Journal of Aerosol Science*, vol. 76, pp. 56–71, 2014.

[21] J. Fabijanic, "An experimental investigation of wheel-well flows," in *International Congress & Exposition*, SAE International, 1996.

[22] T. Régert and T. Lajos, "Numerical simulation of flow field past road vehicle wheel," in *Proc. Third Conference on Mechanical Engineering, Budapest University of Technology and Economics*, pp. 244–248, 2002.

[23] T. Régert and T. Lajos, "Investigation of flow field past rotating wheels of cars," in *Proceedings of Conference on Modelling Fluid Flow (CMFF)*, pp. 387–394, 2003.

[24] T. Régert and T. Lajos, "Description of flow field in the wheelhouses of cars," *International Journal of Heat and Fluid Flow*, vol. 28, no. 4, pp. 616 – 629, 2007.

[25] S. Krajnović and L. Davidson, "Influence of floor motions in wind tunnels on the aerodynamics of road vehicles," *Journal of Wind Engineering and Industrial Aerodynamics*, vol. 93, no. 9, pp. 677–696, 2005.

[26] J. E. Hackett, J. E. Williams, J. B. Baker, and S. B. Wallis, "On the influence of ground movement and wheel rotation in tests on modern car shapes," in *SAE International Congress & Exposition*, SAE International, 1987.

[27] F. Damiani, G. Iaccarino, G. Kalitzin, and B. Khalighi, “Unsteady flow simulations of wheel-wheelhouse configurations,” in *34th AIAA Fluid Dynamics Conference and Exhibit*, American Institute of Aeronautics and Astronautics, 2004.

[28] I. Dimitriou and S. Klussmann, “Aerodynamic forces of exposed and enclosed rotating wheels as an example of the synergy in the development of racing and passenger cars,” in *SAE 2006 World Congress & Exhibition*, SAE International, 2006.

[29] P. Mlinaric, “Investigation of the influence of tyre deformation and tyre contact patch on CFD predictions of aerodynamic forces on a passenger car,” Master’s thesis, Chalmers University of Technology, Gothenburg, Sweden, 2007.

[30] A. L. Oswald and L. J. Browne, “The airflow field around an operating tire and its effect on tire power loss,” in *SAE International Congress & Exposition*, SAE International, 1981.

[31] G. Wickern, K. Zwicker, and M. Pfadenhauer, “Rotating wheels - Their impact on wind tunnel test techniques and on vehicle drag results,” in *SAE International Congress and Exposition*, SAE International, 1997.

[32] J. Wiedemann, “The influence of ground simulation and wheel rotation on aerodynamic drag optimization - Potential for reducing fuel consumption,” in *International Congress & Exposition*, SAE International, 1996.

[33] G. Wickern and N. Lindener, “The Audi aeroacoustic wind tunnel: Final design and first operational experience,” in *SAE 2000 World Congress*, SAE International, 2000.

[34] P. Elofsson and M. Bannister, “Drag reduction mechanisms due to moving ground and wheel rotation in passenger cars,” in *SAE 2002 World Congress & Exhibition*, SAE International, 2002.

[35] S. Koitrand and S. Rehnberg, “A computational investigation of wheel and underbody flow interaction,” Master’s thesis, Chalmers University of Technology, Gothenburg, Sweden, 2013.

[36] S. Koitrand, L. Lofdahl, S. Rehnberg, and A. Gaylard, “A computational investigation of ground simulation for a saloon car,” *SAE Int. J. Commer. Veh.*, vol. 7, 2014.

[37] A. Wäschle, “The influence of rotating wheels on vehicle aerodynamics - Numerical and experimental investigations,” in *SAE World Congress & Exhibition*, SAE International, 2007.

[38] C. Landström, T. Walker, and L. Löfdahl, “Effects of ground simulation on the aerodynamic coefficients of a production car in yaw conditions,” in *SAE 2010 World Congress & Exhibition*, SAE International, 2010.

[39] B. H. Schnepf, *Untersuchung von Einflussfaktoren auf die Umströmung eines Pkw-Rades in Simulation und Experiment.* Dissertation, Technische Universität München, München, Germany, 2016.

[40] C. Landström, *Passenger Car Wheel Aerodynamics.* PhD thesis, Chalmers University of Technology, Gothenburg, Sweden, 2011.

[41] C. Landström, L. Löfdahl, and T. Walker, “Detailed flow studies in close proximity of rotating wheels on a passenger car,” *SAE Int. J. Passeng. Cars – Mech. Syst.*, vol. 2, 2009.

[42] Q. Zhiling, C. Landström, L. Lennart, and L. Josefsson, “Wheel aerodynamic developments on passenger cars by module-based prototype rims and stationary rim shields,” in *FISITA 2010 Automotive World Congress*, FISITA, 2010.

[43] C. Landström, T. Walker, L. Christoffersen, and L. Löfdahl, “Influences of different front and rear wheel designs on aerodynamic drag of a Sedan type passenger car,” in *SAE 2011 World Congress & Exhibition*, SAE International, 2011.

[44] C. Landström, L. Josefsson, T. Walker, and L. Löfdahl, “An experimental investigation of wheel design parameters with respect to aerodynamic drag,” in *Progress in Vehicle Aerodynamics and Thermal Management: Proceedings of the 8th FKFS-Conference*, Expert-Verlag GmbH, 2011.

[45] C. Landström, L. Josefsson, T. Walker, and L. Löfdahl, “Aerodynamic effects of different tire models on a Sedan type passenger car,” *SAE Int. J. Passeng. Cars - Mech. Syst.*, vol. 5, 2012.

[46] F. F. Buscariolo and K. J. Karbon, “Comparative CFD analysis between rotating and static cases of different wheels opening designs over a performance sedan,” in *SAE Brasil 2011 Congress and Exhibit*, SAE International, 2011.

[47] C. Landström, S. Sebben, and L. Löfdahl, “Effects of wheel orientation on predicted flow field and forces when modelling rotating wheels using CFD,” in *8th MIRA International Vehicle Aerodynamics Conference*, 2010.

[48] J. Cederlund and J. Vikström, “The aerodynamic influence of rim design on a sports car and its interaction with the wing and diffuser flow,” Master’s thesis, Chalmers University of Technology, Gothenburg, Sweden, 2010.

[49] A. Cogotti, “Preliminary Information on the New Moving Ground System of the Pininfarina Wind Tunnel,” in *Motorsports Engineering Conference & Exposition*, SAE International, 2006.

[50] A. Cogotti, “Evolution of performance of an automotive wind tunnel,” *Journal of Wind Engineering and Industrial Aerodynamics*, vol. 96, no. 6-7, pp. 667–700, 2008.

[51] E. G. Duell, A. Kharazi, S. Muller, W. Ebeling, and E. Mercker, “The BMW AVZ Wind Tunnel Center,” in *SAE 2010 World Congress & Exhibition*, SAE International, 2010.

[52] A. Hennig, A. Michelbach, N. Widdecke, and J. Wiedemann, “Optimierung der Laufband-Technologie im 1:1-Aeroakustik-Fahrzeugwindkanal,” *ATZ - Automobiltechnische Zeitschrift*, vol. 114, no. 114, pp. 80–85, 2012.

[53] M.-S. Kim, J.-H. Lee, J.-D. Kee, and J.-H. Chang, “Hyundai full scale aero-acoustic wind tunnel,” in *SAE 2001 World Congress*, SAE International, 2001.

[54] S. Mack, T. Indinger, N. A. Adams, and P. Unterlechner, "The ground simulation upgrade of the large wind tunnel at the Technische Universität München," in *SAE 2012 World Congress & Exhibition*, SAE International, 2012.

[55] J. McKillen, J. Walter, and M. Geslin, "The Honda R&D Americas Scale Model Wind Tunnel," *SAE Int. J. Passeng. Cars - Mech. Syst.*, pp. 289–303, 2012.

[56] SAWTC, "SAWTC - Tongji University Shanghai Automotive Wind Tunnel Center - Brochure 2010," 2010.

[57] J. Sternéus, T. Walker, and T. Bender, "Upgrade of the Volvo cars aerodynamic wind tunnel," in *SAE World Congress & Exhibition*, SAE International, 2007.

[58] K. Tadakuma, T. Sugiyama, K. Maeda, M. Iyota, M. Ohta, and Y. Komatsu, "Development of full-scale wind tunnel for enhancement of vehicle aerodynamic and aero-acoustic performance," *SAE International Journal of Passenger Cars - Mechanical Systems*, vol. 7, no. 2, pp. 603–616, 2014.

[59] J. Walter, J. Bordner, B. Nelson, and A. Boram, "The windshear rolling road wind tunnel," *SAE International Journal of Passenger Cars - Mechanical Systems*, pp. 265–288, 2012.

[60] J. Walter, E. Duell, B. Martindale, S. Arnette, R. Geierman, M. Gleason, and G. Romberg, "The DaimlerChrysler full-scale aeroacoustic wind tunnel," in *SAE 2003 World Congress & Exhibition*, SAE International, 2003.

[61] P. Waudby-Smith, T. Bender, and R. Vigneron, "The GIE S2A full-scale aero-acoustic wind tunnel," *SAE Paper*, vol. 2004, no. 724, 2004.

[62] J. Wiedemann and J. Potthoff, "The new 5-belt road simulation system of the IVK wind tunnels - Design and first results," in *SAE 2003 World Congress & Exhibition*, SAE International, 2003.

[63] ANSYS, Inc., *ANSYS FLUENT, Release 15.0, Theory Guide.* ANSYS, Inc, 2013.

[64] G. Bukovnik, W. von der Linden, and G. Brenn, "Impact of rim orientation on road vehicles aerodynamics simulations," in *WCX SAE World Congress Experience*, SAE International, 2020.

[65] G. Falkovich, *Fluid Mechanics: A Short Course for Physicists.* Cambridge University Press, 2011.

[66] F. Moukalled, L. Mangani, and M. Darwish, *The Finite Volume Method in Computational Fluid Dynamics: An Advanced Introduction with OpenFOAM and Matlab.* Springer Publishing Company, Incorporated, 1st ed., 2015.

[67] H. Oertel jr., *Prandtl - Führer durch die Strömungslehre.* Springer Vieweg, 2017.

[68] J. Spurk and N. Aksel, *Strömungslehre.* Springer Vieweg, 2019.

[69] T. Schütz, *Hucho - Aerodynamik des Automobils.* Springer Vieweg, 2013.

[70] R. Blumrich, N. Widdecke, J. Wiedemann, A. Michelbach, F. Wittmeier, and O. Beland, “New FKFS Technology at the Full-Scale Aeroacoustic Wind Tunnel of University of Stuttgart,” *SAE Int. J. Passeng. Cars - Mech. Syst.*, 2015.

[71] J. Williams, “Aerodynamic drag of engine-cooling airflow with external interference,” in *SAE 2003 World Congress & Exhibition*, SAE International, 2003.

[72] A. Gaylard, “The appropriate use of CFD in the automotive design process,” in *SAE World Congress & Exhibition*, SAE International, 2009.

[73] S. Kandasamy, B. Duncan, H. Gau, F. Maroy, A. Belanger, N. Gruen, and S. Schäufele, “Aerodynamic performance assessment of BMW validation models using computational fluid dynamics,” in *SAE 2012 World Congress & Exhibition*, SAE International, 2012.

[74] M. Lanfrit, *Best practice guidelines for handling Automotive External Aerodynamics with FLUENT, Version 1.2.* Fluent Deutschland GmbH, 2005.

[75] P. Peddiraju, A. Papadopoulous, and R. Singh, “CAE frame work for aerodynamic design development of automotive vehicles,” in *3rd ANSA & μETA International Conference*, BETA CAE Systems, 2009.

[76] ANSYS, Inc., *ANSYS FLUENT, Release 15.0, User’s Guide.* ANSYS, Inc, 2013.

[77] T. Hobeika, S. Sebben, and C. Landstrom, “Investigation of the influence of tyre geometry on the aerodynamics of passenger cars,” *SAE Int. J. Passeng. Cars - Mech. Syst.*, vol. 6, pp. 316–325, 2013.

[78] C. Neuper, “Virtual tire models for tire deformations in the industrial aerodynamic CFD development,” Master’s thesis, Graz University of Technology, Graz, Austria, 2020.

[79] C. Vasiu, “Modelling of realistic tire features in CFD,” Master’s thesis, Management Center Innsbruck, Innsbruck, Austria, 2015.

[80] J. H. Ferziger and M. Peric, *Computational Methods for Fluid Dynamics.* Springer Berlin Heidelberg, 2001.

[81] H. K. Versteeg and W. Malalasekera, *An Introduction to Computational Fluid Dynamics: The Finite Volume Method.* Pearson Education Limited, 2007.

[82] F. R. Menter, “Two-equation eddy-viscosity turbulence models for engineering applications,” *AIAA Journal*, vol. 32, pp. 1598–1605, 1994.

[83] D. C. Wilcox, “Reassessment of the scale-determining equation for advanced turbulence models,” *AIAA Journal*, vol. 26, pp. 1299–1310, 1988.

[84] P. Forchheimer, “Wasserbewegung durch Boden,” *Zeitschrift des Vereines Deutscher Ingenieure*, vol. 45, pp. 1782–1788, 1901.

[85] R. A. Granger, *Fluid Mechanics.* Dover Publications, 1995.

[86] T. Kuthada, *Die Optimierung von Pkw-Kühlluftführungssystemen unter dem Einfluss moderner Bodensimulationstechniken.* Schriftenreihe des Instituts für Verbrennungsmotoren und Kraftfahrwesen der Universität Stuttgart, Expert-Verlag, 2006.

[87] T. Kuthada and J. Wiedemann, "Investigations in a cooling air flow system under the influence of road simulation," in *SAE World Congress & Exhibition*, SAE International, 2008.

[88] W. R. Sears and D. P. Telionis, "Boundary-layer separation in unsteady flow," *SIAM Journal of Applied Mathematics*, vol. 28, pp. 215–235, 1975.

[89] W. T. Kelvin Lord, "Hydrokinetic solutions and observations," *The London, Edinburgh, and Dublin Philosophical Magazine and Journal of Science*, vol. 42, no. 281, pp. 362–377, 1871.

[90] H. von Helmholtz, "Über diskontinuierliche Flüssigkeitsbewegungen," *Monatsberichte der Königlich Preussischen Akademie des Wissenschaften zu Berlin*, vol. 23, pp. 215–228, 1868.

Appendix A

Impact of rim orientation on vehicle aerodynamics

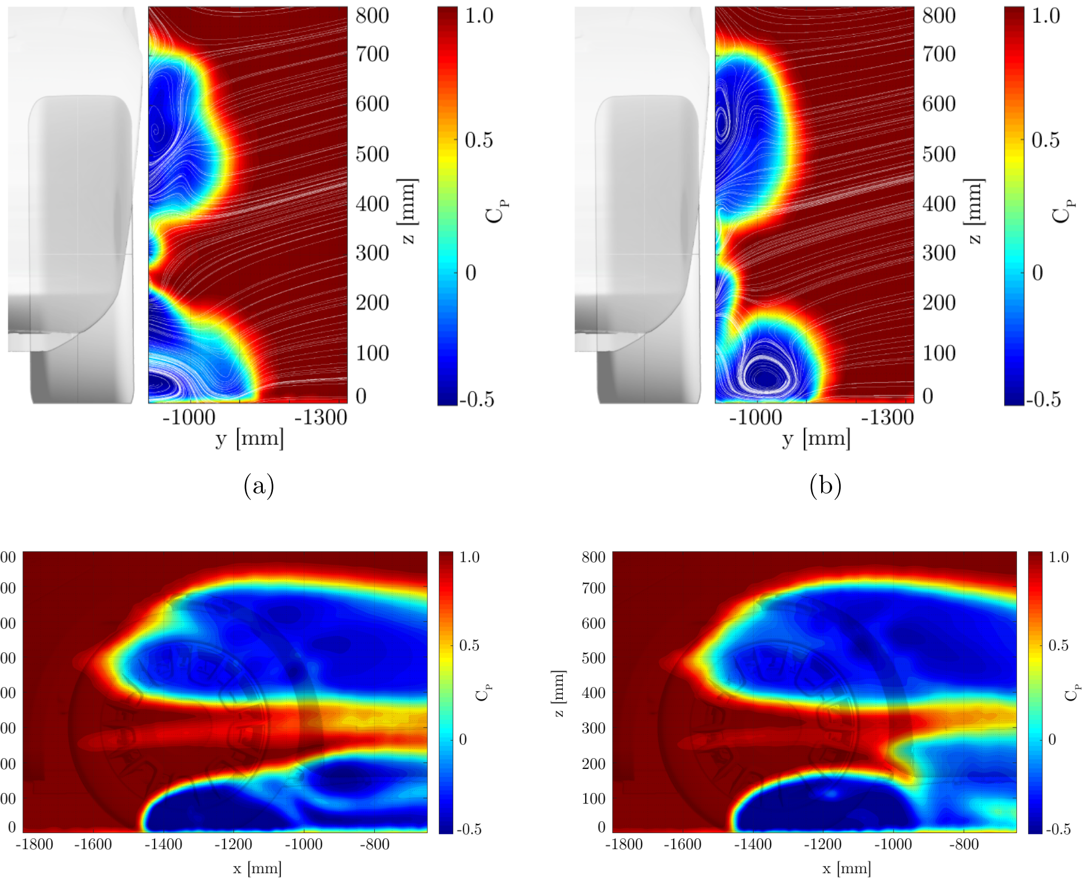

(a)

(b)

(c)

(d)

Figure A.1: Pressure coefficient C_P downstream of the wheel arch for the stationary simulation case with rims *Rim17*. Rim orientation α (*B.17.NR*) (left), and β (*D.17.NR*) (right), at *plane A* with projected streamlines (top) and *plane I* (bottom).

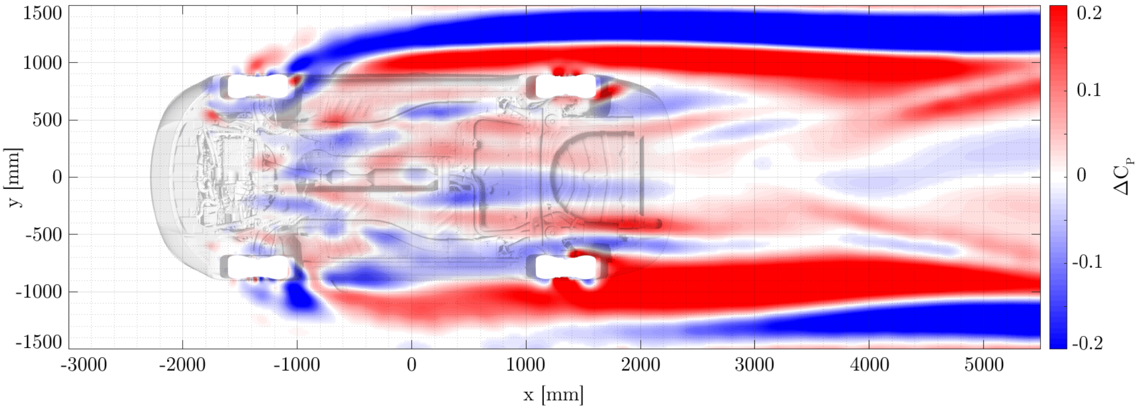

Figure A.2: Pressure coefficient difference ΔC_P between rim orientation α and β in the underbody *plane E* for the stationary simulation cases with *Rim17* (*D.17.NR*-*B.17.NR*).

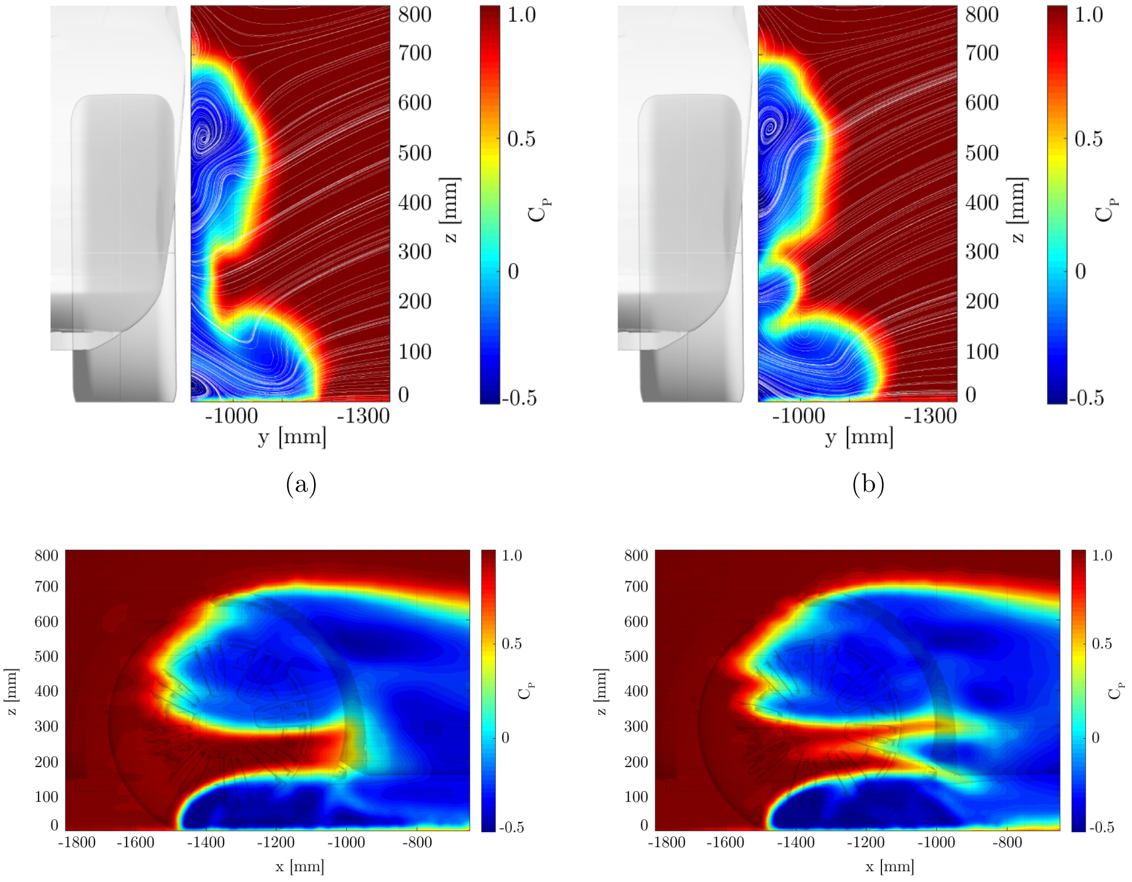

(a)

(b)

(c)

(d)

Figure A.3: Pressure coefficient C_P downstream of the wheel arch for the stationary simulation case with rims *Rim18*. Rim orientation α (*B.18.NR*) (left), and β (*D.18.NR*) (right), at *plane A* with projected streamlines (top) and *plane I* (bottom).

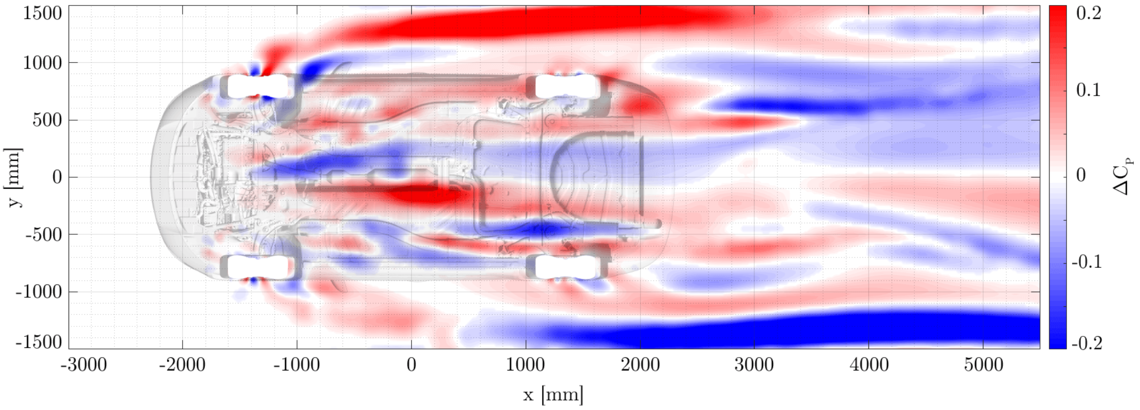

Figure A.4: Pressure coefficient difference ΔC_P between rim orientation α and β in the underbody *plane E* for the stationary simulation case with *Rim18* (*D.18.NR*-*B.18.NR*).

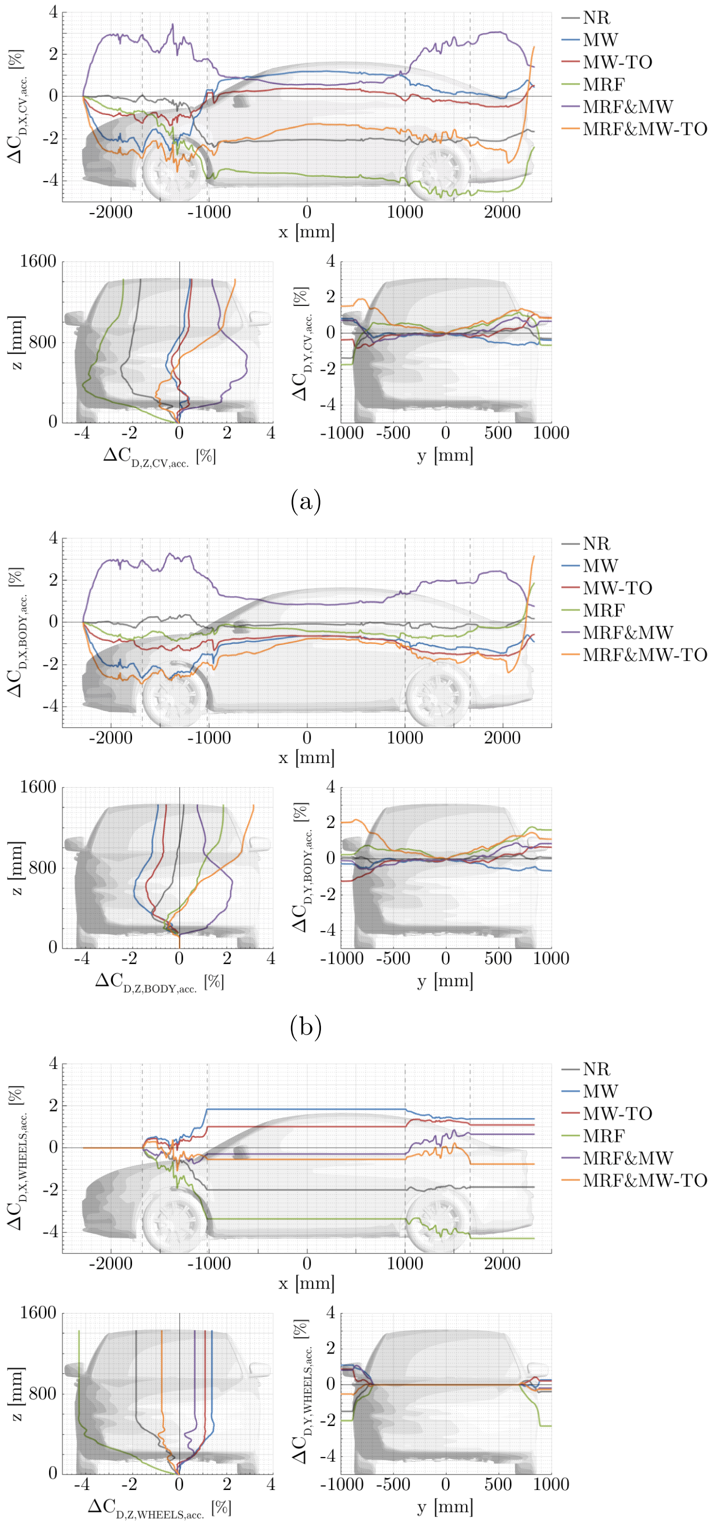

(a)

(b)

(c)

Figure A.5: Development of the accumulated drag coefficient differences of the vehicle $\Delta C_{D,\text{CV}}$ (top), the body $\Delta C_{D,\text{BODY}}$ (center) and the wheels $\Delta C_{D,\text{WHEELS}}$ (bottom) along the vehicle axes for *Rim16* and cooling mockup setup. Simulation cases *C.16.*-A.16.**.

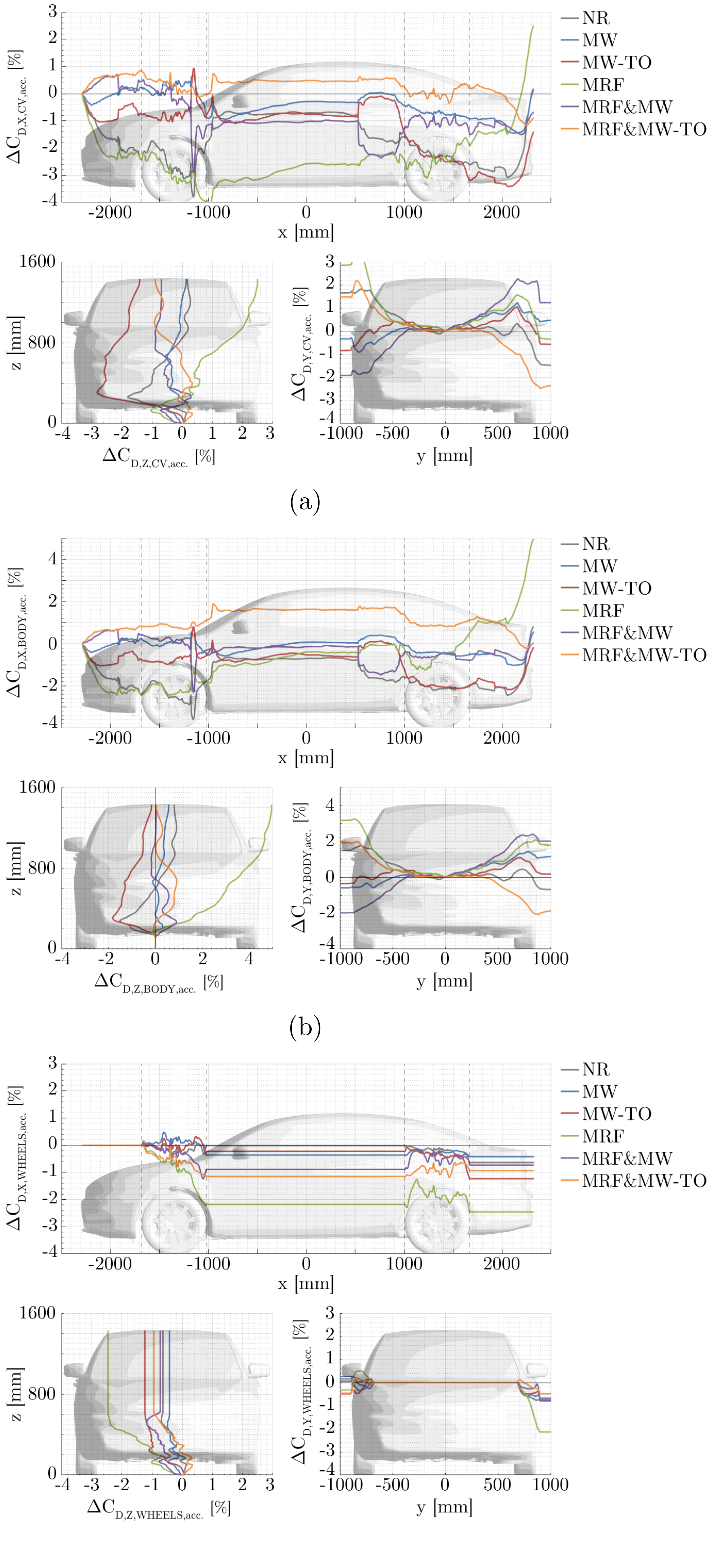

Figure A.6: Development of the accumulated drag coefficient differences of the vehicle $\Delta C_{D,\mathrm{CV}}$ (top), the body $\Delta C_{D,\mathrm{BODY}}$ (center) and the wheels $\Delta C_{D,\mathrm{WHEELS}}$ (bottom) along the vehicle axes for *Rim17* and cooling mockup setup. Simulation cases *C.17.*-A.17.**.

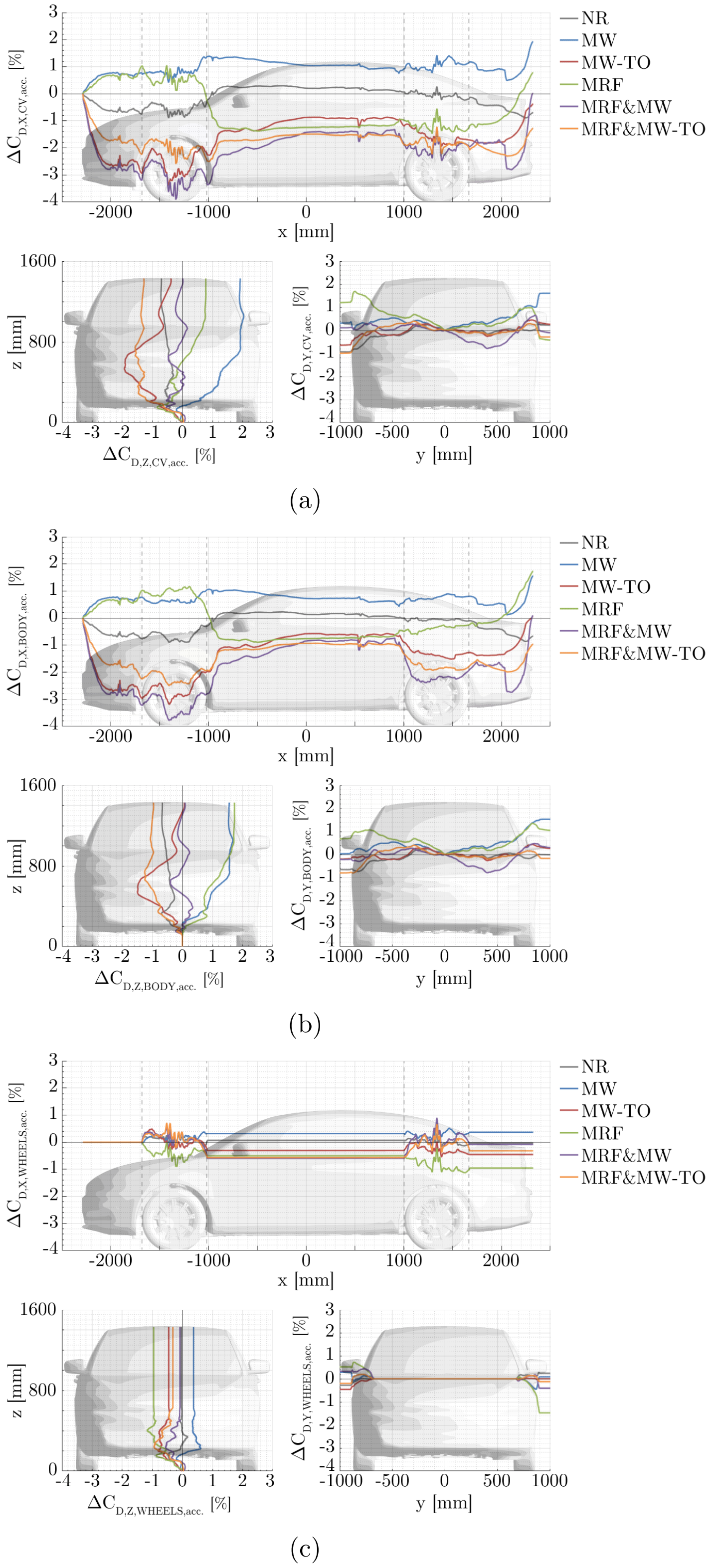

(a)

(b)

(c)

Figure A.7: Development of the accumulated drag coefficient differences of the vehicle $\Delta C_{D,\mathrm{CV}}$ (top), the body $\Delta C_{D,\mathrm{BODY}}$ (center) and the wheels $\Delta C_{D,\mathrm{WHEELS}}$ (bottom) along the vehicle axes for *Rim18* and cooling mockup setup. Simulation cases *C.18.*-A.18.**.

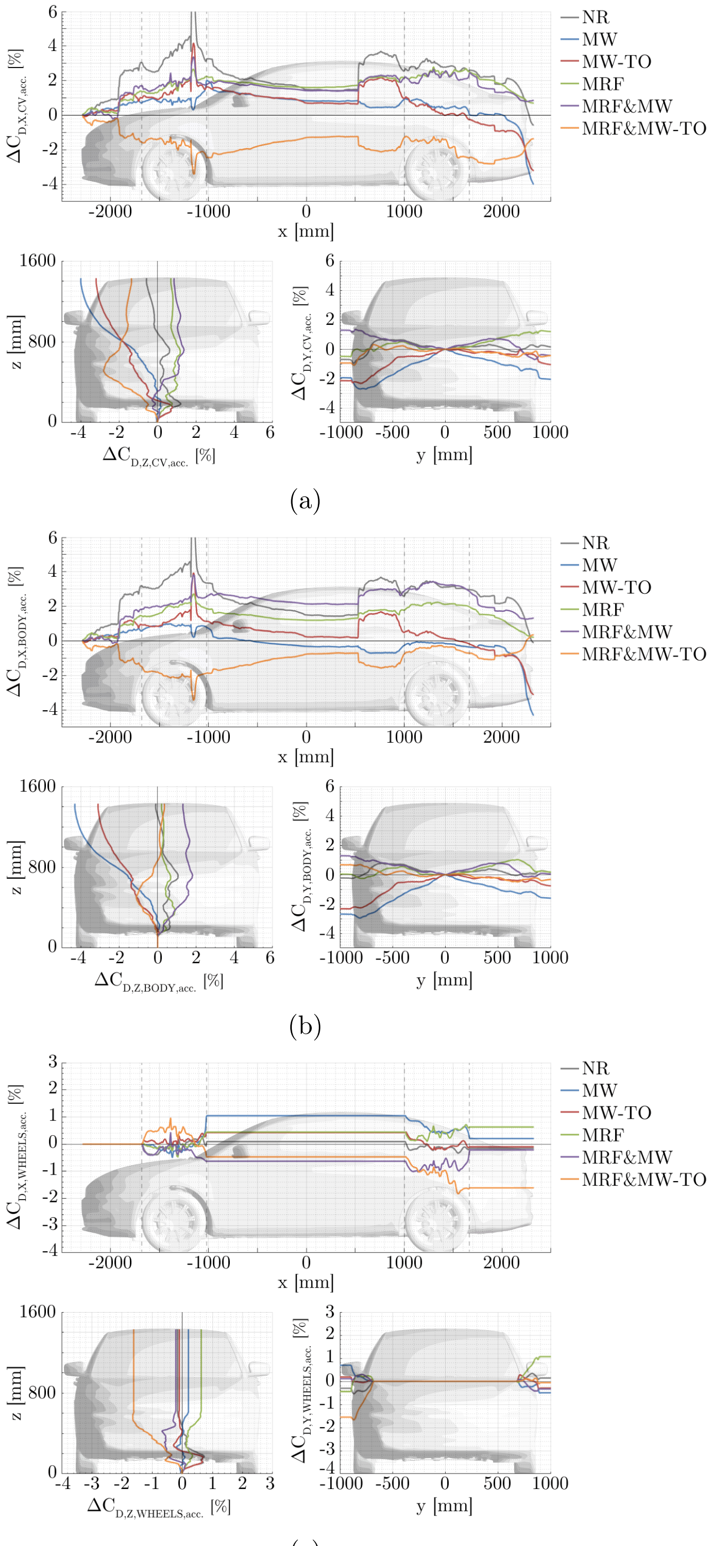

(a)

(b)

(c)

Figure A.8: Development of the accumulated drag coefficient differences of the vehicle $\Delta C_{D,\mathrm{CV}}$ (top), the body $\Delta C_{D,\mathrm{BODY}}$ (center) and the wheels $\Delta C_{D,\mathrm{WHEELS}}$ (bottom) along the vehicle axes for *Rim17* and enabled cooling air flow. Simulation cases *D.17.*-B.17.**.

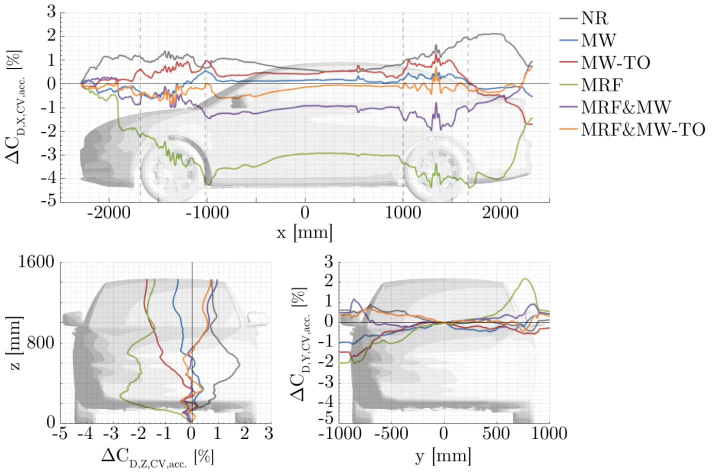

(a)

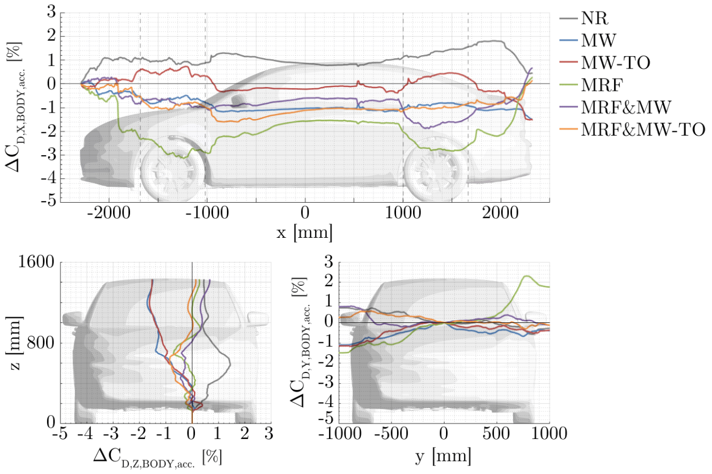

(b)

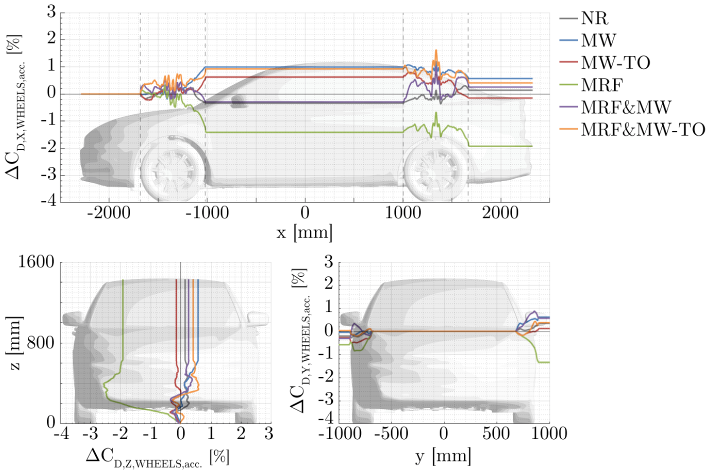

(c)

Figure A.9: Development of the accumulated drag coefficient differences of the vehicle $\Delta C_{D,\mathrm{CV}}$ (top), the body $\Delta C_{D,\mathrm{BODY}}$ (center) and the wheels $\Delta C_{D,\mathrm{WHEELS}}$ (bottom) along the vehicle axes for *Rim18* and enabled cooling air flow. Simulation cases *D.18.*-B.18.**.

Appendix B

Impact of wheel rotation methods on wheel arch aerodynamics

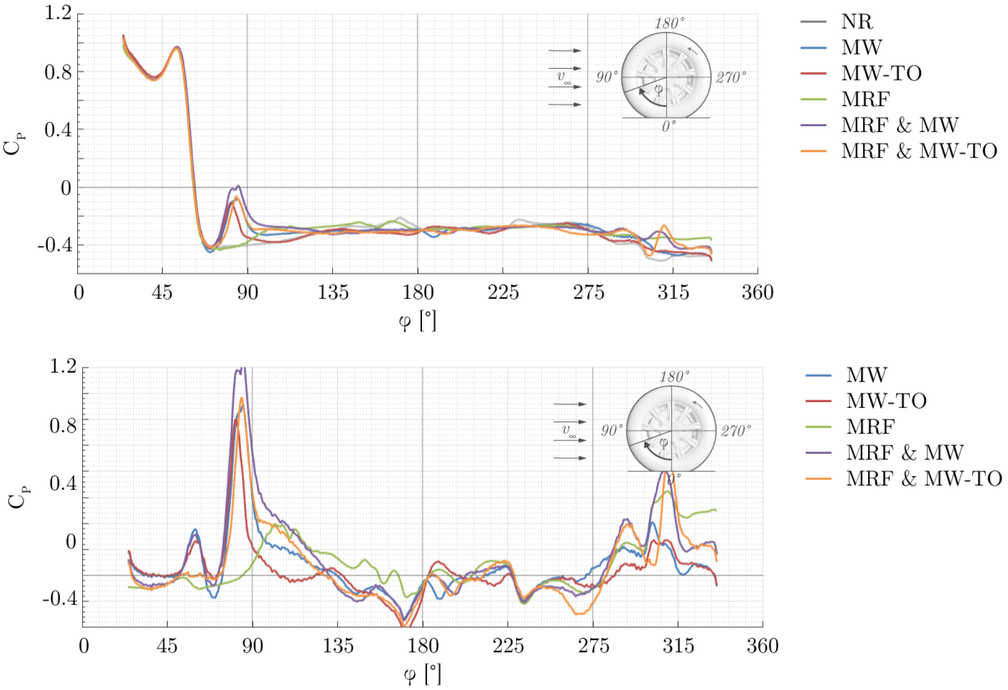

Figure B.1: Pressure coefficient C_P (top) and pressure coefficient differences ΔC_P (bottom) at the tire tread along the centerline of the wheel for *Rim17*. Simulation cases *B.17.** and *B.17.*-B.17.NR*.

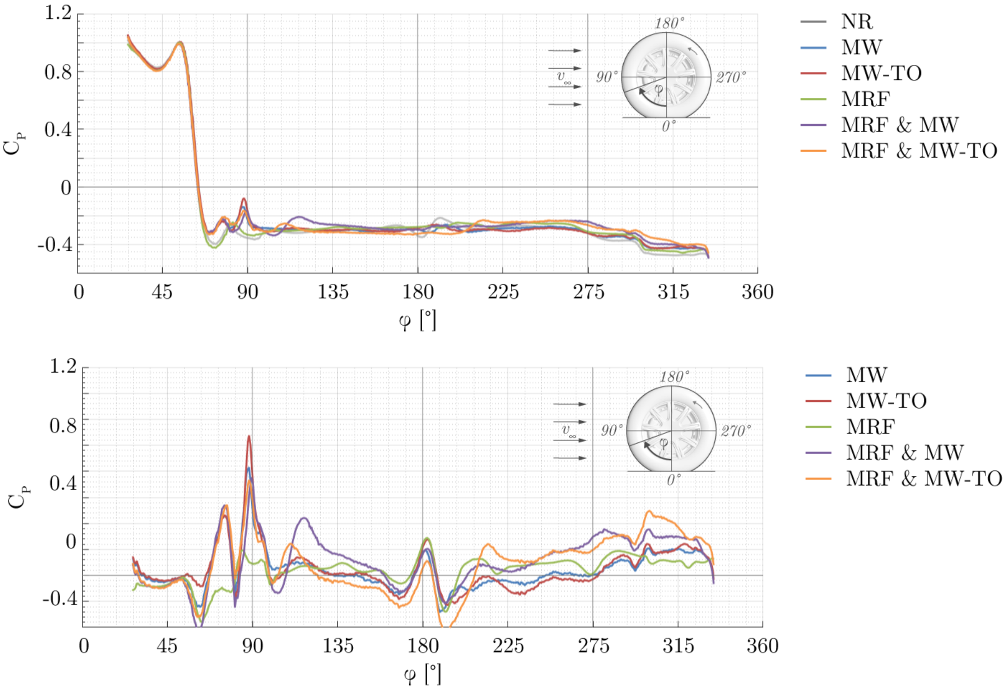

Figure B.2: Pressure coefficient C_P (top) and pressure coefficient differences ΔC_P (bottom) at the tire tread along the centerline of the wheel for *Rim18*. Simulation cases *B.18.** and *B.18.*-B.18.NR*.

Appendix C

Impact of wheel rotation on vehicle aerodynamics

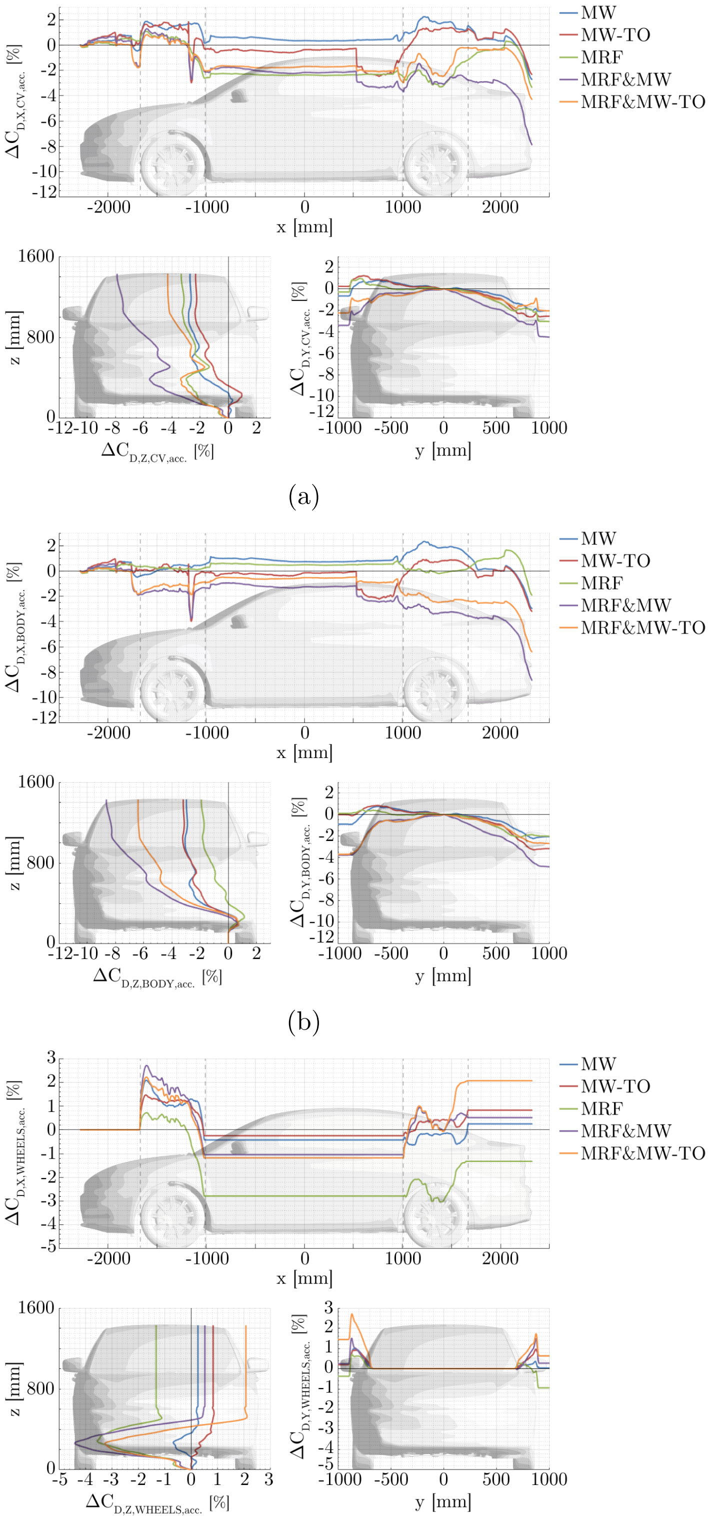

(a)

(b)

(c)

Figure C.1: Development of the accumulated drag coefficient differences of the vehicle $\Delta C_{D,\mathrm{CV}}$ (top), the body $\Delta C_{D,\mathrm{BODY}}$ (center) and the wheels $\Delta C_{D,\mathrm{WHEELS}}$ (bottom) along the vehicle axes for *Rim17* and enabled cooling air flow. Simulation cases *B.17.*-B.17.NR*.

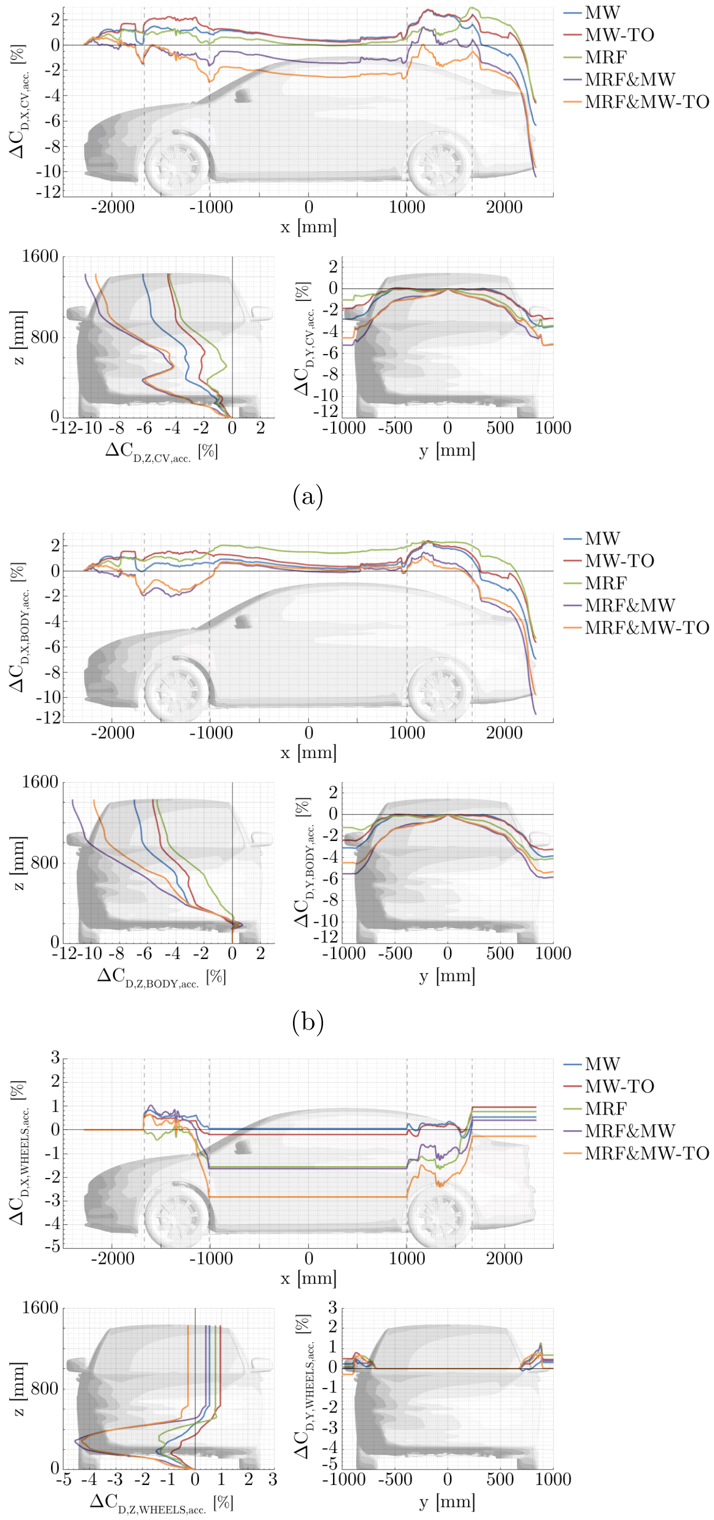

(a)

(b)

(c)

Figure C.2: Development of the accumulated drag coefficient differences of the vehicle $\Delta C_{D,\text{CV}}$ (top), the body $\Delta C_{D,\text{BODY}}$ (center) and the wheels $\Delta C_{D,\text{WHEELS}}$ (bottom) along the vehicle axes for *Rim18* and enabled cooling air flow. Simulation cases *B.18.*-B.18.NR*.